UNIVERSITY OF CATANIA

Department of Civil Engineering and Architecture

A thesis submitted in fulfilment of the requirements for the degree of Doctor of Philosophy

"Assessment and Mitigation of Urban and Territorial Risks"

XXXV Study Cycle

Out-of-plane seismic response of Unreinforced Masonry structures: a Discrete Macro-Element Approach including P-Delta effects

Valeria Cusmano

Supervisors:

Prof. Ivo Caliò

Dr. Bartolomeo Pantò

Co-Supervisors:

Prof. Salvatore Caddemi

Dr. Davide Rapicavoli

Dr. Francesco Cannizzaro

Coordinator:

Prof. Antonino Cancelliere

ABSTRACT

This thesis presents an upgrade of the discrete macro-element model (DMEM), accounting for P-Delta effects (P-Δ), to describe the rocking response of masonry walls subjected to Out-Of-Plane (OOP) loadings.

According to the DMEM strategy, the proposed model describes the wall by a mesh of discrete macro-elements connected by interfaces accounting for material nonlinearities and takes into accounts constitutive and geometric nonlinearities still maintaining a limited computational cost, compared to refined Distinct Element and Finite Element approaches. The model also allows for a straightforward calibration based on macroscopic mechanical masonry parameters following a fiber calibration strategy which encompasses the membrane behaviour on the elements' interfaces. The three-dimensionality of the macro-elements allows to include both the in-plane and the OOP behaviour avoiding limiting the global model to the simulation of the box behavior only, as in the well-known equivalent frame models or other simplified approach in which only the in-plane behaviour of masonry walls is accounted for.

OOP failure mechanisms are one of the main causes of severe damage or structural failure for unreinforced masonry (URM) buildings, including historical and monumental constructions subjected to seismic actions, as pointed out by observations after even not strong earthquakes. The activation of these mechanisms is generally associated with lower seismic excitation and displacements than those necessary for in-plane collapse. However, after their activation, these mechanisms may often evolve towards large displacements, related to rigid-block-like kinematics, that strongly affect the mechanical post-peak response. Therefore, geometrical nonlinearities, often ignored in the numerical models for computational reasons, should be included in the analyses when OOP failure mechanisms dominates the structural response.

This thesis presents a new, simplified, still accurate DMEM P-Delta formulation according to which the global equilibrium is imposed by referring to the undeformed

system configuration, avoiding assembling and updating the geometrical stiffness matrix during the analysis. Then, the system load vector is updated at each step of the analysis, accounting for the additional moments generated by the forces acting on the macro-elements in the deformed configuration. The proposed model is validated in the static field against closed-form analytical solutions of rigid-block-like benchmarks in large displacements and with reference to the results of quasi-static experimental tests already available in the literature. In addition, extensive parametric analyses are performed to investigate the role of the mechanical parameters of masonry and geometrical characteristic of the wall on the rocking response.

Moreover, aiming at investigating the role of dissipation involved on the OOP response, a stiffness-proportional damping model is considered and associated with interface elements to describe the dynamic response of rigid blocks approximating masonry-wall kinematics. With this purpose, a local damping matrix is computed at each interface identifying a rocking section of the OOP failure kinematics. This damping matrix is updated at each step of the analysis keeping it proportional to the local tangential stiffness matrix of the interface and summed to the global damping matrix, accounting for other sources of energy damping not explicitly accounted for in the model. The proposed damping model is then validated by carrying out dynamic free- and harmonic-vibration analyses on quasi-rigid blocks and comparing the results with some experimental tests conducted on quasi-rigid blocks, analytical solutions, and advanced FEM simulations available in the literature. The results demonstrated that the proposed damping model, combined with the newly-developed P-Delta DMEM formulation, accurately predicts the nonlinear rocking response of masonry walls up to the attainment of the critical configuration at which gravity loads becomes un-stabilising.

In the last part of the thesis, representative case studies represented by a church's façade and an entire church are analysed through static and dynamic analyses. P-Delta effects are alternatively considered and neglected in the simulations in order to evaluate their influence on the response and on the evaluation of the ultimate capacity of a real unreinforced masonry structure.

ABSTRACT

(Italian version)

Il presente lavoro presenta un'evoluzione the macro-elemento discrete che tiene conto degli effetti del secondo ordine (cosiddetti effetti P-Delta P-Δ) in grado di descriver la risposta di rocking di muri in muratura soggetti a carichi fuori dal proprio piano.

In accordo con la strategia a macro-elementi discreti, il modello proposto descrive un muro di muratura attraverso una mesh di macro-elementi discreti connessi tramite interfacce che simulano le non linearità costitutive e considera l'effetto delle non linearità geometriche seppur mantenendo un onere computazionale limitato se confrontato con le più accurate strategie di modellazione agli elementi finiti (Finite Element Method FEM) e agli elementi distinti (Distinct Element Method DEM). Il modello consente anche una semplice calibrazione basata su parametri meccanici macroscopici della muratura seguendo una semplice seppur efficace strategia di calibrazione a fibre. La tridimensionalità dei macroelementi consente di includere sia il comportamento nel piano che quello fuori piano evitando di limitare il modello globale alla sola simulazione del comportamento detto "box-type", come nei noti modelli a telaio equivalente o ad altri approcci semplificati in cui viene considerato solo il comportamento nel piano delle pareti in muratura.

I meccanismi di collasso fuori piano sono una delle principali cause di danno o addirittura collasso strutturale per strutture murarie non rinforzate che includono costruzioni storiche e monumentali soggette a carichi di tipo sismico, come dimostrato dalle diverse osservazioni dopo terremoti anche di intensità limitata. L'attivazione di questi meccanismi è generalmente associata a eccitazione e spostamenti sismici inferiori a quelli necessari per il collasso nel piano. Tuttavia, dopo la loro attivazione, questi meccanismi possono spesso evolvere verso grandi spostamenti, associati a cinematiche da blocco rigido, che influenzano fortemente la risposta meccanica e cinematica post-picco. Pertanto, le non-linearità geometriche, spesso ignorate nei modelli numerici per ragioni computazionali,

dovrebbero essere incluse nelle analisi quando i meccanismi di collasso fuori piano dominano la risposta strutturale.

Il presente lavoro presenta una nuova, semplificata ma allo stesso tempo accurata, formulazione degli effetti P-Delta all'interno della strategia di modellazione a macro-elementi discreti secondo cui l'equilibrio globale viene imposto facendo riferimento alla configurazione del sistema indeformata, evitando di assemblare e aggiornare la matrice di rigidezza geometrica durante l'analisi. l vettore di carico del sistema viene, quindi, aggiornato in ogni fase dell'analisi, tenendo conto dei momenti aggiuntivi generati dalle forze agenti sui macroelementi nella configurazione deformata. Il modello proposto è validato in campo statico rispetto a soluzioni analitiche in forma chiusa di benchmark a blocchi rigidi in grandi spostamenti e con riferimento ai risultati di prove sperimentali quasi-statiche già disponibili in letteratura. Inoltre, vengono eseguite ampie analisi parametriche per indagare il ruolo dei parametri meccanici della muratura e delle caratteristiche geometriche della parete sulla risposta di rocking della parete muraria.

Inoltre, al fine di investigare il ruolo della dissipazione coinvolta nel meccanismo di rocking di un blocco rigido, è stato considerato un modello di damping proporzionale alla rigidezza locale delle interfacce. Con questo scopo, è stata calcolata e assemblata un amatrice di smorzamento locale per ogni interfaccia di rocking. Tale matrice di smorzamento viene aggiornata ad ogni step dell'analisi in modo che sia ad ogni instante proporzionale alla matrice di rigidezza tangente delle interfacce. Qualora siano presente alter sorgenti di dissipazione viscosa tale matrici vengono sommate. Il modello di smorzamento proposto è stato quindi validato conducendo analisi dinamiche non lineari in vibrazioni libere e armoniche su modelli di blocco rigido confrontando i risultai con quelli previsti dalla teoria classica proposta da Housner nel 1963 e con test sperimentali riportati in letteratura che includono avanzate simulazioni agli elementi finite. I risultati hanno dimostrato che il modello di smorzamento proposto, combinato con la formulazione P-Delta DMEM di nuova concezione, prevede accuratamente la risposta fuori piano non lineare delle pareti in muratura fino al raggiungimento della configurazione critica in corrispondenza della quale i carichi gravitazionali diventano non stabilizzanti.

Nell'ultima parte della tesi, attraverso analisi statiche e dinamiche non lineari, vengono analizzati casi studio rappresentativi. In particolare, due casi studio sono stati analizzati: uno relative ad una facciata di una chiesa e uno relativo ad un modello di un'intera chiesa. Gli effetti P Delta sono alternativamente considerati e trascurati nelle simulazioni al fine di valutarne l'influenza sulla risposta e sulla valutazione della capacità ultima di una struttura muraria.

List of Content

List of Figures

List of Tables

1. INTRODUCTION

Unreinforced Masonry (URM) structures, including historical and monumental construction, represent a significant percentage of architectural heritage in several seismic areas worldwide, some of which have significant social and cultural value. However, the high vulnerability of these structures has been pointed out by several post-earthquake surveys [1]–[6], highlighting how they suffer severe damage even in the occurrence of moderate magnitude earthquakes, with significant economic, social, and human losses. The seismic assessment of URM structures is one of the most important current research topics for safety reasons, related to the loss of human lives and the need to preserve the existing architectural heritage. For all these reasons, an in-depth knowledge of the dynamic response of existing and historical masonry structures and reliable numerical tools for its prediction are needed. In the last few decades, significant research has been conducted in order to develop reliable and efficient numerical methods, some of which have been implemented into technical regulations to guide practitioners toward seismic assessment and retrofitting of URM structures.

1.1 Seismic response of unreinforced masonry buildings

Masonry can be defined as a heterogeneous material whose macroscopic behaviour is related to the mechanical properties of its components (units and mortar) [7]. Units can be stones or bricks and can be of various materials, shapes and dimensions, interacting through dry or mortar joints by following different patterns [8], [9], significantly affecting the masonry mechanical behaviour. In particular, historical masonry structures have been generally built following simple empirical rules often related to local tradition and construction techniques, adopting irregular units and geometrical layouts. As a result, masonry walls are weakly connected to each other and to other structural elements leading to very complex seismic behavior, which is governed by the interaction between in-plane

and out-of-plane (OOP) responses of masonry walls. For these reasons, different parts of the building can exhibit local seismic response that is mainly related to OOP mechanisms as the overturning of the main façade. At the material level, the constitutive masonry behavior is highly non-linear and characterised by a degrading cyclic response dominated by the low tensile strength, making the numerical simulation of the seismic response of URM structures a challenging task [10], [11].

Therefore, the capacity of existing masonry buildings to resist earthquake excitations (or their vulnerability) is strongly related to the mechanical characteristics of masonry units and joints, the masonry bond, the geometrical construction layouts, and the quality of structural connections between its different elements. All these aspects should be adequately considered in the analysis and seismic assessment.

In-situ post-earthquake observations showed that OOP failures of URM walls constitute the most severe life hazard for this type of construction, particularly in the case of slender façade walls with poor connection to transversal elements or diaphragms [3], [12]. In addition, once activated, the OOP failure mechanism can evolve towards large displacement, generally assumed represented by rigid-block-like kinematics [13], strongly influencing the structural response and this entails a significant increase in complexity in the study of the non-linear behavior of URM structures already characterised by a highly non-linear constitutive behavior even at a small intensity of the seismic load. Figure 1 illustrates two residential URM buildings, which suffered heavy damage during the catastrophic 1908 Messina earthquake, whose estimated magnitude was 7.3 [14], [15]. Both buildings show a collapse scenario with significant parts collapsed and other building portions mainly subjected to in-plane damage of masonry walls in piers and spandrels. In particular, Figure 1a shows a building that suffered the complete overturning of the main facade at the top level, with the related total collapse of the roof. In addition, the corner portion of the building collapsed. Figure 1b shows a heavily damaged building with the complete failure of a corner portion with a detachment of the remaining part in correspondence with the spandrels [16].

(a) (b)

Figure 1 - Messina earthquake (1908): (a) in-plane damaged building; (b) local failure [16]

This behaviour is typical of URM buildings where a global response is not always guaranteed, particularly for historical structures. During the seismic event, the low tensile strength of the masonry walls and the weak or incomplete connections between walls and between walls and slabs can lead to a damage scenario that tends to evolve during the dynamic response [16].

When subjected to strong earthquakes, an undamaged URM building responds to the early stage of a seismic event by global behaviour. However, once the building is damaged, it tends to separate into sub-portions that can behave differently during strong earthquakes. This is particularly true for the facade of URM buildings, which, in many cases, represent the first structural elements to be subjected to local collapse due to a complete detachment from the other parts of the building and a rocking behaviour dominated by a rigid body motion (Figure 2).

Figure 3a shows the damage scenario of a building that suffered in-plane damage of spandrels without being subjected to local collapse during the L'Aquila earthquake (2009). In this case, the building exhibited a global response, and no local failure occurred; this is the response that a URM building should show when subjected to a strong earthquake if correctly designed to resist earthquake loadings. It is expected that the building can suffer in-plane damage to masonry walls, but no local or global collapse should occur. Figure 3b,

instead, shows a totally different scenario of two aggregate URM buildings that suffered heavy damage during the L'Aquila earthquake in 2009. In this picture, a total collapse of a significant portion of a unit of the aggregate is observed while the other unit exhibited a significant rocking out-of-plane response with a complete detachment between the facade and one of the orthogonal walls, resulting in an incipient overturning condition [16].

Figure 2 - Messina earthquakes (1908): OOP failures of external walls [17]

(a) (b)

Figure 3 - L'Aquila earthquake (2009): (a) in-plane and (b) out-of-plane failures of URM buildings [17]

1.2 Numerical modelling strategies to predict the seismic response of unreinforced masonry buildings

The accurate numerical simulation of masonry walls, in terms of non-linear, static or dynamic response, when subjected to seismic excitations, represents a complex computational issue since rigorously requires accounting for constitutive and geometrical nonlinearities. Accurate analyses, employing detailed Finite Element (FEM) or Distinct Element (DEM) models, including both geometric and constitutive nonlinearities in large displacements, imply the adoption of advanced numerical strategies to update the system configuration and the geometrical stiffness matrices during the analyses. Consequently, these approaches present the disadvantage of being very complex, time-consuming, and computationally expensive. However, geometric nonlinearities can be taken into account in a simplified way by considering the so-called second-order (P-Delta) effects. Despite this, the number of P-Delta formulations available in the literature for assessing masonry structures is generally restricted to the use of FEM approaches [18]. Fewer approaches have been proposed based on simplified macro-elements [19], [20], which typically neglect geometric nonlinearities.

Numerous non-linear numerical strategies, characterised by different levels of accuracy and efficiency, have already been proposed to assess the non-linear response of URM walls when subjected to OOP loading. Among these, within the general framework of the force-based approach (FBA), practical tools are based on the macro-block limit analysis approach, which describes the wall as the kinematics of rigid blocks and are used to evaluate the lateral load amplitude activating the OOP mechanism [21]–[24]. These methods are often employed for the seismic assessment of local failures of URM structures in international (*EC8*) and Italian structural codes [26].

Within the framework of FBA, advanced limit analysis formulations have been proposed in order to account for the effects of the lateral and orthogonal walls [27]–[30] and the interaction with horizontal diaphragms [31]. More detailed meso-scale limit-analysis formulations have also been proposed to investigate the torsion-shear behavior [32]–[34]. Nevertheless, FBA can be over-conservative because they tend to neglect the

dynamic reserve of stability, particularly in the case of large-scale structures, which undergo significant displacements before overturning. Moreover, they cannot provide information about the evolution of the mechanism after the activation and the effective displacement capacity. To overcome this limit, displacement-based approaches (DBA) have gained popularity for the evaluation of the seismic response of URM structures [13], [35]–[37]. These methods aim to assess the displacement capacity of the structural system. These strategies are straightforward, and they can also consider the P-Delta effects making them widely used by practitioners.

Another effective method largely used to assess OOP rocking walls is the rigid-block model, which describes the entire wall by a single rigid block overturning around its base vertexes and subjected to ground acceleration time histories. This model response is generally obtained by directly integrating the equation of the motion in large displacements and was first proposed by Housner [38]. Since the wall is assumed rigid, this approximate approach allows for a simplified dynamic analysis with a low computational cost. However, the rigid body assumption does not account for masonry deformability and 3D geometrical layouts or boundary constraints. Moreover, it requires hypotheses on the energy dissipation model that is only related to the impacts of the block, representing an unrealistic assumption for a masonry wall and is also difficult to calibrate.

On the other hand, detailed FEM and DEM approaches, explicitly accounting for 3D OOP boundary conditions, the actual masonry bond, and geometrical nonlinearities, have been proposed in the literature to simulate the non-linear response of masonry structures. Among them, numerical methods characterised by different orders of complexity have been proposed and applied. These strategies include micro-scale [39], [40], meso-scale [8], [41], [42], and continuum FEM approaches [8], [43]. Mesoscale FEM analyses explicitly account for the actual masonry bond through the use of zero-thickness interfaces, while continuum FEM models simulate masonry walls through an homogeneous equivalent medium at the macro-scale [44] under the hypothesis of small deformations and large displacements. DEM approaches are well suited for masonry structures with dry- and mortared joints and allow to perform non-linear static and dynamic analyses accounting for large displacements and the separation of structural parts. In these approaches, the position

and orientation of elements and contacts are updated at each step of the analysis [45]. It makes them particularly suitable to describe local failures, characterising irregular masonry [46]–[48]. However, the disadvantage of FEM and DEM strategies is that, in general, these methods are based on complex 3D or 2D constitutive laws, requiring expert judgments in the model implementation and the interpretation of the results, and cumbersome calibration procedures. Moreover, these methods require a high computational cost making them very useful in research but rarely suitable for practical seismic assessment. For these reasons, over the last few decades, many research groups have proposed simplified numerical methodologies for predicting the non-linear seismic behaviour of URM structures [49], [50]. These engineering-oriented simplified methods, such as the Equivalent Frame Model (EFM) or the Discrete Macro-Element Model (DMEM), are identified in the literature as structural component models or macro-models since they simulate masonry walls as an assemblage of macroscopic structural elements. Because of its simplicity and low computational demand, the EFM is adopted by a number of national and international regulations in combination with nonlinear static analysis [51]. It simulates piers and spandrels using one-dimensional elements connected by rigid nodes [52]–[54]. However, despite the advantages of the EFM method, it is worth underlining some limitations: i) discretisation of structure with an irregular position of openings is sometimes ambiguous or not possible, ii) geometric inconsistency of the approach, as it represents a plane portion such as masonry panels with a mono-dimensional element, iii) presence of areas which cannot be damaged, generally identified as rigid links. Moreover, frame model approaches generally neglect the OOP response of masonry walls, and their use is restricted to assessing the global response of masonry buildings. Recently an enhanced frame-like macro-element incorporated the OOP response, also accounting for second-order effects has been proposed in the literature [19], [20], [55].

The present study aims to cover this research gap by upgrading the DMEM introduced by Caliò et al. [50], with the inclusion of geometric nonlinearities related to P-Delta effects. The DMEM was originally proposed to overcome the limitations of EFM and could simulate the IP response of masonry panels. Subsequently, DMEM was extended to 3D kinematics to account for masonry walls' coupled in-plane and OOP behaviour when

subjected to earthquake loadings [56], [57]. The model presents many advantages, compared to previous proposed models for masonry structures, related to the geometrical consistency, the low computational cost, the possibility to couple discrete and finite elements, the straightforward model calibration, the possibility to be used at macro and meso-scale [58]. The novelty proposed in this study consists in accounting for second-order P-Delta effects in a simplified but robust way within a time-efficient discrete macro-element (DMEM) strategy in order to simulate the effects of geometrical non-linearities and exploit the use of DMEM to perform realistic dynamic analyses of URM rocking walls.

1.3 Outline

This thesis aims to introduce, validate, and apply a P-Delta formulation within the framework of the DMEM strategy for the seismic assessment of masonry structures. To provide a better description and explanation of the research topics and results, the thesis has been partitioned into seven sections, as follows:

1. ***Section 1 – INTRODUCTION***: A brief introduction of the research problem and the associated motivation, including the thesis's focus and the document's outline.

2. ***Section 2 – OUT-OF-PLANE SEISMIC ASSESSMENT TECHNIQUES FOR UNREINFORCED MASONRY STRUCTURES,*** presents a brief literature review concerning the most common strategy to assess the seismic behavior of URM structures. These techniques, following the work of Ferreira et al. [59], are divided into three main families: (i) numerical methods, which include finite-, discrete-, and macro-element methods; (ii) Analytical assessment techniques, namely force- and displacement-based approach and experimental in situ or laboratory tests. For each of these assessment techniques, the main works are cited and briefly discussed.

3. ***Section 3 – OUT-OF-PLANE IN STANDARDS***, describes the problem of the assessment of the out-of-plane behavior of masonry walls within the current scenario of national and international technical regulations. A brief presentation of three standards is given in this section, namely the Eurocode (EC8), the Italian Code (NTC18), and the American Code (ASCE/SEI 41 2017).

4. ***Section 4 – DISCRETE MACRO-ELEMENT METHOD (DMEM),*** aims to describe the simplified numerical tool proposed by Caliò et al. and herein upgraded to account for second-order effects. The method can simulate the coupled in-plane and out-of-plane seismic behavior of unreinforced masonry structures in static and dynamic fields. The main kinematic and mechanical aspects of this method are presented and extensively discussed.

5. ***Section 5 – P-DELTA EFFECTS WITHIN THE DISCRETE MACRO-ELEMENT METHOD,*** reports the P-Delta formulation within the macro-element method (DMEM) discussed in Section 4, which has been implemented in the structural software HiStrA (Historical Structural Analyses) and validated, in the static field, through the comparison with analytical solutions and experimental results [60], already reported in the literature. Moreover, extensive parametric analyses are performed to investigate the role of the mechanical parameters of masonry and geometrical characteristic of the wall of the rocking response.

6. **Section 6 – DYNAMIC SIMULATION OF RIGID BLOCKS,** aims to validate the P-Delta formulation in dynamic field carrying out undamped free-vibration analysis on rocking rigid block comparing the results with those predicted by the classical theory of rigid blocks proposed by Housner [38]. Moreover, a non-classic stiffness-proportional damping model associated with interface elements is developed to describe the loss of energy related to the

impact which characterize the dynamic of rigid blocks. The proposed damping model is validated by carrying out dynamic free- and harmonic-vibration analyses on quasi-rigid blocks and comparing the results with some experimental tests conducted on quasi-rigid blocks, analytical solutions, and advanced FEM simulations available in the literature.

7. **Section 7 – DYNAMIC SIMULATION OF UNREINFORCED MASONRY WALLS INCLUDING P-DELTA EFFECTS** presents the application of the P-Delta formulation to a different case study. In particular, a masonry church's façade undergoing two-sided rocking and a real masonry church are studied both under static and dynamic excitations. P-Delta effects are alternatively considered and neglected in order to obtain first useful outcomes on the importance to keep into consideration the geometric nonlinearities in the prediction of the ultimate capacity of a URM construction both in terms of strength and displacement.

8. **Section 8 – Conclusions** summarizes the new developments introduced within the Discrete Macro-Element Strategy and the obtained results, pointing out the capability of the model to accurately reproduce the rigid-block dynamic behavior and the OOP response of URM structures when subjected to seismic excitation even in presence of relatively large rotations, while maintaining the typical computational efficiency of the DMEM.

1.4 Research target

The main target of this research is to provide an accurate and efficient numerical tool for the seismic assessment of existing URM masonry structures subjected to out-of-plane mechanisms, allowing numerical simulations to consider both in-plane and out-of-plane wall responses and their mutual interaction taking into account all sources of nonlinearities.

With this target, the thesis aims to bring an original contribution to the numerical methodologies for the seismic assessment of unreinforced masonry (URM) structures toward the inclusion of the effects of geometric nonlinearities within a comprehensive analysis of the structure, conducted without adopting the conventional separation between in-plane and out-of-plane wall responses and a priori hypotheses on the failure mechanism, often adopted in engineering practice and academic research.

1.5 Methodology

The research is based on a simplified macroscopic description of masonry walls. In particular, the new formulations and the numerical analyses are developed and performed by adopting the discrete macro-element method (DMEM). This method brings the great advantage of limiting the computational effort compared to detailed modelling approaches, like finite element (FEM) or distinct element (DEM) models.

The model is formulated in the static and the dynamic fields and implemented within the HiStrA (Historical Structure Analysis) software [61]. In particular, the dynamic implementation of the model is enriched by a non-classic damping model associated with interface elements, describing the energy dissipation associated with the impact during the rocking motion. The model is used to perform non-linear static (pushover) and dynamic analyses. The predictions of the newly-developed DMEM model are compared to the results of more detailed FEM simulations, analytical solutions, and experimental tests available in the literature. In addition, parametric investigations and Incremental Dynamic Analyses (IDAs) are performed on a real case study of a masonry church as a representative of a structural typology highly vulnerable to OOP failure mechanisms.

2. OUT-OF-PLANE SEISMIC ASSESSMENT OF URM WALLS

Existing masonry constructions, representing most architectural heritage worldwide (buildings, towers, castles, churches, etc.), are among the most spread structural typologies built without following seismic design standards. These structures are often characterised by complex and irregular geometrical schemes and weak structural connections, making them high-vulnerable to out-of-plane (OOP) failure mechanisms. Even in the presence of good connections, OOP failure mechanisms can occur in slender parapets, long unrestrained top spandrels, and vertical spanning walls. OOP generally occurs at lower intensities than those causing in-plane failure mechanisms, as evidenced by post-earthquake observations. In the last decades, the scientific community devoted a consistent effort to the numerical description and assessment of URM structures. Despite this, describing the dynamic response of masonry walls subjected to OOP rocking behaviour and predicting their ultimate seismic capacity represent challenging tasks and current open issues within Earthquake Engineering. This is due to the complex mechanical behaviour, the inhomogeneity characterising the masonry material, and the complex interaction between the different parts of the building [62], [63].

The OOP ultimate response of URM walls is dominated by large displacements. Therefore, apart from the material non-linearities, geometrical non-linearities and second-order effects also assume great importance. Indeed, the OOP collapse of URM walls subjected to seismic excitation is primarily associated with an excess displacement demand rather than the attainment of the static OOP strength of the wall. In this regard, many experimental and analytical studies [35], [60], [64], [65] have shown how dynamically loaded walls can sustain acceleration greater than that implied by their static capabilities. Given the complexity of the problem, several modelling and assessment strategies, different for accuracy in describing the mechanical behavior of masonry and typology of structural

analysis, have been proposed. Historically, the first attempt came from Rondelet (1812), who first framed the OOP behavior of masonry walls in terms of stability rather than strength. He identified three main failure mechanisms as a function of the boundary conditions and the geometry of the wall (Figure 4). The awareness of such vulnerability has encouraged the development of assessment strategies of varied complexity.

Several methods and computational tools are currently available for the assessment of the OOP behavior of URM structures, taking into account both constitutive and geometric non-linearities with different levels of accuracy and complexity. In this work, following the classification proposed by Ferreira et al. (2015), reported in *Figure 5*, three main families are identified: numerical methods, analytical methods and experimental tests. Each one of these assessment methods is described in the following sections, where the most important references and applications are reported and briefly discussed.

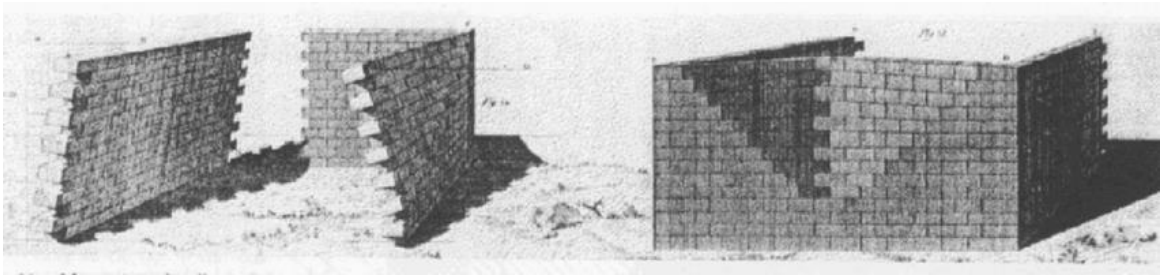

Figure 4 - OOP mechanisms by Rondelet (1812)

2.1 Numerical Methods

As already discussed, the numerical modelling of the seismic behavior of URM structures represents a complex task due to significant constitutive and geometric nonlinearities even at relatively low values of the seismic excitation. In addition, the anisotropic nature of masonry, strictly related to the specific bond masonry arrangement [66], rigorously would require 3D constitutive laws difficult to implement and to calibrate on the basis of traditional in situ tests. Moreover, monumental URM structures are often characterised by uncertainties in the definition of the actual structural geometry, not being clear in distinguishing between structural and non-structural parts. In the last half-century,

the research community devoted a consistent effort to the computational analysis of URM structures to develop tools for predicting and assessing their structural behavior.

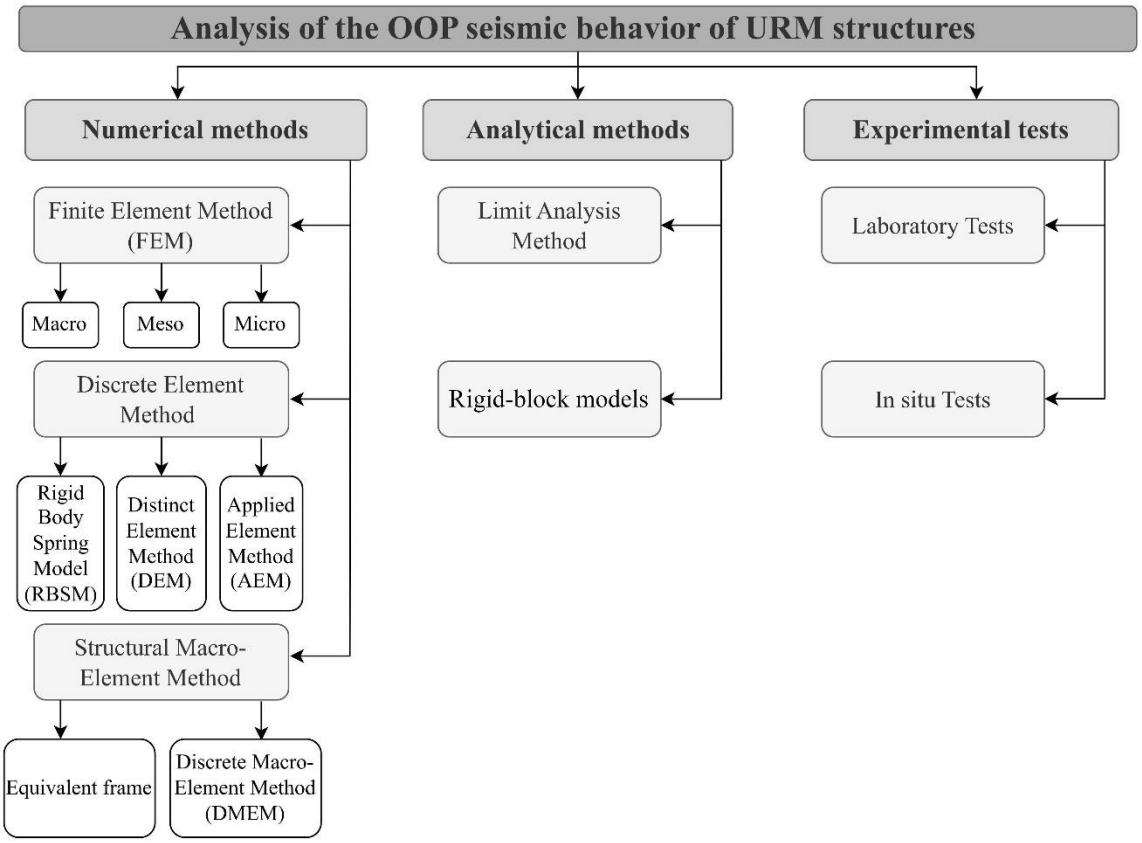

Figure 5 – Existing techniques for assessing the OOP seismic behavior of URM structures

Given the complexity of the seismic behavior of masonry structures, different approaches characterised by different complexity and scale of representation, as well as different strategies of analysis, have been proposed [67]. Moreover, geometric nonlinearities assume great importance when performing a non-linear seismic analysis on a URM masonry structures undergoing geometrical and material nonlinearities [68]. This entails a significant increase in complexity in the study of the non-linear behavior of URM structures already characterised by a highly non-linear constitutive behavior even at a slight intensity of the seismic load. On the other hand, the accurate numerical simulations of the non-linear incremental static or dynamic response of masonry walls subjected to seismic excitation, considering both constitutive and geometrical nonlinearities, represent a very

complex computational issue that has been the subject of extensive research over the last decades and that represents the main goal of this thesis project.

Some accurate analyses employing detailed finite element (FEM) or distinct element (DEM) models [41], [44], [45], [47], [69]–[71] which account for both geometric and constitutive nonlinearities in large displacements, requiring the adoption of advanced numerical strategies to update the system configuration and the geometrical stiffness matrices during the analyses, have been proposed in the literature. Such approaches model the masonry material using different representation scales, i.e., equivalent continuum, macro-blocks, or discrete representations. FEM allows a more versatile application as masonry can be represented either through a homogeneous equivalent media (macro-modelling) or by a discrete representation of units and joints (micro-modelling). Linear and nonlinear static and dynamic analyses are eligible. Nonetheless, additionally to the significant amount of data needed to characterise the nonlinear response of materials, these approaches when performed at real scale structure are time-consuming and computationally expensive.

In order to satisfy the need of having reliable results with limited elaboration times, several authors proposed alternative approaches, performed at the macro-scale, according to which the structures are described as an assemblage of macroscopic structural elements representative of macro-portion of the masonry panels. Because of their simplicity and computational efficiency, these alternative approaches are widely adopted in engineering practice.

In the subsequent paragraphs, a brief review of the main numerical modelling strategies used for the analysis of the OOP behavior of URM structures is reported. In particular, numerical methods are classified into three main categories: Finite Element Method (FEM) Approach, Distinct Element Method (DEM) Approach and Macro-element Method (MEM) Approach.

2.1.1 Finite Element Method (FEM) Approach

Finite Element Method is one of the most adopted numerical methods for accurately evaluating the seismic response of URM structures subjected to in-plane and OOP loadings. This approach can be applied both at the macro and the micro scale (detailed models).

When applied for obtaining a detailed description of the nonlinear response can effectively describe complex masonry structures with complex geometry, general 3D loading scenarios, and complex mechanical material behaviour, taking into account numerous factors affecting the masonry response, like dimensions and characteristics of units and joints and the effects of the masonry bond, for large scale simulations a detailed model often will require partition modelling strategies as those proposed by Izzuddin et al. [72]

Therefore, depending on the level of accuracy, it is possible to use different model strategies [73]: micro-models, which explicitly describe the constitutive elements of the masonry (units and joints) and the interfaces between them; macro-scale models, describing the masonry as an equivalent homogenised continuum material; meso-scale models which represents an intermediate approach between macro and micro models and approximating masonry joints by weakness layers modelled by zero-thickness interface elements.

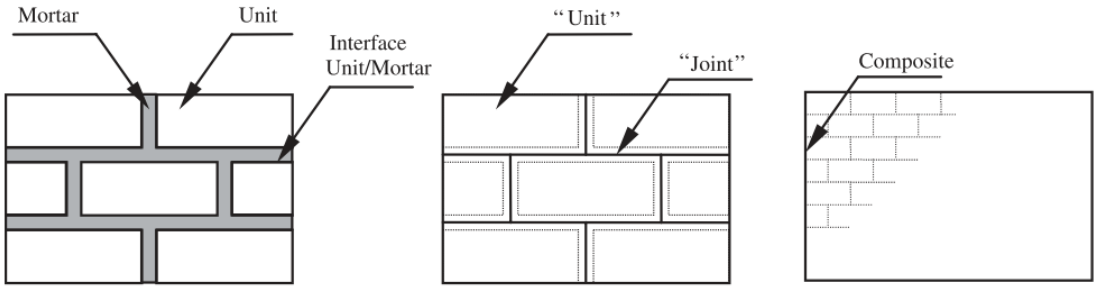

Figure 6 - Modelling strategies for masonry structures [73]*: (a) micro-modelling, (b) meso-modelling and (c) macro-modelling strategies*

2.1.1.1 Micro-modelling strategy

In this approach, elastic and inelastic properties of both unit and mortar are taken into account: constituent elements of the masonry, namely unit and mortar, and interfaces between them, are modelled individually (Figure 6a). Due to the high computational burden required by this approach, its application is limited only to limited portions of masonry structures and academic research. This strategy is considered a reliable tool for the assessment of the seismic response of this typology of structures since it allows the simulation of failure mechanisms such as the crushing of masonry units as well as cracking or sliding of mortar joints.

2.1.1.2 Meso-modelling strategy

According to a meso-scale approach, each joint, consisting of mortar and the two unit-mortar interfaces, is lumped into an average interface while the units are expanded in order to keep the geometry unchanged Figure 6b. Masonry is considered a set of elastic blocks bounded by potential fracture/slip lines at joints.

Meso-modelling is an interesting alternative to combine benefits from extreme micro and macro modelling scales. Most of the mesoscale models for URM masonry presented so far account for the in-plane behavior.

According to Macorini and Izzudin (2011), such models cannot be effectively employed to assess the structural performance of URM elements under complex loading conditions, as in the case of the seismic action, which presents both in-plane and out-of-plane components. Even so, these authors tackled this issue by defining a new interface element for the geometric and material non-linear analysis of URM structures, which enables the representation of any 3D arrangement of masonry and allows the investigation of both the in-plane and the out-of-plane responses of URM panels.

2.1.1.3 Macro-modelling strategy

A macro-modelling strategy does not distinguish between individual units and joints but treats masonry as an equivalent, homogeneous, anisotropic continuum (Figure 6c). As noticed, homogenized modes for masonry attempt to combine the two distinct phases of the units and joints and their respective constitutive laws to determine the overall elastic properties of masonry.

Several authors proposed different homogenization procedures for macro-modelling approaches stressing the fact that moderate changes in the material parameter can lead to different predominant failure mechanisms [73]. Milani et al. (2011) used a macro-scale approach to reproduce the nonlinear behavior of masonry walls in the case of large displacement through a simplified "homogenized" procedure.

The nonlinear incremental response of the structure is accounted for by a specific quadratic programming routine where second-order effects are suitably addressed by the geometric stiffness matrix.

2.1.2 Discrete Element Method Approach

In the discrete macro-element approach, the masonry is modelled through an assemblage of blocks interacting with each other through interface elements. The discrete Element Approach is now well suited for masonry with both dry [74] and mortared joints but still requires a full representation of the blocks (masonry units) arrangement [45].

In the framework of Discrete Element Approaches must be cited the Rigid Body Spring Model (RBSM), the Distinct Element Method (DEM), and the more recent Applied Element Method (EAM).

2.1.2.1 Rigid-body spring model (RBSM)

The Rigid-Body Spring Model (RBSM) was introduced, for the first time, by Kawai in 1978 [75]. He started from the following idea: when a structure reaches its ultimate state of loading, it crushes into pieces, and after that, each part moves as a rigid body.

This simple idea falls in RBSM approach in which a portion of masonry (Figure 7) can be simulated by a set of rigid blocks (rigid bodies) (Figure 7b), which are assembled by means of springs (Figure 7c). It is worth noting that the RBSM is a 2D model, but it is able to reproduce specific OOP mechanisms.

Each contact of the rigid body is composed of a couple of orthogonal links together with an additional longitudinal one. The stiffnesses related to orthogonal and longitudinal links are denoted respectively as k_x and k_v for vertical contacts, and k_y or k_s for contacts in a horizontal direction. Three DOFs describe the kinematics of each rigid block: two of them are associated with horizontal and vertical displacements u and v, and the remaining one is related to the rotation φ of the rigid block.

The axial and flexural mechanisms are governed by the two orthogonal springs located at the edges of the rigid blocks presenting a value of stiffness, k_x and k_y, in Figure 8a associated with Young's modulus of masonry without considering the effects of Poisson's ratio. The proper simulation of the flexural response requires the estimation of an optimum distance d at which the orthogonal springs are placed (Figure 8b). Such distance is generally considered as a third of the middle length of the rigid block e in a given contact direction. The shear behaviour of the rigid blocks is ruled by the additional longitudinal links whose values of stiffness k_s and k_v are related to the shear modulus of the masonry material (Figure 8c). The flexural and shear mechanisms of the deformable elements are influenced by the Poisson's ratio [69]. The RBSM was further upgraded for the assessment of the seismic response of masonry structures in the dynamic field, as reported by Casolo and Peña [76]. The post-elastic response of these models is ruled by nonlinear behaviour associated with flexural and shear mechanisms. The constitutive law that governs the flexural response consists firstly of a low value of tensile strength f_t in which the post-peak branch is described by a rapid degradation of the strength. Due to the brittle behaviour that characterizes the flexural response, the dissipation of hysteretic energy during unloading cycles related to the tensile response does not present a significant value. On the other hand, the compressive behaviour is described by limited ductility once it reaches the value of compressive strength f_c. The shear behaviour is associated with the

mechanical behaviour of the mortar joints, and it is governed by a Mohr-Coulomb yielding criterion in which the residual shear capacity depends on the vertical axial load.

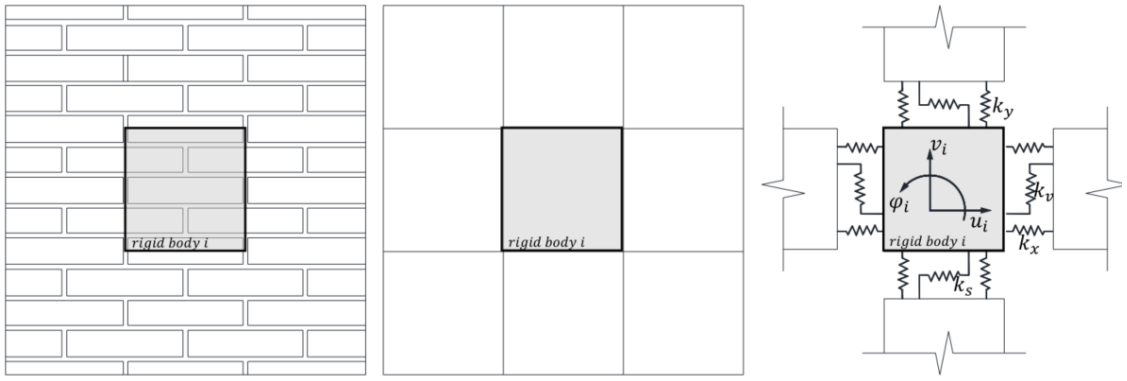

Figure 7 - Scheme of two masonry-like texture; a common rigid element discretization is shown in the centre [69]

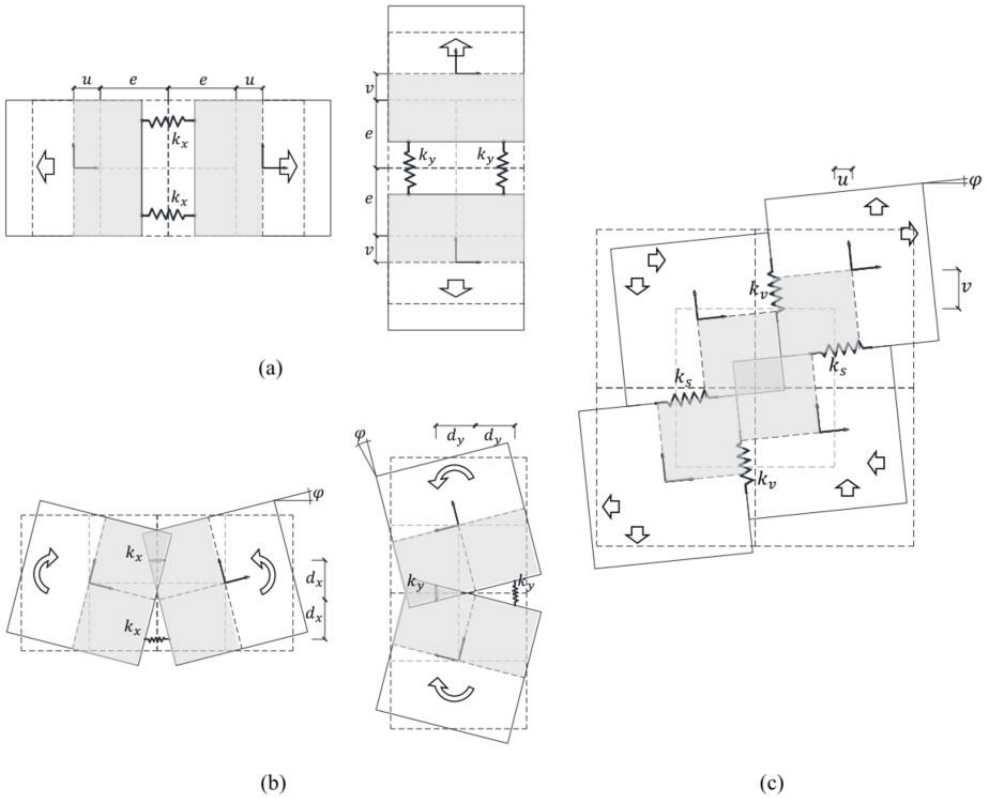

Figure 8 – Failure mechanisms simulated by RBSM due to: (a) horizontal and vertical axial loading, (b) in-plane bending loading, (c) shear loading [69]

2.1.2.2 Distinct Element Method (DEM)

The DEM approach consists of the assemblage of either rigid or deformable elements, representing blocks whose interaction is conducted using concentrated links. Originally developed for geotechnical aspects [77], the distinct element method (DEM) has been used for the structural analysis of masonry, taking advantage of its capability of accurately representing irregular geometries.

The first DEM model was developed by Cundall [77], aiming at the evaluation of the behavior of rocks and soils using plane elements and further upgrading by means of spatial elements [78]. The DEM based on this hypothesis enables an independent meshing of the blocks without the necessity of node matching; and therefore, allows different typologies of geometric interactions. The masses of the system are concentrated in the nodes, and both acceleration and displacements are computed with references to this nodes during each time step.

DEM takes into account the effective morphology and arrangement of the blocks, crack opening, and joint sliding, which typically induce structural damage or collapse, and accounts for large displacements and rotations by automatically updating the position of the blocks and their interactions during the analysis and for this reason, finite displacement and rotation can be taken into account. The complete detachment between blocks is also considered [71] and new contacts are automatically created during the analysis, allowing the modelling of the dynamic collapse behavior of complex structures.

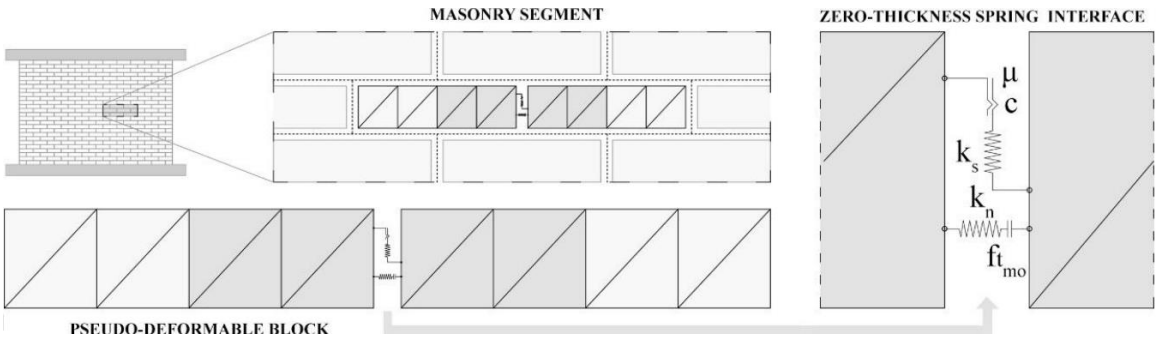

Figure 9 - Discretization of a masonry segment according to the DEM [71]

Explicit time-stepping algorithms are commonly used for DEM, where the equations of motion are integrated using a central-difference scheme [79], [80]. However,

the main problem related to DEM is that the calibration of the contact links is not straightforward and generally based on experimental data applying empirical relations. The main difference between DEM and RBSM is that according to DEM approach, each rigid element represents a single masonry unit while, each rigid element in the RBSM approach represents a macro-portion of the masonry wall (Figure 7 and Figure 9).

2.1.2.3 Applied Element Method (AEM)

The Applied Element Method (AEM) was introduced for the first time by Meguro et al. (2002) to simulate controlled structural demolition of reinforced concrete buildings [81], [82]. It allows linear and nonlinear, static and dynamic, and small and large displacement analysis. Such an approach is very similar to RBSM.

The AEM is based on the division of the structural members into virtual elements connected through springs: each unit is modelled as a rigid body that interacts with the adjacent ones by means of an equivalent zero-thickness interface. Each spring entirely represents the stresses, strains, deformations, and failure of a certain portion of the structure. The main advantage of this method is that it can follow the structural behavior from the initial loading stages until collapse with reliable accuracy and in reasonable CPU time.

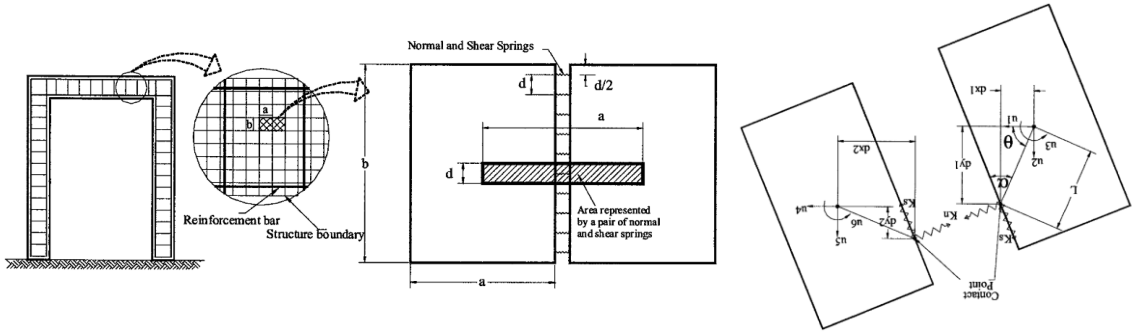

Figure 10 - Modelling of the structure in AEM: (a) Element generation in AEM, (b) Spring distribution and area of influence, (c) Element shape, contact point and DoFs [81]

Its accuracy in the large displacement range is verified by comparing the numerical results with theoretical ones: agreement is very good [81].

In the two-dimensional model, each element has three DOFs, which represent the element's rigid body motion (Figure 10), and they are connected to each other at discrete points by a pair of normal and shear springs with stiffness, respectively:

$$K_n = \frac{EdT}{a} \qquad 2.1$$

$$K_S = \frac{GdT}{a} \qquad 2.2$$

where *d* is the distance between springs, *T* is the element thickness, *a* is the length of the representative area, *E* the material Young's modulus, and *G* is the material shear modulus.

Unlike other methods (such as FEM) in the AEM, there is no need to determine the geometrical stiffness matrix to take into account the large displacement. The large displacement procedure is based on the following expression:

$$\mathbf{K\Delta U} = \mathbf{\Delta f} + \mathbf{R_m} + \mathbf{R_g} \qquad 2.3$$

in which:

- **K** is the nonlinear stiffness matrix;
- **ΔU** is the incremental displacement vector;
- **Δf** is the incremental load vector;
- $\mathbf{R_m}$ is the residual force vector due to cracking or incompatibility between spring stress and strain;
- $\mathbf{R_g}$ is the residual force vector due to geometrical changes in the structure during loading.

In [81] the application of AEM in large displacement is explained. In particular, it follows the following steps:

1. Assume that $\mathbf{R_m}$ and $\mathbf{R_G}$ are null and solve Eq. 2.3 to get $\Delta \boldsymbol{u}$.

2. Modify the structural geometry according to the calculated incremental displacements.

3. Modify the direction of the spring force vectors according to the new element configuration. The geometrical changes generate incompatibility between the applied forces and internal stresses.

4. Verify whether cracking occurred and calculate $\mathbf{R_m}$. In elastic analysis, $\mathbf{R_m}$ is zero.

5. Calculate the element force vector, $\mathbf{F_m}$, by summing the forces of the springs around each element.

6. Calculate the geometrical residuals around each element with the following expression in which **f** is the applied force vector:

$$\mathbf{R_g} = \mathbf{f} - \mathbf{F_m} \qquad 2.4$$

Small deformations are assumed during each increment.

7. Calculate the stiffness matrix for the structure with the new configuration considering stiffness changes due to cracking or yielding.

8. Repeat the entire process.

To compare this approach to DEM approach, it is worth noting also that DEM considers interface springs located at the unit vertices, and their number is limited to four per contact area, which may lead to stress localisation phenomena or unconservative results, especially when considering out-of-plane mechanism. Using AEM, instead, an unlimited number of springs, uniformly distributed at the interface, can be employed.

The applicability of such an approach to the modelling of URM structures was investigated ad verified by comparing numerical results with a wide range of experimental outcomes in [83].

A commercial software called “Extreme loadings for structures” is based on this method. Despite its simplicity, the method, can provide reliable predictions. However, it generally requires very refined mesh discretisation, corresponding to a large number of DoFs, leading to a high computational cost.

2.1.3 Structural Macro Element Method Approach

In order to overcome the high computational cost which characterized the numerical strategies discussed before, during the last decades, several researchers proposed numerical models based on simplified mechanical schemes according to which masonry can be modelled by an assemblage of macro-elements. This methodology is based on the fact that some structural elements are found in a recurring way in historic buildings, and each wall can be described by an assemblage of a single or a few macro-portions, called "macro-element". The main advantage of these methods is the high reduction of the computational burden.

Several macro-element approaches were proposed in which structures are described as an assemblage of macroscopic structural elements. A distinction can be made between Equivalent Frame Model (EFM) and Plane Model. The former consists of the modelling of the masonry wall by means of equivalent frames, which are composed of rigid elements connected to deformable ones. Approaches such as the POR [84] and SAM [54] methods can classify into this category. EFMs are today suggested by several national and international standards in combination with the nonlinear static (pushover) analysis [51].

On the other hand, the plane models consider a two-dimensional representation of masonry structures. Approaches such as Multi-fan Panel [85], [86], Variable Geometry [87], [88], Three-layer [49], and Strut-and-tie models belong to this category.

Because of their simplicity and low computational demand, EFMs are one of the most widely diffused methods of analysis in engineering practice [89]. However, despite the advantages, it is worth underlining some limitations, i.e., i) discretisation of structure with an irregular position of openings is sometimes not possible, ii) geometric inconsistency as they model plane portion such as masonry panels with mono-dimensional element, iii) presence of areas which cannot be damaged. Finally, these approaches are not able to simulate the OOP response of masonry walls, and for this reason, they are not widely discussed in this study.

2.1.3.1 Three-layer model

Firstly proposed by Gambarotta and Lagomarsino [90] and Brenchich and Lagomarsino [49] the three-layer model was able to predict the global response of box-behavior masonry buildings, for which the OOP mechanisms are prevented. Therofore, the model was able to describe the in-plane response of masonry walls. According to this strategy, masonry walls are modelled by means of macro-elements connected by means of rigid elements, as shown in Figure 11a and Figure 11b for two- and three-dimensional masonry structures, respectively. The deformable panels or macro-elements aim at simulating the behaviour of masonry components such as piers and spandrels which are characterized by a localised failure mechanism. On the other hand, the rigid elements connecting the deformable panels do not experience any significant damage concentration. Each deformable macro-element is divided into three layers aiming at simulating the flexural behaviour and shear deformation of masonry walls. The flexural mechanism is governed by the bottom (1) and top (3) zero-thickness layers, whereas the shear mechanism is ruled by an additional central layer (2), as reported in Figure 12.

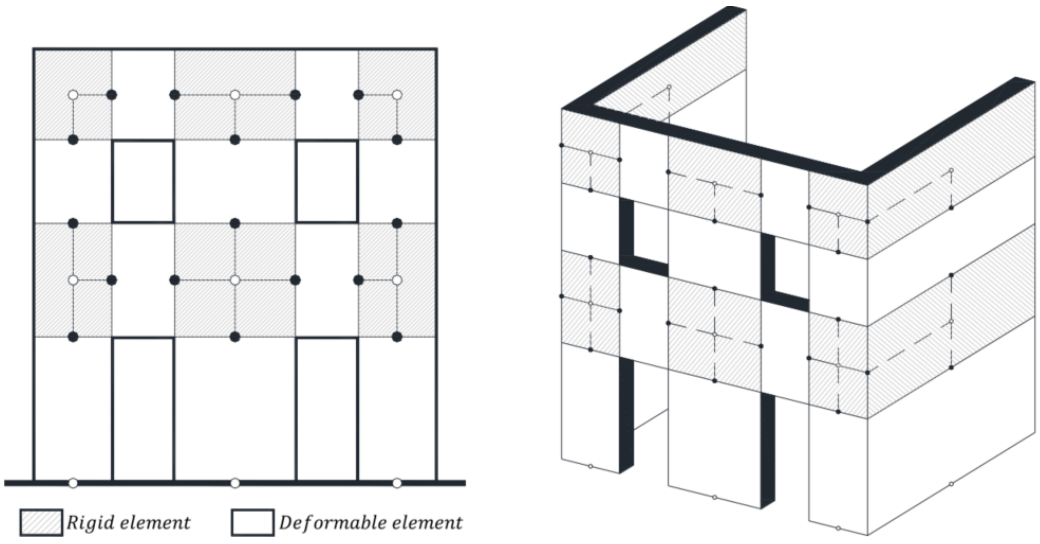

(a) (b)

Figure 11 - Three-layer model: (a) two- and (b) three- dimensional representation of masonry structures (Figure from [49]*)*

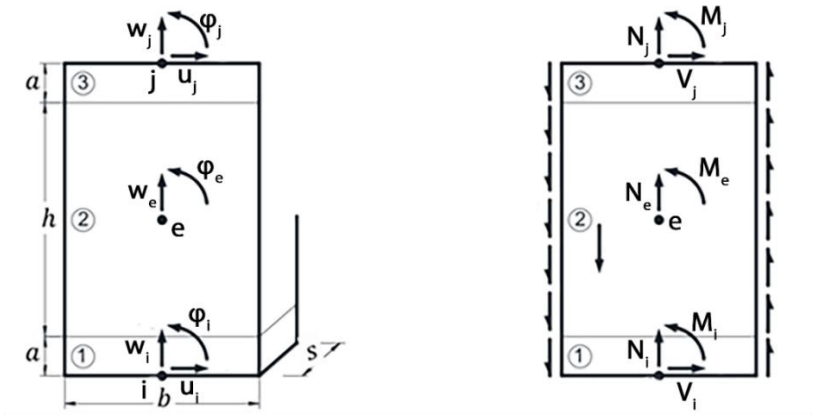

Figure 12 – Three-layer model: (a) kinematic and (b) static variables of the deformable macro-elements (Figure from [49]*)*

The model has been further developed by Penna et al. [91], including cyclic constitutive laws for the in-plane flexural and shear mechanisms of masonry panels. According to the three layer model, the panel is defined by two nodes (*i* and *j* in Figure 12*)*, and since the central part is assumed as a rigid body with the possibility to have only shear deformations, under the hypothesis of small displacements, the kinematic of each macro-element can be fully described by eight Lagrangian parameters: six of them are associated with the in-plane rigid-body degrees of freedom associated to the two nodes, the remaining two correspond to additional translation and rotation DOFs of the central layer (Figure 12a). The Lagrangian parameters are collected in the vector reported in Eq. 2.5. In this regard, the static variable of each macro-element is described by eight components as shown in Figure 12b, and given by the vector **q** in Eq. 2.6

$$\mathbf{a}^{T} = \begin{bmatrix} u_i & w_i & \varphi_i & u_j & w_j & \varphi_j & w_e & \varphi_e \end{bmatrix} \qquad 2.5$$

$$\mathbf{q}^{T} = \begin{bmatrix} V_i & N_i & M_i & V_j & N_j & M_j & N_e & M_e \end{bmatrix} \qquad 2.6$$

The element was implemented in the software TREMURI [52] and presents the great advantage of being simple and computationally efficient. However, despite its simplicity and low computational cost, such an element is not able to simulate the OOP

behavior of masonry walls, making it unsuitable for the seismic assessment of historical and monumental structures for which the box-type behavior is an unrealistic hypothesis.

The model was recently upgraded by Bracchi et al. [20] in order to account for second-order effects. In particular, in the new macro-element, the equilibrium equations of the macro-element, originally referred to as the undeformed configuration (Figure 13a), are written in the deformed one (Figure 13b)

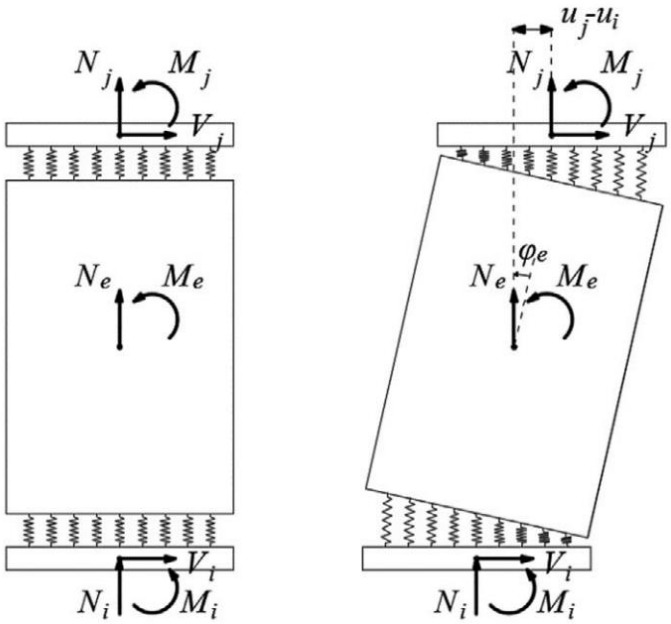

Figure 13 - Equilibrium in the (a) first- and (b) second-order configuration [20]

The lever arm (h) of the horizontal shear force (V) is assumed constant and equal to h since, for common masonry panels, the vertical displacement is small with respect to the height of the element. On the contrary, the lever arm ($u_j - u_i$) of the vertical axial forces is updated during the analysis according to the deformed configuration of the panel and generating an additional moment.

The authors found that in the presence of a pure rocking response, piers achieving in-plane drift ratios higher than 10% are affected by second-order effects.

The above-described model has been upgraded by Vanin et al. [19] in order to simulate the spatial response of masonry walls, accounting for second-order effects. The

model was implemented in OpenSees, the macro-element is formulated as a one-dimensional element defined by three nodes, two at the element ends and one at the midspan, all defined in three-dimensional space. It consists of an assemblage of two panels subjected to the same average shear deformation and separated by three nonlinear sections accounting for deformations due to axial strains. The kinematic of this element is presented in Figure 14. The shear response is controlled by a non-linear interface located at mid-height of the element, in which all shear deformations of the two panels are lumped (Figure 14b). The flexural response is described by three sections that can model coupled in-plane and out-of-plane rocking. The midspan section of the element allows the one-way out-of-plane bending to be modelled in a simplified way. The element nodes are located at the extremities and at the midspan of the element.

The end nodes (named i and j in Figure 14) are standard three-dimensional node whose degrees of freedom describe three displacements and three rotations in space. The internal node e defines the displacements of the extremities of block A and B (points A' and B' in Figure 14 in three directions, from which the finite rotation of the two blocks can be derived. As a consequence each macro-element possess 18 local degrees of freedom (Figure 15a) which are collected in the vector $\mathbf{u}_{\mathbf{local}}$ reported in Eq. 2.7 to which corresponds the vector $\mathbf{q}_{\mathbf{local}}$ as expressed in Eq. 2.8.

From the vector of local displacements, the 12 displacements ($\mathbf{u}_{\mathbf{basic}}$) (Figure 15b) defining those at the flexural sections, the shear deformations of the panels, and a constant torsional deformation along the element can be obtained as reported in Eq. 2.9. To avoid complex co-rotational formulation while still accounting for second-order effects for moderate displacements, the element was implemented using only P-Δ formulation (Eq. 2.9), derived as a second-order Taylor-series expansion of the exact equations.

$$\mathbf{u}_{\mathbf{local}} = \left[u_i, v_i, w_i, \varphi_{xi}, \varphi_{yi}, \varphi_{zi}, \quad u_j, v_j, w_j, \varphi_{xj}, \varphi_{yj}, \varphi_{zj}, \quad u_{eA}, v_{eA}, w_{eA}, u_{eB}, v_{eB}, w_{eB} \right]^T \qquad 2.7$$

$$\mathbf{q}_{\mathbf{local}} = \left[N_i, V_{yi}, V_{zi}, T_{xi}, M_{yi}, M_{zi}, \quad N_j, V_{yj}, V_{zj}, T_{xj}, M_{yj}, M_{zj}, \quad N_{eA}, V_{yA}, V_{zA}, N_{eB}, V_{yB}, V_{zB} \right]^T \qquad 2.8$$

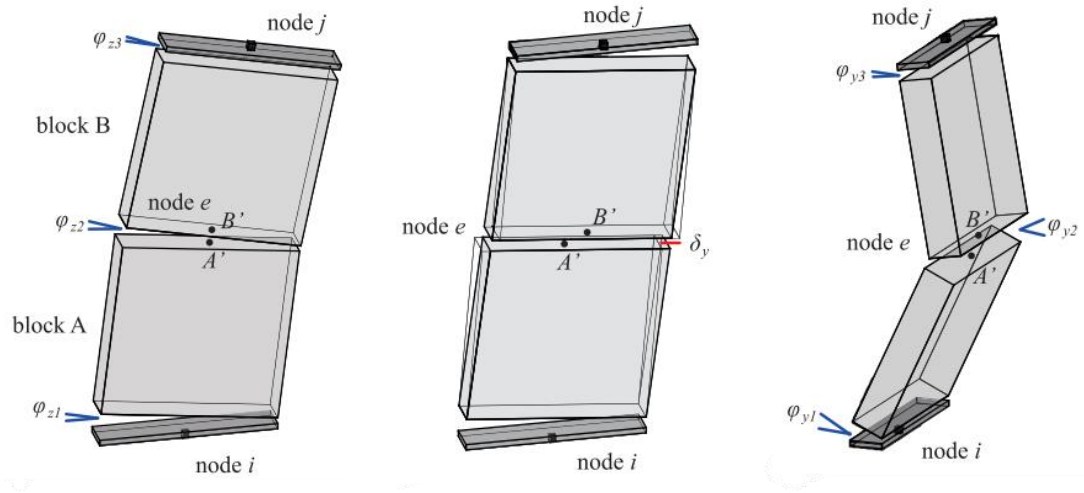

(a) (b) (c)

Figure 14 - Deformation modes of the macro-element: (a) in-plane flexure, (b) in-plane flexure and shear and (c) out-of-plane response [19]

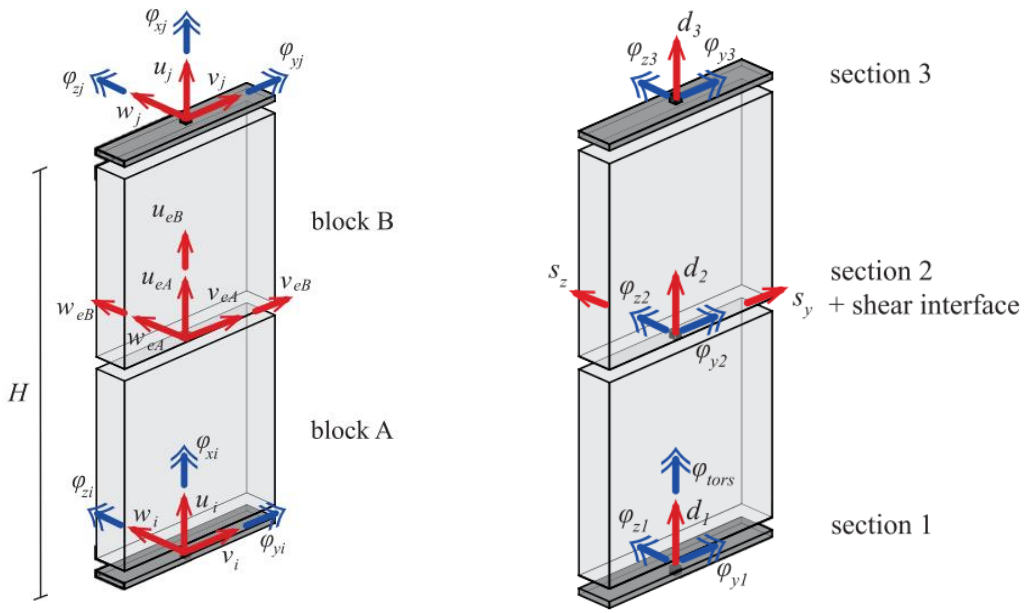

(a) (b)

Figure 15 - Definition of (a) local and (b) basic degrees of freedom of the macro-element [19]

$$\mathbf{u}_{\mathbf{basic}}^{(P-\Delta)} = \begin{bmatrix} d_1 \\ \varphi_{z1} \\ \varphi_{y1} \\ d_2 \\ \varphi_{z2} \\ \varphi_{y2} \\ d_3 \\ \varphi_{z3} \\ \varphi_{y3} \\ s_y \\ s_z \\ \varphi_{tors} \end{bmatrix} = \begin{bmatrix} u_{eA} - u_i + \dfrac{\left(v_{eA} - v_i\right)^2 + \left(w_{eA} - w_i\right)^2}{H} \\ -\varphi_{z1} - \left(v_{eA} - v_i\right)\dfrac{2}{H} \\ -\varphi_{y1} - \left(w_{eA} - w_i\right)\dfrac{2}{H} \\ -u_{eA} + u_{eB} \\ \left(-v_{eA} - v_{eB} + v_i + v_j\right)\dfrac{2}{H} \\ \left(-w_{eA} - w_{eB} + w_i + w_j\right)\dfrac{2}{H} \\ -u_{eB} + u_j + \dfrac{\left(v_{eB} - v_j\right)^2 + \left(w_{eB} - w_j\right)^2}{H} \\ \varphi_{zj} + \left(v_{eB} - v_j\right)\dfrac{2}{H} \\ \varphi_{yj} + \left(w_{eB} - w_j\right)\dfrac{2}{H} \\ v_{eB} - v_{eA} \\ w_{eB} - w_{eA} \\ \varphi_{xj} - \varphi_{xi} \end{bmatrix} \qquad 2.9$$

The section models adopted for the three flexural sections and the shear interface shown in Figure 15 provide the local response in terms of sectional forces and the stiffness matrices of these sections. The vector of basic forces $\mathbf{q}_{\mathbf{basic}}$ is assembled as reported in Eq. 2.10.

The equilibrium matrix can be derived by formulating the equilibrium conditions in the deformed configuration of the nodal forces. The second-order effects are included in the vector $\mathbf{q_0}$ and are added to the sectional forces in the basic system. Once such forces are expressed in the local system through the incremental equilibrium matrix $\mathbf{\Gamma_E}$, a second vector $\mathbf{p_0}$, containing the reactions to the applied element loads in the local system, needs to be subtracted to ensure equilibrium at the nodes (Eq. 2.11).

$$\mathbf{q_{basic}} = \left[N_1, M_{z1}, M_{y1}, \quad N_2, M_{z2}, M_{y2}, \quad N_3, M_{z3}, M_{y3}, \quad V_y, V_z, T_{tors} \right] \qquad 2.10$$

$$\mathbf{q_{local}} = \mathbf{\Gamma_E}(\mathbf{q_{basic}} + \mathbf{q_0}) - \mathbf{p_0} \qquad 2.11$$

2.1.3.2 The Discrete Macro-Element Method (DMEM)

The Discrete Macro-Element Model was firstly introduced by Caliò et al. [92] and then upgraded by several authors in order to make it able to simulate the in-plane and out-of-plane nonlinear behavior of masonry structures under seismic excitation. Since this thesis is focused on DMEM approach, this numerical method is properly and fully discussed in Section 4.

2.2 Analytical Methods

As represented in Figure 5, two main analytical methodologies are generally adopted for assessing the out-of-plane mechanisms of URM walls based on the theorems of the limit analysis and Housner's rigid block theory. These methodologies are generally associated with two different assessment strategies: the Force-based assessment (FBA) and the displacement-based assessment (DBA) approaches.

The FBA defines the wall safety factor in terms of acceleration, particularly as the ratio between the acceleration that activates the mechanism to the PGA expected in situ. Conversely, DBA approaches compare the system demand and capacity in terms of displacement. A detailed description of the assessment techniques is out of the scope of this thesis. However, more details on this topic can be found in [59], [93]. Finally, it is worth mentioning that several researchers over the past few decades corroborate the assumption that the OOP behavior of masonry walls is more correlated to velocity and displacement demands rather than acceleration values which are more related to the developments of forces [60].

2.2.1 Force-Based vs Displacement-Based Approaches

Limited attention has been given to the dynamic out-of-plane response of masonry walls. Indeed, FBA was initially recommended because URM is considered a very brittle material. Nonetheless, the recent possibility, due to the potentiality offered by computers today and some experimental campaigns, to study the out-of-plane dynamic behavior of wall structures has demonstrated that URM walls, subjected to dynamic loads, can resist acceleration higher than their static strength [60], [94], [95]. Hence, Displacement-Based Approaches (DBA) have also gained popularity for the seismic evaluation of masonry structures [13].

In 1985 Priestley et al. [62], by introducing the concept of ductility within an energy framework, demonstrated that the level of seismic loading required to cause failure, especially for face-loaded walls, tends to greatly exceed the prediction obtained by simple ultimate strength calculations. The topic was discussed in more detail in Doherty (2000) [60]. A few years later, a SDOF idealization of the rocking behavior of vertical spanning (VS) or parapet URM was proposed by Doherty et al. (2002) [35]. They presented a new simplified linearized displacement-based procedure in which a tri-linear relationship is used to characterised to the non-linear force-displacement relationship of URM walls. This procedure is founded on the reserve capacity of rocking unreinforced masonry walls to displace OOP without overturning, arising as the wall's post-cracking response is governed by stability mechanisms, that is to say, geometric instability of URM walls will only occur when the mid-height displacement exceeds its stability limit. The proposed idealized tri-linear force-displacement relationship represents the actual curvilinear relationship and encompasses axial and flexural deformations and rocking displacement for single-leaf walls.

Griffith et al. (2003) [96] systematically evaluated the presented simplified procedure to evaluate the response of URM walls subjected to OOP excitations by means of the tri-linear force-displacement curve and demonstrated that the collapse of the wall is mainly conditioned by its maximum strength and displacement capacity rather than its initial stiffness. In this work, the wall is idealized as a rigid body on simple one-way bending. A procedure to evaluate trilinear model for multi-leaf walls was proposed by

Derakhshan, Griffith and Ingham (2013) [97]. These procedures include, first, the calculation of rigid bilinear relationship (Figure 16a,b) and next the trilinear relationship (Figure 16c) using three defining parameters, i.e., Δ_1, Δ_2, F_0*. The amplitude of the force plateaux is therefore controlled by the ratio between Δ_1 and Δ_2, on the other hand the initial slope of the tri-linear curve is governed by the force amplitude F_0* and the value of Δ_1.

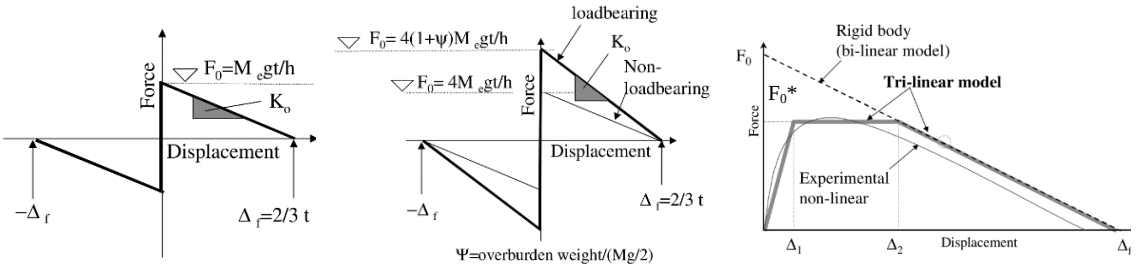

(a) (b) (c)

Figure 16 - Force-displacement relationship. Rigid bi-linear model for a) parapet wall, b) vertical spanning wall, c) tri-linear idealizations [35]

Doherty et al. (2002) proposed the value of the ratio between Δ_1 and Δ_2 as a function of the condition of the walls, distinguishing between "undamaged", "moderately degraded", and "severely degraded" conditions.

One of the main conclusions obtained by these studies was that the lateral static strength and the ultimate displacement of unreinforced masonry walls subjected to OOP are only conditioned by: geometry, boundary conditions, and applied vertical forces (including self-weight). In this kind of analysis, the uncertainties in the mechanical properties of the material (especially the elastic modulus and the compressive and tensile strength of masonry) do not significantly affect the results.

2.2.2 Limit Analysis models

These analytical approaches are based on limit analysis theorems which have the great advantage of being simple to use and independent of many material properties but, for this reason, related to very simplified materials models.

Limit analysis was one of the first methods used for the safety assessment of

masonry structures. The limit analysis is set within the theoretical frame of plasticity theory for masonry structures, as formulated by Heyman (1996) [98]. Heyman was the first who apply this theory to the analysis of masonry structures [98]. His works were based on the assumption that limit theorems of plasticity (lower-bound theorem and upper-bound theorem) can be applied to masonry structures only if i) masonry has no tensile strength (it can resist infinite compression), and ii) no sliding will occur within the masonry. According to this formulation, the failure in URM structures can only occur due to instability rather than material failure. According to this, the application of the static theorem leads to a lower-bound solution based on equilibrium equations, while the application of the kinematic theorem provides an upper-bound multiplier of the collapse load factor. The solution that satisfies the hypotheses of both theorems, equilibrium, compatibility, and material conditions, is the correct solution and provides the collapse load multiplier for the specific problem.

The application of the limit analysis to a given URM building requires the preliminary formulation of all possible failure mechanisms, followed by the identification of the one associated with the lowest value of the load multiplier, able to maintain a limit equilibrium configuration. The method consists in assuming a reasonable number of collapse mechanisms involving the entire structure or part of it and deriving the relative kinematic multipliers in order to identify the minimum value corresponding to the collapse multiplier. Several developments have been made in the use of limit analysis without the strict applicability of the limit theorems, which led to the so-called *non-standard* limit analysis.

In 1989 Giuffrè [99] presented original works based on a series of post-seismic damage surveys carried out in the sequence of Irpinia and Syracuse earthquakes in Italy, wherein the author underlined the complex nature of the possible out-of-plane mechanism in URM walls and taking into account the load pattern that caused each of the possible modes showing that in most of the cases, the damages were caused by OOP behavior, rather than IP failure.

Two years later (1991) [100] he stated that it is possible to study only a part of the building because the lack of structural connections in existing masonry structures leads to

every structural portion supporting its own loads without the participation of the adjacent parts. This considerably simplifies the analysis of existing masonry buildings because it is limited by a series of "sub-structures", but it increases the number of possible collapse mechanisms to be controlled. Therefore, given the complex nature of the possible out-of-plane mechanisms and taking into account the load patterns that cause each of the possible modes, the study of this type of mechanisms must be performed on an individual basis, identifying the different loads, geometry, and boundary conditions controlling each mechanism.

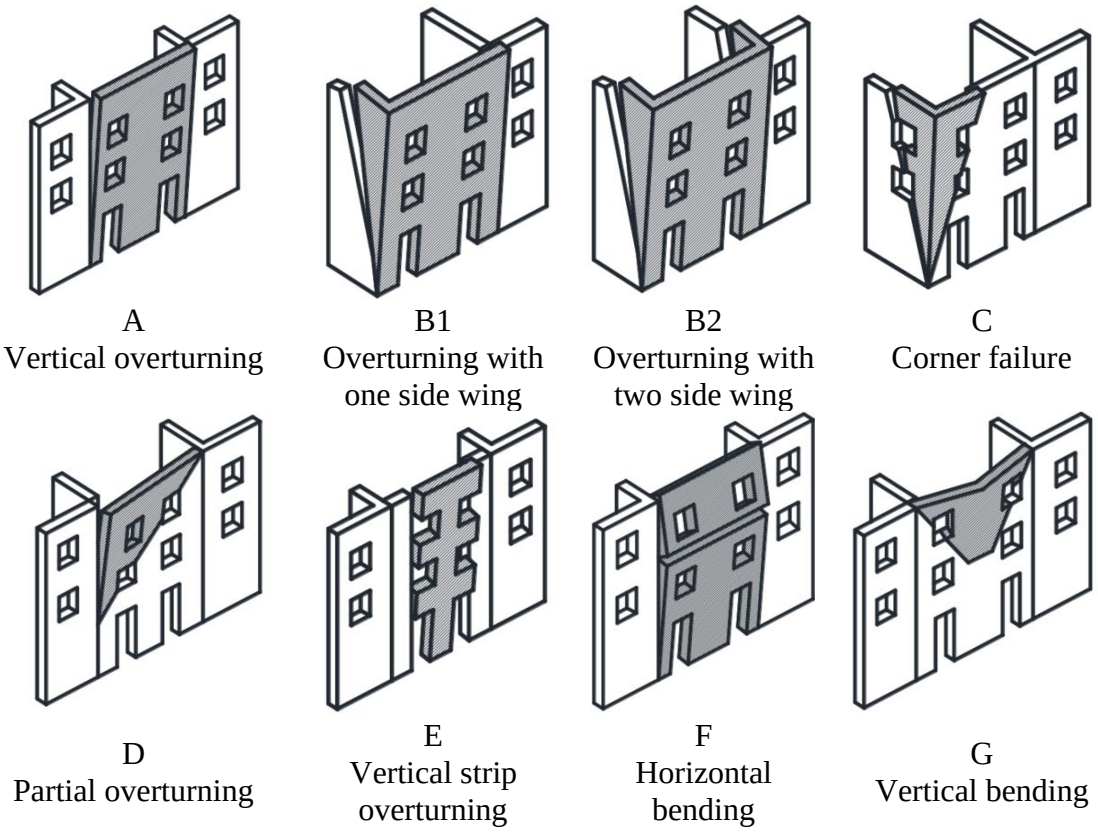

Figure 17 - Typical out-of-plane collapse mechanisms for historic masonry buildings [101]

After this early work, several authors proposed failure modes and new out-of-plane mechanisms with different load-pattern, geometry, and boundary conditions. D'Ayala and Speranza (2003) [101] developed a collection of simple mechanical models based on limit state analysis and macro-elements (Figure 17). According to this proposal, the load factor is described by the ratio between the lateral acceleration, a, and the gravitational

acceleration, g, under the assumption that dead load and horizontal forces are applied at the center of mass of the portion of the building involved the mechanism and are expressed as a function of the gravity constant; the masonry walls are simulated as a system of rigid bodies articulated by hinges; the masonry is simulated by a discontinuum model with friction. The failure mode associated with the minimum load factor is the most likely to occur. The collapse modes and the resulting analytical models account for connections, loading and restraints effects of horizontal structures, presence of strengthening devices (such as ties and ring beams).

Following the limit analysis approach, several authors have studied more sophisticated upgraded formulations in order to take into account frictional resistance for the combing rocking-sliding, horizontal-flexure, and torsion-bending interactions [24], [28], [29]. The major advantage of limit analysis is the simplicity of the approach, allowing the development of practical computational tools characterized by a reduced number of input parameters. This fact makes the limit analysis very used in the professional field for the assessment of historic masonry structures for which the input data are usually very difficult or even impossible to obtain. Nevertheless, the fact that limit analysis leads to very conservative results because the OOP seismic behavior tends to be governed by maximum displacement rather than by maximum strength is a clear limitation of the methods [101].

2.2.3 Rigid-Block Models

As reported by Makris and Konstantinidis (2003) [102], reconnaissance reports after a strong earthquake include the uplift, rocking, and in some cases, the overturning of a variety of slender structures. This fact increases the need to understand and predict this kind of failure and has motivated a large number of studies on the rocking response of rigid blocks, which would be applied in the evaluation of the rocking response of masonry structures under earthquake excitations.

The problem of a rigid block (RB) on a rigid foundation experiencing lateral dynamic loading has been of interest to researchers for many years. Several analytical and numerical models have been proposed to study this phenomenon, starting from Housner (1963) [38], who was the first to examine free and forced vibration of a rigid rectangular

block set to rocking when the bouncing does not occur and the coefficient of friction is sufficiently large to prevent sliding between the block and the base introducing what is known as the classical theory discussed below. Following Housner's work, Priestley, Evison, and Carr (1978) [103] presented a study comparing Housner's theory results for the free rocking of the rigid block with experimental results from a simple structural model with different foundation conditions (Figure 18).

In 1980, Aslam, Scalise, and Godden [104] studied the rocking and overturning response of blocks of various sizes and aspect ratios under strong earthquakes, also considering the effects of the coefficient of restitution and vertical load. This study points out the sensitivity of the results in small changes in base geometry and coefficient of restitution. In the same year and following the same line, Yim, Chopra e Penzien (1980) [105] developed a numerical procedure to solve the non-linear equations of motion governing the rocking motion of rigid blocks on rigid bases subjected to horizontal and vertical ground motions. The authors stressed the fact that the rocking response is very sensitive to small changes in its size and slenderness ratio.

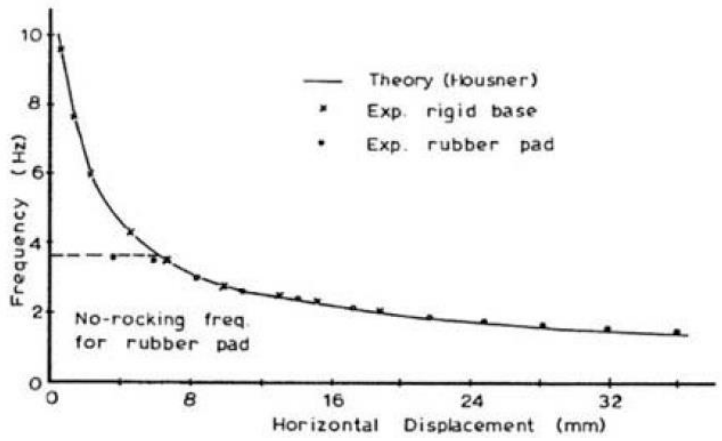

Figure 18 - Comparison between Housner's theory for free rocking of rigid blocks and experiment for Priestley's model [103]

Following these first studies, a large number of works deal with the dynamic of a rigid rocking block. In 1983 Ishiyama [106] studied the conditions of rocking activation and overturning of rigid blocks under earthquake excitations and obtained, by considering a sinusoidal base input, lower limits for seismic Intensities Measures (IMs): PGA, PGV

and PGD. From his study was evident that PGA influenced the activation of rocking but cannot be a proper IM for overturning except for very small blocks. Overturning is, instead, mainly related to PGD.

Years later, Makris and Konstantinidis (2003) [102] highlighted the differences between the oscillatory response of a single-degree-of-freedom (SDOF) oscillator (regular pendulum) and the rocking response of a rigid block (inverted pendulum). In 2008 Sorrentino et al. [107] applied the rigid-body-based principles with the study of the rocking response of URM facades. The authors investigate the one-sided rocking behavior of typical masonry facades of Gaeta in Central Italy, proving that one-sided rocking is more dangerous than two-sided rocking and that the static results can be overly conservative, leading to unnecessary retrofitting actions.

Sorrentino (2011) experimentally assessed the coefficient of restitution, which govern the rocking response at each impact [108]. Subsequently, Shawa et al. (2012) [109] developed a modelling strategy to reproduce the out-of-plane dynamic behavior of masonry façade walls taking advantage of the discrete nature of these elements, consisting of a façade separated from the transverse walls.

Starting from existing rocking models, which concentrate damping at the impact, the authors developed a model that considers the asymmetry provided by the transverse walls and from out-of-plumb of the wall in the configuration at rest. The analytical coefficient of restitution was deduced based on a set of experiments performed on masonry walls undergoing free-rocking oscillations.

Furthermore, the influence of both seismological parameters [110] and certain structural characteristics, such as the presence of additional loads, due to, e. g., masses from floor and/or roof elements and vaults [111], [112], tie bars [63], [112], and transverse walls [108], [109], [113], were the subjects of different researches.

Alongside the SDOF-based approaches, which have been extensively studied, only a few works have been presented that deal with the analysis of the rocking behavior of rigid blocks resorting to multi-degrees-of-freedom (MDOF) approaches.

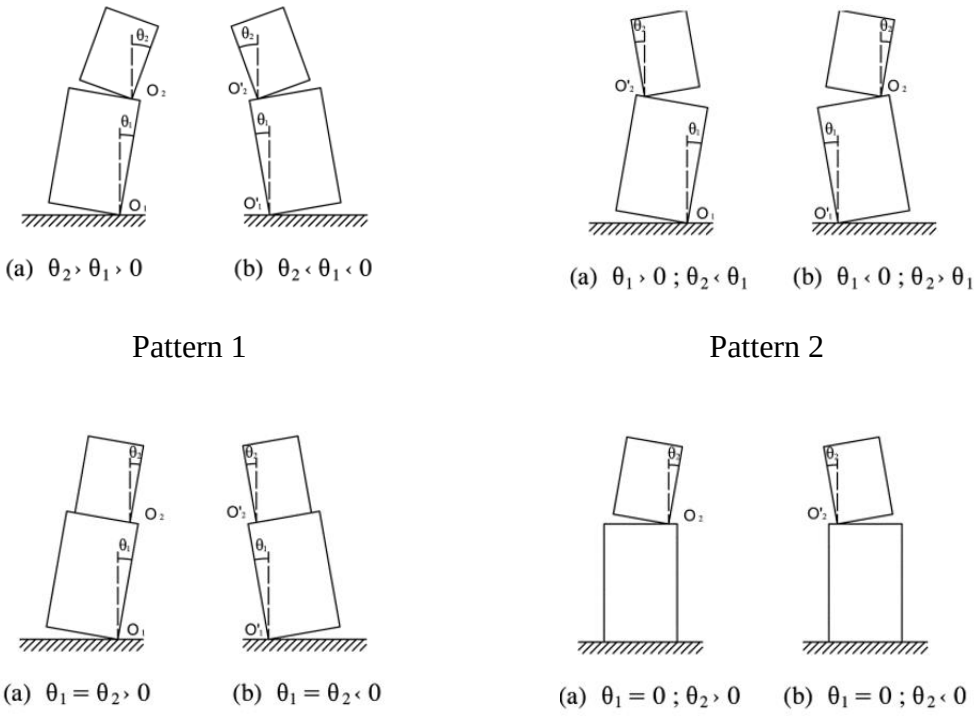

Figure 19 - Rocking patterns for a system of two stacked rigid blocks [114]

As highlighted by D'Ayala and Shi (2011) [115], even for the simplest case of a system composed of two blocks, the rocking problem becomes very complex. In 1990, Psycharis [116] presented an analysis of the dynamic behavior of a system consisting of two rigid blocks without sliding subjected to horizontal and vertical ground motion. The authors identify four possible patterns of response and impact, assuming conservative angular momentum (Figure 19). Although, such a procedure proved to be too complicated, and the equations of motion and energy dissipation had to be formulated for every possible mode of response. Every non-linear equation of motion has been integrated for each pattern. Following Psycharis' work, Spanos, Roussis, and Politis (2001) [114] studied the dynamic behavior of a system composed of two blocks assuming no sliding, and derived, for each pattern, the non-linear equations governing the rocking response of the system subjected to horizontal and vertical ground motion. Numerical results for both free and seismic responses have been derived.

Other studies have been proposed in order to study the motion of the two blocks and the patterns of relative motion and sliding [115], to develop a 2-DOF model for the analysis of the dynamic out-of-plane behavior of a single wall considering the hypothesis of the flexible diaphragm [117] or to describe the OOP response of one-way spanning unreinforced masonry walls including the effects of crack height, overburden load and mortar compressive strength [97].

2.2.3.1 Housner's classical theory

Housner (1968) was the first who examined free and forced vibration of a rectangular block set to rocking when the bouncing does not occur and the coefficient of friction is sufficiently large to prevent sliding between the block and the base and showed that the rocking frequency decrease with initial rotation amplitude, also presenting what was called as scale-effects, by which the larger of two similar geometrical blocks could survive the excitation while the smaller block topples [38].

Housner was the first author that solved the equation of motion of a rigid block subjected to rocking in closed form. According to this model, the rigid block of height 2h and width 2b, shown in Figure 20, will oscillate about the center of rotation O and O' when it is set to rocking.

The significant properties of rigid blocks are:

- Its weight, $W = mg$;
- Its inertia moment, $I_0 = \frac{4}{3}\, m\, (b^2 + h^2)$, about the point O;
- The location of the center of gravity a distance h above the base, a distance b from the side of the block;
- The radial distance from the center of rotation to the center of gravity, $R = \sqrt{b^2 + h^2}$, when the block is at rest, R makes an angle α with the vertical side.
- The tilting of the block from the vertical is measured by the angle θ.

In the case of free vibration, when the block is rotated through an angle θ, the weight of the block will exert a restoring moment $WR\sin(\alpha - \theta)$. The equation of motion is then:

$$I_0\ddot{\boldsymbol{\theta}} = -WR\sin(\alpha - \boldsymbol{\theta}) \qquad 2.12$$

Being $\alpha = \text{arctg}(B/H)$. *Eq.* 2.12 subjected to the conditions $\boldsymbol{\theta}(0) = \theta_0$ e $\dot{\boldsymbol{\theta}}(0) = \dot{\theta}_0$, has the solution:

$$\boldsymbol{\theta} = \alpha - (\alpha - \theta_0)\cos(p\mathbf{t}) \qquad 2.13$$

where $p^2 = WR/I_0$ is a frequency parameter of the block referring to the pendulum frequency.

From a physical perspective, the frequency parameter p refers to the pendulum frequency of the block as if it is hanging from its pivot point and not the classical natural frequency, which usually measures cycles of vibration per second. This discrepancy stems from the fact that the natural frequency and period of the rocking motion are amplitude-dependent and, thus, unsuitable for characterizing a structure.

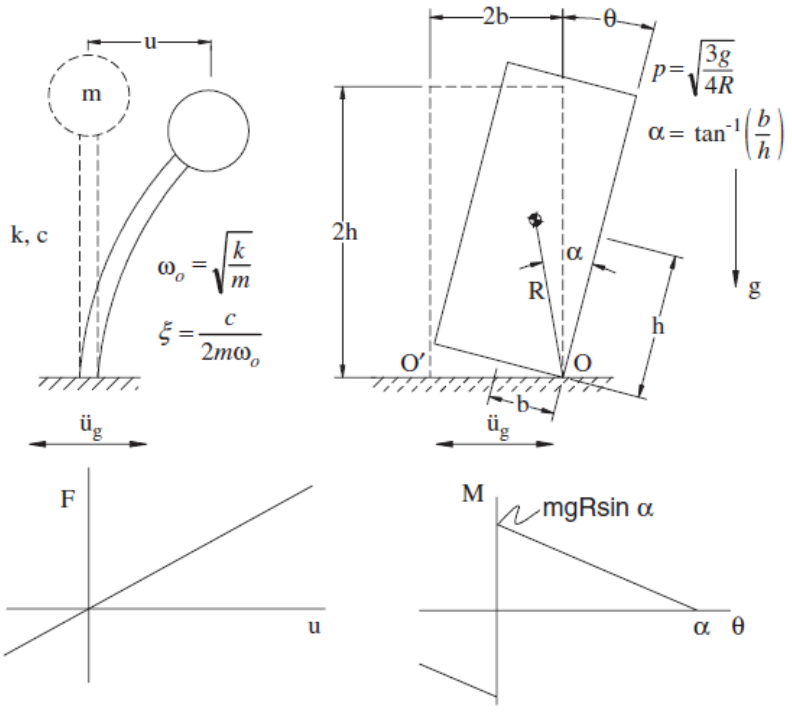

Figure 20 – Rectangular Rigid block (Housner 1963)

Eq. 2.13 describes the rotation of the block about point O as it falls back into the vertical position. The block will then tilt about the point O', and if there is negligible energy loss during impact, the block will rotate through an angle $\theta = -\theta_0$. The block will then fall back again to the vertical position and will rise about point 0 until θ is again equal to θ_0. At this instant, one complete cycle will have been completed. The time, T, required to complete this cycle is the period of free vibration. The block will fall from $\theta = \theta_0$ to $\theta = 0$ in a time t = T/4 and at this instant Eq. 2.13 becomes:

$$0 = \alpha - (\alpha - \theta_0)\cosh\left(p\frac{T}{4}\right) \qquad 2.14$$

Therefore, the period T can be written as a function of p and the ratio $\frac{\theta_0}{\alpha}$:

$$T = \frac{4}{p}\cosh^{-1}\left(\frac{1}{1-\theta_0/\alpha}\right) \qquad 2.15$$

From Eq. 2.15 is evident that the period is strongly dependent upon the amplitude ratio θ_0/α. In particular, when the ratio θ_0/α is close to unity, the period is long; instead, when the ratio is close to zero, the period is short (Figure 21).

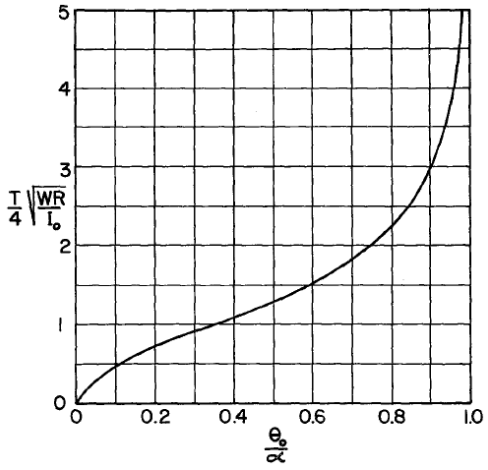

Figure 21 - Period of Vibration of rigid block vs amplitude of rotation

Energy dissipation is assumed to occur entirely at the impact, in which the rotation is switched from one base edge of the block to another. The impact, which is considered as

an instantaneous event where the system is characterized by infinite stiffness, induces a reduction of the velocity, quantified by the coefficient of reduction *e* ranging from 0 to 1. A value of $e = 0$ corresponds to a totally inelastic impact, while $e = 1$ indicates a perfectly elastic impact. Conservation of the angular moment about the center of rotation, just before and after each impact, gives the analytical relationship for a maximum value of the coefficient of restitution (Eq. 2.17), which correlates with the velocity of the block just after (t_i^+) and before (t_i^-) the impact (Eq. 2.16), highlighting that the energy loss during the impact is strongly related to the geometry of the block and not the material properties (mass or stiffness). Some experimental observations showed different values of the restitution coefficient than those predicted by the classic theory suggesting that continuum energy dissipations due to flexural masonry deformation and plastic deformations at the rocking interfaces contribute significantly to the energy dissipation process [102]. In a recent work, Tomasetti et al. [118] found values of the coefficient of restitution coefficient ranging from 0.84 to 0.91.

$$\dot{\boldsymbol{\theta}}(t_i^+) = e \cdot \dot{\boldsymbol{\theta}}(t_i^-) \qquad 2.16$$

$$e = 1 - \frac{3}{2}\sin^2 \alpha \qquad 2.17$$

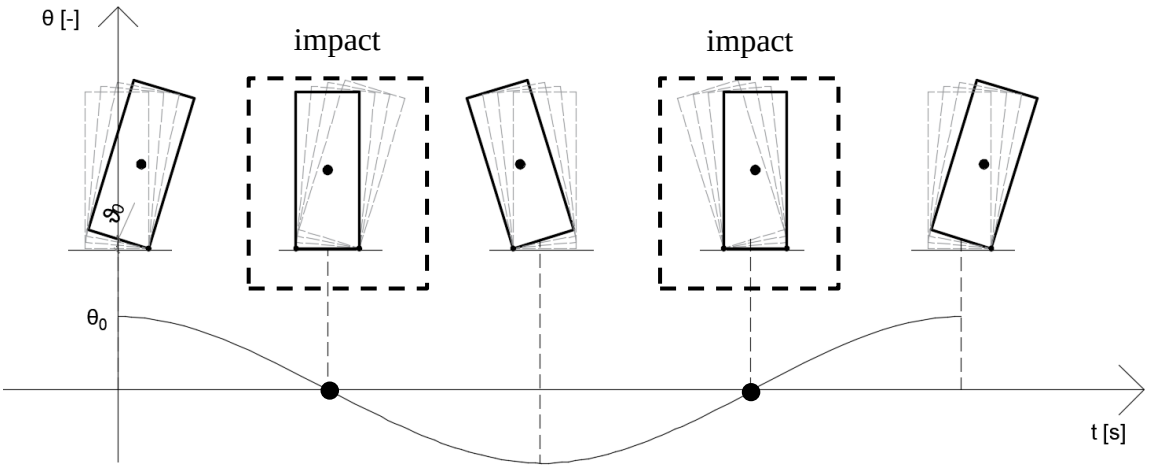

Figure 22 - Free Vibration rocking motion of a rectangular rigid block

Damping consideration for the rocking behavior

As the complexity of the structure increases, e.g., more degrees of freedom, different boundary conditions, or introduction of flexible interfaces, among others, the classical rocking theory becomes complicated.

Hence, alternative analytical and numerical models have been proposed to capture the transient nonlinear dynamic response of various rocking configurations [114], [119], [120]. At the same time, recent developments in computational approaches used for modelling masonry structures are gaining momentum, particularly block-based models, which have been found capable of reproducing the dynamic response of masonry walls while also being able to model masonry texture and interaction with surrounding structural elements. These include the finite-element (FE) methods and the discrete-element (DE) methods, among others. However, despite their widespread use, the applications of these models usually lack a reliable treatment of energy loss due to the non-smooth behavior of impacts during rocking motion [121], [122].

The numerical model often treats energy dissipation in a different manner than the classical theory; Specifically, instead of the instantaneous event-based approach that the classical rocking theory assumes, energy loss is regarded as a continuous process through rocking motion, usually simulated via viscous definition and hysteretic constitutive relationship. In particular, by definition, viscous models assume that the damping forces ($\mathbf{f_D}$), expressed in Eq. 2.18, are proportional the velocity, $\dot{\mathbf{u}}$

$$\mathbf{f_D} = \mathbf{C} \cdot \dot{\mathbf{u}} \qquad 2.18$$

in which **C** is the global damping matrix of the system.

Viscous damping models are mathematical artifices employed to simulate the source of dissipation, and they can be treated as a material characteristic assigned at each DOFs of the structure, and in this case, the dissipation process is distributed along the structure. Nevertheless, this kind of viscous damping model is not consistent with the physical phenomenon of impacts considering the localized nature of the damping problem

in the rocking motion. Different viscous damping models have been proposed to describe the energy dissipation during the response history of a structure (Figure 23).

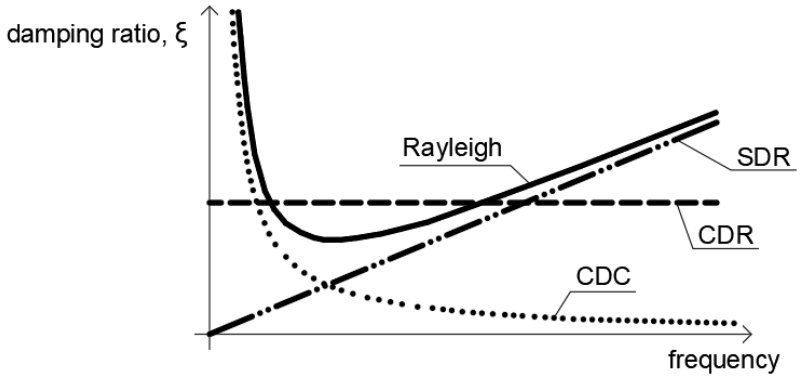

Figure 23 - Viscous damping models with respect to the frequency content

The most widely used damping model are those represented in Figure 23. In particular, constant damping coefficient (CDC) model retains the same value of **C** throughout the response history. This is equivalent to a mass-proportional (MP) damping definition, thus damping out low-frequency content. MP damping consists of the application of a force resulting from the product of the absolute velocity of the block, the mass of the block, damping ratio, and rotational frequency, with a direction opposite to the velocity vector. This type of damping decreases non-linearly with increasing the frequency, resulting in a plausible damping ratio for higher frequency motion but producing an overdamped response at a low frequency that potentially leads to the artificially restricted motion of the blocks. Thus, MP damping is generally non recommended for problems that involve large displacements of blocks, which implies low-frequency oscillations [123]. Another well-established model associates a constant damping ratio (CDR) with all frequencies. This definition allows an update of the stiffness matrix but not the damping ratio ξ during the response history, resulting in an equivalent dissipation of all the frequency content. Nevertheless, it is usually challenging to define a constant damping ratio for all the frequencies.

Alternatively, when the phenomena to be modelled imply high-frequency oscillation, a stiffness-proportional damping ratio (SDR) is desirable in order to avoid unrealistic behavior. SDR allows the damping ratio ξ to follow the changes in the stiffness

matrix during the analysis if the full Newton-Raphson method is used. As a result, the high-frequency content of the response is highly dissipated. However, the computational time of certain problems may then become impractically long because the application of SPR damping requires a time step very small [123]. Finally, a combination of both mass and stiffness proportional models acting at the same time, known as Rayleigh damping, damps out both the low and high range of the frequency content.

Often, authors assume that the SDR damping model presents a convenient approach to model the damping of rocking structures [122], [123], associated with a localized damping model because, during rocking, when impact occurs, a huge increase in the frequency content takes place for a very short, yet finite, time and displacement. In addition, proper treatment of impact requires a proper definition of the value of c (or, equally, the value of ξ).

Particularly for the rocking problem, a relationship between the coefficient of restitution e and damping ratio ξ is critical to ensure energy equivalence between the classical rocking theory and the numerical viscous damping model. Several authors proposed ξ– e relationship in literature.

More specifically, Priestley et al. (1978) [103] first examined the energy loss equivalence of the classical impulsive dynamics theory and the viscous decay of an elastic oscillator. Later, Makris and Konstantinidis (2003) [102] simplified the ξ– e expression of Priestley et al. (1978), assuming damping independent of the rocking amplitude. Anagnostopoulus (2004) [124] studied the energy equivalence between the restitution coefficient *e* and a spring-dashpot viscous model based on the two colliding masses scheme and Imanishi et al. (2012) [125] proposed equivalent formulations. DeJong (2009) [126] simulated the rocking block with corner spring dashpots adopting a SDR damping formulation to critically damp either the axial frequency, the corner frequency, or the rotational frequency. More recently, Tomasetti et al. (2019) followed a calibration process of a single degree of freedom (SDOF) analytical formulation of rocking structures adopting different formulations of viscous models (i.e., CDC, CDR, and SDR), proposing an empirical expression to evaluate the equivalent damping ratio ξ_{eq} which has to be associated to the initial elastic frequency of the system ($\omega_L = \sqrt{K_L/m_{eff}}$), where m_{eff} is

the effective mass of associated to the system and K_L is the initial stiffness. The influences on the response of additional parameters, such as the interface stiffness, rocking amplitude, and aspect ratio, were also investigated. Finally, Vlachakis et al. (2021) formulated a ξ–e empirical "ready to use" relationships able to reproduce the impulsive dynamics' energy loss characteristics and subsequently ensure dynamic equivalence between the classical rocking theory and the numerical viscous damping model. They found through a phenomenological calibration methodology [122] the value of the equivalent damping ratio for both one- and two-side rocking which is related to the axial stiffness of the base interface, and depend on the geometric characteristic of the block. The performance of the new model is evaluated through comparisons with experimental tests from the literature. In general, the novel numerical model performs reasonably well for the two-sided free-rocking case, with only slightly faster energy dissipation than its experimental counterpart. Table 1 provides a summary of the ξ– e relationships available in literature applicable to the rocking problem accompanied by their basic assumptions.

Considering the numerous options for the application of damping and the multiple factors that influence the results described above, one can find it challenging to choose a correct damping approach with sufficient confidence. It was found that several authors have previously assigned damping values without a thorough discussion when using DEM and FEM dynamic simulations, probably due to a lack of explanatory literature available on the topic.

A valid attempt to establish guidance to support future modelling research using DEM strategy was recently made by Galvez et al. (2022) [123], which used the Rayleigh damping distribution model implemented in 3DEC to study the differences between mass proportional and stiffness proportional damping configurations. In conclusion, he found that, when considering numerical simulations that incorporated mass proportional damping and led to results that were seemingly well-matched to experimental tests, it was found that the apparent robustness of decisions pertaining to the adopted input parameters was deceptive in most cases. Consequently, stiffness-proportional damping was recommended for numerical rocking simulations.

References	Relationship
Priestley et al. (1978) [103]	$\xi_{eq} = \frac{1}{n \cdot \pi} ln \left\{ \frac{\theta_0}{\alpha} \left[1 - \sqrt{1 - e^{2n} \left[1 - \left(1 - \frac{\theta_0}{\alpha} \right)^2 \right]} \right]^{-1} \right\}$
Giannini and Masiani (1990) [127]	$\xi_{eq} = \frac{2 \cdot (1 - e)}{\pi \cdot (1 + e)}$
Makris and Konstantinidis (2003) [102]	$\xi_{eq} = -0.68 \cdot \ln(e)$
Anagnostopoulus (2004) [124]	$\xi_{eq} = -\frac{\ln(e)}{\sqrt{\pi^2 + (\ln(e))^2}}$
Cheng (2007) [128]	$\xi_{eq} = \frac{(1 - e^2)}{\pi \cdot (1 - \Delta/b)}$
DeJong (2009) [126]	$\xi_{eq} = \frac{b}{2h}; \ \xi_{eq} = \frac{b}{R}; \ \xi_{eq} = 100\%$
Imanishi et al. (2012) [125]	$\xi_{eq} = -\frac{\ln(e)}{\sqrt{4\pi^2 + (\ln(e))^2}}$
Tomasetti et al. (2019) [118]	$\xi_{eq} = -0.218 \ a_1 - 0.195 \ln(e)$
Vlachakis et al. (2021) [122]	$\xi_{eq,2S} = -0.000292 \cdot \left(\frac{H}{B} \right)^{0.935} \cdot k_{n,base}^{0.343} \cdot ln(e_{2S})$ $\xi_{eq,1S} = -0.0807 \cdot \left(\frac{H}{B} \right)^{0.2548} \cdot k_{n,base}^{-0.1283} \cdot ln(\lvert e_{1S} \rvert)$

Table 1 – ξ-e relationship for the rocking problem

Note: Δ/b = amplitude of motion; a_1 = alternative definition of system's stiffness based on a tri-linear force-displacement relationship

2.3 Experimental Tests

During the last decades, several experimental works have been done aiming at the assessment of the out-of-plane behavior of masonry elements by experimental-laboratory campaign or in-situ tests. Overall other evaluation techniques, experimental works have the great advantage of dealing with real structures and observations rather than analytical or numerical models. Despite what one may think, laboratory tests of masonry constructions deal with some limitations and difficulties, mainly regarding the correct reproduction of the existing materials and in-situ conditions. Moreover, also the need to have scaled masonry models to perform shaking table tests may strongly influence the reliability of the results [129].

2.3.1 Laboratory Tests

An extensive experimental campaign was carried out by ABK (1984) [94] to study the dynamic out-of-plane behavior of URM walls, aiming at developing a methodology for the mitigation of seismic hazards in existing masonry buildings. For this reason, twenty unreinforced masonry walls with slenderness ratios varying from 14 to 25 were subjected to dynamic out-of-plane tests with acceleration varying from 0.1g to 0.4g. The tests demonstrated that the resistance of the walls to out-of-plane collapse was dependent on the PGV and the input at the base and the at the top of the walls. In 1991, Tomaževič, et al. [130] investigated the influence of the roof rigidity on the out-of-plane behaviour of stone masonry buildings by the application of shaking table tests on scaled specimens. From such experimental campaign, it was possible to determine the crack pattern and failure mechanisms associated with masonry structures in the presence of flexible diaphragms.
Another extensive laboratory programme was conducted in 1998 by Benedetti, et al. [131] aiming at the evaluation of the response of masonry structures before and after the application of a retrofitting procedure. For the purpose of such investigation, fourteen half-scaled specimens were subjected to seismic inputs until a considerable damage pattern was identified.

A new approach oriented to the study of the out-of-plane collapse mechanism of

simple URM walls was presented in 2002 by Doherty [35]. This work also involved a series of shaking table tests whose results demonstrated that, for the ultimate conditions, out-of-plane walls are more susceptible to displacement demand rather than acceleration. Also, Lam et al. (2003) [132] carried out experimental shaking table tests which pointed out the fact that response spectral displacement, as opposed to acceleration, is a better indicator of ultimate performance, and also it was observed that the displacement response of the wall varies linearly with the frequency of the applied excitation. Griffith et al. (2007) [133] presented an experimental campaign aiming at assessing the OOP behavior of URM structures subjected to two-way bending loading. In this campaign 8 full-scale URM walls with different geometry and axial loads were subjected to static tests using a system of airbags in order to obtain cyclic load-displacement relationships. As a result, the authors stressed the observation of a substantial post-peak capacity in terms of both displacements and strengths.

Al Shawa et al. (2012) [109] performed 34 shaking table tests on a tuff masonry u-shaped structures composed of a single façade with two transversal walls finding interesting results regarding the influence of input motion on the overturning of the façade.

A more recent investigation, on a u-shaped non-symmetric configuration, was conducted in 2017 by Candeias et al. [134] aiming at assessing the out-of-plane behaviour of two URM structures by means of shaking table testing. The prototype was composed of one main gable wall and two non-symmetric return walls. A uniaxial seismic input was increasingly applied in the direction perpendicular to the main gable wall up to failure.

More recently, Meriggi et al. (2019) [48] performed shaking table tests on two full-scale wall specimens built in tuff and stone masonry in out-of-plane bending.

2.3.2 In Situ Tests

On the other hand, the out-of-plane behaviour of masonry structures has also been assessed by means of in-situ experimental testing. However, the literature regarding this topic is quite limited.

The first in situ experimental campaign aiming at studying the OOP seismic

behavior of URM structures was carried out by Costa in 2002 [135], in which stone masonry walls were subjected to cyclic out-of-plane loading by means of an attached device composed of steel frames, aiming at discussing the role of testing techniques in the definition of adequate rehabilitation and strengthening procedures pre- and post-earthquake.

Another in-situ campaign test was conducted by Tumialan in 2003 [136] in which seven masonry specimens were subjected to out-of-plane loading up to failure by means of a hand driven hydraulic jack. In particular, two of the seven specimens were tests as-built while the remaining five were tested after being reinforced.

In 2008 Arêde et al. [137] performed an experimental in-situ campaign on traditional masonry houses abandoned after the 1998 earthquake that hit the Faial island of the Azores. In this experimental campaign, five different specimens were tested, aiming to study the OOP behavior and the efficacy of some of the strengthening techniques recommended for post-earthquake interventions.

In 2009 Dizhur et al. [138] developed an in-situ testing program under which airbag tests were performed on two non-load-bearing partition walls at the William Weir Wing of Weir House in Wallington. The walls were subjected to a uniform distribution of out-of-plane loading and unloading by means of an arrangement of airbags, placed centrally and symmetrically to the walls in order to assess the stiffness degradation. One wall was tested in its as-built conditions, and the second was retrofitted with carbon fiber-reinforced polymers (CFRP). Testing confirmed that the boundary conditions in real buildings can significantly affect the experimental response and also confirmed that the FRP solution is an excellent low-invasive option for seismic strengthening of unreinforced masonry buildings. A similar investigation was later conducted by Ismail et al. [139] aiming at evaluating the out-of-plane behaviour of strengthened masonry structures. Masonry walls from a historic house in New Zealand in as-built conditions and strengthened with near surface mounted twisted steel bars were tested in-situ by means of an airbag system. An additional laboratory experimental programme was conducted for the validation of the results obtained in-situ.

3. TECHNICAL REGULATIONS

Despite the importance of OOP mechanisms, only a few international regulations implement reliable assessment procedures to evaluate the safety factors against these mechanisms, in some cases, based on empirical or oversimplified approaches. For a comprehensive review of this topic, the reader is referred to Sorrentino et al. [140].

This section presents a brief description of the procedures implemented in the European regulations (Eurocode 8), the Italian (NTC18), and the American (ASCE/SEI 41-13) codes. The symbols have been homogenised for consistency by taking Eurocode 8 [25] as the main reference.

3.1 Eurocodes

Eurocode 8 (EC8 2004) reports in Section 9 specific rules for masonry buildings. In particular, in Section 9.6, it is established that for the verification of safety against collapse, the design resistance of each structural element should be evaluated in accordance with Eurocode 6, which is not specific for seismic action and involves a strength approach any one of three methods (Eurocode 6: Design of Masonry Structures. 2005 - Section 6.4.1) which are discussed below.

Following EC6, the first method to assess OOP mechanisms consists of using a capacity reduction factor Φ which considers the effects of slenderness and the eccentricity of vertical loads due to initial eccentricities and the earthquake inertia forces (EC6. 2005 - Section 6.1.2). A second method, included in EC6 (EC6 2005, Section 6.3.1), follows the FBA. More specifically, the horizontal and vertical design moment M_{Ed} per unit length and height of the wall, respectively, is calculated taking into account the panel boundary conditions and the wall aspect ratio. Values of the bending coefficients are suggested in the code (EC6 2005, Annex E) as a function of the orthogonal ratio, μ, of the design flexural strengths of the masonry and referring to 12 fully restrained/simply-supported/free-edge

boundary conditions. The design value of a masonry wall's OOP resistant moment, M_{Rd}, evaluated independently in the two main masonry directions, depends on the panel boundary conditions and the design flexural strength of masonry in that direction. The beneficial impact of the vertical stress may be taken into account when a vertical load is present, and vertical bending is being considered.

Finally, EC8 (2004, Section 4.3.5.2) suggests evaluating the design value of uniform lateral load to the panel, equivalent to inertia forces, as S_a/q, where S_a is the elastic spectrum and $q = 2.0$ is the behavior factor for non-structural elements [140].

3.2 ASCE/SEI 41 (2017)

In the USA, OOP performance of URM walls of existing buildings is addressed in ASCE/SEI 41 (2017, Section 11.3.3). As required by Section 7.2.11 of ASCE/SEI 41, out-of-plane stability of URM walls shall be evaluated for out-of-plane inertial forces by considering components to span vertically between diaphragm levels when effective wall-to-diaphragm connections are present, or to span horizontally between intersecting walls, columns, or pilasters, or to span with two-way action.

According to ASCE/SEI 41 (2017), which gives the acceptance criteria for URM walls subjected to OOP actions, for the Immediate Occupancy Structural Performance Level, flexural cracking in URM walls caused by OOP inertial loading shall not be permitted. On the other hand, flexural cracking caused by OOP inertial loading shall be permitted for the Life Safety and Collapse Prevention Structural Levels, provided that the cracked wall remains stable during dynamic excitation. Moreover, for the Collapse Prevention Structural Level, vertical-spanning walls should have a height-to-thickness ratio less than or equal to the tabulated values depending on the position of the wall up the height of the building and the spectral pseudo-acceleration at T = 1.0 s. These values are derived from the tests ABK (1984) conducted on vertically spanning walls. The code also discusses the role of non-near-source and near-source ground motion, for which these values are sometimes unconservative. Moreover, the role of the “scale effect” (the thicker of two walls with the same slenderness ratio is more stable) and the position of the intermediate cracks,

which often do not occur at the mid-height [97], is also discussed. Finally, the code specifies the acceleration, *a*, for which the wall needs to be checked:

$$a = \max\left\{4S_e(T = 0.2s);\quad 1\right\} 0.1\chi \qquad 3.1$$

where χ is the factor for calculating the OOP wall forces, equal to 1 for collapse prevention, 1.3 for life safety and 2 for immediate occupancy, and acceleration are measured in g.

3.3 Italian technical standards (2018)

Italian code (NTC2018), in the chapter about masonry new-construction buildings, accounts for vertical bending alone. The formulation is similar to the capacity reduction factor Φ of EC6. In addition, the Italian code provides the design acceleration value to use in the checks.

A more comprehensive methodology is reported in the section on existing buildings, and the commentary on the Italian Code (CSLLPP 2019, Section C8.4) recommends the assessment of local-collapse mechanisms. This approach starts from the rigid-body approach studied by Giuffrè (1996) and is discussed in [13], [93]. In particular, the commentary on the Italian Code generalizes the displacement-base assessment to any OOP mechanism, and it is based on a series of theoretical and experimental studies on a large number of possible ultimate configurations compatible with external boundary conditions [64], [101], [144]. In addition, later studies underlined the possibility of considering stabilising effects of compressive strength involving an indentation of the pivot point along the contact section and of friction stresses due to the interlocking with transverse walls without changing the fundamental framework [22]–[24], [30], [93], [108], [145].

Each collapse configuration, defined by the displacement d_k of a control point, is studied in terms of the pushover curve, and the collapse load multiplier λ is calculated based on the Virtual Work Theorem. The curve starts with the static horizontal multiplier λ_0, a non-dimensional value of the acceleration necessary to activate the rocking mechanism

(under the hypothesis that the system's behavior is rigid). It ends when the load multiplier equals zero, and the instability is reached. Then, following the capacity spectrum method (Fajfar 1999) the pushover curve is defined, assuming the displacement shape to be virtual displacements at the initial configuration. Subsequently, the displacement, d_k, is converted in the equivalent spectral displacement, d^*, by the following transformation:

$$d^* = d_k \frac{\sum_i P_i \delta_{x,i}^2}{\sum_i \delta_{x,k} P_i \delta_{x,i}} \qquad 3.2$$

being $\delta_{x,i}$ the virtual horizontal displacement of the point of application of the generic i-th weight force P_i and $\delta_{x,k}$ the virtual horizontal displacement of the control point k. Than, the equivalent spectral acceleration is given by:

$$a(d^*) = \frac{g\lambda(d^*)}{e^*} \qquad 3.3$$

where e^* is the fraction of participating mass of the mechanism.

The commentary on the Italian Code suggests two equivalent static procedures: force-based and displacement-based. For the damage-limitation Limit Stat (DLS) the force-based procedure involves the following checks:

$$a_0^* \geq \max\left\{a_g S; \quad S_e(T_1)\psi\lambda\right\} \qquad 3.4$$

with a_0^* the acceleration capacity of the mechanism at rest, $S_e(T_1)$ the DLS horizontal ground acceleration response spectrum evaluated at the fundamental period T_1, of the building in the considered direction, whose modal participation factor is λ and whose mode ψ is evaluated at the centroid of the mechanism's restraints, and S is the site response coefficient. The second acceleration demand inside the curly brackets needs to be checked if the local mechanism involves a portion of the building at a specific height, where the acceleration is generally amplified with respect to the free field.

The commentary to the Italian Code suggests simplified formulations to estimate the modal building parameters. For the Life-Safety Limit State (LLS), the design ground

motion parameters are divided by a behavior factor q=2.0. In the case of LLS a, displacement-based assessment is also possible. The spectral displacement capacity, d_u*, is the minimum between 40% of the mechanical instability displacement and the displacement which corresponds to a local instability of the structural element. The procedure involves the following checks:

$$d_u^* \geq \max\left\{ S_{De}(T_S); \quad S_{De}(T_1)\psi\lambda \frac{\left(\frac{T_S}{T_1}\right)^2}{\sqrt{\left(1-\frac{T_S}{T_1}\right)^2 + 0.02\frac{T_S}{T_1}}} \right\} \qquad 3.5$$

where $S_{De}(T_S)$ is the elastic displacement response spectrum evaluated at the mechanism secant period T_S, equal to

$$T_S = 2\pi\sqrt{\frac{d_S^*}{a_S^*}} \qquad 3.6$$

with $d_S^* = 0.4\, d_u^*$, and a_S^* is the acceleration of the response curve for $d^* = d_S^*$. The two procedures have been studied in Al Shawa O. et al. (2012) where the displacement-base procedure proved to be less scattered and less conservative.

3.4 Assessment procedures

Different assessment procedures have been proposed in the literature, and implemented in the current national (and international) regulations, based on the results of nonlinear static analysis. All these procedures are based on approximating the real multi-degrees of freedom (MDOF) system by means of an equivalent simple oscillator with a single degree of freedom (SDOF system). However, depending on how this SDOF system is defined, the procedure can be distinguished in: i) capacity spectrum method (CSM), according to which the equivalent SDOF system consists of an elastic oscillator with a secant stiffness and an equivalent viscous damping and ii) N2 method (adopted in NTC18)

which consider elasto-plastic SDOF systems with initial stiffness and evaluate the displacement demand through constant-ductility inelastic spectra. Presently, the N2 method is the most popular method to assess the seismic performance of existing buildings. Nevertheless, it has yet to be fully explored in the case of irregular URM buildings and URM buildings without rigid diaphragms. A brief description of the N2 method, as implemented in the Eurocode and Italian standards, is reported in the following.

The first step of the procedure consists of defining a non-linear SDOF system with effective mass expressed by:

$$m^* = \sum m_i f_i \qquad 3.7$$

whose constitutive curve is obtained by dividing the base shear force (V_b) and the displacement of the control point (d) of the real MDOF system by the modal participation factor defined as follow:

$$\Gamma = m^* / \sum m_i \phi_i^2 \qquad 3.8$$

with m_i the mass at the i-th level and ϕ_i a predefined form of lateral displacements, normalized to 1 at the control point, generally considered coincident to the fundamental mode of vibration in the load direction. After that, an equivalent nonlinear SDOF system with peak strength F_y and ultimate displacement d_u^* is first defined according to the following equations:

$$F_y = \frac{V_{b,\max}}{\Gamma} \qquad 3.9$$

$$d_u^* = \frac{d_m}{\Gamma} \qquad 3.10$$

being $V_{b,max}$ and d_m the peak-strength and the corresponding displacement of the real MDOF system (Figure 24a). The yield displacement (d_y^*) is evaluated by imposing an energetic equivalence between the non-linear and the bi-linear system.

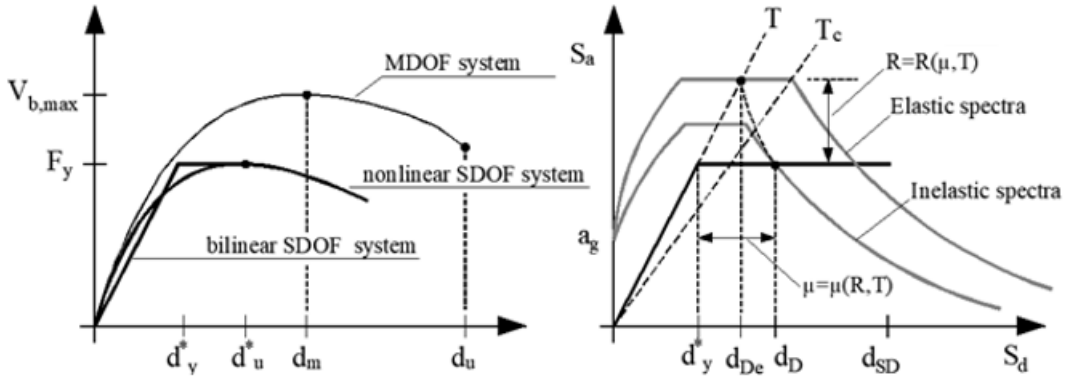

(a) (b)

Figure 24 - Seismic assessment procedure performed through the application of a) N2-method for the evaluation of the SDOF system and b) the capacity spectrum method for the evaluation of the displacement demand

The bi-linear SDOF system is drawn in the spectrum acceleration (S_a) – spectra displacement (S_d) space, together with the elastic spectrum (Figure 24b). In this space, the parameters characterizing the SDOF system are the yield acceleration $S_{ay} = F_y/m^*$ and displacement $S_{dy} = S_{Ay}T^2/(4\pi^2)$. The elastic acceleration (S_{ae}) and displacement (S_{de}) of the equivalent elastic system are determined by the intersection between the line corresponding to the period $T = 2\pi\sqrt{m^* d_y^*/F_y}$ and the elastic spectrum. Consequently, the reduction factor (R), defined as the ratio between the elastic spectrum and the inelastic spectrum, results: $R = S_{ae}/S_{ay}$. Known R, assuming a relation $R = R(\mu, T)$ with μ the ductility demand, the displacement demand of the non-linear system is equal to $S_d = \mu S_{de}$/R.

$$S_d = \mu S_{De} / R \qquad 3.11$$

It is worth mentioning that all seismic assessment procedures, including the N2 method, have been developed for reinforced concrete frame structures, then extended to URM masonry structures through their adoption in the international codes. However, URM structures present very different ranges of periods and dissipation mechanisms if compared to those pertinent to reinforced concrete constructions, strongly depending on the failure mechanism activated [17], [54]. Therefore, a reliable prediction of the inelastic

displacement demand should be based on cyclic pushover analyses rather than monotonic analyses. On the other hand, international regulations do not consider this issue, only explicitly considering the structural period and ductility. This may result in underestimating the displacement demand, mainly for buildings with short periods, more sensitive to the hysteretic dissipation capacity [17]. In order to find a solution to this issue, recently Guerrini et al. [147] analysed a large number of URM prototypes characterized by different hysteretic behaviours proposing, as a result of that study, an improved μ-R-T relationship related to the global hysteresis cycles of the structure evaluated by performing cyclic pushover analyses.

4. DISCRETE MACRO-ELEMENT METHOD (DMEM)

This section presents a novel simplified approach for the seismic assessment of URM structures initially proposed by Caliò et al. [92] and subsequently upgraded in numerous works, as briefly described in the following. Such a modelling strategy has been implemented in the structural software 3DMacro and HiStrA [61].

Starting from the pioneering work in 2004 [148], a research team at the University of Catania proposed a new original Macro-Element Modelling strategy. This approach was based on the subdivision of the structure into several macro-portions, each represented by a shear-deformable quadrilateral, interacting with the adjacent elements through a nonlinear zero-thickness discrete interfaces.

The first implementation of the DMEM approach was based on a 2D element [92], able to simulate the main IP failure mechanism of a masonry panel, not being able to describe the OOP behavior. To overcome this limit, the macro-element was improved to investigate OOP response of URM structure by developing a three-dimensional macro-element, able to simulate the interaction between the in-plane and OOP nonlinear responses of masonry walls or curved elements [149]. The latter elements, used to model arches and vaults, are fundamental in the buildings' local and global static behaviour, especially in the monumental ones [150], [151]. In this 3D formulation, the base element is a shell macro-element characterized by an irregular geometry, variable thickness along the element, and skew perimetral interfaces, allowing the model to discretise single or double-curved geometries. Both experimental and numerical validations showed the capability of the proposed approach to be applied to predict the static nonlinear response of URM structures under different loading conditions [151]. A more recent implementation was conducted to assess the seismic behaviour of URM structures subjected to earthquake excitations by introducing a consistent or lumped mass matrix [152]. As demonstrated [57], the DMEM

strategy showed its capability to simulate dynamic response characterised by combined in-plane/OOP failure mechanisms. The limited number of DOFs associated with each macro-element makes this approach highly efficient compared to the classical finite element formulations [17].

In its last formulation, the DMEM is able to describe the seismic behavior of URM structures characterised by complex and curved geometry, considering both the in-plane and out-of-plane response of masonry panels, under static and dynamic loadings.

In the following subsection, a brief introduction of the different DMEM formulations, already presented in the literature, is discussed. The newly P-Delta formulation, reported in Section 5, is implemented within the DMEM strategy.

4.1 The 2D macro-element

In the initial two-dimensional formulation of the DMEM model [92], each macro-element (panel) can be represented by a simple equivalent mechanical scheme consisting of an articulated quadrilateral with four rigid edges connected by four hinges and two diagonal non-linear links. The kinematics of the element is described by four degrees of freedom, three related to the in-plane rigid body motion: two translations (U, V) (Figure 25a,b), and one rotation (Φ) (Figure 25c), and the remaining DOF associated with the shear deformability of the panel in its plane (γ) (Figure 25d).

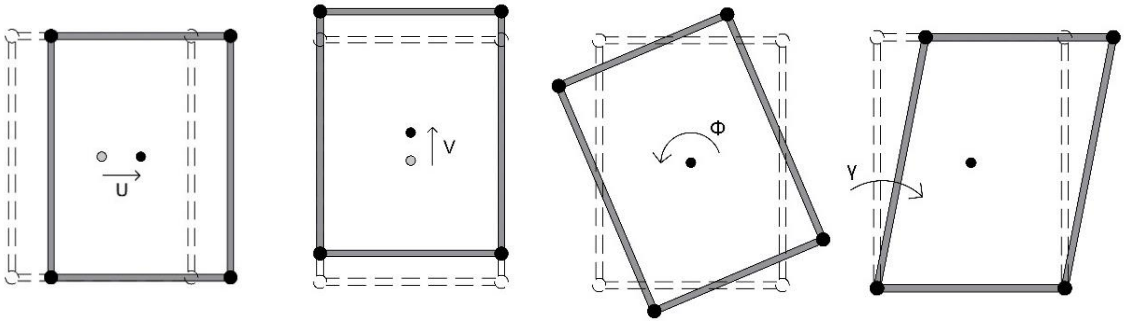

Figure 25 - Degrees of freedom of the basic 2D macro-element

The interaction between adjacent panels is enabled through zero-thickness linear interface elements (Figure 27a). Each interface comprises a discrete distribution of non-linear links: one link placed parallel to the edges of the connected panels, which governs the sliding behavior, and a discrete distribution of non-linear links perpendicular to the edges, responsible for the membrane and flexural behavior. The kinematic of each interface element is described by six local degrees of freedom, two along its length and the reaming four in the perpendicular direction, representing the relative displacement between the connected panels, and directly related to the panels' DOFs, and not requiring additional DOFs (Figure 26).

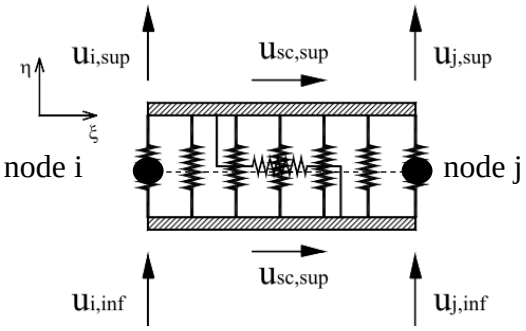

Figure 26 - Local degrees of freedom of the interface

The adopted model has the advantage of allowing the interaction with the adjacent elements along the overall perimeter (Figure 27a), making it possible to use the model with different mesh discretisation, when necessary for a better description of the failure mechanism. It is worth noting that a more detailed response and a better representation of the collapse mechanism are obtained when using a more discretised mesh.

The DMEM describes masonry as a continuum and homogeneous material (Figure 27b). However, its mechanical scheme also allows modelling brick-masonry at the mesoscale level, in which each unit is modelled by a single macro-element, and mortar joints are modelled by the interface (Figure 27c) [58]. Although mesoscale DMEM discretisation requires a significant increment of DOFs, it remains significantly lower than that required by FEM mesoscale strategies presented in the literature [153].

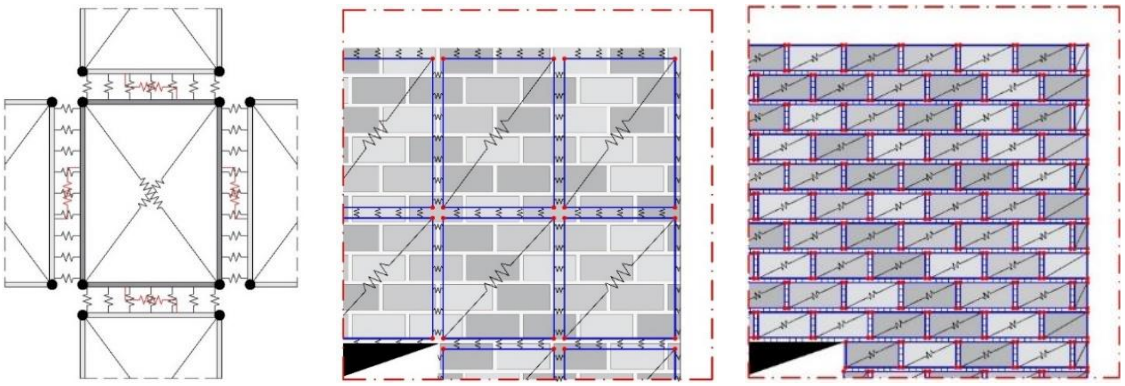

(a) (b) (c)

Figure 27 – DMEM strategy: (a) equivalent mechanical scheme, (b) Macro-scale and (c) mesoscale discretisation of a brick-masonry panel.

The geometric consistency of the DMEM also allows an efficient simulation of infilled frame structures employing a hybrid approach in which the beams are modelled with inelastic frame elements and the infill is modelled through a mesh of plane macro-elements [154].

The 2D macro-element has been conceived for the simulation of the non-linear IP response of masonry walls when subjected to horizontal loading. It is worth noting that each of these IP mechanisms, namely flexural, shear diagonal and shear sliding, are governed by a specific set of non-linear links after properly calibrating them. In particular, the IP flexural mechanism, associated with the rocking of masonry in its plane, is simulated by the discrete distribution of non-linear links orthogonal to the plane, denoted as transversal N-links (Figure 28a-b). The shear-sliding mechanism, related to the slipping of masonry along the interface, is controlled by the single non-linear link placed along the length of the interface elements (Figure 28c-d). Finally, the two diagonal links simulate the shear diagonal mechanism associated with the formation of diagonal cracks (Figure 28d-e) caused by tensile principal stresses in the case of irregular masonries or sliding at the bed joints in regular brick bonds. To enable a reliable simulation of the masonry in-plane response, robust and objective calibration procedures have been developed to evaluate the mechanical properties of each link typology based on the macroscale mechanical parameters of masonry and the geometry of the panel.

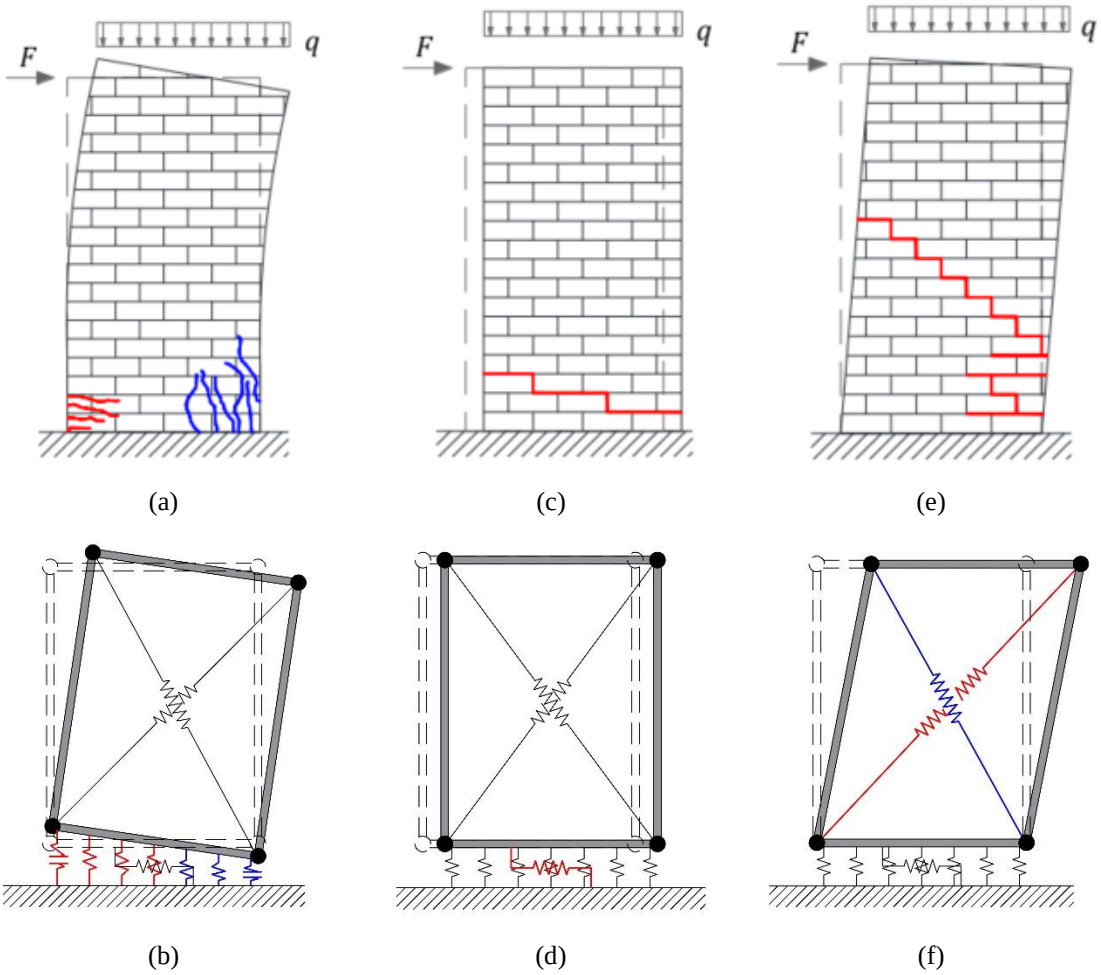

Figure 28 - IP mechanisms of masonry structures and corresponding simulation using DMEM approach: (a, b) flexural, (c, d) shear-diagonal, (e, f) shear-sliding

4.2 The spatial irregular macro-element

The 2D macro-element allows the simulation of a masonry wall's seismic behavior when loaded in its plane but ignores the OOP response. For these reasons, its use is recommended only for structures that show a box-type behavior. To overcome this limit, the macro-element was upgraded by introducing the needed degrees of freedom and additional sets of non-linear links to simulate the OOP collapse mechanism [151].

The mechanical scheme of the 3D macro-element is still represented by an articulated quadrilateral of four rigid plates connected by hinges and a single diagonal non-

linear link. Its kinematics is now governed by seven DOFs that describe the IP and OOP rigid body motion and the IP shear deformability [150].

An additional upgrade was conducted to represent curved masonry structures, such as vaults or domes, using three-dimensional panels with irregular geometry whose average surface belongs, by hypothesis, to a plane. Figure 29 shows the overall evolution of the presented macro-element.

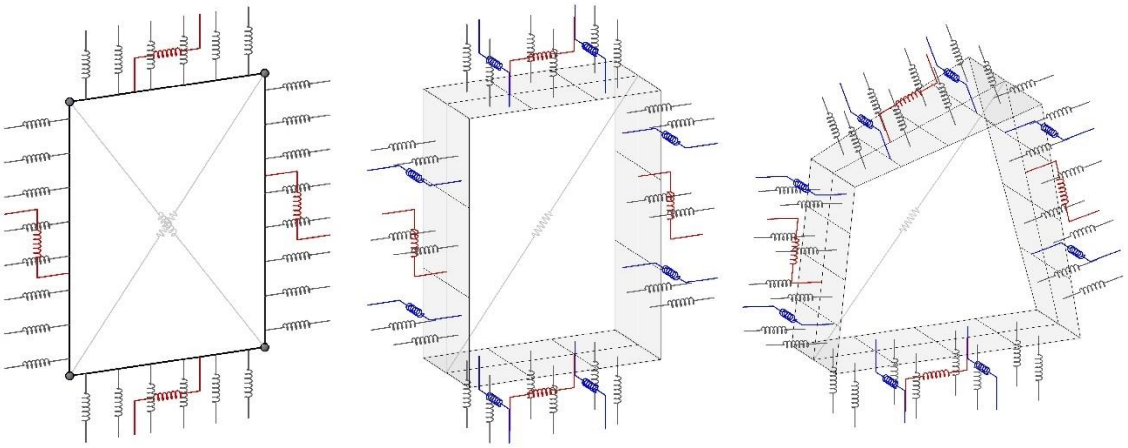

(a) (b) (c)

Figure 29 - DMEM evolution: a) Plane Element, b) Spatial Regular Element, c) Spatial irregular element

The discretization of curved structures is made using two different sets of grids. The first set of grids is composed of curved lines defined by means of horizontal planes (red lines in Figure 30a) distributed along the height of the masonry element. On the other side, the second set of grids is also composed of curved lines which are defined by vertical planes that rotate around a fixed axis in the masonry element (blue lines in Figure 30a). Based on this discretization, a single computational element (Figure 30b) is characterized by four vertex vi (i=1,…4) together with their corresponding thickness t_i and unit vector mi, normal to the element surface. The parameters that define each discretized element are better illustrated in Figure 30c. In this regard, the central plane surface of an irregular macro-element is defined by connecting the four middle vertexes of the discretised element, as shown in Figure 30d. The thickness of the irregular macro-element is obtained by projecting the original configuration of the discretised element into the newly defined

central plane surface. If the orientation of the thickness of each vertex is coplanar to the initial unit vector of the discretised element, the definition of the unit vector n_i corresponding to the irregular macro-element is required (Figure 30e).

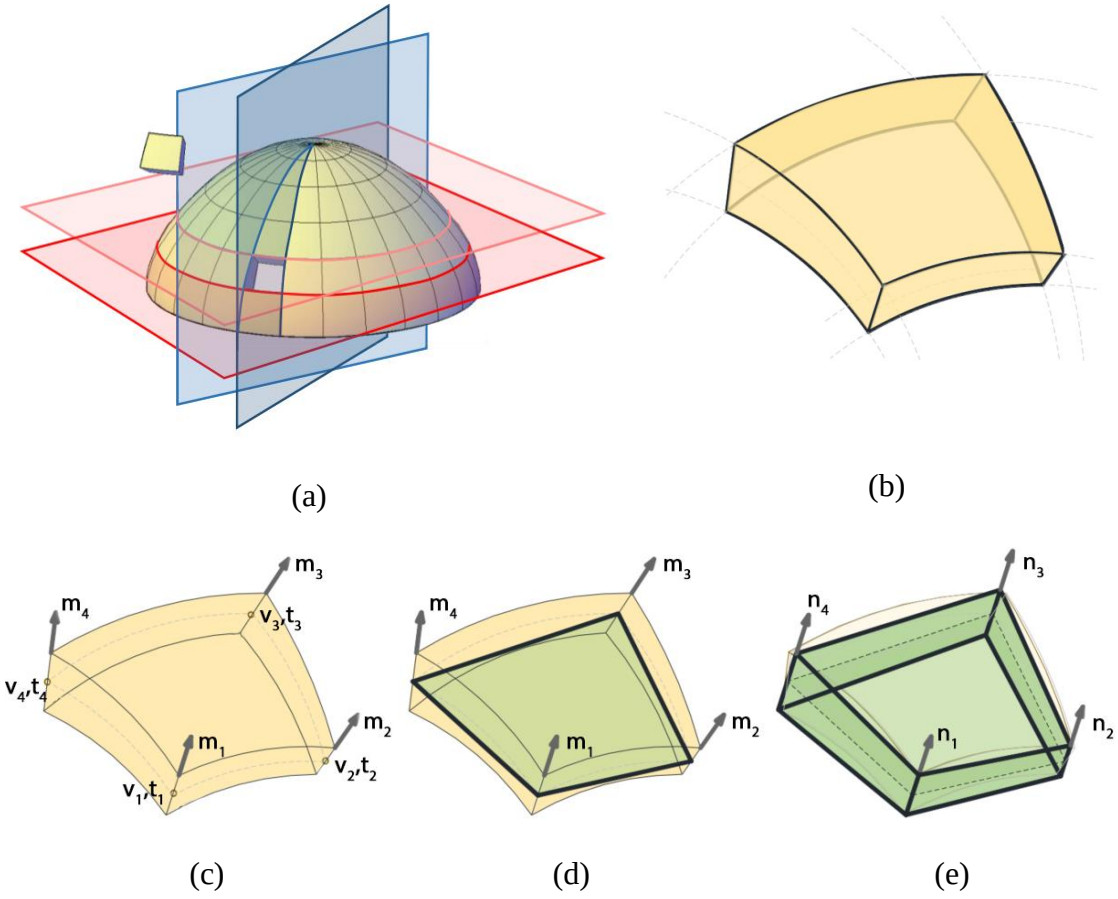

Figure 30 – Modelling of curved structures: a) discretization procedure, b) discretised element, c) middle vertexes, d) central surface, e) unit vectors of irregular macro-element (Figure from [155], [156]*)*

The mechanical scheme of this irregular macro-element presents no major modifications with respect to the regular one. It is still composed of four rigid plates connected by four hinges and one diagonal nonlinear link.

The connection between adjacent elements is still conducted by means of interface elements, which is now discretised into a matrix of $m \times n$ non-linear links. Moreover, the interface elements are endowed with additional OOP shear-sliding nonlinear links required to control the OOP sliding mechanism and the torsional behavior around the axis

perpendicular to the plane of the interface. Consequently, the kinematic of the interface element is now fully described by twelve degrees of freedom (six for each of the two plates). The first six describe the flexural behavior (Figure 31a), while the remaining is the sliding behavior, both in-plane and out-of-plane (Figure 31b). The detailed kinematics description of the irregular element is reported in Section 5. In the following some details on the macro-element constitutive calibration are reported.

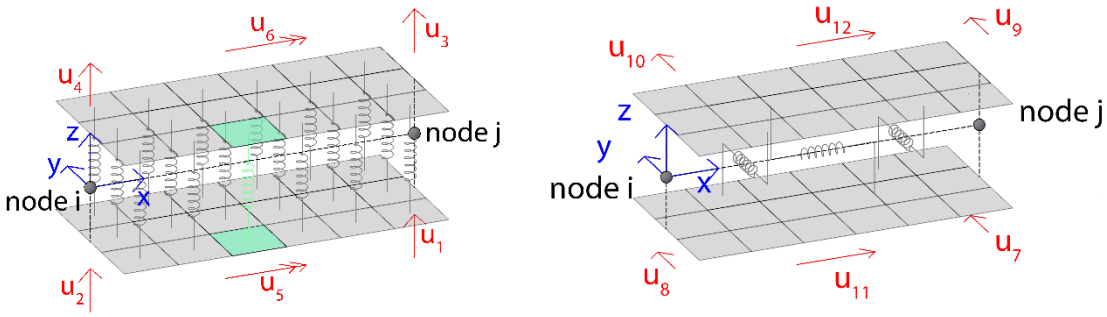

(a) (b)

Figure 31 - a) Flexural and b) sliding Lagrangian parameters of the three-dimensional interface

4.3 Calibration of the non-linear links

This section reports the calibration procedure associated with the nonlinear links concerning the regular two-dimensional or three-dimensional spatial panels. Nevertheless, the calibration of the nonlinear links related to irregular three-dimensional panels presents no theoretical modifications but a more sophisticated procedure due to geometrical complications, which is beyond the scope of this thesis. A detailed description of the calibration procedure for irregular macro-elements can be found in [155].

According to the latter reference, macro-element nonlinear links are divided into:

- Transversal (or orthogonal) nonlinear links (Figure 32a): they simulate the axial and bi-dimensional flexural responses of masonry structures;
- Diagonal nonlinear links (Figure 32b): it rules the in-plane shear diagonal behavior;

- In-plane sliding links (Figure 32c): they describe the sliding in-plane behavior due to the slipping of mortar joints;
- Out-of-plane sliding links (Figure 32d): they describe the out-of-plane sliding behavior due to the slipping of mortar joints out-of-plane and also the torsional behavior.

The number of the transversal nonlinear links, adopted in the interface elements, is selected according to the desired level of accuracy of the non-linear response.

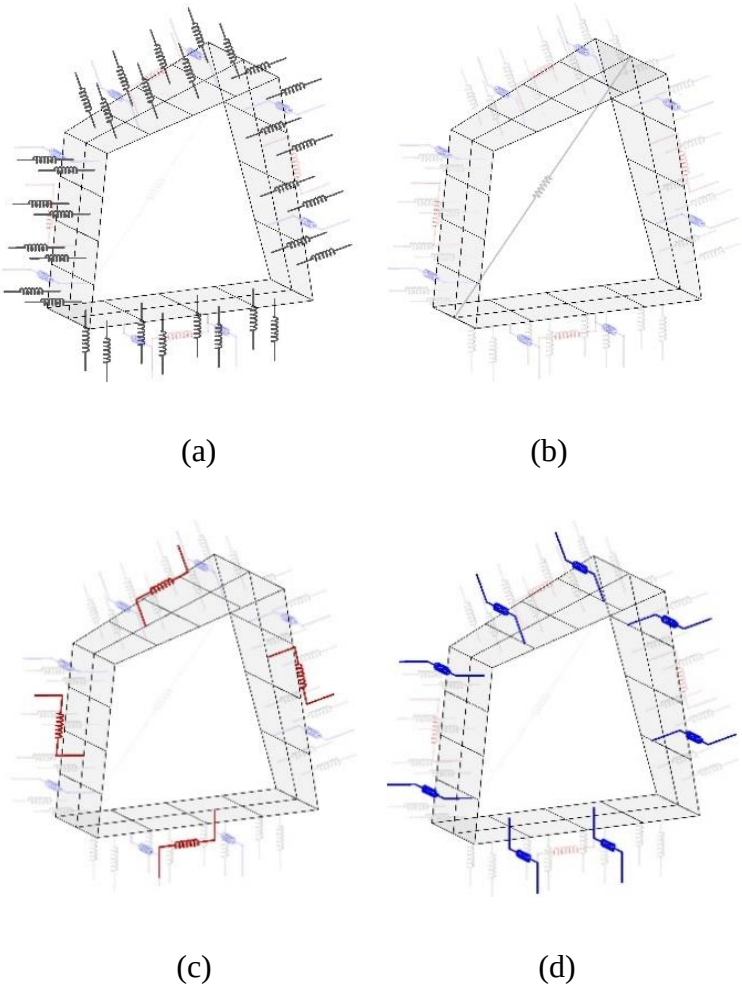

Figure 32 - Nonlinear links; a) Transversal nonlinear links, b) Diagonal nonlinear link, c) In-plane sliding links, d) Out-of-plane sliding links

4.3.1 Transversal nonlinear links

The definition of the elastic and nonlinear mechanical properties of this set of links is based on a fibre calibration procedure in which a single equivalent link represents a masonry strip corresponding to two adjacent panels, as illustrated in Figure 33a.

The calibration procedure comprises two steps. First, each masonry strip representing the two adjacent macro-elements (e.g., panels l and k) in a given material direction is replaced by two nonlinear links in series. Then, each couple of transversal nonlinear links in series is replaced by a single equivalent nonlinear link, as depicted in Figure 33b, following the simple rules described in [92]. It is worth noting that the behaviour of masonry as an orthotropic material is conducted by a separate calibration of horizontal and vertical interface elements using the corresponding mechanical properties in the given direction.

Following the fibre-discretisation strategy, the initial stiffness of each link in series is related to the axial rigidity of the masonry strip to which it corresponds, which is characterised by the masonry Young's modulus E_n (in the considered direction), the influence area A_{sn} corresponding to the panel cross-section discretisation, and L_n the half-length of the panel in the direction parallel to the link (with $n=l, k$). Equations 4.1 and 4.2 provide the initial stiffness K_{in} of each of the links in series and the initial stiffness K_i of the equivalent link, respectively.

The yielding forces in tension F_{ytn} and compression F_{ycn} of each transversal link in series (Eq. 4.3 and Eq. 4.4) are related to their influence area and the tensile and compressive strengths of the corresponding panel, respectively. If two adjacent panels present different tensile or compressive strengths or different geometry, the yielding forces in tension F_{yt} and compression F_{yc} of the equivalent link are defined as the minimum and maximum values between the two corresponding forces of the links in series as expressed in Eq. 4.5 and 4.6.

The yielding force in compression of the link equivalent to the two links in-serie corresponds to the minimum, in terms of absolute value, between their two compression strengths.

$$K_{in} = 2\frac{E_n \cdot A_{S_n}}{L_n} \quad 4.1$$

$$K_i = \frac{K_{i_k} \cdot K_{i_l}}{K_{i_k} + K_{i_l}} \quad 4.2$$

$$F_{yt_n} = A_{S_n} \cdot f_{t_n} \quad 4.3$$

$$F_{yc_n} = A_{S_n} \cdot f_{c_n} \quad 4.4$$

$$F_{yt} = \min(F_{yt_k}, F_{yt_l}) \quad 4.5$$

$$F_{yc} = \max(F_{yc_k}, F_{yc_l}) \quad 4.6$$

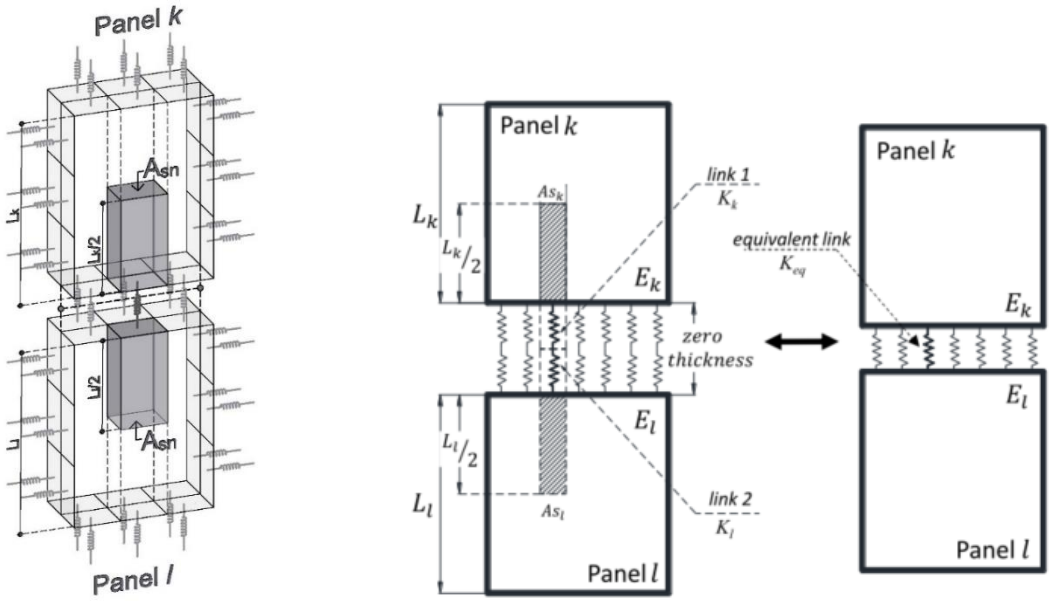

(a) (b)

Figure 33 - Transversal nonlinear links: a) definition of masonry strip; b) fibre calibration procedure

The nonlinear behavior of the transversal links can be characterised according to any uniaxial constitutive law. In HiStrA software [61], three different constitutive laws for tensile and compressive responses have been adopted (Figure 34). The first one is related

to an elastoplastic behaviour in which the post-yielding stiffness is defined by means of a ratio α_t or α_c, as illustrated in Figure 34a. Two other constitutive laws are defined in which the tensile response is simulated by means of linear (Figure 34b) and exponential (Figure 34c) softening curves in which the ultimate displacement for tension u_{ut} and compression u_{uc} are identified by defining the corresponding values of the yielding force (F_{yt}, F_{yc}) and fracture energy (G_t , G_c). At the same time, the response in compression can be simulated by two curves, linear (Figure 34b) and parabolic (Figure 34c). The cyclic behaviour associated with the transversal nonlinear links was adapted from the hysteretic model introduced by Takeda [157] and implemented in OpenSees [158]. The hysteretic model is characterised by a coefficient that modifies the stiffness governing the unloading cycles. This unloading coefficient, denoted as β, can present a value ranging between 0 and 1. Figure 35 illustrates the cyclic behaviour of a transversal nonlinear link in which the tensile and compressive responses are ruled by exponential and parabolic curves, respectively. Three different unloading behaviours can be observed in this figure. The first one corresponds to an unloading cycle with an initial stiffness, and it is characterised by a β coefficient equal to 0. This behaviour is described throughout segments BC and EF for tension and compression, respectively. The second one corresponds to an unloading cycle with an intermediate stiffness, in which the β coefficient presents a value different to 0 or 1. In Figure 35, this unloading cycle in tension is depicted by segment GH, whereas in compression segment IJ applies. The last unloading cycle is governed by a stiffness oriented to the origin (secant stiffness), and the β coefficient presents a value equal to 1 as depicted by segments KO and LO. It is worth noting that tensile and compressive behaviours may present different unloading cycles; and therefore, their corresponding unloading coefficient β_t and β_c are defined independently. Once a nonlinear link reaches a zero force, the unloading cycle finishes, and the loading in the opposite direction begins. As illustrated in Figure 3.14, this reloading is oriented to the maximum displacement reached in the previous cycle. Segments CD, HE, and OI correspond to the compressive reloading due to unloading cycles in tension based on initial, intermediate, and secant stiffness, respective. On the other hand, segments FB and JG are the corresponding tensile reloading cycles associated with compressive unloading.

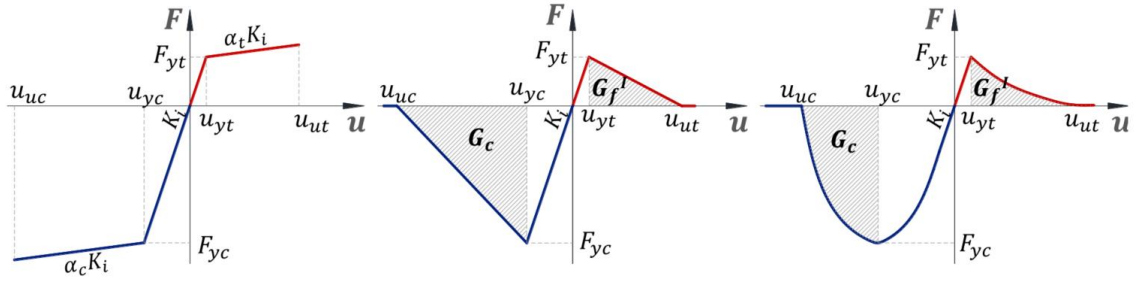

(a) (b) (c)

Figure 34 - Constitutive laws for transversal links: a) elastoplastic, b) linear-softening, c) exponential and parabolic softening [156]

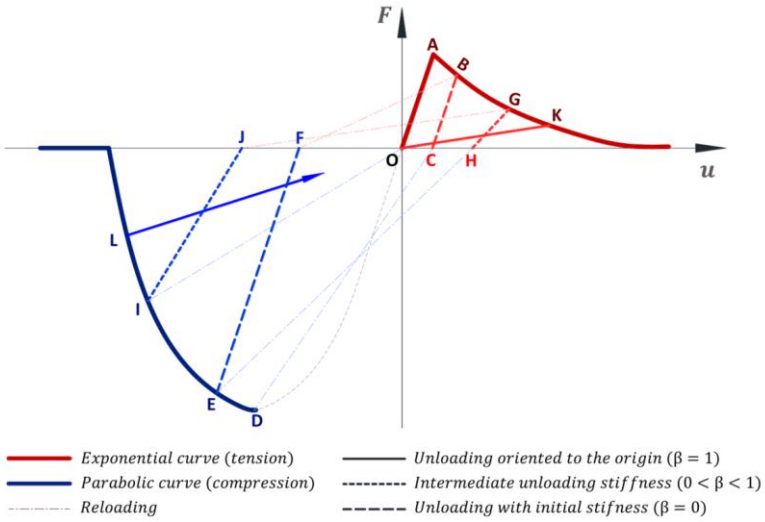

Figure 35 - Cyclic constitutive model of the transversal nonlinear links

4.3.2 Diagonal Shear nonlinear link

The diagonal shear nonlinear link describes the in-plane shear failure mechanism, which can be associated with tensile cracking along with the principal directions of the material (diagonal shear failure) or sliding along with bed mortar joints. The diagonal shear nonlinear link has the fundamental role to preside over the diagonal shear failure collapse. The elastic properties of this link are calibrated by enforcing an equivalence between a

finite portion of masonry with pure shear deformability and a single macro-element.

The masonry is characterised by the shear modulus *G*, the transversal area A_t, the panel height h, and base b. Applying a shear force V on a masonry panel discretised by a single macro-element (Figure 36b), the deformation δ is given by Eq. 4.7 for the homogeneous media (δ_{hom}) and the corresponding relationship in the macro-element is reported in Eq. 4.8 (δ_{dis}). The initial elastic stiffness k_D of the diagonal link is obtained by equating Eq. 4.7 and Eq. 4.8 and it is expressed in Eq. 4.9 in which θ is defined as $\arctan(b/h)$. It is worth noting that as the global in-plane shear response of an URM wall is simulated by two different set of nonlinear links, the value k_D depends on a shear factor denoted as α_s, which ranges between 0 and 1. A value of α_s equal to 1 means that the global initial stiffness is entirely associated with the diagonal link, and the in-plane sliding links are assumed to be rigid. On the other hand, if α_s presents a value lower than 1, the global in-plane shear response is given by the contribution of diagonal and sliding in-plane nonlinear links. For $\alpha_s = 0$ the blocks behave rigidly. Thus, there is no diagonal shear deformation.

$$\delta_{hom} = \frac{V \cdot h}{G \cdot A_t} \qquad 4.7$$

$$\delta_{dis} = \frac{V}{\cos^2\theta \cdot k_D}\alpha_s \qquad 4.8$$

$$k_D = \frac{G \cdot A_t}{h \cdot \cos^2\theta \cdot \alpha_s} \qquad 4.9$$

For the shear failure of URM piers associated with diagonal cracking many different yielding criteria can be adopted [159], [160] all accounting for a shear resistance strongly dependent on vertical compression stresses in the wall, σ_0.

In the macro-element strategy Mohr-Coulomb and Turnsek-Cacovic criteria [159] are considered. These criteria consider the confinement condition due to normal stress to estimate the overall shear-diagonal capacity of URM structures. In the case of Mohr-

Coulomb criterion, which has been accepted by Eurocode 6 (Design of masonry structures) [141] the shear strength is defined according to Eq. 4.10

$$f_v(\sigma_0) = f_{y0} + \mu_d \cdot \sigma_n \qquad 4.10$$

Where f_{y0} is the shear strength under zero compression stress, μ_d is a friction coefficient defining the contribution of compressive stresses σ_n. The value of f_{y0} and μ_d should be determined by experimental tests. This criterion is the same suggested for the description of the sliding-shear failure, although characterised by appropriate values of f_{y0} and μ_d that in general do not coincide with the corresponding values that govern the sliding-shear failure (see Section 4.3.3).

In the proposed macro-modelling approach, the two mechanisms are controlled separately.

Instead, in the case of Turnsek-Cacovic criterion, the shear strength of the masonry piers, is defined according to Eq. 4.11

$$f_v(\sigma_0) = f_t \sqrt{1 + \frac{\sigma_0}{1.5 \cdot f_t}} \qquad 4.11$$

Where f_t is the tensile strength of masonry, σ_0 is the average compression stress due to vertical load N.

The yielding force of the diagonal shear link in the discrete macro-element strategy it is therefore equal to

$$F_D = \frac{f_v(\sigma_0) \cdot A_t}{\cos\theta} \qquad 4.12$$

Aiming at introducing a degrading behavior, the cyclic response of the diagonal nonlinear links is also governed by the hysteretic model introduced by Takeda [157].

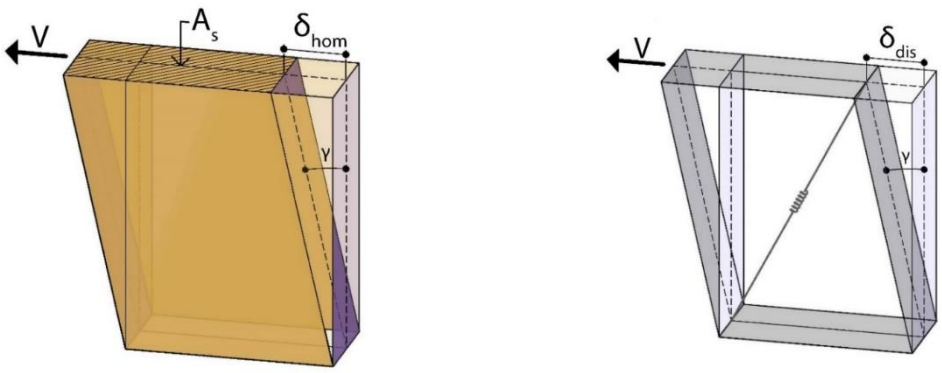

(a) (b)

Figure 36 - Equivalence for the calibration of the diagonal nonlinear links: (a) finite portion of masonry with pure shear deformability, and (b) single macro-element

4.3.3 Sliding nonlinear links

Alongside the diagonal shear behavior, the overall in-plane shear mechanism of URM structures is also associated with the slipping of mortar joints. This kind of shear mechanism is described as the relative motion between two adjacent elements and is governed by a set of three nonlinear links. One, denoted as in-plane sliding nonlinear link, is situated along the edges of the connecting interface elements and a couple of nonlinear links, known as out-of-plane nonlinear links responsible for the out-of-plane slipping of the mortar joints. It is worth noting that this couple of links simulate the nonlinear torsion response of URM structure. The initial stiffness K_s related to the sliding mechanism is associated with the panels' shear modulus G, the effective length defined as the summation of the half-length of adjacent panels ($L_k/2 + L_l/2$), and the influence area A_s of the corresponding nonlinear link. The expression which provides the initial stiffness K_s for in-plane and out-of-plane nonlinear links is given by Eq. 4.13. It is worth pointing out that A_s represents the tributary area of the links, which is different for the in-plane and OOP links, coinciding with the entire contact area and the contact area of the half interface for the in-plane and OOP links, respectively (Figure 37).

Conversely, the out-of-plane shear mechanism is solely associated with the nonlinear links along the thickness of the interface element, and there is no need to introduce a shear factor in the out-of-plane direction. On the other hand, aiming at maintaining a suitable torsional elastic calibration, although maintaining a simplified calibration strategy, the torsional stiffness K_Φ which governs the torsional response, is evaluated by enforcing an equivalence between a beam model and the corresponding macro-element model. Based on this equivalence, and once the elastic shear stiffness has been assigned, it is possible to determine the distance d between the out-of-plane nonlinear links, whose expression is given by Eq. 4.16, to simulate the torsion response. The elastic torsional stiffness (Eq. 4.14) is associated with a torsional rigidity factor J_ϕ given by Eq.4.15, in which s corresponds to the thickness of the panel, evaluated considering a rectangular elastic element of thickness s and width B. More detailed on the calibration of the out-of-plane sliding and torsional links can be found in [151].

$$K_s = \frac{G \cdot A_s}{\left(\frac{L_k}{2} + \frac{L_l}{2}\right) \cdot (1 - \alpha_s)} \qquad 4.13$$

$$K_\Phi = \frac{G \cdot J_\Phi}{\left(\frac{L_k}{2} + \frac{L_l}{2}\right)} \qquad 4.14$$

$$J_\Phi = B \cdot s^3 \left[\frac{1}{3} - 0.21\frac{s}{B}\left(1 - \frac{s^4}{12 \cdot B^4}\right)\right] \qquad 4.15$$

$$d = 2s\sqrt{\frac{1}{3} - 0.21\frac{s}{B}\left(1 - \frac{s^4}{12 \cdot B^4}\right)} \qquad 4.16$$

The shear sliding response of URM structures is associated with a frictional phenomenon along the mortar joints. Such a mechanism can be adequately described by means of a Mohr-Coulomb yielding criterion. Based on this approach, the current yielding force F_y of the in-plane and out-of-plane links is defined by defining the cohesion c and

friction coefficient μ_s of the masonry material, the current contact area A, and the normal force N applied to the interface element as expressed in Eq. 4.17. It is worth noting that the definition of the current contact area A of the sliding links is influenced by the behaviour of the discretised matrix of transversal links.

$$F_y = c \cdot A + \mu_s \cdot N \qquad 4.17$$

The cyclic nonlinear behavior is characterised by an elastic perfectly-plastic constitutive model in which the unloading and reloading stiffness are equal to the initial one.

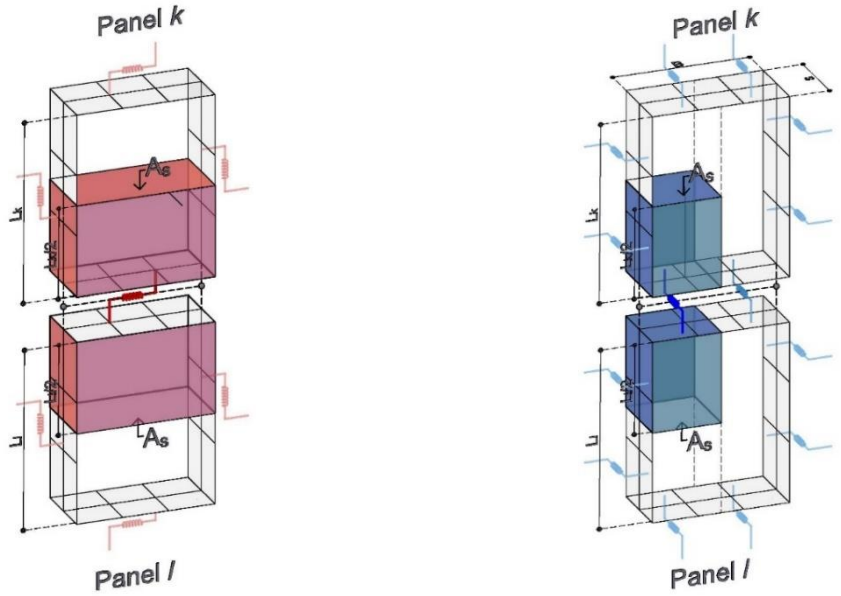

(a) (b)

Figure 37 - Shear-sliding mechanism: (a) in-plane, and (b) out-of-plane nonlinear links and their corresponding tributary area

5. P-DELTA FORMULATION WITHIN DISCRETE MACRO-ELEMENT METHOD

The main concern in OOP seismic behavior of masonry walls is the existence of large displacements (or equivalently rotations) during rocking motion, which might cause instability and eventually overturning of the structure. Therefore, the associated challenges behind this peculiar seismic behavior should be properly addressed with advanced analytical and numerical simulations that can capture, with the needed accuracy, the transient nonlinear dynamic behavior of rocking structures. After the activation of the rocking mechanism, the system response can evolve towards large displacements in this latter case, due to the typical slender geometry of masonry walls, the stabilising effects of vertical loads could progressively reduce until the achievement of the critical condition in which vertical loads will no longer play stabilizing moments. A rigorous description of geometrical nonlinearities, within the context of DMEM, would require the adoption of large displacement kinematics with the definition of the geometrical stiffness matrix and its step by step updating. Furthermore, a more complex theoretical formulation and, above all, a significant increase of the associated computational cost would also be required. Aiming at maintaining the benefits of the DMEM a simplified but robust and efficient P-Delta approach is proposed, leading to a reasonable accuracy for engineering applications while maintaining a simple theoretical formulation and, above all, a low computational effort. More specifically, the P-Delta effects are described by updating the element force vector applied to each macro-element, accounting for the additional moments produced by the membrane action directly applied to the element in its current configuration. Since the momentum equilibrium is performed for each macro-element, both the external forces and

the internal ones transferred by the interfaces must be considered.

The theoretical description reported in the following first provides a detailed description of the kinematics of the irregular macro-element, then provides the calculation of the additional loading contribution due to the P-Delta effects and the evaluation of the equilibrium conditions for each macro-element, including the P-Delta effects.

Finally, the new DMEM model, including P-Delta effects, is validated in the static field by comparing the results obtained using DMEM with those obtained by the analytical solution and some experimental tests presented in the literature.

5.1 Element's kinematic

In this section the kinematic of the irregular spatial macro-element is presented. As discussed in the previous chapter, each irregular macro-element is identified by four vertexes ($v_1,\ldots,v_4$) which identify the plane of the element (π). A single macro-element is geometrically characterized by the length of each side ($l_1,\ldots,l_4$) and internal angles ($\alpha_1,\ldots,\alpha_4$), which characterise the element irregularity.

A local fixed reference system, referred to the global cartesian coordinates, is associated within each macro-element, with origin O and axis x,y and z, whose versors are indicated with **i**, **j** and **k** (Figure 38a) and such that:

- The origin O coincides with the barycentre of the generic element (assumed coincident with the centre of mass);
- **i** is directed like the side 1-2 of the quadrilateral and oriented in the direction that goes from vertex 1 to vertex 2;
- **j** lies on the middle plane of the element, perpendicular to **i** and is oriented upwards;
- **k** is perpendicular to the plane of the element and such as to form a right-handed triad with the other two;

The element kinematic is completely described by seven Lagrangian parameters only collected in the vector **d (**Eq. 5.1). The first six parameters ($U, V, W, \Phi, \Theta, \Psi$), are related to the spatial rigid motion, three translations and three rotations associated to global

displacements of the origin of the local reference system. A further internal Lagrangian parameter γ, is related to the generalized macro-element shear deformation and has been associated with the angle variation between the panel edges connecting the vertex v_1 to vertex v_2 and the vertex v_1 to vertex v_4, respectively (Figure 38b). The zero-thickness plane interfaces π_i (i=1,..4), (Figure 38a), whose orientation is associated with unit vectors $\mathbf{n}_i$ (i=1,..4), cut and identify the element along its perimeter and rule the connections with the adjacent elements. Different thicknesses can be considered at each of the panel's corners (t_1,..,t_4) leading to direct and easy modelling of linear variable cross-thickness elements. Local reference systems $\mathbf{e}_{n1}$, $\mathbf{e}_{n2}$, $\mathbf{e}_{n3}$ (n=1,..4) are also associated with each interface, as shown in Figure 38c, for the description of the interfaces' kinematics. More details on the DMEM kinematics can be found in [150] [161]. It is worth noticing that no additional Lagrangian parameters are needed to describe the kinematics of interfaces. Therefore, the total degrees of freedom of the model are directly given by 7xN being N, the number of elements. This aspect strongly contributes to containing the model's computational burden.

$$\mathbf{d}^{\mathrm{T}} = \begin{bmatrix} U & V & W & \Phi & \Theta & \Psi & \gamma \end{bmatrix} \qquad 5.1$$

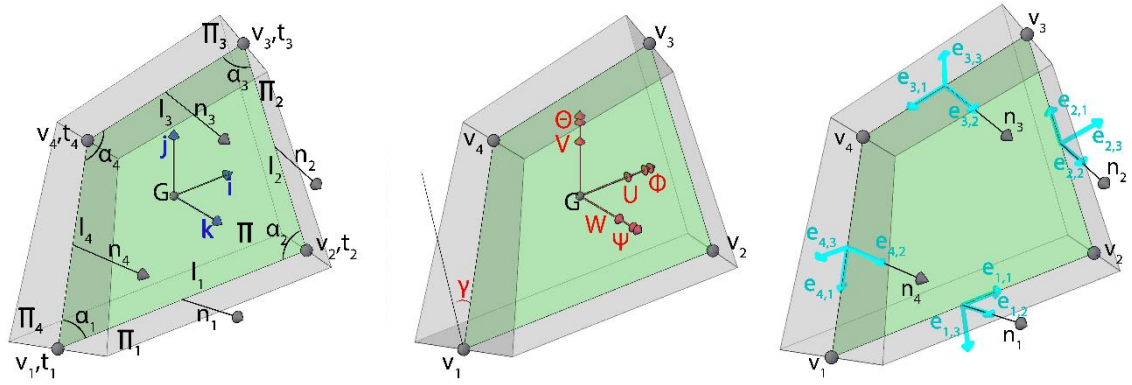

Figure 38 - 3D Discrete Macro-Model: (a) panels definition and local reference system ; (b) Lagrangian parameters of the panel; (c) Local reference system of the perimeter interfaces.[161]

Considering second-order linearised kinematics for the adopted macro-element, a direct expression between the displacements of the n-th vertex (n = 1,…,4) of the irregular

quadrilateral ($\mathbf{u}_{vn}$), in the local reference system, and the seven Lagrangian parameters (Eq. 5.1), can be established as reported in Eq. 5.2. This relation is partially related to the rigid body motion DOFs and in part to the additional internal DOF associated with the generalised shear deformability.

$$\mathbf{u}_{vn} = \begin{bmatrix} \mathbf{I}_{3x3} & \boldsymbol{\Omega}_{vn} & \boldsymbol{\Gamma}_{vn} \end{bmatrix} \mathbf{d}; \quad \text{with } (n = 1,\ldots,4) \tag{5.2}$$

being $\mathbf{I}_{3x3}$ a 3x3 identity matrix and $\boldsymbol{\Omega}_{vn}$ a matrix related to the rigid rotation of the element, defined as follows:

$$\boldsymbol{\Omega}_{vn} = \begin{bmatrix} 0 & 0 & -y_{vn} \\ 0 & 0 & x_{vn} \\ y_{vn} & -x_{vn} & 0 \end{bmatrix} \tag{5.3}$$

with: x_{vn}, y_{vn}, the coordinated of the vertex v_n in the local reference system; $\boldsymbol{\Gamma}_{vn}$ (n=1,..4) a vector accounting for the contribution of the generalized shear deformation that, for each vertex, can be written as:

$$\boldsymbol{\Gamma}_{v1} = \begin{bmatrix} 0 \\ 0 \\ 0 \end{bmatrix}; \boldsymbol{\Gamma}_{v2} = \begin{bmatrix} 0 \\ 0 \\ 0 \end{bmatrix}; \boldsymbol{\Gamma}_{v3} = \begin{bmatrix} -l_4 \sin\alpha_2 \sin\alpha_1 / \sin\alpha_3 \\ -l_4 \cos\alpha_2 \sin\alpha_4 / \sin\alpha_3 \\ 0 \end{bmatrix}; \boldsymbol{\Gamma}_{v4} = \begin{bmatrix} -l_4 \sin\alpha_1 \\ -l_4 \cos\alpha_1 \\ 0 \end{bmatrix} \tag{5.4}$$

Being α_n (n=1,..4) the corner angles, which are measured at the middle plane of the element (Figure 38a). It is worth noticing that the generalized shear deformation is defined in the middle plane of the macro-element and is assumed independent of the z coordinate.

An intrinsic reference system (ξ, η) is introduced (Figure 39c) aiming at evaluating the displacement of any point P(x,y,z) belonging to the volume of the element (Figure 39a). The point P is projected on the plan of the element (π), identifying the point $P_\pi(x,y)$ in Figure 39b, which corresponds to $P_\pi(\xi,\eta)$ in the intrinsic space (Figure 39c) through the bi-linear polynomial transformations (Eq. 5.6). According to the iso-parametric formulation, the displacement of the point $P_\pi(\xi,\eta)$ in the local reference system can therefore be obtained

by interpolating the displacements of the vertexes using the interpolating function in Eq. 5.6, and the results are reported in Eq. 5.5.

$$\mathbf{u}(\xi,\eta)=\begin{bmatrix} N_{v1}(\xi,\eta) & 0 & 0 & \dots & N_{v4}(\xi,\eta) & 0 & 0 \\ 0 & N_{v1}(\xi,\eta) & 0 & \dots & 0 & N_{v4}(\xi,\eta) & 0 \\ 0 & 0 & N_{v1}(\xi,\eta) & \dots & 0 & 0 & N_{v4}(\xi,\eta) \end{bmatrix} \cdot \begin{bmatrix} \mathbf{I_{3x3}} & \mathbf{\Omega_{v1}} & \mathbf{\Gamma_{v1}} \\ \mathbf{I_{3x3}} & \mathbf{\Omega_{v2}} & \mathbf{\Gamma_{v2}} \\ \mathbf{I_{3x3}} & \mathbf{\Omega_{v3}} & \mathbf{\Gamma_{v3}} \\ \mathbf{I_{3x3}} & \mathbf{\Omega_{v4}} & \mathbf{\Gamma_{v4}} \end{bmatrix} \cdot \mathbf{d} \qquad 5.5$$

Where:

$$\begin{aligned} N_{v1}(\xi,\eta) &= \frac{(1-\xi)(1-\eta)}{4}; \\ N_{v2}(\xi,\eta) &= \frac{(1+\xi)(1-\eta)}{4}; \\ N_{v3}(\xi,\eta) &= \frac{(1+\xi)(1+\eta)}{4}; \\ N_{v4}(\xi,\eta) &= \frac{(1-\xi)(1+\eta)}{4} \end{aligned} \qquad 5.6$$

Eq. 5.5 in compact form can be written as follows

$$\mathbf{u}(\xi,\eta)=\mathbf{N}(\xi,\eta)\begin{bmatrix} \mathbf{I_{3x3}} & \mathbf{\Omega_{v1}} & \mathbf{\Gamma_{v1}} \\ \mathbf{I_{3x3}} & \mathbf{\Omega_{v2}} & \mathbf{\Gamma_{v2}} \\ \mathbf{I_{3x3}} & \mathbf{\Omega_{v3}} & \mathbf{\Gamma_{v3}} \\ \mathbf{I_{3x3}} & \mathbf{\Omega_{v4}} & \mathbf{\Gamma_{v4}} \end{bmatrix} \cdot \mathbf{d} = \mathbf{\Psi}(\xi,\eta,\gamma) \cdot \mathbf{d} \qquad 5.7$$

being $\mathbf{\Psi}(\xi,\eta,\gamma)$ a 3x7 matrix (Eq. 5.8) collecting seven shape functions governing the element kinematics.

$$\mathbf{\Psi}(\xi,\eta,\gamma)=\begin{bmatrix} \mathbf{\Psi}_1(\xi,\eta,\gamma) & \mathbf{\Psi}_2(\xi,\eta,\gamma) & \dots & \mathbf{\Psi}_7(\xi,\eta,\gamma) \end{bmatrix} \qquad 5.8$$

Each shape function is a vector with three components that can be easily derived using Eq. 5.5. It is worth noticing that the shape functions depend on the shear deformation parameter and are unaffected by the local coordinate *z*. The independence on the *z* coordinate of the local reference system comes from the adopted shear kinematics, since

each plan parallel to middle plane π is characterized by the same shear deformation. It is worth noting that Eq. 5.7 is referred to local reference system in terms of the intrinsic coordinates but provides the displacement of any point of the macro-element in the global reference system.

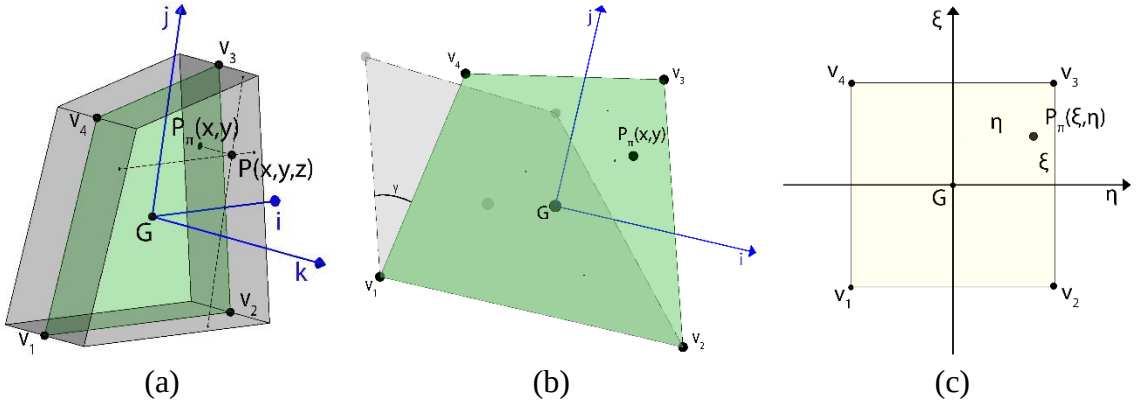

Figure 39 – a) Spatial macro-element in cartesian coordinates, b) Macro-element's middle plane, c) intrinsic iso-parametric reference system [161]

5.2 Calculation of the equivalent external force vector

The vector u(ξ,η) expressed in Eq. 5.7, provides the displacement components in the local reference system for each point of the macro-element, given the generalized shear deformation independent of the local coordinate *z*. Considering a force distribution **f**(x,y), belonging to the middle plane of macro-element (π), the corresponding vector of equivalent forces $\mathbf{F_0}$, associated with macro-element degrees of freedom, can be evaluated through the external virtual work [162]:

$$L_{ve} = \iint_A \mathbf{f}^T(x,y)\tilde{\mathbf{u}}(x,y)dA \qquad 5.9$$

Being A the load application area and $\tilde{\mathbf{u}}(x,y)$ is a virtual displacements field that in view of Eq. 5.7 can be written in terms of intrinsic coordinates and the virtual displacements ($\tilde{\mathbf{d}}$) corresponding to the adopted degrees of freedom, expressed in Eq. 5.1, as follow:

$$\tilde{\mathbf{u}}(\xi,\eta) = \boldsymbol{\Psi}(\xi,\eta,\gamma)\tilde{\mathbf{d}} \qquad 5.10$$

In view of Eq. 5.9 and Eq. 5.10, the external virtual work can therefore be written as

$$L_{ve} = \int_{-1}^{1}\int_{-1}^{1} \mathbf{f}^{\mathbf{T}}(\xi,\eta)\tilde{\mathbf{u}}(\xi,\eta)J(\xi,\eta)d\xi d\eta = \int_{-1}^{1}\int_{-1}^{1} \mathbf{f}^{\mathbf{T}}(\xi,\eta)\boldsymbol{\Psi}(\xi,\eta,\gamma)J(\xi,\eta)d\xi d\eta\ \tilde{\mathbf{d}} \quad \forall\tilde{\mathbf{d}} \qquad 5.11$$

Being J(ξ,η) the Jacobian of the transformation. Eq. 5.11 provides the vector of equivalent forces $\mathbf{F_0}$ for each macro-element for any load distribution applied the middle plane of the macro-element:

$$\mathbf{F_0} = \int_{-1}^{1}\int_{-1}^{1} \mathbf{f}^{\mathbf{T}}(\xi,\eta)\boldsymbol{\Psi}(\xi,\eta,\gamma)J(\xi,\eta)d\xi d\eta \qquad 5.12$$

If the force distribution is applied with a *z* eccentricity, with respect to the middle plane, the corresponding moment must be added to the vector $\mathbf{F_0}$, which accounts only for the loading distribution applied in the middle plane of the element.

The general expression reported in Eq. 5.12 can be evaluated according to the type of load distribution. In particular, we can distinguish between point, line, and area loads.

5.2.1 Point loads

Considering a finite number *n* of external force $\mathbf{F_j}$ (j = 1, 2, 3, …, n) acting in as many points of the considered macro-element.

$$\mathbf{F_j} = \begin{bmatrix} F_{j,x} \\ F_{j,y} \\ F_{j,z} \end{bmatrix} \quad \text{with } (j = 1, 2, 3, \ldots, n) \qquad 5.13$$

The external virtual work (Eq. 5.11) can be written for the point loads as reported below

$$L_{ve} = \sum_{j=1}^{n} \mathbf{F_j^T} \cdot \tilde{\mathbf{u}}(x, y) = \left[\sum_{j=1}^{n} \mathbf{F_j^T} \cdot \boldsymbol{\Psi}(\xi, \eta, \gamma) \right] \cdot \tilde{\mathbf{d}} \qquad \forall \tilde{\mathbf{d}} \tag{5.14}$$

Therefore, the vector of equivalent forces $\mathbf{F_{0,(7x1)}}$ in case of concentrated loads is expressed as follow:

$$\mathbf{F_{0,(7x1),point}} = \sum_{j=1}^{n} \mathbf{F_j^T} \cdot \boldsymbol{\Psi}(\xi, \eta, \gamma) \tag{5.15}$$

5.2.2 Line loads

Considering a line distribution load conditions along a line (Figure 40) whose parametric equations in the local reference system of the macro-element are known and expressed as a function of a single parameter, *t*, as reported in Eq. 5.16.

$$\Gamma \rightarrow \begin{cases} x = x(t) \\ y = y(t) \end{cases} \qquad t \in [t_0, \quad t_1] \tag{5.16}$$

The parametric expression of the three components for the load **f**(t) is given by:

$$\mathbf{f}(t) = \begin{bmatrix} f_x(t) \\ f_y(t) \\ f_z(t) \end{bmatrix} \tag{5.17}$$

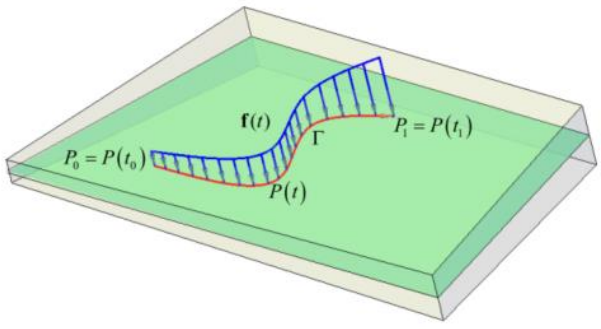

Figure 40 - Line distribution load condition (figure from [155]*)*

The expression of the external virtual work is given by:

$$L_{ve} = \int_{\Gamma} \mathbf{f}^{T}(s)\ \tilde{\mathbf{u}}(s)ds \qquad 5.18$$

Where *s* is the curvilinear abscissa. In order to solve the integral reported in Eq. 5.18 it is necessary to perform a change of variables to return to the integration domain [-1, 1]. It is worth noting that this methodology is valid for a line Γ of any shape for which the parametric equations are provided. For simplicity, a linear load distribution along a segment between the points $P_0(x_0,y_0)$ e $P_1(x_1,y_1)$ is here considered. For this particular load condition the parametric equations can be written:

$$P(t) \equiv \begin{cases} x(t) = x_0 \dfrac{1-t}{2} + x_1 \dfrac{1+t}{2} \\ y(t) = y_0 \dfrac{1-t}{2} + y_1 \dfrac{1+t}{2} \end{cases} \qquad t \in [-1,1] \qquad 5.19$$

Carrying out the above change of variables, we thus obtain

$$dx = \frac{x_1 - x_0}{2} dt \qquad 5.20$$

$$dy = \frac{y_1 - y_0}{2} dt \qquad 5.21$$

$$ds = \sqrt{(dx)^2 + (dy)^2} \qquad 5.22$$

from which

$$ds = \frac{1}{2}\sqrt{(x_1 - x_0)^2 + (y_1 - y_0)^2}\,dt = \frac{L}{2} dt \qquad 5.23$$

where L is the distance between the two external points of the line Γ of application of the load. Therefore, the external virtual work will be given by:

$$L_{ve} = \int_{-1}^{1} \mathbf{f}^{T}(t)\ \tilde{\mathbf{u}}(s)\frac{L}{2}dt = \frac{L}{2}\int_{-1}^{1} \mathbf{f}^{T}(t)\ \boldsymbol{\Psi}(\xi(t),\eta(t),\gamma)dt\cdot\tilde{\mathbf{d}} \qquad \forall\tilde{\mathbf{d}} \tag{5.24}$$

Once again, it is necessary to change the reference system from cartesian to intrinsic. The expression of ξ(t) and η(t) are reported in Eq. 5.25

$$\begin{cases} \xi(t) = \xi_0\dfrac{1-t}{2} + \xi_1\dfrac{1+t}{2} \\ \eta(t) = \eta_0\dfrac{1-t}{2} + \eta_1\dfrac{1+t}{2} \end{cases} \qquad t\in[-1,1] \tag{5.25}$$

In this way there is a one-to-one correspondence between the points $Z_0(\xi_0, \eta_0)$ and $Z_1(\xi_1, \eta_1)$ in the intrinsic reference system (Figure 41b) and $P_0(x_0, y_0)$ and $P_1(x_1, y_1)$ in the local cartesian reference system (Figure 41a).

Therefore, the vector of equivalent forces $\mathbf{F_0}_{,(7x1)}$ in case of linear loads distribution is evaluated as follows:

$$\mathbf{F_0}_{,(7x1),linear} = \frac{L}{2}\int_{-1}^{1} \mathbf{f}^{T}(t)\bullet\boldsymbol{\Psi}(\xi(t),\eta(t),\gamma)dt \tag{5.26}$$

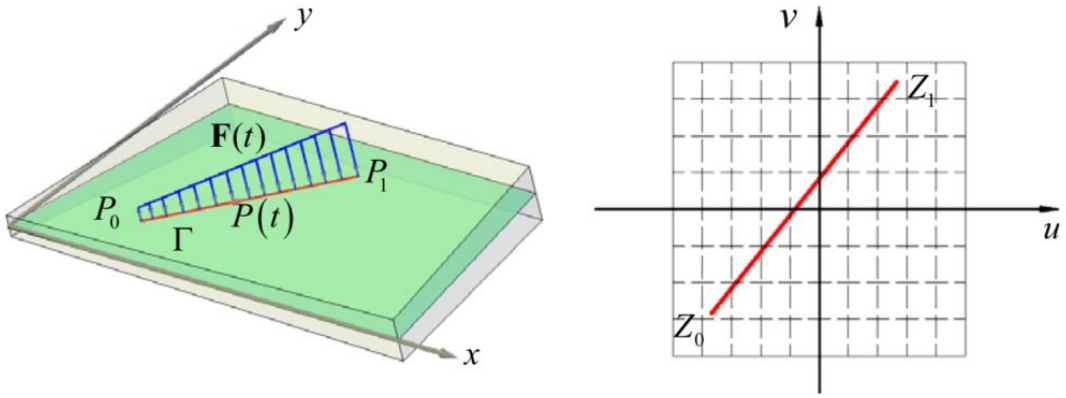

a b

Figure 41 - Linear load distribution in a) Local cartesian and b) intrinsic reference system. (Figure from [155]*)*

5.2.3 Area loads

Let us consider a load distribution along an area of application over the middle plane of the element. The load distribution is defined in the local reference system, denoting with p(x,y) the intensity of the load and with **r**(x,y) the unit vector which identifies the direction of the load point-by-point, it is possible to evaluate for the generic point of the macro-element the three components of the load through the following expression:

$$\begin{cases} f_x(x,y) = p(x,y)\ \mathbf{r}(x,y)\cdot\mathbf{i} \\ f_y(x,y) = p(x,y)\ \mathbf{r}(x,y)\cdot\mathbf{j} \\ f_z(x,y) = p(x,y)\ \mathbf{r}(x,y)\cdot\mathbf{k} \end{cases} \qquad 5.27$$

For simplicity in the present study, it is assumed that the area load distribution acts on the entire surface of the element. Given the intensity and the direction of the loads at the vertexes, the load at each point of the element can be calculated through linear interpolation of the shape function $N_{vi}(\xi,\eta)$ reported in Eq.5.6. The load can therefore be expressed in the intrinsic reference system as:

$$\mathbf{f}(\xi,\eta) = p(\xi,\eta)\mathbf{r}(\xi,\eta) \qquad 5.28$$

With

$$p(\xi,\eta) = \sum_{i=1}^{4} p_i N_i(\xi,\eta) \qquad 5.29$$

$$\mathbf{r}(\xi,\eta) = \sum_{i=1}^{4} \mathbf{r}_i N_i(\xi,\eta) \qquad 5.30$$

Being p_i and $\mathbf{r}_i$ the intensity and the direction of the load at the i-th vertex of the element (i=1,…,4).

Therefore, the external virtual work for an area load distribution can be written as:

$$L_{ve} = \int_{-1}^{1}\int_{-1}^{1}\sum_{i=1}^{4} p_i N_i(\xi,\eta)\left[\sum_{i=1}^{4}\mathbf{r}_i N_i(\xi,\eta)\right]\boldsymbol{\Psi}(\xi,\eta,\gamma)J(\xi,\eta)\ d\xi d\eta\cdot\tilde{\mathbf{d}} \qquad \forall\tilde{\mathbf{d}} \qquad 5.31$$

Finally, the equivalent the vector of equivalent forces $\mathbf{F_0}_{,(7x1)}$ in case of area loads distribution is evaluated as follows:

$$\mathbf{F}_{\mathbf{0},(7x1),area} = \int_{-1}^{1}\int_{-1}^{1}\sum_{i=1}^{4} p_i N_i(\xi,\eta)\left[\sum_{i=1}^{4}\mathbf{r}_i N_i(\xi,\eta)\right]\boldsymbol{\Psi}(\xi,\eta,\gamma)J(\xi,\eta)\ d\xi d\eta \qquad 5.32$$

A particular case when it deals with area load distribution is the calculation of the nodal forces equivalent to the self-weight. In this case, the expression reported in Eq. 5.32 must be written under the hypothesis of the constant load direction and intensity proportional to the thickness, t(ξ,η), of the element in each point.

$$\mathbf{f}(\xi,\eta) = \rho t(\xi,\eta)\mathbf{g} \qquad 5.33$$

Where ρ is the mass volume density and **g** is the gravity acceleration whose modulus is equal to 9.81 m/s^2. From Eq. 5.12 and Eq. 5.33 it follows that the vector equivalent to the area load distribution due to the self-weight can be evaluated as follow:

$$\mathbf{F}_{\mathbf{0},(7x1),mass} = \rho\int_{-1}^{1}\int_{-1}^{1}\sum_{i=1}^{4}\mathbf{g}^{T}\boldsymbol{\Psi}(\xi,\eta,\gamma)t(\xi,\eta)J(\xi,\eta)\ d\xi d\eta \qquad 5.34$$

Finally, the total equivalent force vector is obtained considering the contribution of each type of load distribution, as expressed below.

$$\mathbf{F}_{\mathbf{0},(7x1)} = \mathbf{F}_{\mathbf{0},(7x1),mass} + \mathbf{F}_{\mathbf{0},(7x1),area} + \mathbf{F}_{\mathbf{0},(7x1),linear} + \mathbf{F}_{\mathbf{0},(7x1),point} \qquad 5.35$$

More details on the equivalent external force vector can be found in [155].

5.2.4 The additional loading contribution due to P-Delta effects

Let us consider a generic force field **f**(x,y) applied to a generic area A belonging to the middle plane of a macro-element, as represented in Figure 42 in which, for a sake of simplicity, is represented the resultant of the area load distribution (indicated as **F**) applied in its barycenter Q and (*) indicates the positions of nodes at the current configuration. The corresponding vector moment ($\boldsymbol{M_{P-\Delta}}$) describing the P-Delta effects, referring to the current configuration of the element identified by the current degrees of freedom **d**, is given by

$$\mathbf{M_{P\text{-}\Delta}}(\mathbf{f}) = \iint_{A} (\mathbf{u}(x,y) - \mathbf{u_G}) \wedge \mathbf{f}(x,y)\, dA \qquad 5.36$$

Being x,y the coordinates of the loading application point referred to the element local system, **u**(x,y) the corresponding displacement field. In view of Eq. 5.7, Eq. 5.36 can be written as

$$\mathbf{M_{P\text{-}\Delta}}(\mathbf{f}) = \int_{-1}^{1}\int_{-1}^{1} \left[\boldsymbol{\Psi}(\xi,\eta,\gamma) - \boldsymbol{\Psi}_G\right]\cdot\mathbf{d} \wedge \mathbf{f}(\xi,\eta) J(\xi,\eta) d\xi d\eta \qquad 5.37$$

Considering $\mathbf{P}_i$ (*i=1,..,4*) the resultant of the internal forces that the macro-element receives from the other panels through the interface elements applied in the generic point $c_j(\xi_{c_j}, \eta_{c_j}, z_{c_j})$, the corresponding P-Delta moment is given by

$$\mathbf{M_{P\text{-}\Delta}}(\mathbf{P}) = \sum_{j=1}^{4}\left[\mathbf{u}(\xi_{cj}, \eta_{cj}, z_{cj}) - \mathbf{u}_G\right] \wedge \mathbf{P}_j \qquad 5.38$$

Where ξ_{cj}, η_{cj} and the intrinsic coordinates of the projection of c_j in the mid-plane of the element and z_{cj} the eccentricity of c_j from that plane.

Considering both the external and along-interface forces applied to the elements, the total P-Delta moment for each macro-element can be expressed as:

$$\mathbf{M}_{\mathbf{P\text{-}\Delta}} = \mathbf{M}_{\mathbf{P\text{-}\Delta}}(\mathbf{f}) + \mathbf{M}_{\mathbf{P\text{-}\Delta}}(\mathbf{P}) \qquad 5.39$$

Finally, The P-Delta vector moment $\mathbf{M}_{\mathbf{P-\Delta}}$ expressed by Eq. 5.39 is related to the current configuration of the element and is considered through an additional external element vector forces, $\mathbf{F}_{\mathbf{P\text{-}\Delta}}(\mathbf{u})$, as follows

$$\mathbf{F}_{\mathbf{P\text{-}\Delta}}(\mathbf{u}) = \begin{bmatrix} 0 & 0 & 0 & \mathbf{M}_{\mathrm{P-\Delta},(1\times 3)} & 0 \end{bmatrix}^{\mathrm{T}} \qquad 5.40$$

P-Delta effects are considered in both static [161] and dynamic field. In the following the iterative Newton-Raphson procedure in the case of static loadings (Section 0) and the integration method for the dynamic equation of motion (Section 6.1.1) are discussed.

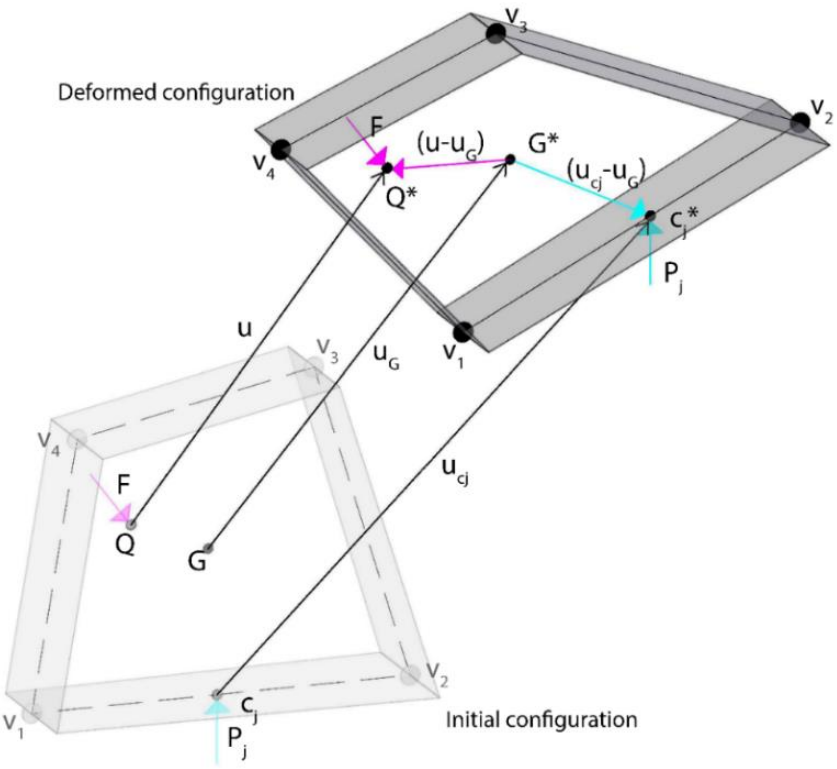

Figure 42 - P-Delta effects due to rigid rotations and shear in-plane deformation

5.1.1. The Newton-Raphson Integration method

The equation of equilibrium in the static field, considering P-Delta effects, can be written as follow:

$$\mathbf{f}_S(\mathbf{u}) = \mathbf{p} + \mathbf{F}_{\mathbf{P\text{-}\Delta}}(\mathbf{u}) \qquad 5.41$$

in which

- $\mathbf{f}_S(\mathbf{u})$ is the elastic forces' vector;
- $\mathbf{p}$ is the vector of the applied loads, evaluated in the initial configuration of the element;
- $\mathbf{F}_{P\text{-}\Delta}(\mathbf{u})$ is the vector of P-Delta effects (Eq. 5.40).

To perform incremental nonlinear static analyses using the new DMEM formulation, the vector of the P-Delta effects is included within a standard Newton Rapson procedure. At the generic j-th iteration of the i-th step of the analysis, the global equilibrium of the system can be written as follows:

$$\mathbf{R}^{(j)} = \mathbf{p} + \mathbf{F}_{P\text{-}\Delta,i}(\mathbf{u}_i) - \mathbf{F}_{int,i}(\mathbf{u}_i^{(j)}) \qquad 5.42$$

where, $\mathbf{R}^{(j)}$ represents the current unbalance vector. According to the Newton Raphson strategy, the increment of internal forces in the elastic prediction stage is evaluated as:

$$\Delta\mathbf{F}_{int,i}^{(j)} = \mathbf{F}_{int,i}(\mathbf{u}^{(j+1)}) - \mathbf{F}_{int,i}(\mathbf{u}^{(j)}) = \mathbf{k}_i^{(j)} \cdot \Delta\mathbf{u}_i^{(j)} = -\mathbf{R}^{(j)} \qquad 5.43$$

where $\mathbf{k}_i^{(j)}$ can alternatively represent the tangent stiffness matrix computed considering the material nonlinearities, and updated at each iteration or kept constant during the iterations ($\mathbf{k}_i^{(0)}$) if a modified Newton Raphson strategy is employed [163].

From Eq. 5.43, it is obtained:

$$\Delta\mathbf{u}_i^{(j)} = -\left(\mathbf{k}_i^{(j)}\right)^{-1}\mathbf{R}^{(j)} \qquad 5.44$$

and, the displacement vector is updated as follows:

$$\mathbf{u}_i^{(j+1)} = \mathbf{u}_i^{(j)} + \Delta\mathbf{u}_i^{(j)} \qquad 5.45$$

Then, the updated displacement vector ($\mathbf{u_i^{(j+1)}}$) is used to compute the vectors of internal forces by integrating the nonlinear constitutive laws of each element. Finally, the unbalance for the new iteration is evaluated by Eq. 5.42. Once the convergence is reached the vector of P-Delta effects is updated.

5.3 Model validation

In this section, the numerical predictions obtained by the proposed model are compared to the analytical results obtained by considering the rigid block assumption. Under this hypothesis, the system does not show lateral displacements until the un-stabilising moment, due to the lateral forces, reaches the stabilizing value related to the wall self-weight and to the applied vertical loads.

Once the incipient rocking condition is achieved the rocking mechanism is activated and the system monotonic load-displacement curve follows a softening branch due to geometrical nonlinearities [60], [65], [96], [164], as qualitatively reported in Figure 43.

The effects of corner imperfection of the rigid block can lead to a reduction of the lateral resistance of the rigid system and the effect of block deformability will produce both a reduction of the resisting moment and a displacement of the system due to the system flexibility (Figure 43).

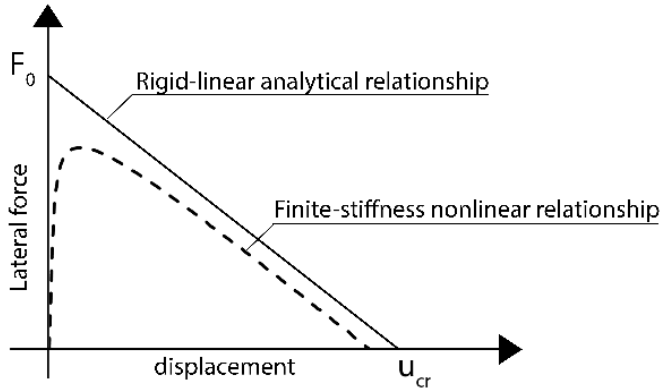

Figure 43 - Force-displacement relationships for rigid and deformable rocking walls

This latter behavior will be encounter in the numerical simulations performed by the DMEM being the wall characterized by a finite stiffness as a consequence the rigid body assumption has to be considered as a limit condition.

As benchmark models two isolated walls, whose mechanisms are characterized by the rotation around horizontal hinges, are considered (Figure 44). More specifically, a parapet wall (PW) of height *h*, thickness *t* and weight *W* (Figure 44a), and a simply-supported wall (SSW), constituted by two rigid blocks of height h_1 and h_2, weight W_1 and W_2 respectively and thickness *t*, spanning vertically between supports at ceiling/floor levels, are considered, as shown in (Figure 44b). Only two one-way bending moment schemes are considered in order to avoid to consider the influence of combined flexural-shear-torsion wall response ([151], [165]), the role of this latter interaction in presence of geometrical nonlinearities could be the object of future developments, such as the consideration of more complex 3d rocking scenario, (as, for examples, free-standing objects). The analytical expressions of the force-displacement (F-u) law is a bi-linear curve and therefore can be described by evaluating the parameters F_0 and u_{cr}, identifying the activation force and the ultimate displacement, respectively, reported in Table 2, for each of the two considered mechanisms. Before undergoing non-linear rocking behavior, URM walls are characterized by a linear and perfectly rigid response. Once the mechanism is triggered, the rigid-softening restoring force-displacement law becomes the reference curve until the displacement value equal to u_{cr} is reached, corresponding to which the lateral force becomes zero. It can be observed that the displacement capacity is essentially a function of the wall thickness, whereas the strength capacity is significantly influenced by the wall boundary conditions [60].

In the simulations reported in the following, two different geometric layouts, characterized by different values of wall slenderness, are considered, as specified in Table 3. The analyses are conducted initially considering no external forces (P=0) applied to the wall (considering the force related to the masonry self-weight). Then, some parametric analyses are conducted considering different values of the external forces (see Figure 47 and Figure 48), assuming zero eccentricity so that the pre-compression force P is centred on the geometric barycentre of the block.

All the numerical analyses (nonlinear static and dynamic) reported in this work are performed using an Intel(R) Core(TM) i7-9750H CPU @2.60GHz.

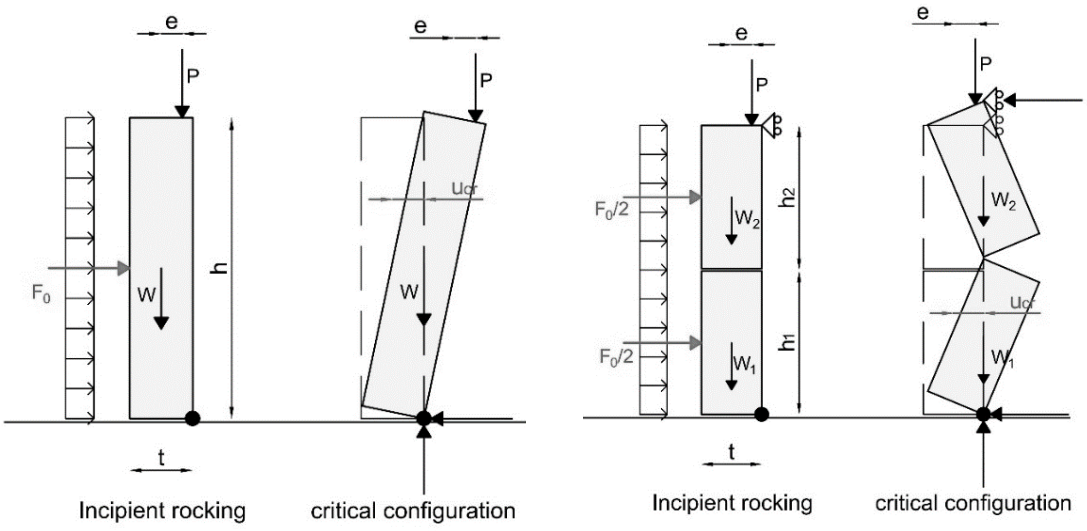

Figure 44 - Rocking masonry walls: (a) Parapet Wall (PW) and (b) Simply-Supported Wall (SSW)

Mechanism	F_0	u_{cr}
PW	$\frac{1}{h}(W+P)\cdot t+\frac{2}{h}P\cdot e$	$\frac{2/h\cdot(W+P)\cdot t/2-2/h\cdot P\cdot e}{2/h\cdot(W+2\cdot P)}$
VSW	$\frac{2}{h_1}(W+P)\cdot t+\frac{P}{h-h_1}(t+2\cdot e)$	$\frac{2/h_1\cdot(W+P)\cdot t+P\cdot(t+2\cdot e)/(h-h_1)}{2/h_1\cdot(W+P)+2\cdot P/(h-h_1)}$

Table 2 - Force-displacement relationship. Force capacity (F_0) and instability displacement (u_{cr}) associated with parapet wall and vertical spanning wall mechanisms

Wall	h [mm]	t [mm]	l [mm]	t/h [-]	W [kN]
Specimen 1	1000	120	375	0.12	1.18
Specimen 2	1000	250	754	0.25	4.94

Table 3 - Geometrical characteristics of the walls

The DMEM models are developed considering a single panel in the case of the PW and two panels for the SSW. In the latter case, it is considered $h_1=h_2=h/2$. The interface

links of the macro-element are characterised by assuming a no-tension material (namely, tensile strength $\sigma t = 0$ MPa and fracture energy in tension $Gt = 0$ N/mm), linear elastic in compression, with k_n representing the stiffness of a unitary area, which is set sufficiently high to approximate an almost rigid block.

5.3.1 Numerical-analytical comparison

The results obtained by the DMEM for the two (PW and SSW) walls and the two different geometries are shown in Figure 45, compared to the corresponding analytical capacity curves of the rigid-block models. The results are normalised by the ultimate force (F_0) and critical displacement (u_{cr}) corresponding to the case of zero compression load P. In the analyses, the number of interface transversal links rows, discretising the wall thickness, has changed from 5 to 50 to investigate the influence of this discretization parameter on the wall response. In particular, the number of rows of links, being centred on the competent area, affects the approximation of the wall thickness and the location of the rotation point. Namely, using 50 rows, the effective model thickness (coincident with the distance between the two extreme links) is equal to 117.6 mm in the case of Specimen 1 and 245 mm in the case of Specimen 2, corresponding to an error of 2%. It is apparent that this error can be controlled by considering a different geometrical distribution of the nonlinear links in the fibre discretization of the wall section. However, a classical fibre discretization has been adopted in the numerical simulations. The transversal stiffness (k_n) of the masonry wall is set equal to 5E+08 N/m^3, according to the assumption already adopted in the referenced paper [122]. Observing the graphs in Figure 45, it can be noted that the DMEM model well describes the overall response of the walls since the force-displacement curve tends to the theoretical rigid-block response as the number of links increases. Small differences between the numerical and the analytical responses are observed in the pre-peak and peak load stages due to the finite stiffness of the DMEM model, as already qualitatively highlighted in Figure 43. These differences are more evident for specimen 1-PW, which is characterised by a higher value of slenderness. In all the cases, the response is very close to the analytical limit case when more than twenty rows are

employed in the discretization. In the following simulations, the interfaces are discretised using fifty rows of links to guarantee a very well model accuracy, although for practical applications, ten rows could be sufficient to obtain satisfactory results. It is worth noticing that the number of links does not significantly affect the computational burden and computing time since the overall degrees of freedom are associated to the number of macro-elements only.

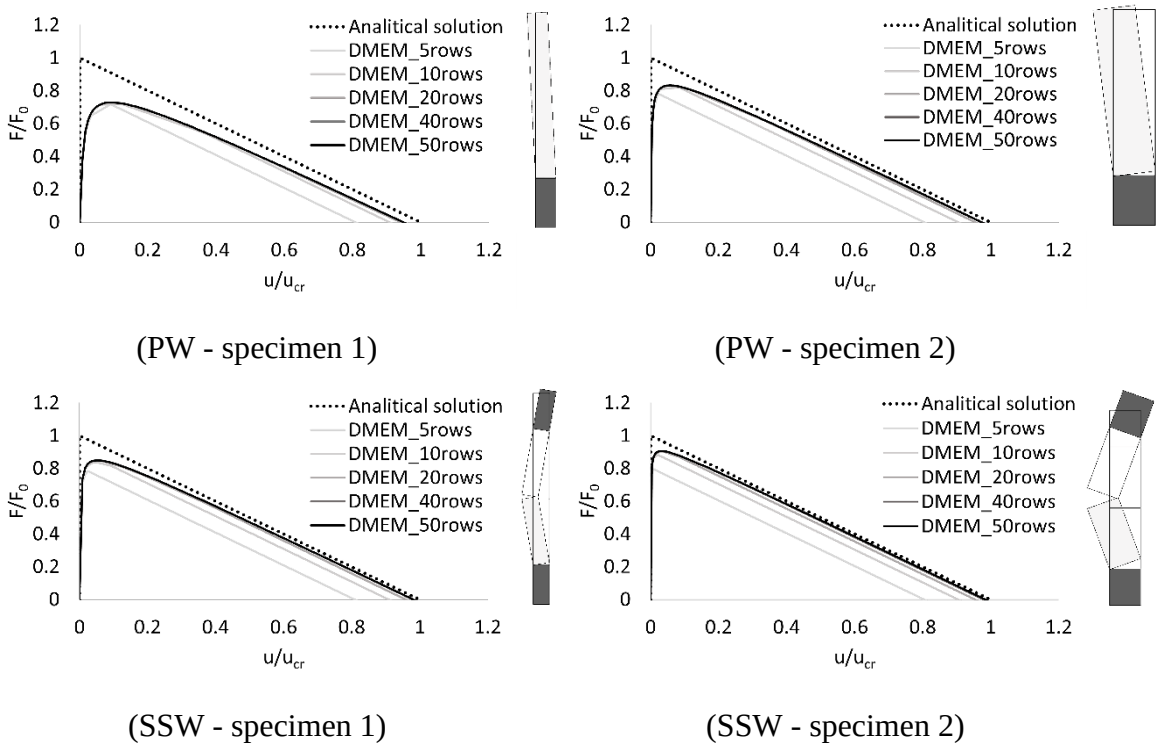

Figure 45 - Force-displacement relationship varying the number of rows of links

Figure 46 shows force-displacement relationships varying the interface stiffness k_n from 5E+7 to 2E+10. It can be observed that numerical response is strongly affected by this parameter both in terms of peak force and ultimate displacement capacity. As expected, the greater the stiffness of the base, the more the numerical curve approaches the results predicted by the rigid block theory, at the expense of a more significant computational burden. Higher values of normal stiffness are not consistent with the behaviour of real masonry walls and reduce the model performances leading to an increase in the average number of iterations.

The comparisons here reported aim to validate the proposed DMEM and also to

show the limits of the rigid block behaviour assumption. Slenderer wall (specimen 1) appears more sensitive to the variation of the interface stiffness, ranging the ultimate force from 40% to 60% of the corresponding theoretical peak force of the PW and SSW rigid block (Figure 46). In specimen 2, the corresponding ultimate force reductions results in 60% and 80% (Figure 46). These values are consistent with the simplified SDOF approach proposed by [35], [60], [96], showing a peak force close to 0.75 of the theoretical rigid-block peak force. A less influence of interface stiffness on the critical displacement is observed. The largest difference on the ultimate displacement between the DMEM and the rigid-block models is about 20%, for the PW of specimen 1, while the interface stiffness does not significantly affect the ultimate displacement of SSW specimens.

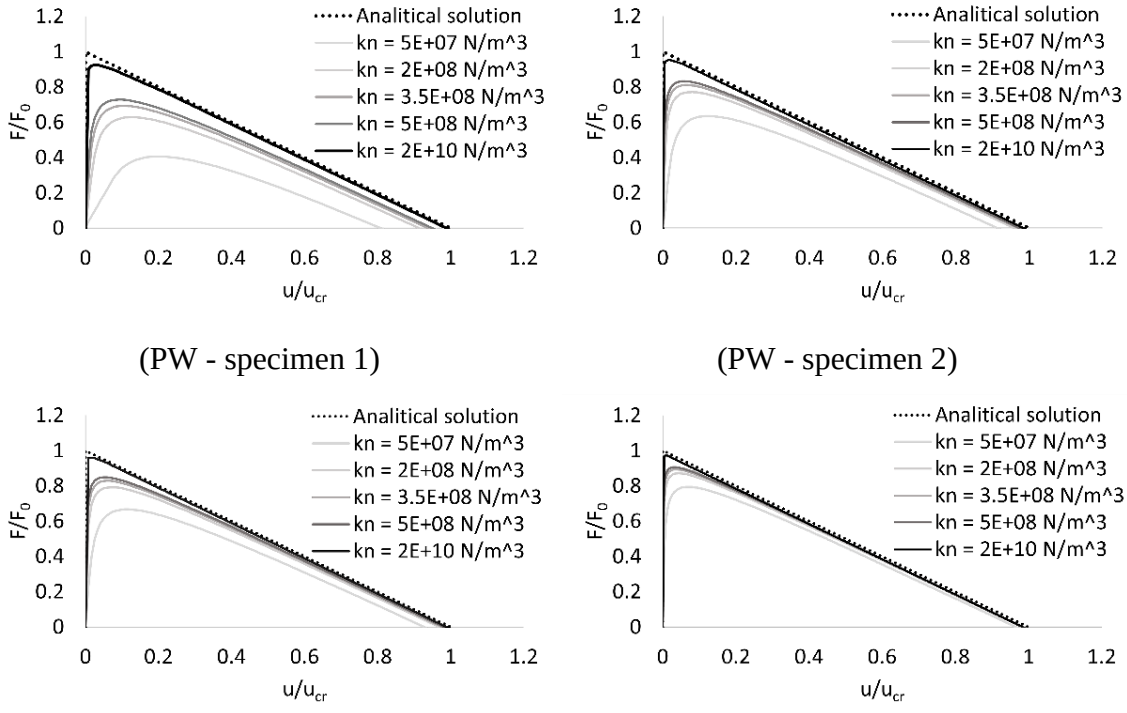

Figure 46 - Force-displacement relationship varying k_n

As a further investigation, the influence of an applied axial load is also evaluated by comparing numerical and analytical results in terms of force-displacement relationships (F-u) by varying the axial compression force applied at the top of the wall. It can be observed how the presence of a vertical pre-compression plays a fundamental role in the

stability of these types of mechanisms as it increases the value of the capacity in terms of strength but decreases its capacity in terms of displacement (Figure 47). These results are related to the role played by the applied load at the top of the wall produces an overturning action when a top displacement of half depth of the wall is reached. This latter reduced displacement capacity is enhanced by the wall flexibility.

As already observed in previous results, the most significant differences correspond to PW and SSW walls of specimen 1. In particular, PW walls show a progressive inconsistency between the rigid-block curve and the DMEM prediction with the axial load increase, reaching a difference of 35% and 43% between the numeric and analytical peak load in the case of specimen 1 and specimen 2, respectively, when the compression load is 0.15MPa. These differences reduce by 60% and 80% in the corresponding specimens of the SSW walls. A lower but still significant dependency of the ultimate displacement on the compression load is observed, with the maximum discrepancy between the numeric and analytical model of 20% registered in the case of specimen 1 of PW. These results are particularly significant regarding the assessment of historical construction when PW mechanism is more likely to be activated and, as evidenced by the above results, the presence of a significant compression load can make rigid-block predictions more unrealistic.

Finally, in Figure 48, the role of P-Delta effects is quantified by comparing the results obtained by the previous and novel formulations of the DMEM model, neglecting and considering the P-Delta effects, respectively. In the figure, the continue line corresponds to the numerical solution obtained considering P-Delta effects, while the dashed line represents the solution obtained by neglecting their effects. Both are compared with the analytical solution represented by the dotted line. The comparisons highlight how neglecting the P-Delta effects not only influences the prediction of the ultimate displacement but also affects the accuracy in terms of peak load prediction. From Figure 48, it is also evident how the P-Delta effects become significant at a rather low displacement magnitude. Considering the cases investigated in this section, that threshold can be assumed to be around 10% and 20% of the ultimate displacement for specimen 1 and specimen 2, respectively. It is worth noting that the computational time necessary for the pushover

analyses of the benchmarks reported above is the same with and without P-Delta effects. For this reason, it can be stated that P-Delta effects are computationally efficient and do not increase the computational cost in terms of time compared to the case in which they are neglected.

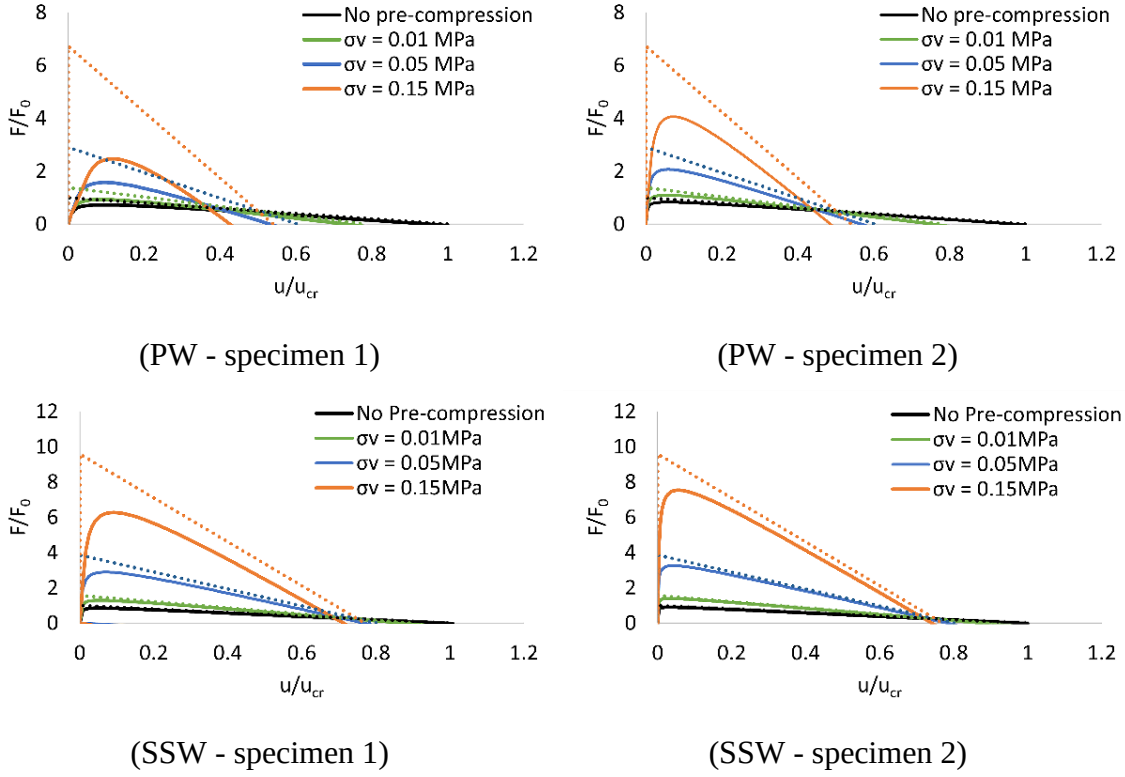

Figure 47 - Force-displacement relationships varying the wall pre-compression force

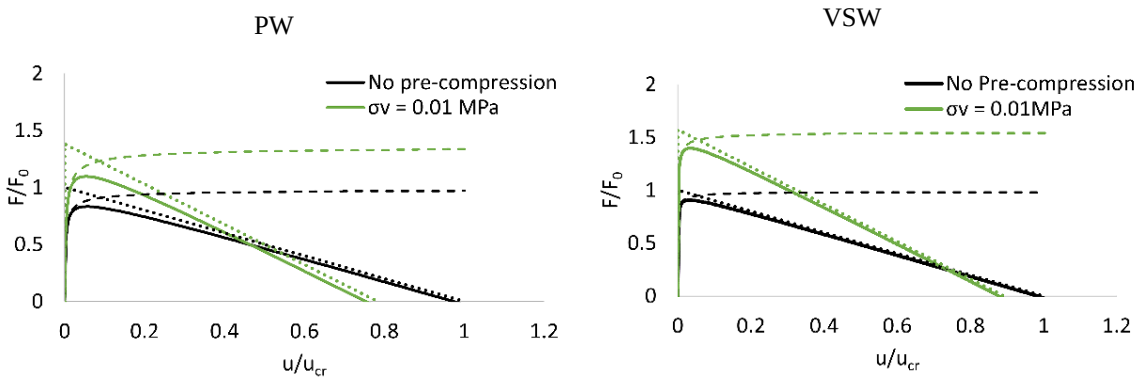

Figure 48 - Force-displacement relationship considering (continue line) and neglecting (dashed line) P-Delta effects for Specimen 2

5.3.2 Numerical-experimental comparison

In this section, the proposed 3D-DMEM modelling strategy is employed to simulate a series of experimental tests consisting in isolated walls subjected to a one-way OOP bending moment, carried out by [60] and numerically investigated by different authors ([60], [166]–[168]). The comparison between the numerical DMEM prediction with experimental observations and the results of more refined modelling strategies enables evaluating the accuracy of the proposed model in describing the OOP rocking behavior of URM walls.

Experimental tests

The experimental campaign has been performed at the Chapman Structural Testing laboratory of the University of Adelaide and the results are reported in [60] and in [166]. The tests have been carried out on simply-supported walls with and without pre-compression, representing load-bearing and non-load-bearing walls in URM buildings, which were subjected to monotonic static loads and dynamic excitations along the OOP direction (Figure 49a). The specimens consisted in single-leaf brick-masonry walls, 110 mm thick, 1500 mm height and 950 mm width. Standard extruded clay brick units with dimensions 230x110x76 mm^3 and a typical Australian mix of 1:1:6 (cement:lime:sand) mortar were used in the tests, and 10mm mortar joints were adopted as well per standard construction practices in Australia. The average density of specimens was determined to be 1800 kg/m^3.

The tests were conducted on uncracked and cracked specimens to investigate the influence of pre-existing structural damage on the OOP wall response. In the present study, the simulations are conducted considering only the uncracked specimens subjected to static loads. One specimen was subjected to an initial axial load designed to provide a uniform precompression s_v = 0.15 MPa to simulate the conditions of a real wall in a multistorey building. In all the static tests, the lateral load (F) was uniformly applied at the wall mid-height using a hand pump-driven hydraulic actuator. A rigid steel frame prevented the

lateral OOP displacements at the base and top sections of the wall (Figure 49a). In the specimen with zero axial load, both the vertical displacement component and the rotation at the top wall section were allowed. In the specimen with initial axial load, the vertical displacement and rotation at the top section were partially restrained due to a spring, which was put in unilateral contact with the top wall section to transfer initial vertical load and simulate the presence of a slab interacting with the wall. However, the real values of the elastic stiffnesses were not measured experimentally. Finally, during the experimental campaign, tests on masonry prisms, to determine the masonry flexural and compression strengths and Young's module, resulted in 0.49MPa, 13.4MPa and 5,322 MPa, respectively.

Numerical simulations and comparisons

The DMEM model has been performed by adopting a refined mesh. Namely, a number of 18 macro-elements, corresponding to the number of brick layers of the specimen, and 19 interfaces equally distributed along the wall height discretized with seven rows of links have been considered.

In the analyses, the top restraint of the model with precompression is modelled by considering a rigid element at the top section of the wall, connected with the wall by a no-tension interface (simulating the dry joint between the wall and the steel apparatus used in the test). The rigid element is then fully restrained against rotation and elastically restrained against vertical displacements (Figure 49c) whose stiffness has been evaluated by fitting the experimental results as discussed later. The elastic and nonlinear masonry material parameters required to calibrate the DMEM model have been chosen according to [167] and [168] and are summarised in Table 4. In particular, the tensile strength of the mortar joint (σ_t) is assumed, according to [169], 1/3 of the masonry flexural strength provided by Doherty (2000) [60]. An elastoplastic constitutive law with softening governed by fracture energies in tension and compression is used for the transversal links. An elasto-plastic Mohr-Coulomb criterion is used for the shear sliding interface mechanisms. Pushover analyses have been performed to obtain the complete pre- and post-cracking force-

displacement curve for the case of $\sigma_v = 0$ (Figure 50a) and $\sigma_v = 0.15$MPa (Figure 50b), compared with the experimental results and the FEM predictions results reported in (Minga 2017). The results obtained by DMEM are also reported in terms of collapse mechanisms (Figure 51). The pushover curve of the DMEM model in Figure 50b has been obtained by fitting the stiffness of the top spring k_{spring} equal to 1560 N/mm, after having validated the model for $\sigma_v = 0$. In both the analysed specimens, the pre-peak branch is linear elastic with high stiffness, up to a maximum force that depends on the boundary and loading conditions. Once the maximum force is reached, which corresponds to the cracking of the mid-height interface element, the curve shows a sudden drop in resistance in the case of $\sigma_v = 0$ the softening continues up to the residual strength of approximately 0.4 kN. Differently, the load-bearing wall recovers the lateral strength showing a much more ductile response, due to the effect of the top restraint. The overall DMEM response agrees well with experimental results and FEM predictions for both the specimens investigated.

E_m [MPa] Young's modulus	σ_t [MPa] Tensile strength	σ_c [MPa] Compressive strength	G_t [N/mm] Fracture energy in tensile	G_c [N/mm] Compressive fracture energy	c [MPa] Cohesion	tg(φ) [-] Friction coefficient
1560	0.163	6.2	0.05	1.00	0.23	0.58

Table 4 - Mechanical parameters of masonry

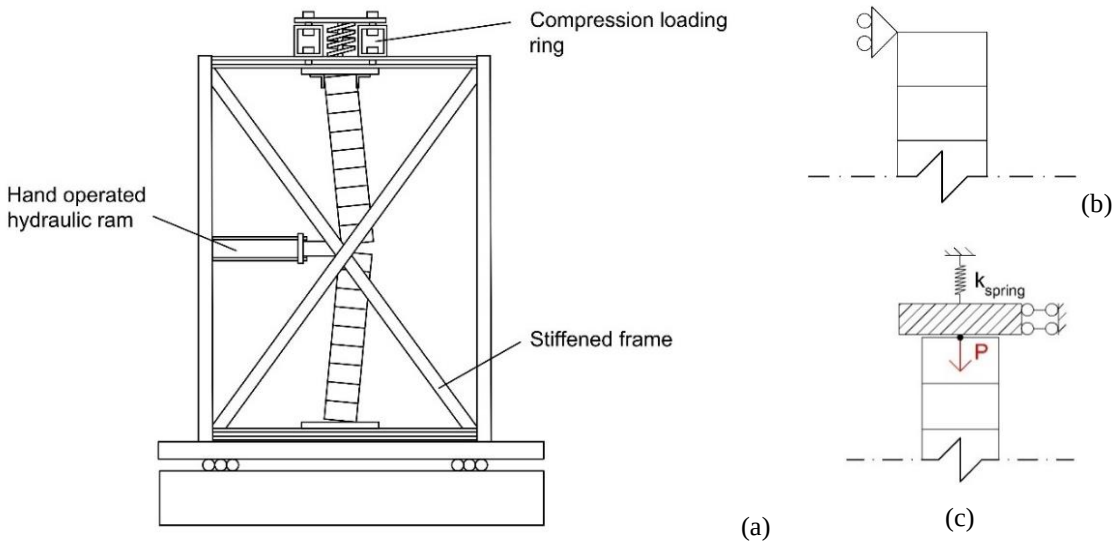

Figure 49 - (a) Static push test configuration; (b) non load-bearing and (c) load-bearing boundary conditions

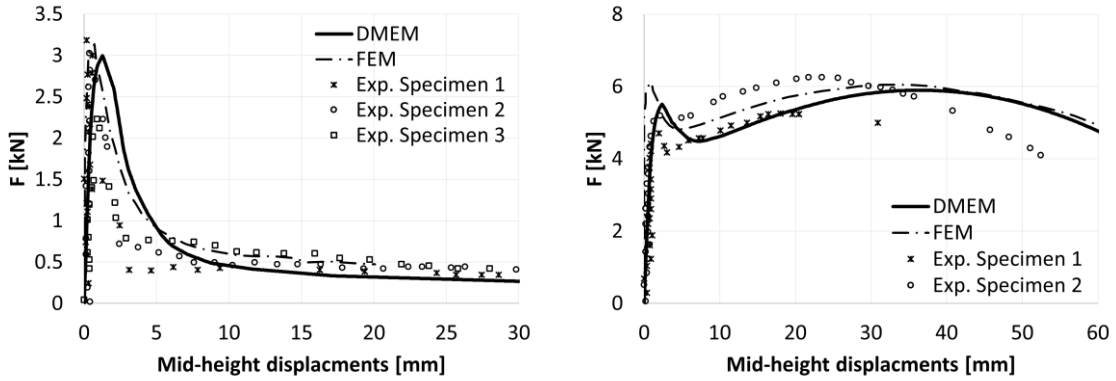

(a) (b)

Figure 50 - Experimental-numerical comparison of pushover curves: (a) σv = 0 MPa; (b) σv = 0.15 MPa

(a) (b)

Figure 51 - Collapse mechanisms for : (a) σv = 0 MPa; (b) σv = 0.15 MPa

As a further investigation, parametric analyses have been performed on the wall with zero pre-tension, to investigate the role of the mesh size and the number of interface transversal links.

The simulations were conducted considering two different mesh discretisation. Namely, the fine mesh, already adopted in the simulation above, and a coarse mesh, obtained doubling the element size concerning the fine mesh and three different interface discretisation: 5-10-20 rows of interface transversal links.

Figure 52 shows the responses of the DMEM model obtained by varying the mesh

size while keeping constant the number of rows of links equal to 20. Figure 52b shows the results obtained by changing the number of rows of links while adopting the fine mesh. In the graphs, the experimental results and numerical FEM predictions are reported for comparison. Observing Figure 52, it is possible to conclude that the parameters investigated do not significantly affect the DMEM model's accuracy.

Moreover, the DMEM model could provide reliable predictions of the wall response, even adopting a coarse mesh and a low number of rows of links, with clear benefit in terms of the model's efficiency.

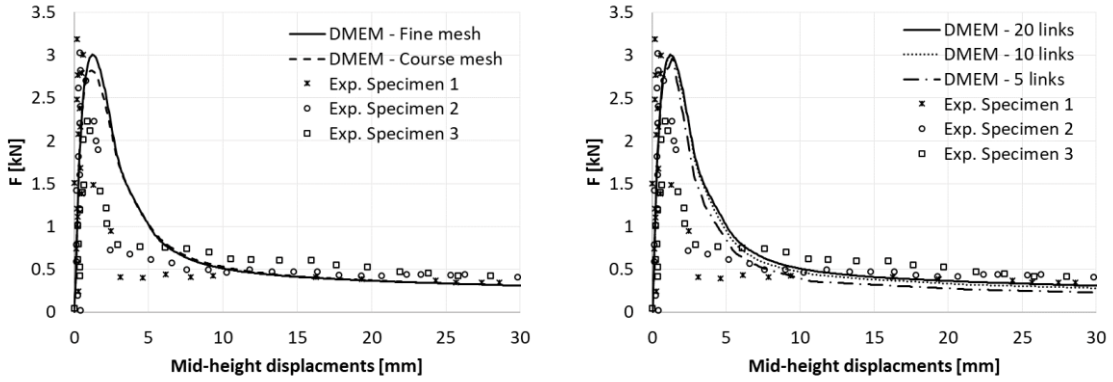

(a) (b)

Figure 52 - Parametric analysis varying: (a) the dimension of the mesh (b) the rows of links

Furthermore, for the load-bearing case, numerical results obtained with different values of the stiffness of the top spring (k_{spring}) are reported in Figure 53. In particular, two limit values are considered, corresponding to +50% and -50% of the reference value used to fit the experiments in Figure 50b. From Figure 53, it is apparent how this parameter affects the post-peak wall response and its ultimate displacement capacity. In the final analysis, the influence of masonry deformability on the rocking behaviour of the specimen is investigated. Analyses are performed on the specimen with no precompression ($\sigma_v = 0$) varying the masonry Young's modulus by doubling and halve the reference value reported in Table 4. The results are reported in Figure 54 concerning the refined mesh (Figure 54a) and the coarse mesh (Figure 54b) discretisation.

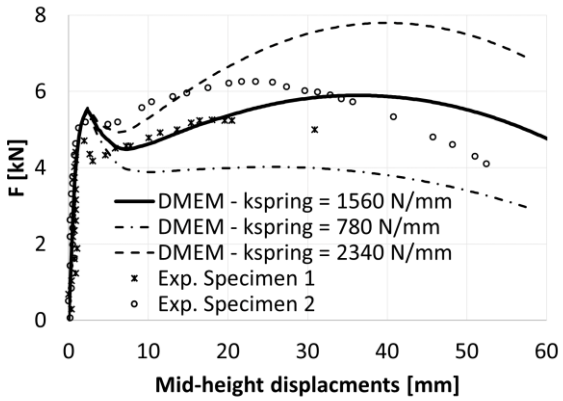

Figure 53 - Load-bearing condition with different values of the top spring's stiffness

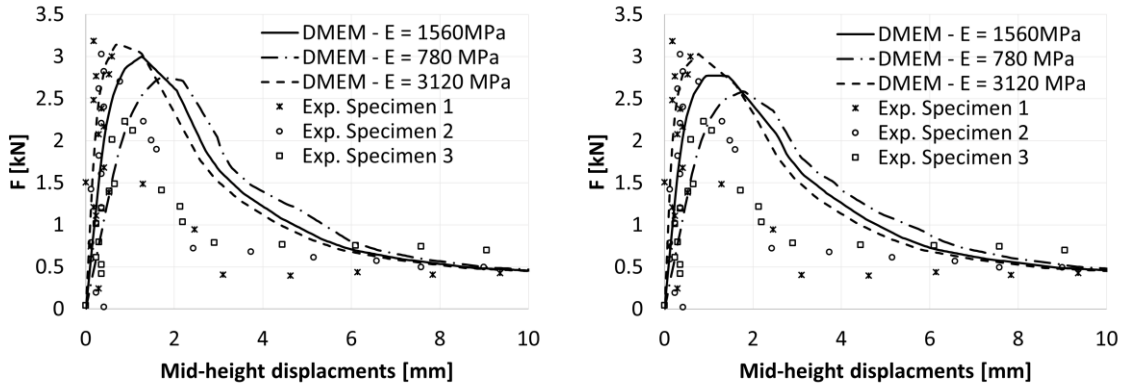

(a) (b)

Figure 54 - Parametric analysis varying masonry Young's modulus: (a) refined mesh (b) course mesh

Comparing the graphs reported in Figure 54a and in Figure 54b, it can be concluded that the mesh discretisation does not significantly affect the wall response, confirming the results reported in Figure 50a. Moreover, it is clear how the masonry deformability influences the pre-peak response and the peak load. More specifically, the lateral wall strength showed a variation of approximately 20% due to the Young's modulus variation.

5.3.3 Parametric analysis

In this section, the role of the main masonry mechanical parameter is investigated by considering the specimens considered in the previous section without applying any axial

load. Figure 55 shows the first parametric investigation on the influence of tensile strength, the analyses are performed considering an elasto-brittle constitutive law for three different values of axial strength. It can be observed how the masonry strength significantly influences the pre-peak response, strongly influencing the ultimate load of the mechanisms. Namely, the ultimate load corresponding to a tensile strength of 0.15 MPa is over double the ultimate load corresponding to the no-tension material model. Nevertheless, once the rocking is activated, the mechanism evolves following the softening branch obtained considering a no-tension material.

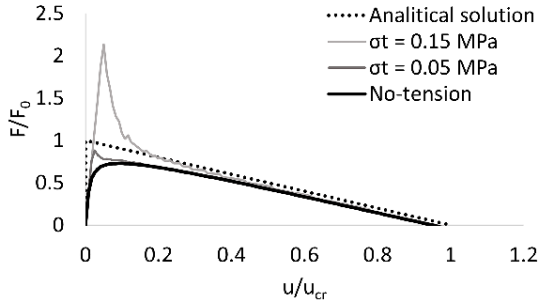

(PW Specimen 1)

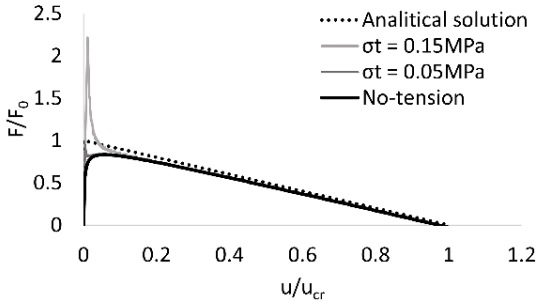

(PW Specimen 2)

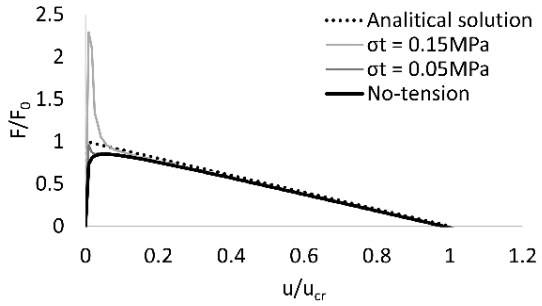

(SSW Specimen 1)

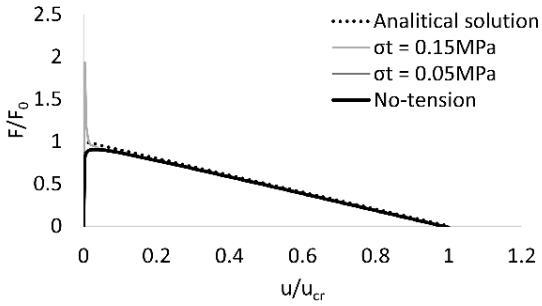

(SSW Specimen 2)

Figure 55 - Force-displacement relationship varying the tensile strength (σt)

In Figure 56, a linear-softening post-elastic behavior is considered with different values of fracture energy and keeping constant the tensile strength equal to 0.15Mpa. Higher values of fracture energy lead to an increased peak load and a moderate increase in displacement capacity immediately after the peak-load displacement. That influence becomes negligible for the less slender specimen 2. However, then the mechanism evolves towards the rigid block curves.

This result confirms how the ultimate rocking behaviour is mainly governed by the geometrical parameters when geometrical nonlinearities are considered. Material strength and fracture energy contribute only to the pre-peak response, influencing only the activation of the rocking and increasing the ultimate load. In the investigated range of variation of the fracture energy, the ultimate load ranged from 2 to approximately 5, and the displacement capacity displacement is affected up to 60% of the ultimate one (in the case of the PW wall specimen 1) (Figure 56). The slender specimen 1 is much more affected, in terms of capacity displacement by fracture energy than specimen 2.

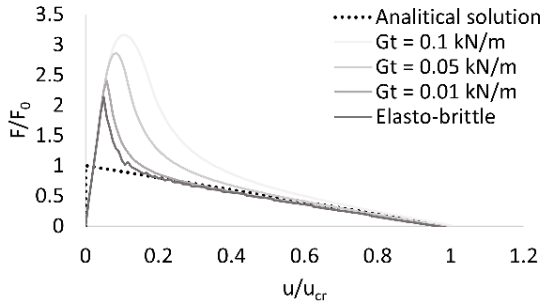

(PW Specimen 1)

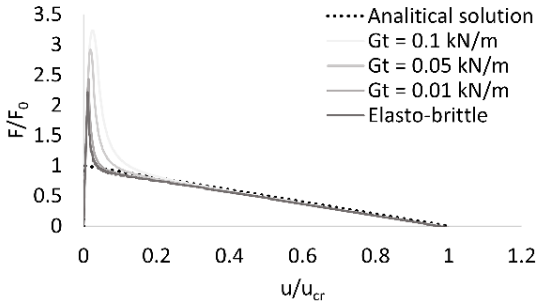

(PW Specimen 2)

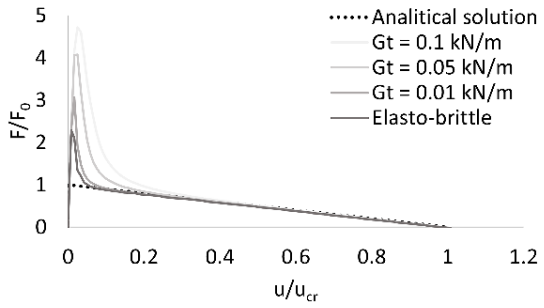

(SSW Specimen 1)

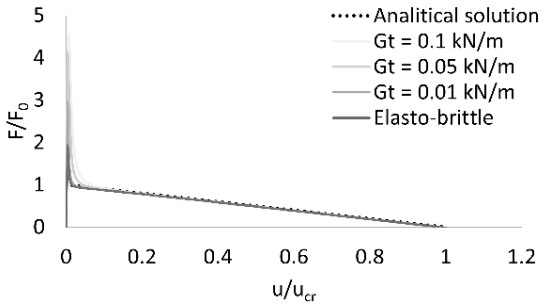

(SSW Specimen 2)

Figure 56 - Force-displacement relationship varying the tensile Fracture Energy (Gt)

6. SIMULATION OF RIGID BLOCK DYNAMICS

The dynamic response of rocking rigid blocks has been studied for over 60 years. As already said in Section 2, numerous structures are modelled as rocking blocks, i.e. tall buildings, URM walls with poor connection, parapet walls, etc.

The first researcher who derived the equation of motion for a rectangular rigid block free to rock at the base was Housner (1963) [38], who established a rocking model known as the classical theory, which many researchers have widely referred to in the past. As proposed by Housner, the equations of motion are derived, assuming a high frictional coefficient at the interface between the block and the ground so that sliding cannot occur, furthermore the rocking motion have been investigated under the hypothesis of small rotations. The source of dissipation have been associated to a loss of kinetic energy when an impact with the rigid supports takes place leading to a discontinuous dissipation model being instantaneous since related to the impact instants only.

This section aims at assessing the accuracy of the P-Delta DMEM formulation when simulating the dynamic response of rocking rigid blocks and evaluate the role played by P-Delta effects in the response of these remarkable benchmarks. With this aim, the two specimens, PW1 and PW2, investigated in Section 5, whose geometric characteristics are reported in Table 2, are considered.

The DMEM predictions are compared to the analytical responses of rigid blocks under free vibrations induced by an initial rotation. Firstly, free-vibration nonlinear analyses are carried out, assuming that the impact at the base is perfectly elastic (undamped systems). Then, a non-classic damping model associated with the rocking interfaces is formulated and implemented within the DMEM strategy to simulate the energy loss associated with each impact. It is worth noting that the damping matrix is classic at a level of the interface, while it is non-classic at the system level. Finally, free- and harmonic-damped vibration analyses are conducted to evaluate the model's accuracy, compared to the

analytical solution of an ideal rigid block proposed by Housner and to the results of detailed FEM simulations [122] and experimental tests available in the literature [170].

6.1 The damping model

This section presents a non-classic damping model used to describe the energy dissipation caused by impacts during the dynamic rocking motion of rigid-block systems. A viscous damping is associated with the interface elements involved in the rocking motion (i.e., connecting two macro-portions behaving as a quasi-rigid blocks).

Let us consider the generic *i*-th interface involved in the rocking motion. The local interface damping matrix ($\mathbf{c}_{loc,i}$) is assumed proportional to the interface tangent stiffness matrix ($\mathbf{k}_{loc,flex,i}$), as reported in Eq. 6.1, where α is a model parameter to be calibrated. It is worth noting that the local damping matrix is at each step proportional to the tangent stiffness and not to the elastic stiffness matrix in order to concentrate the loss of energy at the interface closure, corresponding to the impact of the rigid block system.

$$\mathbf{c}_{loc,i} = \alpha \cdot \mathbf{k}_{loc,flex,i} \qquad 6.1$$

The element viscous forces ($f_{d,i}$) are assumed to be proportional to the velocities of the flexural degrees of freedom of the interfaces ($\dot{\mathbf{u}}$), as defined in Figure 57a and Figure 57b in the case of unrestrained and restrained interfaces, respectively. It follows:

$$\mathbf{f}_d(\dot{\mathbf{u}}) = \mathbf{c}_{loc} \cdot \dot{\mathbf{u}} = \mathbf{c}_{loc} \cdot \begin{bmatrix} \dot{\mathbf{u}}_1 \\ \dot{\mathbf{u}}_2 \\ \dot{\mathbf{u}}_3 \\ \dot{\mathbf{u}}_4 \\ \dot{\mathbf{u}}_5 \\ \dot{\mathbf{u}}_6 \end{bmatrix} \qquad 6.2$$

It is worth noticing that no energy dissipation is associated with the sliding deformations of the interfaces.

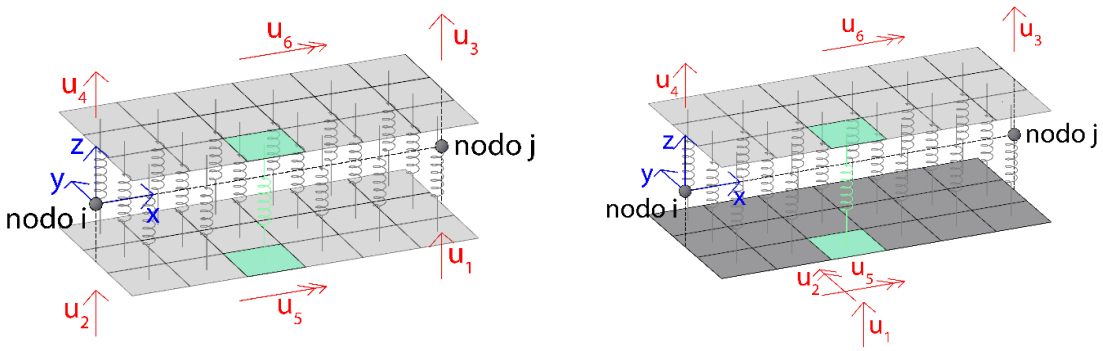

Figure 57 - a) Not constrained, b) constrained interfaces' DOFs of interest

The parameter α in Eq. 6.1 is evaluated according to Eq. 6.3, where ξ_{eq} is an equivalent viscous damping ratio describing the dissipative properties of the physical contact surfaces represented by the interface and $f_{rot,contact}$ is the elastic rotational frequency of the kinematic rocking motion, i.e., the natural frequency of the system with all the rocking interfaces at the complete contact.

$$\alpha = \frac{2\xi_{eq.}}{f_{rot,contact}} \qquad 6.3$$

Referring in the following to the simplest case represented by single rigid body rocking around its base interface, and considering the empirical formulation proposed by Vlachakis et al. (2021), the expressions of ξ_{eq} reported in Eq. 6.4 is considered.

$$\xi_{eq} = -0.000292\left(\frac{H}{B}\right)^{0.935} \cdot k_{n,base}^{0.343} \cdot \ln(e) \qquad 6.4$$

and the rotational frequency of the system at the contact can be expressed as follows:

$$f_{rot,contact} = \frac{l}{2\pi}\sqrt{\frac{k_{rot,contact}}{I_{rot}}} \qquad 6.5$$

where I_{rot} is the rotational mass moment of inertia about the center of the interface section, *t* and *l*, the interface dimensions in the direction parallel and orthogonal to the plane of

rocking, k_n the normal stiffness of the interface per unit of area and $k_{rot,contact}$ is calculated as reported in Eq. 6.6.

$$k_{rot} = \frac{1}{12} k_n (2t)^3 (2l) \qquad 6.6$$

The global damping matrix **c** of the system is obtained by assembling the interface local damping matrices $\mathbf{c}_{loc}$.

As a result of the changing of the local stiffness matrix, the damping matrix changes during the simulations and it has to be updated at each step of the analysis. It requires some changes in the numerical integration of the equations of the motion, as discussed in the following section.

6.1.1 Integration of the equations of the motion

In this section, the numerical integration method is specialised for the case of the damping matrix changes during the analysis, according to the damping model described in the previous section (see Eq. 6.8). Moreover, the contribution related to the P-Delta loads' vector is also introduced within the integration of the equation of motion using Newmark's method.

In the dynamic field the equation of equilibrium contains the inertia ($\mathbf{F}_I = \mathbf{m\ddot{u}}$) and the damping forces ($\mathbf{F}_D = \mathbf{c}(\mathbf{u}) \cdot \dot{\mathbf{u}}$), and it can be written as follow:

$$\mathbf{m\ddot{u}} + \mathbf{c}(\mathbf{u}) \cdot \dot{\mathbf{u}} + \mathbf{f}_S(\mathbf{u}) = \mathbf{p} + \mathbf{F}_{P-\Delta}(\mathbf{u}) \qquad 6.7$$

in which:

- **m** is the mass matrix;
- **c** is the damping matrix;
- $\mathbf{f}_S(\mathbf{u})$ is the elastic forces' vector;
- $\mathbf{F}_{P-\Delta}(\mathbf{u})$ is the P-Delta loads' vector.
- **p** is the external forces' vector

Writing 6.7 in incremental form, which is convenient for nonlinear system, for the generic j-th iteration of the i-th step, considering that the damping matrix is updated at each step of the analysis, it can be written:

$$\mathbf{m}\Delta\ddot{\mathbf{u}}_i + \Delta\mathbf{F}_{D,i} + \Delta\mathbf{F}_{int,i} = -\mathbf{R}^{(j)} \qquad 6.8$$

In the predictor phase:

$$\mathbf{m}\Delta\ddot{\mathbf{u}}_i + \mathbf{c}_i\Delta\dot{\mathbf{u}}_i + \mathbf{k}_i\Delta\mathbf{u}_i = -\mathbf{R}^{(j)} \qquad 6.9$$

where $\mathbf{R}^{(j)}$ represents the dynamic unbalance vector and is equal to

$$\mathbf{R}^{(j)} = \mathbf{p} + \mathbf{F}_{P\text{-}\Delta,i}(\mathbf{u}_i) - \mathbf{F}_{int,i}(\mathbf{u}_i^{(j)}) - \mathbf{c}_i\dot{\mathbf{u}}_i - \mathbf{m}_i\ddot{\mathbf{u}}_i \qquad 6.10$$

The Newmark's Method is based on the following equations:

$$\dot{\mathbf{u}}_i = \dot{\mathbf{u}}_{i-1} + \left[(1-\gamma)\Delta t\right]\ddot{\mathbf{u}}_{i-1} + (\gamma\Delta t)\ddot{\mathbf{u}}_i \qquad 6.11$$

$$\mathbf{u}_i = \mathbf{u}_{i-1} + (\Delta t)\dot{\mathbf{u}}_{i-1} + \left[(0.5-\beta)(\Delta t)^2\right]\ddot{\mathbf{u}}_{i-1} + \left[(\beta)(\Delta t)^2\right]\ddot{\mathbf{u}}_i \qquad 6.12$$

Where γ and β are parameters of the model and Δt the integration time step.

These two equations combined with the equilibrium equation at the end of the time step, provide the basis for computing u_{i+1}, $\dot{u}_{i+1}$, $\ddot{u}_{i+1}$ at the time (i+1) from the known u_i, $\dot{u}_i$, $\ddot{u}_i$ at the time (i).

Eq. 6.11 and Eq. 6.12 can be written as follow:

$$\Delta\dot{\mathbf{u}}_i = (\Delta t)\ddot{\mathbf{u}}_i + (\gamma\Delta t)\Delta\ddot{\mathbf{u}}_i \qquad 6.13$$

$$\Delta\mathbf{u}_i = (\Delta t)\mathbf{u}_i + \frac{(\Delta t)^2}{2}\ddot{\mathbf{u}}_i + \beta(\Delta t)^2\Delta\ddot{\mathbf{u}}_i \qquad 6.14$$

Eq. 6.14 can be rearranged to obtain the increment of acceleration as a function of the current velocities and accelerations and the increment of displacements as follows:

$$\Delta\ddot{\mathbf{u}}_i = \frac{1}{\beta(\Delta t)^2}\Delta\mathbf{u}_i - \frac{1}{\beta\Delta t}\dot{\mathbf{u}}_i - \frac{1}{2\beta}\ddot{\mathbf{u}}_i \qquad 6.15$$

Substituting Eq. 6.15 into Eq. 6.13, it can be obtained:

$$\Delta\dot{\mathbf{u}}_i = \frac{\gamma}{\beta\Delta t}\Delta\mathbf{u}_i - \frac{\gamma}{\beta}\dot{\mathbf{u}}_i + \Delta t\left(1-\frac{\gamma}{2\beta}\right)\ddot{\mathbf{u}}_i \qquad 6.16$$

Substituting Eq. 6.15 and 6.16 into Eq. 6.8 and carrying out the calculation

$$\begin{aligned}&\left(\mathbf{m}\frac{1}{\beta(\Delta t)^2} + \mathbf{c}_i\frac{\gamma}{\beta\Delta t} + \mathbf{k}_i\right)\Delta\mathbf{u}_i^{(j)} = \\ &= \mathbf{R}^{(j)} + \left(\mathbf{m}\frac{1}{\beta\Delta t} + \mathbf{c}_i\frac{\gamma}{\beta}\right)\dot{\mathbf{u}}_i + \left(\mathbf{m}\frac{1}{2\beta} + \mathbf{c}_i\Delta t\left(\frac{\gamma}{2\beta}-1\right)\right)\ddot{\mathbf{u}}_i\end{aligned} \qquad 6.17$$

Consistently with the classic formulation of Newmark's method, imposing:

$$\hat{\mathbf{k}}_i = \left(\mathbf{m}\frac{1}{\beta(\Delta t)^2} + \mathbf{c}_i\frac{\gamma}{\beta\Delta t} + \mathbf{k}_i\right) \qquad 6.18$$

And

$$\Delta\hat{\mathbf{p}}_i = \mathbf{R}^{(j)} + \left(\mathbf{m}\frac{1}{\beta\Delta t} + \mathbf{c}_i\frac{\gamma}{\beta}\right)\dot{\mathbf{u}}_i + \left(\mathbf{m}\frac{1}{2\beta} + \mathbf{c}_i\Delta t\left(\frac{\gamma}{2\beta}-1\right)\right) \qquad 6.19$$

Eq. 6.17 can be written as:

$$\hat{\mathbf{k}}_i\Delta\mathbf{u}_i^{(j)} = \Delta\hat{\mathbf{p}}_i \qquad 6.20$$

Finally,

$$\mathbf{u}_i^{(j+1)} = \mathbf{u}_i^{(j)} + \Delta\mathbf{u}_i^{(j)} \qquad 6.21$$

Analogously to the static case the updated displacement vector ($\mathbf{u_i^{(j+1)}}$) is used to update the vectors of internal forces, for the next iteration, by integrating the nonlinear constitutive laws of each element and the vector accounting for the P-Delta moments.

6.1.2 Dissipated energy

The loss of energy, which in reality is associated with an instantaneous impact, is described by the DMEM strategy through the negative work done by the interface viscous dumping forces as long as the flexural stiffness of the interface is not zero. This limit state is reached when all links are yielded in tension, and only the external row of links is active. Due to the elastic deformability and finite tensile strength of the links, the interface opening and closure happen gradually in a finite interval of time.

Calling N_{step} the number of analysis steps required for an opened interface to close completely, the loss of dissipated energy can be calculated as follows:

$$\mathbf{E_d} = \sum_{i=1}^{N_{step}} \Delta E_{d,i} = \sum_{i=1}^{N_{step}} \left(\frac{\mathbf{F_{d,i}} + \mathbf{F_{d,i-1}}}{2} \right)^T \cdot \Delta \mathbf{u_i} \qquad 6.22$$

being $\mathbf{F_{d,i+1}}$ and $\mathbf{F_{d,i}}$ the dissipative force at the step i and i-1, and $\Delta\mathbf{u_i}$ is the vector of the displacement increment of the flexural DOFs of the interface.

6.2 Undamped free-vibrations

As the first investigation in the dynamic field, undamped free-vibration simulations are performed on the three specimens varying the value of initial rotation θ_0.

The first two specimens are those used to validate the P-Delta effects in the static field, while the third specimen is characterised by an intermediate slenderness ratio.

The geometric characteristics of the specimens are reported in Table 5.

Wall	h [mm]	t [mm]	l [mm]	θ_{cr} = t/h [-]	W [kN]
Specimen 1	1000	120	375	0.12	1.18
Specimen 2	1000	250	754	0.25	4.94
Specimen 3	1000	170	500	0.17	2.24

Table 5- Geometrical details of the investigated specimens

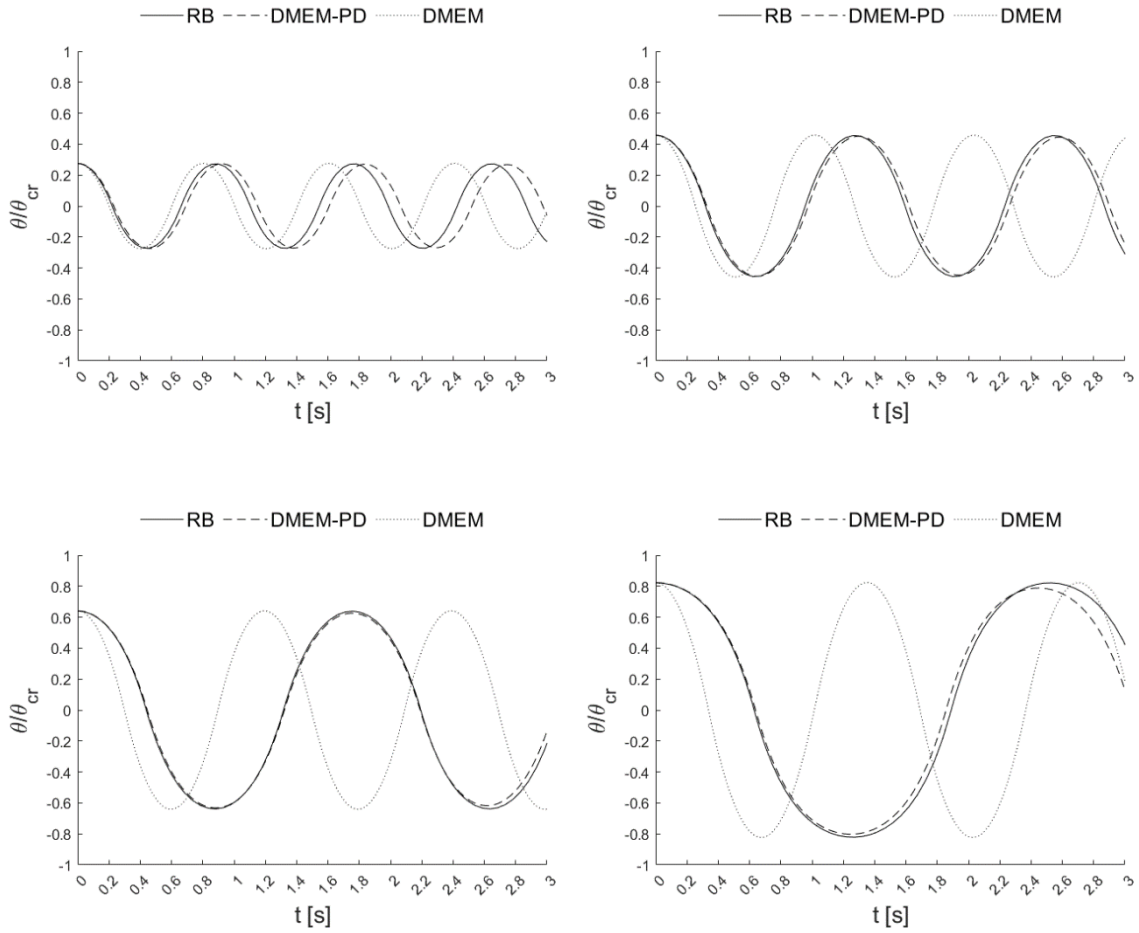

Figure 58 - Displacement time-histories for PW1

A concentrated mass matrix is considered for the DMEM model, where the mass of each macro-element is concentrated to its barycentric point. More details can be found in [171]. The nonlinear dynamic analyses are performed using HiStrA [61], employing the

Newmark method with a time step of 0.002 s and the Newmark's parameters β and γ equal 0.25 and 0.5, respectively. Finally, an energy-based convergence criterion with absolute tolerance of 1E-07 Nm is adopted in the simulations. In the analyses, the number of transversal links was set equal to 12, 25, and 17 for specimen 1, specimen 2 and specimen 3, respectively, to maintain the error of the effective thickness in each specimen less than 1cm. The masonry wall's transversal stiffness (k_n) is set equal to 5E+08 N/m^3, according to the assumption already adopted in the referenced paper [122].

Figure 58, Figure 59, and Figure 60 show the base rotation time histories, normalised by the critical rotation (θ_{cr} = t/h), for the three specimens (PW1, PW2 and PW3) obtained by the DMEM model, applying increasing initial rotations from about the 30% to 80% of the critical rotation, for all the three specimens.

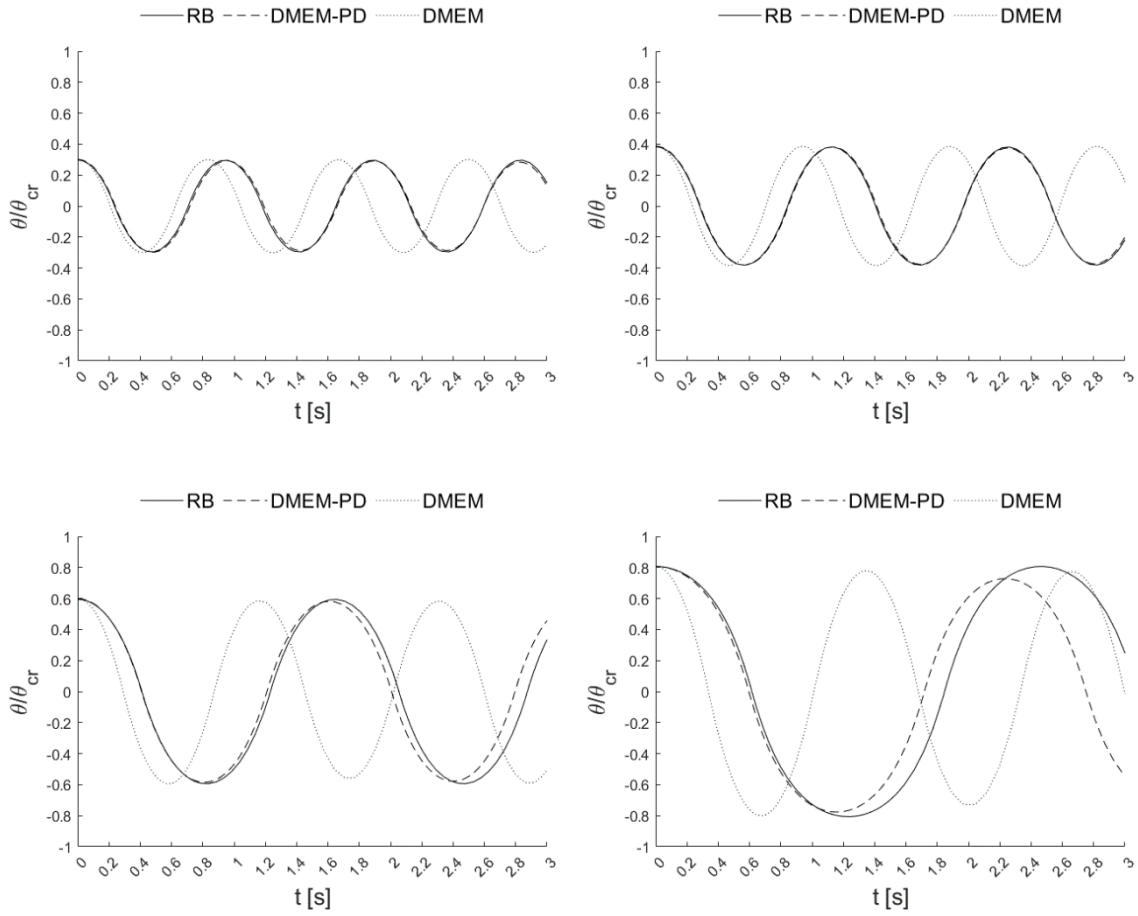

Figure 59 - Displacement time-histories for PW2

The P-Delta effects are alternatively considered (DMEM-PD) and neglected (DMEM) compared with the rigid-block (RB) solution obtained considering large displacements. It can be observed that the higher the initial rotation, the greater the need to consider the P-Delta effects. Nevertheless, even for quite small initial rotations, the P-Delta effects have significant influence on the period of vibration of the wall making the dynamic response consistent with that of the rigid block.

A further study was conducted on the period of vibration varying the initial rotation. Again, the results are compared with the analytical value of period predicted by the classical theory, trough the Eq. 2.15.

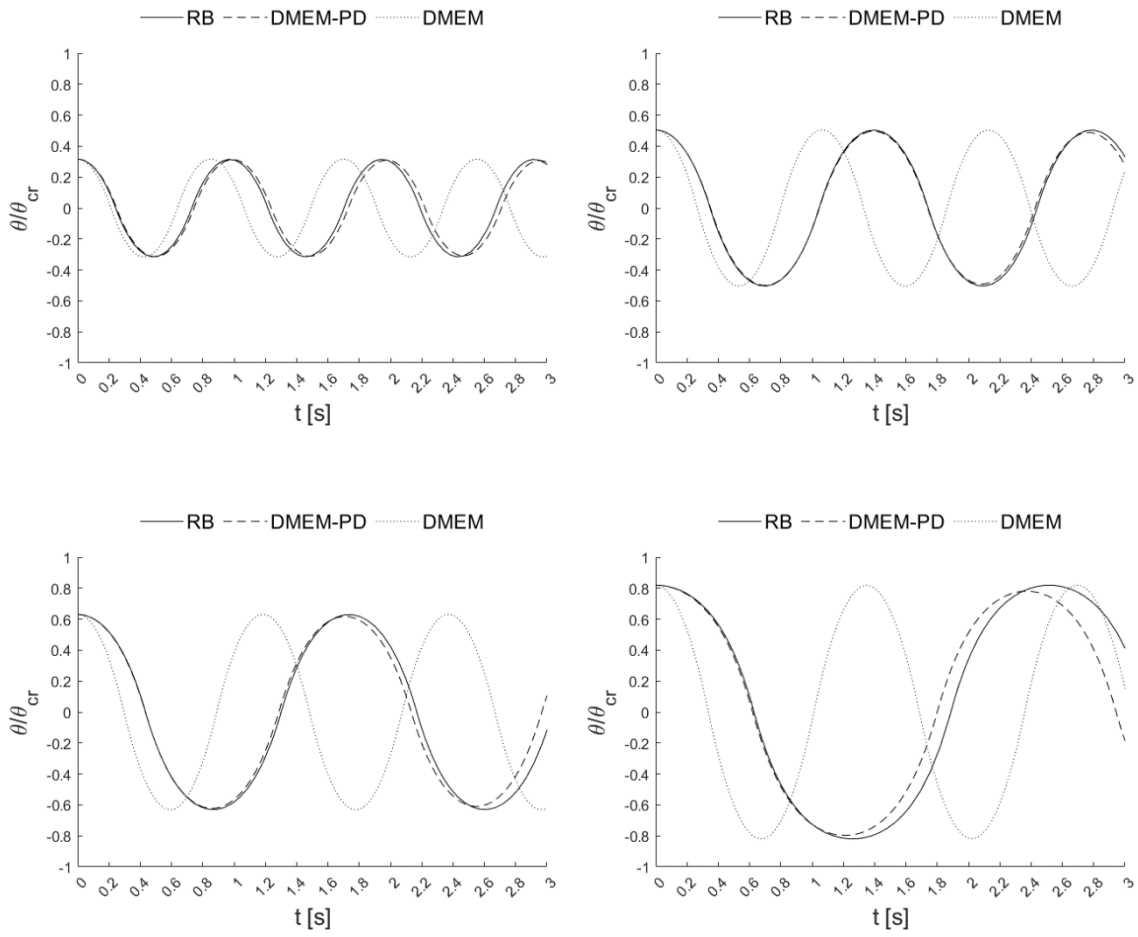

Figure 60 -Displacement time-histories for PW3

The vibration period of the DMEM model is evaluated as the time needed for the model to return to the initial position at the end of the first oscillation. Numerical damping is observed in the DMEM analyses, which increases as the initial rotation increases. Figure 61 shows the period of vibration versus the initial rotation for the three specimens. In the figure, continuous lines indicate the values of analytical solutions, dashed lines indicate the numerical DMEM predictions with P-Delta effects, and dotted lines indicate DMEM predictions without P-Delta effects.

In all the specimens considered, P-Delta effects need to consistently predict the period of vibration as initial rotation reaches 25% of the critical rotation, equal to 0.11, 0.24, and 0.16 radiant, respectively, in the case of specimen 1, specimen 2, and specimen 3. In particular, considering the three investigated specimens, the error in the period exceeded 10% as the initial rotation reached 30% of that critical.

Conversely, DMEM predictions obtained considering P-Delta effects result in a good agreement with the analytical solutions in a significantly more extensive range of oscillations. Namely, considering the three investigated specimens, the percentage error on the predicted period resulted in less than 10% until the initial rotation reached 85% of the critical one. After this limit, the approximated kinematics considered in the DMEM model does not allow for reproducing the results of the analytical solutions. More specifically, in the case of specimen 1, characterised by the higher slender ratio, even for initial rotation equal to 90% of the critical one, the error on the period is about 7.5%. For Specimen 2, characterised by the lower slender ratio, the error is 13% for initial rotations equal to 90% of the critical one and goes up to 21% when the initial rotation reaches 95% of the critical one.

Finally, an intermediate trend is shown by specimen 3, with an error less than 10% and 15%, corresponding to an initial rotation equal to 90% and 95% of the critical one, respectively.

The obtained results are also summarised in Table 6, which reports the average of the percentage errors varying the range of initial rotations considering (“P-D” in Table 6) and neglecting (“SD” in Table 6) P-Delta effects (then following the Small Displacement theory) for the three considered specimens.

$\theta_0/\ \theta_{cr}$	< 20%		20 - 40%		40 - 60%		60 - 80%		> 80%	
	P-D	SD	P-D	SD	P-D	SD	P-D	SD	P-D	SD
Specimen 1	8	7.5	4.0	11.0	1.5	22.5	1.0	34.5	7.5	50.0
Specimen 2	7.5	5.0	2.5	11.0	1.0	22.5	3.5	36.5	13.2	55.0
Specimen 3	6.0	4.0	2.5	12	1.0	23.0	1.5	35.5	8.5	52.5

Table 6 - Percentage error on the period of vibration

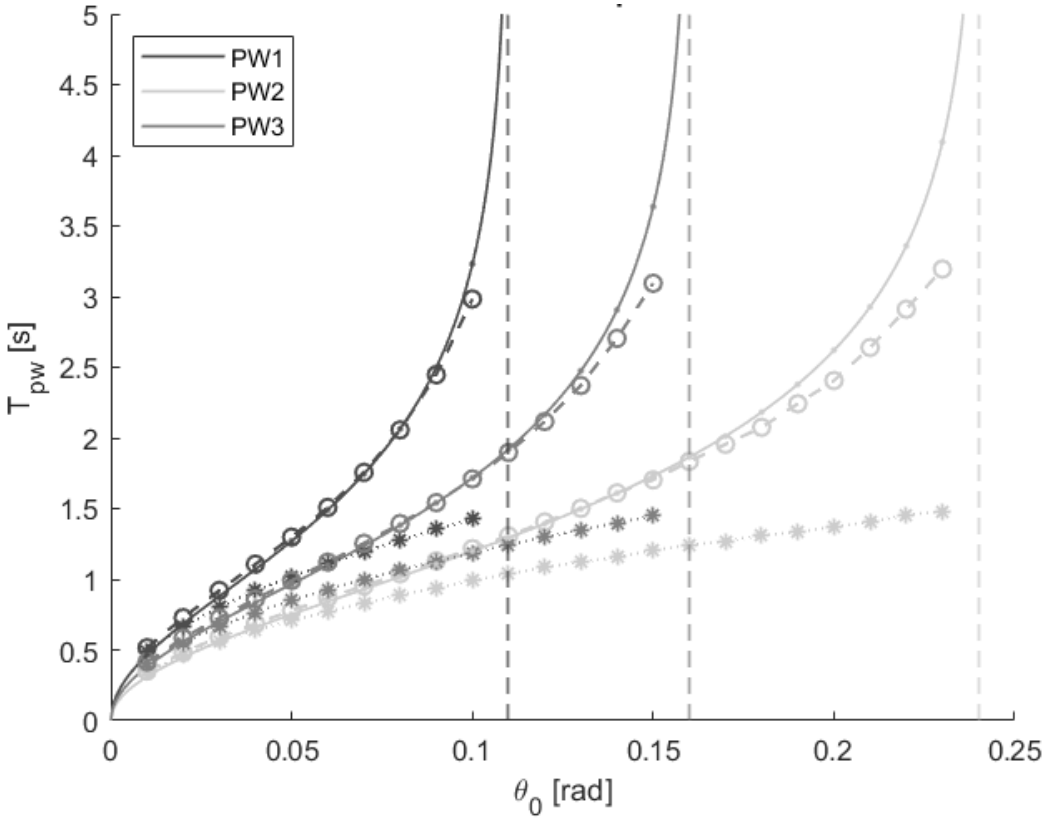

Figure 61 - Period of vibration vs amplitude of initial rotation

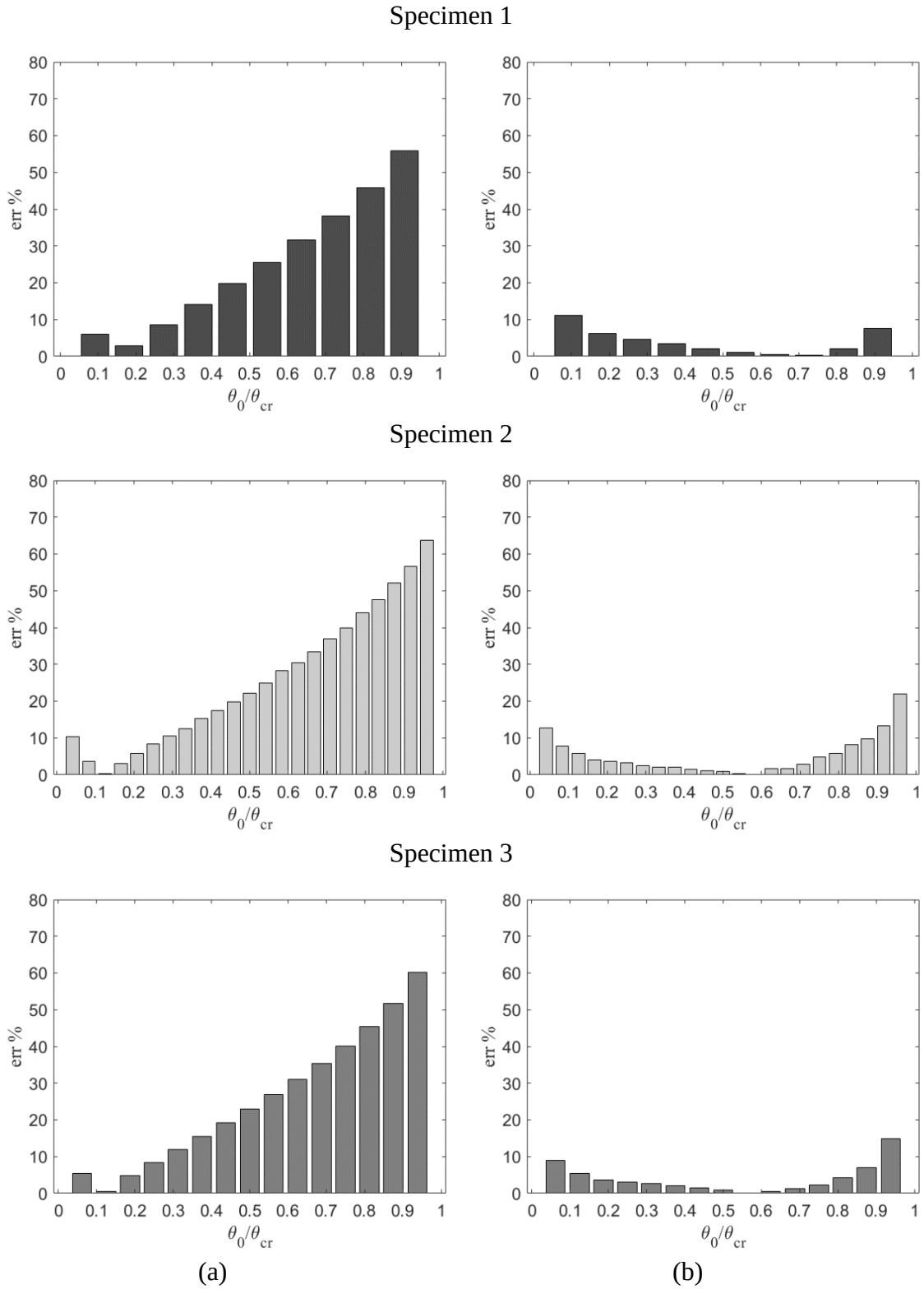

Figure 62 - Percentage error on the period of vibration (a) neglecting and (b) considering P-Delta effects

6.3 Damped free- and harmonic-vibrations

The three specimens, already considered in the case of undamped vibrations, are used to validate the newly-implemented interface damping model. For these samples, experimental data are available from an extensive campaign conducted by Peňa et al. [170] on granitic blocks. During that campaign, the coefficient of restitution (e_{exp}) has been evaluated. This parameter is used in this study to evaluate the equivalent damping ratio (ξ_{eq}) adopting the empirical relationship proposed by Vlachakis et al. [122], for two-side rocking. The geometric and dynamic parameters characterising the three specimens are summarised in Table 7.

The normal interface stiffness k_n [N/m^3] was not measured experimentally. Therefore, a value of 5E+08 N/m^3 is adopted in the analyses, consistently with Vlachakis et al. [122].

Figure 63 reports the free-rocking response of the three specimens, predicted by the proposed model. The adopted Newmark parameters are fixed as $\beta = 0.3025$ and $\gamma = 0.6$ in order to damp the high frequency due to the large value of stiffness used. In the figure, the DMEM results are compared the rigid-block analytical solution considering $e = e_{exp}$ and the results of finite element simulations obtained by Vlachakis et al. [122].

Wall	e_{exp} [-]	ξ_{eq} [%]
Specimen 1	0.978	4.53
Specimen 2	0.936	6.79
Specimen 3	0.973	4.03

Table 7 - Damping parameters

The comparisons show a good agreement between the experimental, analytical and numeric responses in terms of period, confirming that the proposed DMEM model can reproduce the response of damped systems with good accuracy.

This result can be further appreciated if one also considers that the different specimens are characterized by different values of slenderness and different initial rotations and, thus, different coefficients of restitution (Eq. 2.19), demonstrating the robustness of the proposed model.

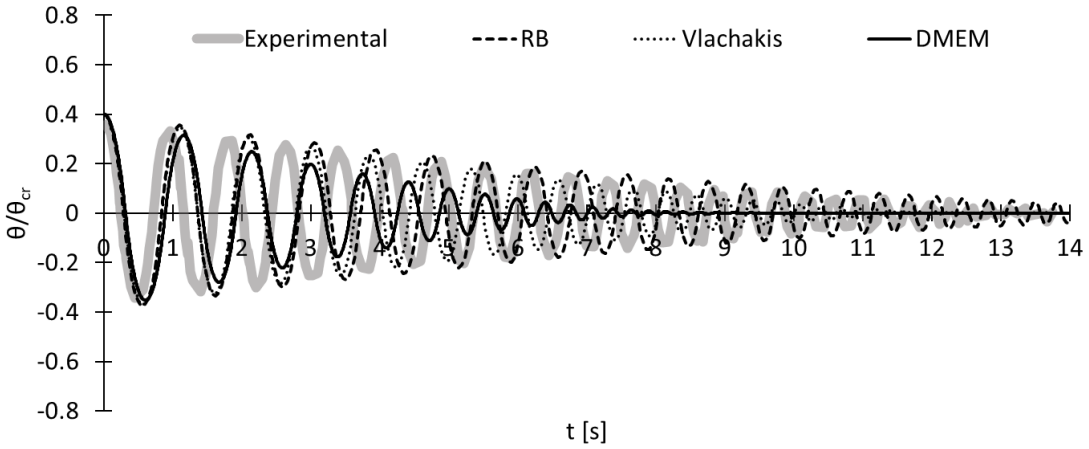

(a)

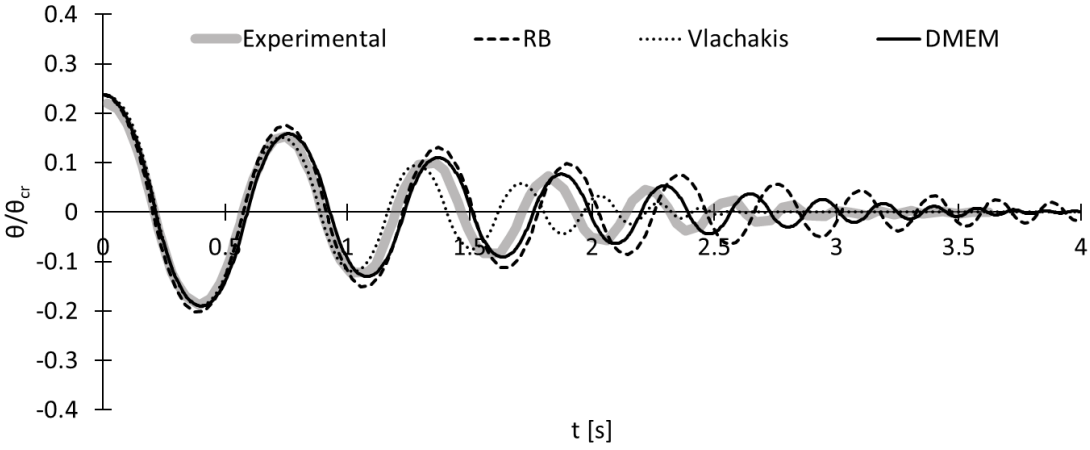

(b)

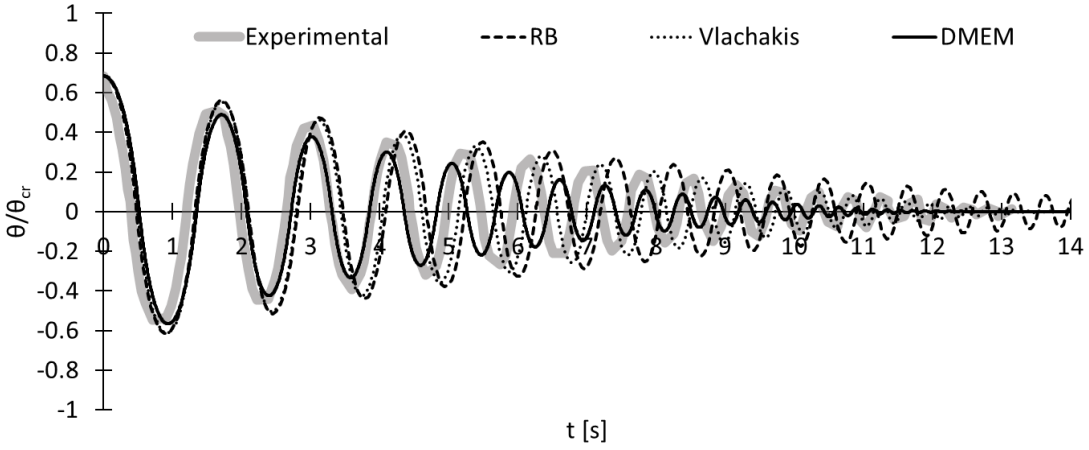

(c)

Figure 63 - Two-side free-rocking response for: a) Specimen 1, b) Specimen 2; c) Specimen 3

In terms of energy dissipation, in all the investigated specimens numerical models overestimate the damping faster than the experiments and analytical solution. However, a very good agreement is observed between the proposed simplified model and the FEM predictions. More specifically, the FEM response (indicated with "Vlachakis" in Figure 63) completely damps out after 10, 2.5 and 13 seconds, respectively in the case of specimens 1, 2 and 3; while the corresponding DMEM responses damp out after 9, 3.5 and 12 sec. In particular, "damping out" means that the block has stopped rocking. Both FEM and DMEM results in very good agreement with experiments in the first cycles of the response while diverging from that for smaller rocking angles. That result has already been observed in [122] and is most probably related to the inaccuracy of the empirical relationship used to calibrate the equivalent damping coefficient, which is independent on the rotation amplitude. On the contrary, it is well-known the dependency of dissipation on the rocking amplitude [122]. The related loss of energy, both in terms of increment and total damping energy, is calculated together with the interface "contact ratio", which represents the ratio between the contact and the total area of the interface A_c/A_{tot}, ranging from 1 (total contact) and zero (interface completely open).

The time histories of the cumulated (E_d) and instantaneous (ΔE_d) dissipated energies, and the contact ratio are shown in Figure 64. It can be observed that the maximum increment of the damping energy corresponds to the impact, which are characterized by a displacement of the control point equal to zero (block in vertical position) and a compressive ratio equal to one. On the other hand, when the interface is open (small value of the compressive ratio) the increment of the damping energy is equal to zero, and consequently, the total energy remains constant until the next impact shows a stepwise trend.

It is worth noting that such a damping model is related to an empirical relationship, which aims at evaluating the loss of energy associated with the impact at the rocking interface of a rigid block, and for this reason, it cannot be used to simulate a more general damping problem. Further calibration and formulations are needed in order to employ this kind of localised damping model in a more general problem aiming at simulating the overall damped energy of URM structures that exhibit OOP collapse mechanisms.

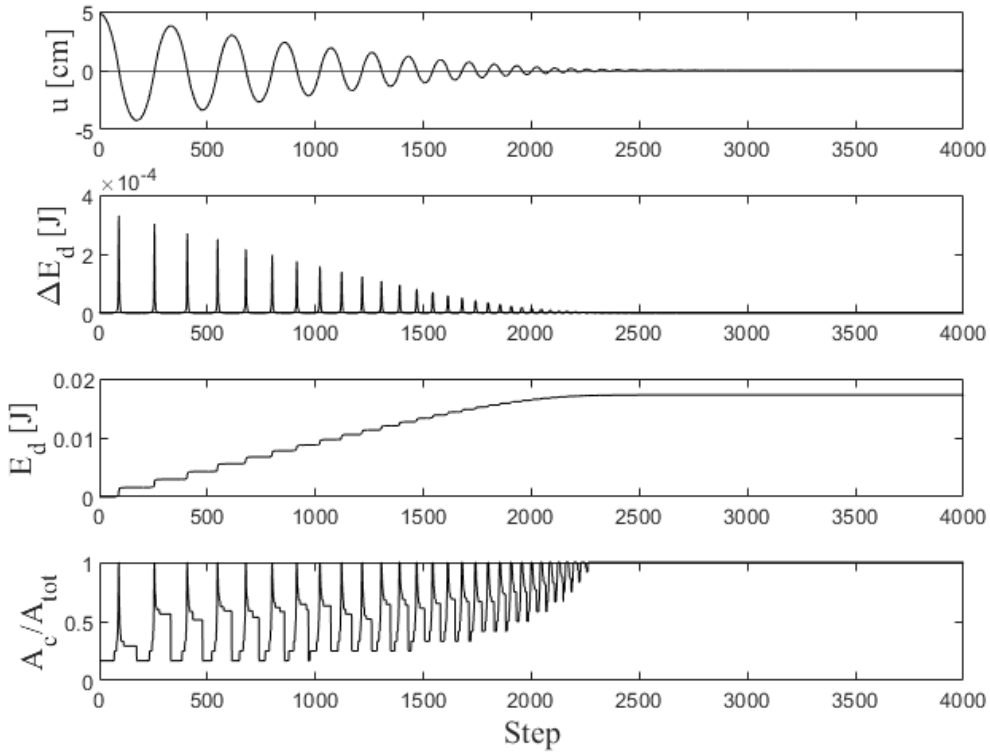

(a)

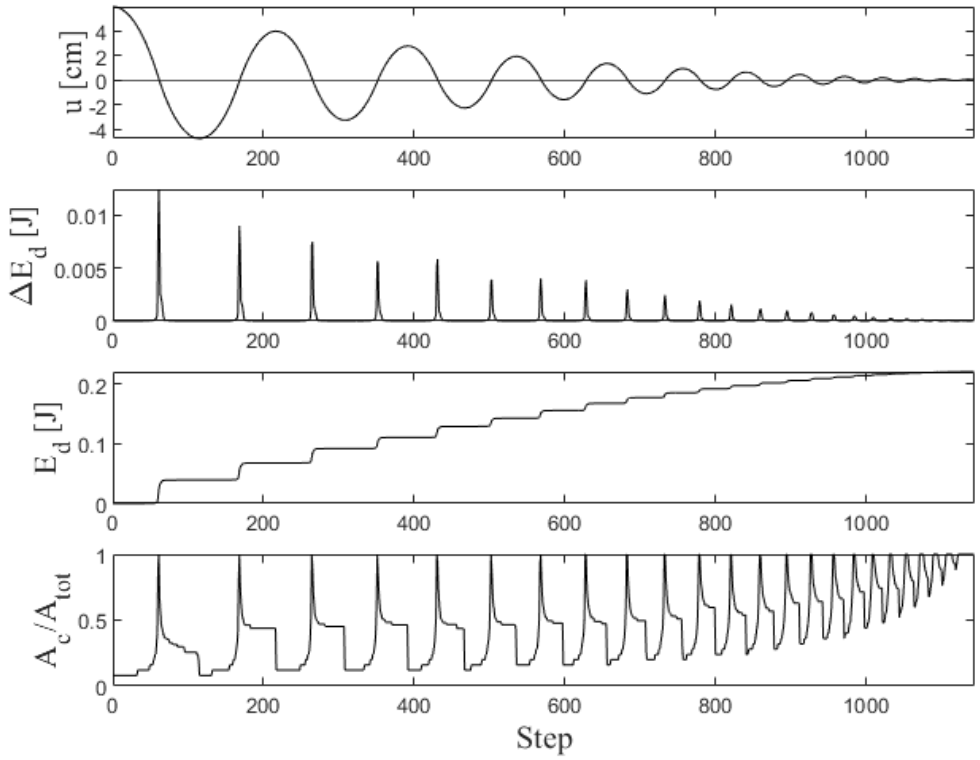

(b)

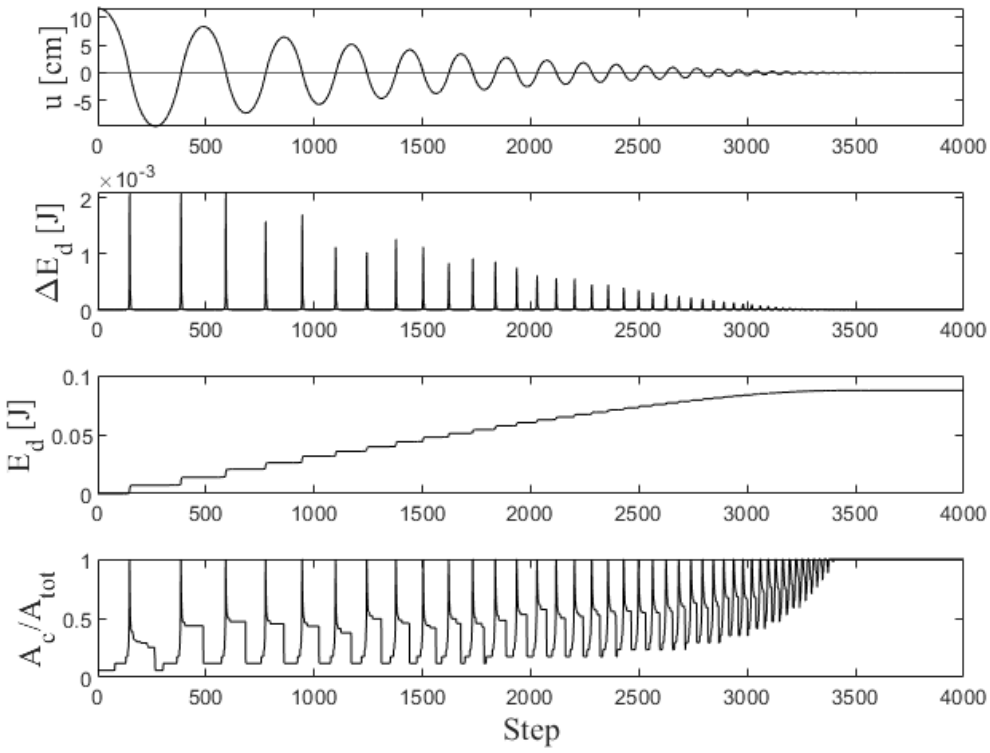

(c)

Figure 64 - Displacement time-history, increment of damping energy, total damping energy and compressive ratio vs step for: a) Specimen 1, b) Specimen 2, c) Specimen 3

As a further investigation, the accuracy of the proposed model is evaluated considering harmonic vibrations with reference to specimens 2 and 3 subjects to sinusoidal excitations with a frequency equal to 3.3 Hz and 5 Hz, amplitude equal to 6 mm and 5 mm, and a duration of 20 and 10 sec., respectively.

The responses predicted by the DMEM model are shown in Figure 65, compared to the FEM predictions obtained by Vlachakis et al. [122]. It can be observed that the DMEM model effectively replicates the experimental response in terms of period and peaks with adequate accuracy, both in the transient and stationary phases of the response.

Finally, the model sensitivity on the analysis' step size is investigated. Parametric free-vibration analyses are carried out, varying the step from the largest value of 0.005 s to the smallest value of 0.002 s. The results are reported in Figure 66 compared to the analytical solution of the classical theory.

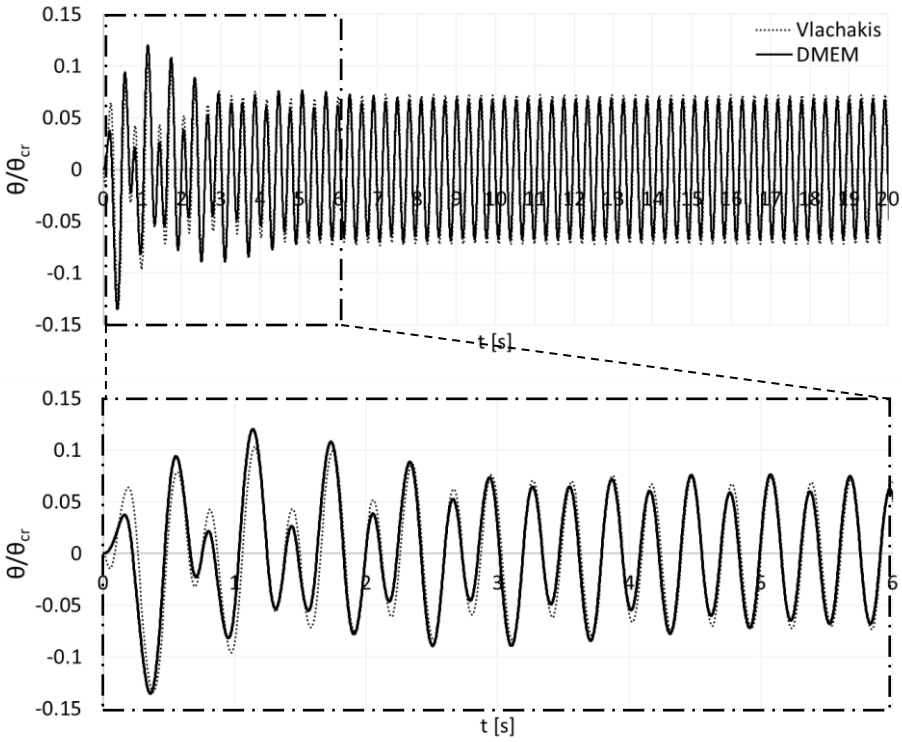

(a)

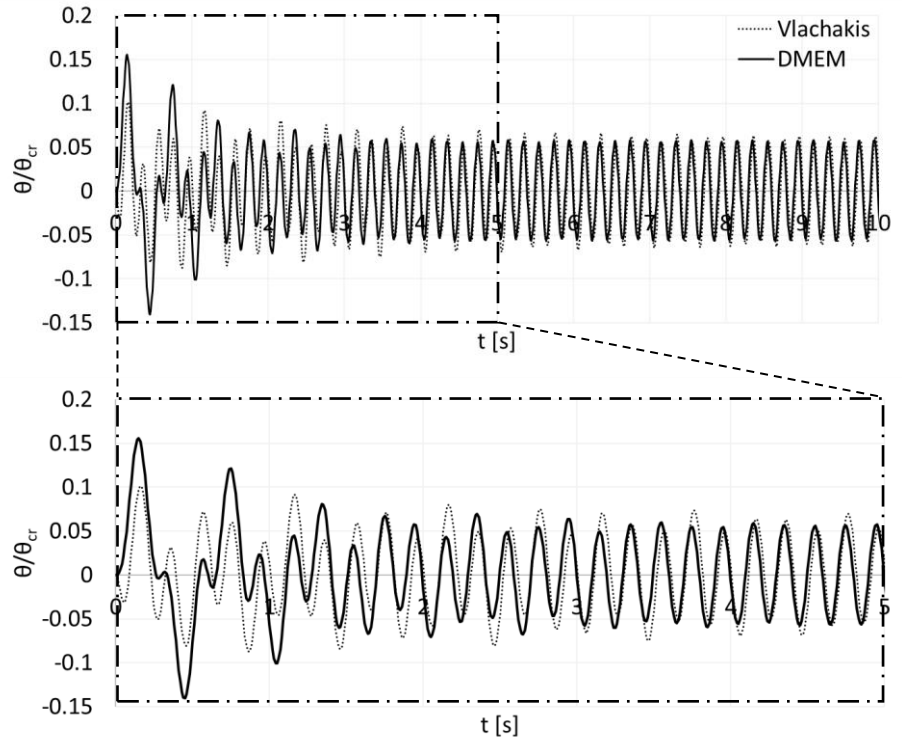

(b)

Figure 65 - Harmonic vibrations for a) Specimen 2 and b) Specimen 3

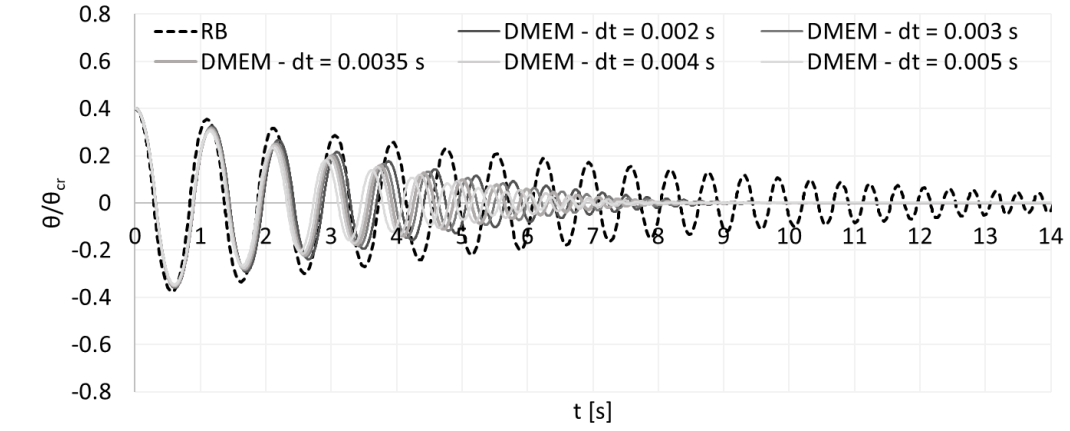

(a)

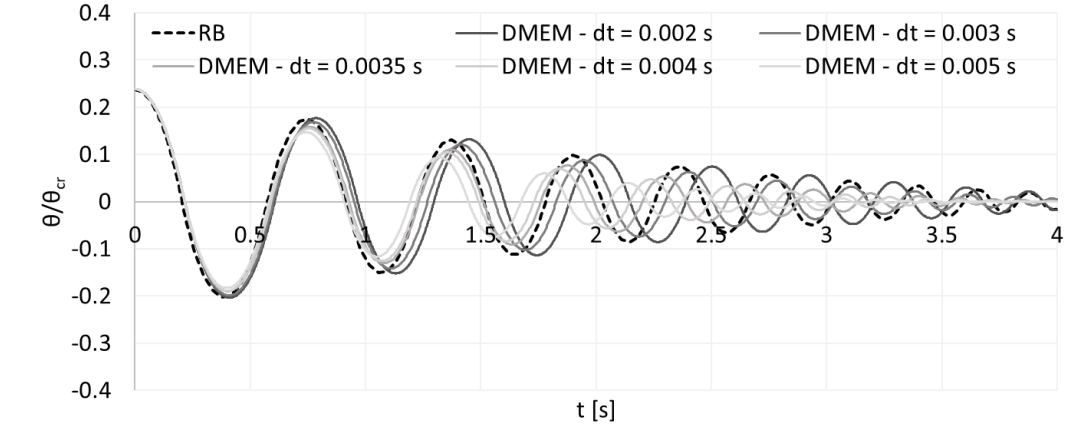

(b)

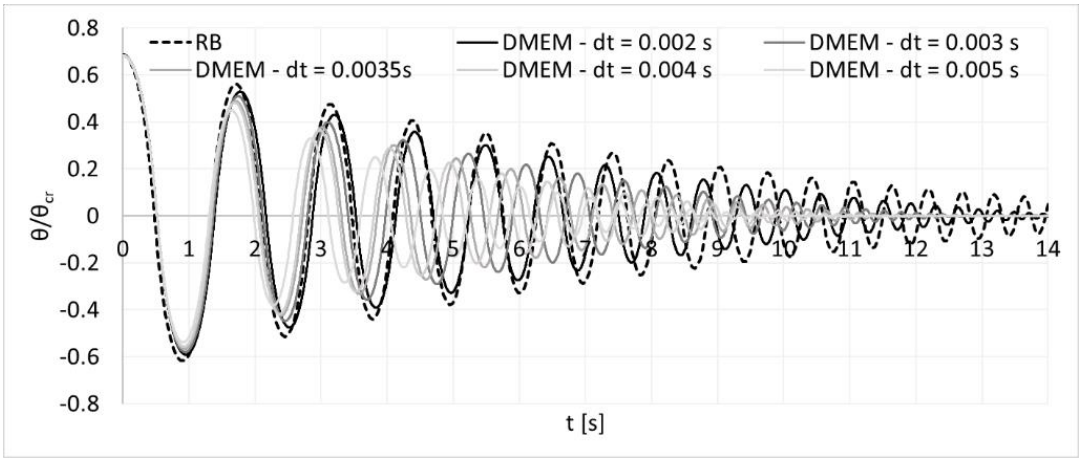

(c)

Figure 66 - Free rocking response varying the step size for: a) Specimen 1, b) Specimen 2 and c) Specimen 3

Figure 66 clearly shows that the slenderest specimen (Specimen 1) is less sensitive to the step size, while the smaller the slenderness, the greater the sensitivity to the analysis' step size. More simulations and applications are needed to better understand the sensitivity to the time step to detect which are the causes and what could be done to reduce this issue. Nevertheless, the error in the period can be justified by the simplified calibration of the damping coefficient, independent of the displacement amplitude. However, taking into account the first complete cycle of vibration, the error on the period made using the DMEM strategy, with respect to the rigid block solution, ranged from about 1% to 8%, as the time step ranged from about 1E-02 to 1E-04 the elastic period of the system, respectively.

As regard the computational time needed for the nonlinear dynamic analysis of the three PW benchmark studied before, the computation time was coincident in the case when the P-Delta effects were included or neglected.

7. DYNAMIC SIMULATION OF UNREINFORCED MASONRY STRUCTURES INCLUDING P-DELTA EFFECTS

In this section, the new P-Delta macro-element model is applied to the simulation OOP behavior of different URM structures. In order to investigate the influence of including P-Delta effects within a nonlinear numerical analysis, the latter are alternatively considered and neglected in order to show the capability of the model to reproduce the complex OOP behavior of a URM structure and the importance of considering the geometric nonlinearities, particularly for masonry monumental structures characterised by slender walls often badly connected to the orthogonal walls. In particular, two URM case studies investigating the OOP behaviour of the main façade of the San Michele Church in Lisciano and of the church of San Nicolò di Capodimonte are considered. For the first case study nonlinear dynamic analysis are carried out under both harmonic excitations and earthquake input motions. On the second case study, static nonlinear analysis are conducted considering two different models, namely a global model of the entire church and a simplified model in which the lateral orthogonal walls are modelled using a set of nonlinear links adequately calibrated accounting for the connections to the orthogonal walls. These analyses are conducted by varying the quality of connection with the lateral walls by means of a "bond coefficient" in order to investigate the influence of the boundary conditions when P-Delta effects are considered. In all the nonlinear dynamic analyses conducted on the first case study, a classic viscous Rayleigh damping was assumed.

7.1 The case study of the San Michele church in Lisciano

This section investigates the dynamic behavior of the façade of San Michele church located in Lisciano, central Italy, which exhibited an incipient out-of-plane failure mechanism during the 2016-2017 Central Italy earthquake swarm.

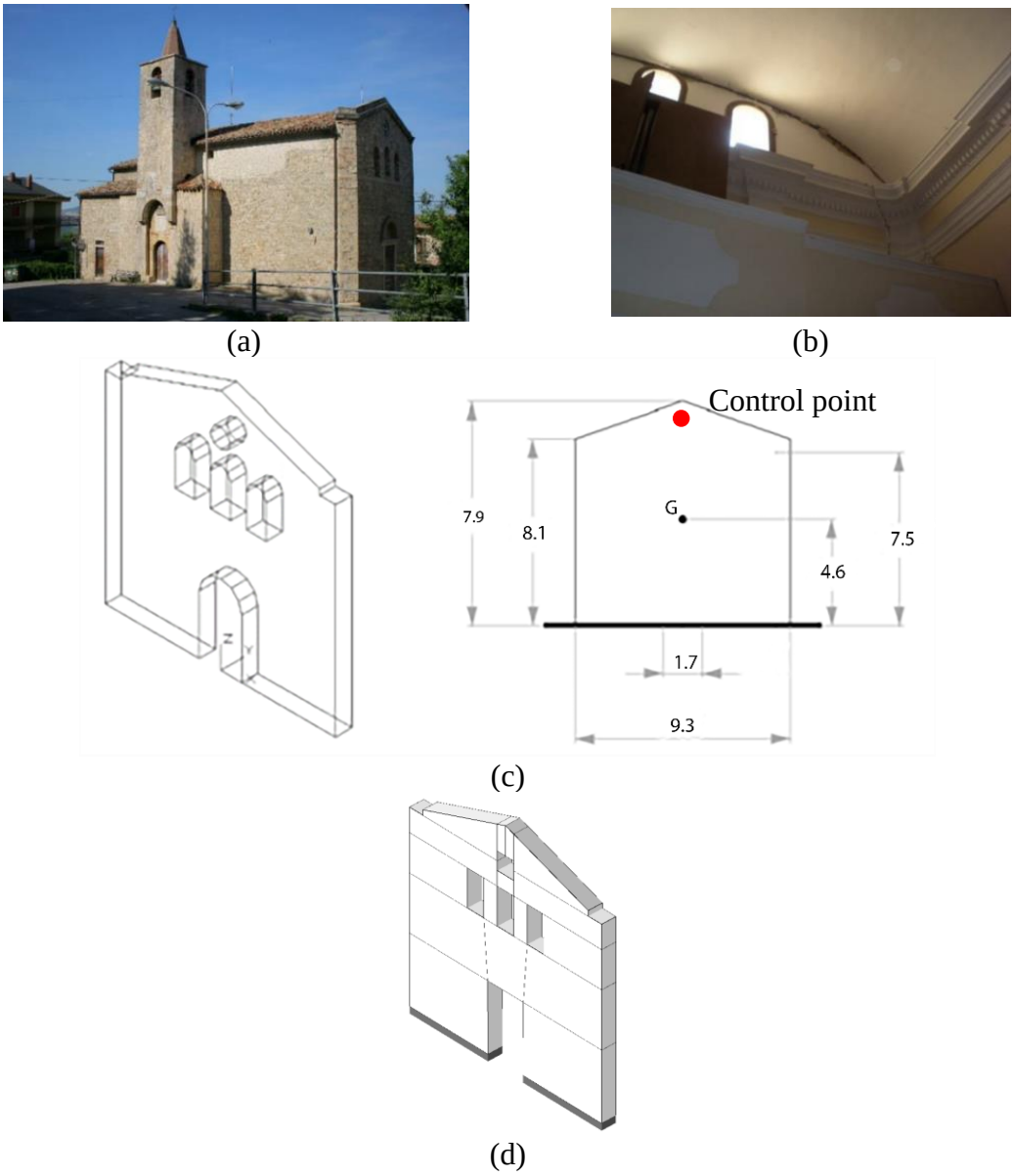

Figure 67 - San Michele church; (a) global view, (b) view from inside, (c) dimensions of the façade (in meters), (d) structural DMEM model

The church has already been investigated in the literature [172], [173]. It includes a single nave with a rectangular plan (10 m x 20 m) and an unsymmetric bell tower interacting with the main building (Figure 67a,b). The façade is 9.30 m wide, 0.65 m thick and 9.70 m high. Its slenderness ratio α is about 0.07, obtained as the arctangent of the ratio of half-thickness and the height of the center of mass (0.325 m/4.6 m) (Figure 67c). More details on the features of the church can be found in [172], [173]. In the following the , the free-standing condition of the façade is considered, representing a scenario in which the façade is fully separated from the rest of the church.The DMEM model of the church's façade is supposed to be elastic, being the nonlinearities concentrated only at the base interface, which is characterised by an elastic stiffness for a unit area equal to 5E+08 N/m^3, elastic behaviour in compression, and two alternative constitutive laws in tension: a no-tension material and an elastoplastic material with a tensile strength equal to 0.05 MPa. The structural model is made of 16 macro-elements for a total of 112 degrees of freedom. An image of the structural model is reported in Figure 67b.

The simulations are performed by applying harmonic and earthquake inputs to investigate the effects of different dynamic excitations on the façade's dynamic response and stability when P-Delta effects are considered.

7.1.1 Harmonic vibrations

A set of harmonic nonlinear dynamic analyses are carried out on the structural model applying a sinusoidal input in the direction orthogonal to the plane of the façade with increasing amplitude. In particular, 840 nonlinear dynamic analyses are carried out, considering two alternative constitutive laws in tension: a no-tension material and an elastoplastic material with a tensile strength equal to 0.05 MPa. Seven values of the amplitude (A [cm/s^2]) ranging from 10 cm/s^2 to 100 cm/s^2 and varying the frequency (ω [Hz]), for each amplitude, between 0.025 Hz and 3.0 Hz.

The analyses are conducted considering and neglecting the P-Delta effects aiming at evaluating their influence. Figure 68 shows the displacement response spectra of the harmonic response of the façade for all the considered amplitude values. In particular,

Figure 68a shows the results relative to the no-tension material, while Figure 68b shows those relative to σ_t = 0.05 MPa. It can be observed that the range of frequencies that causes the overturning of the façade, with the same amplitude, increases significantly when P-Delta effects are taken into account regardless of the tensile strength value considered. It is also evident that when the P-Delta effects produce a decrease in the value of the maximum amplification frequency.

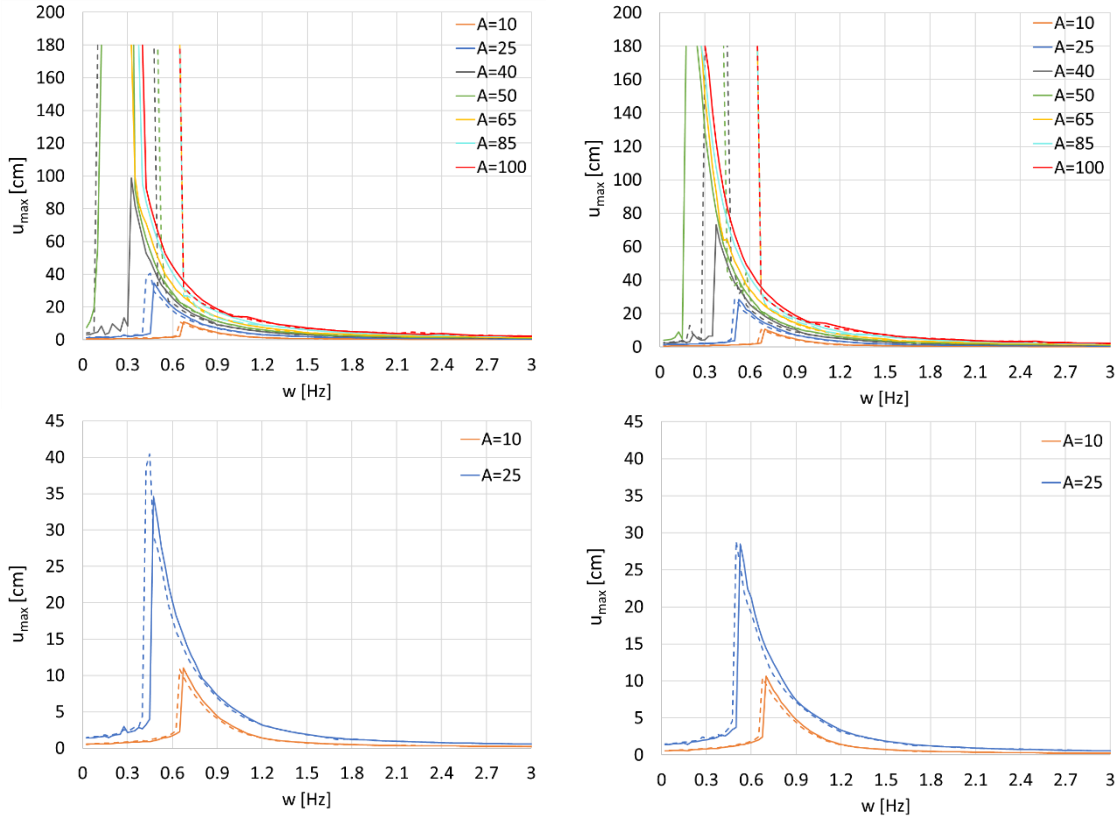

Figure 68 - Displacement response spectra of the facade subjected to harmonic oscillations: a) no-tension material, b) σ_t=0.05 MPa

Figure 69 shows the "un-safe" domain at each amplitude of the harmonic input. Namely the figure shown the range of the frequencies for which the block reaches the collapse for a specific value of the amplitude of the harmonic input. It is clear that the un-safe region is smaller when the P-Delta effects are neglected. Moreover, it can be observed that when P-Delta effects are taken into consideration the region corresponding to collapse has the same dimension regardless of the tensile strength value. In particular, the tensile

strength value has an influence only for the smallest amplitude value of the harmonic input that causes the collapse (40 cm/s^2) and, more in detail, for this amplitude value, the collapse occurs in the frequency range ranging from 0.1 to 0.5 Hz (Figure 69a) and from 0.3 to 0.5 Hz (Figure 69b) for the case of no-tension material and σ_t = 0.05 MPa respectively. Conversely, when the P-Delta effects are neglected, the overturning region is strongly dependent on the mechanical properties of the model. This is due to the fact that for large displacements, that occurs for larger value of the signal's amplitude, the geometrical nonlinearities govern the rocking seismic response, and the latter is almost independent on the mechanical parameters of the masonry material. Intermediate amplitude values should be considered to have a more accurate domain.

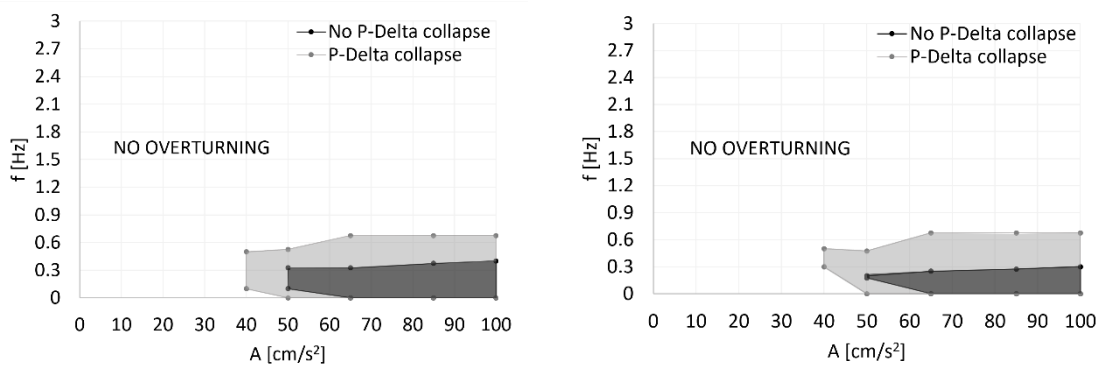

(a) (b)

Figure 69 - Capacity domain under harmonic oscillations: a) no-tension material, b) σ_t=0.05 MPa

7.1.2 Earthquake excitations

This sub-section reports the results of nonlinear time history analyses performed applying three registrations from 2016-2017 Central Italy earthquakes, which are characterized by high values of Peak Ground Acceleration (PGA), Peak Ground Velocity (PGV), and PGA/PGV ratio. The considered earthquakes and their parameters are reported in Table 8. Namely the most significant 20 seconds of Amatrice 2016 (AMT), Norcia 2016 (NOR) and a signal recorded in the T1213 station (T1213) 2016 have been considered. In

particular, AMT and T1213 have the highest PGA and PGV, while NOR has the highest PGV/PGA ratio. The relative accelerograms are reported in Figure 70.

	PGA [m/s2]	PGV [m/s]	PGV/PGV [s]
AMT	5.216	0.379	0.07
NOR	3.057	0.562	0.18
T1213	7.793	0.607	0.08

Table 8 – Intensity measures of selected seismic inputs

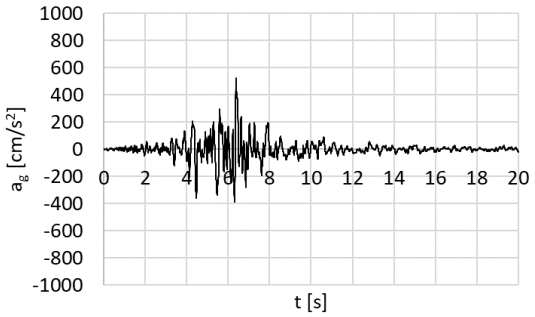

(a)

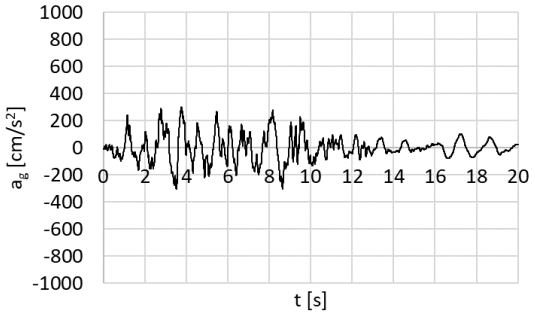

(b)

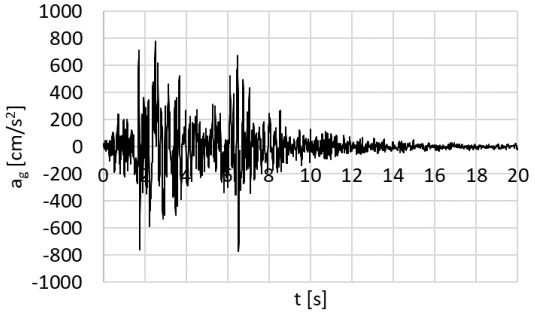

(c)

Figure 70 - Seismic records: a) AMT, b) NOR, c) T1213

For all the three seismic records, Incremental Dynamics Analyses (IDAs) are performed considering and neglecting P-Delta effects. The construction of the IDA curves involves performing a series of nonlinear dynamic analysis for each record by scaling it to multiple levels of intensity.

In this work, the displacement of the control point was defined as Engineering Demand Parameter (EDP), while the PGA and the PGV are alternatively selected as intensity measures (IMs).

The IDAs curves are built by scaling the signals by an scale factor (SF) ranging from 0.05, to 1.20. For each scaled accelerogram, the maximum value of the displacement of the control point is registered. The effects of the tensile strength of the rocking interface are studied using three different values of σ_t. Namely, a no-tension material, $\sigma_t = 0$ MPa, and two finite values, $\sigma_t = 0.05$ MPa and $\sigma_t = 0.1$ MPa, are considered being the latter a high value of tensile strength that can be considered as an upper limit.

The IDAs curves are reported in Figure 71 both in terms of PGA and PGV for all the seismic records. From Figure 71 it is evident that for small values of displacements, there are small differences between the curves obtained considering or neglecting the P-Delta effects. In particular, for AMT and T1213, which have the highest PGA and PGV, the curves with and without P-Delta effects have the same trend up to a displacement that is equal to half of the wall thickness (32.5 cm) approximately, instead for NOR, they have the same trend up to almost 80% of the wall thickness (52 cm). Moreover, from the same figure, it is also apparent that when the P-Delta effects are considered, the bearing capacity of the façade, both in terms of PGA and PGV, is less sensitive to the signal with respect to the analyses conducted neglecting them.

Finally, the same observation can be made for the influence of the tensile strength of the rocking interface, and this is because when the displacements are large, the geometric effects have a greater influence, also in the dynamic response, than the constitutive nonlinearities.

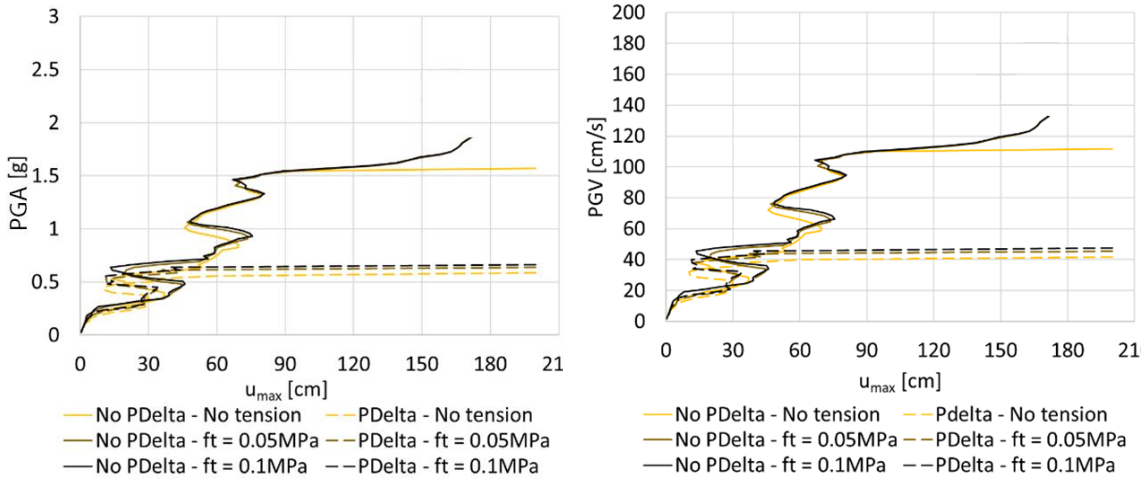

(a)

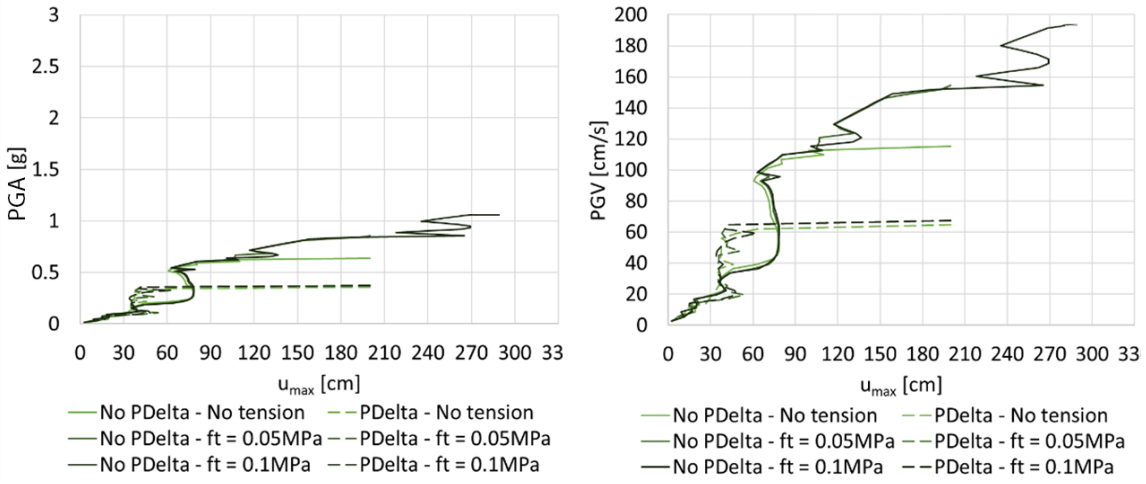

(b)

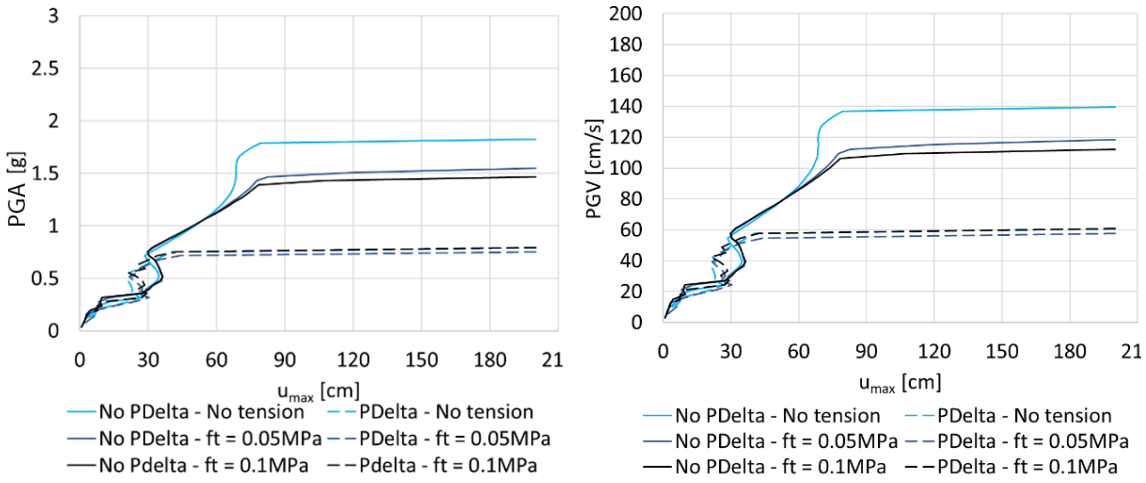

(c)

Figure 71 - IDAs curves obtained considering: a) AMT, b) NOR, c) T1213

7.2 The case study of San Nicolò di Capodimonte in Camogli

This section considers the Church of San Nicolò di Capodimonte (Camogli, Genova, Italy) as a case study, which has already been investigated in the literature by using different modelling approaches [164], [174]. A view of the Church and its geometrical representation are reported in *Figure 72*. The church is made of blocks representative of a typical ancient church characterized by a longitudinal plan, in the form of the Latin Cross with a long single nave of about 18 m, crossed by a transept 14 m large.

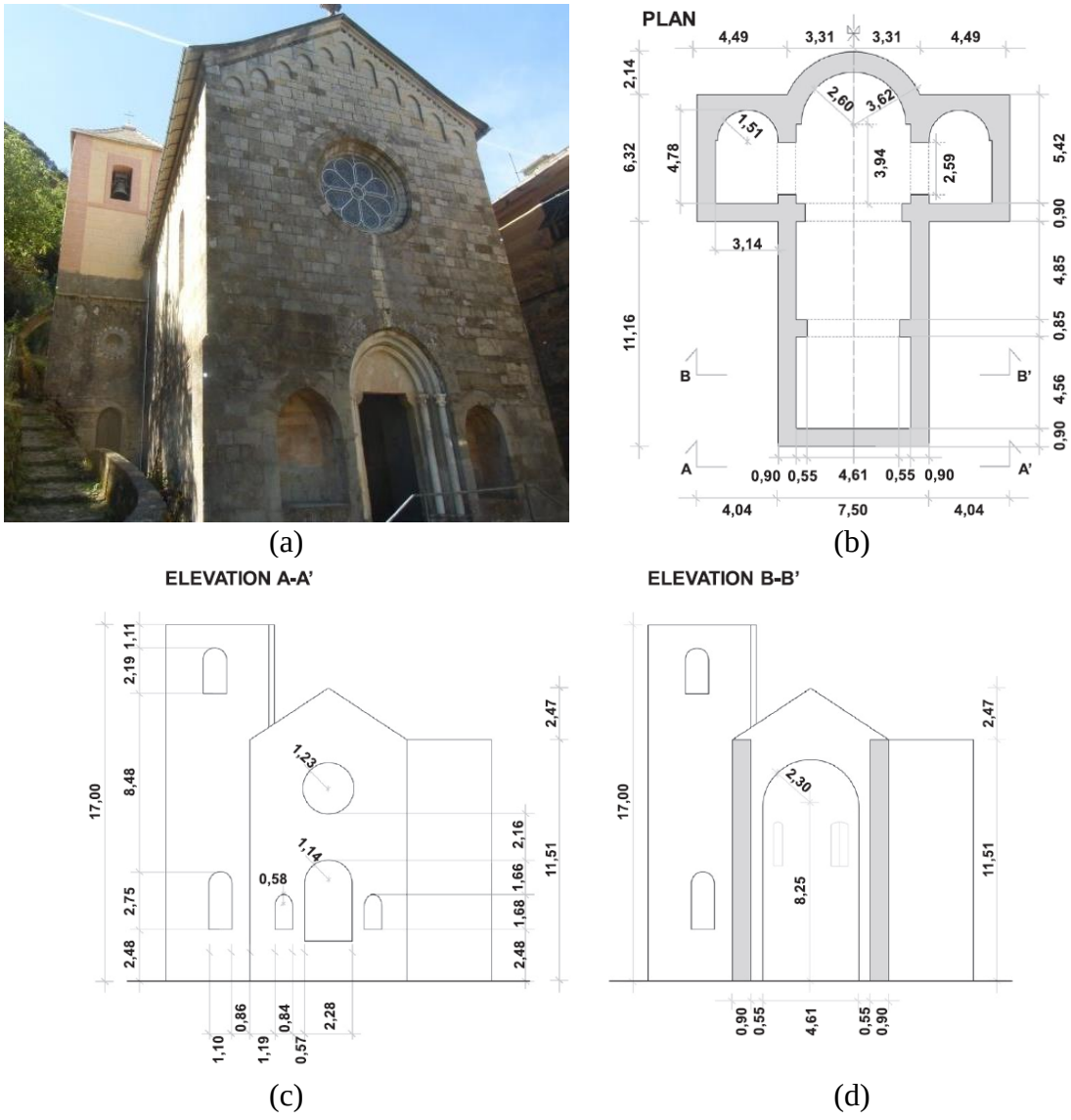

Figure 72 - a) San Nicolò di Capodimonte church, b) plan of the Church, c) elevation A-A', d) elevation B-B' (figure from [164]*)*

The construction also comprises a 17 m height bell tower and a 14 m height chapel located at the side of the transept. The contribution of the roof structure is not taken into consideration, according to Malena et al. (2019) [164] and Funari et al. (2021) [174].

The geometric model was generated in Autodesk using 2D (3D-face) elements and, for the curved parts of the church (i.e., the chapel, the bell tower, and the apse), 3D Polyfacemesh elements consistently with those reported in and in [164] and in [174].

7.2.1 The adopted structural models

Two models have been developed and used to perform nolinear static analyses, namely a 3D global model (DMEM-G) and a simplified model comprising only the façade (DMEM-F) are developed to perform the simulations.

The out-of-plane (OOP) behavior of masonry walls, especially for tall and slender walls such as church facades, is significantly influenced by boundary conditions, especially horizontal restraints due to orthogonal walls, timber beams, or tie-rods. For these reasons, there is a need to have global models capable of simulating the complex interactions between all the structural elements. Nevertheless, global models may be computationally expensive and time-consuming [175]. Therefore, simplified façade models that simulate the structural horizontal restrained through horizontal links have been introduced in the literature [113], [176], where “compressive” links simulate the impact between the façade and the lateral walls. In contrast, the stabilising effects of the horizontal links in tension is neglected in the models. Afterward, Casapulla et al. [177] introduced a horizontal distribution of orthogonal links to simulate the effect of lateral walls, possessing non-zero compression and tensile stiffnesses, so employed to perform incremental dynamic analyses. The latter strategy is employed in this study in the case of the model DMEM-F, in which the retaining walls are accounted for by equivalent non-linear links working in tension and compression with the same elastic stiffness, with nonlinear mechanical parameters evaluated considering a cohesive-friction strength criterion, describing the brick interlocking between the façade and the retaining walls, and considering the axial load due to the masonry self-weight [175].

The deformability properties, namely the Young's and shear modules, the compressive strength, and the self-weight, are chosen according to Italian standards [26] for natural-stone masonry. In addition, the tensile strength and cohesion are assumed to equal 0.01 MPa, to simulate a quasi-no-tension friction material consistently to [164], [174]. Finally, the tensile fracture energy is assumed to equal 0.001N/mm. The mechanical parameters of masonry adopted in the analyses are summarised in Table 9.

Young's modulus	Shear modulus	Compressive strength	Tensile strength	Tensile fracture energy	Cohesion	Friction coefficient
E [MPa]	G [MPa]	σ_c [MPa]	σ_t [MPa]	G_t [N/mm]	c [MPa]	μ [-]
1500	500	3.8	0.01	0.01	0.01	0.6

Table 9 - Mechanical masonry parameters.

The P-Delta effects are alternatively considered and neglected to evaluate their effects on the ultimate strength and displacement capacity of the façade. Once again, the two computational models have, been developed in the structural code HiStrA (Historical Structural Analysis) [61]. The displacement control analyses were conducted using the "Arc Length" method. The results are reported in terms of capacity curves and collapse mechanisms at the last step of the analysis. The global model (DMEM-G) includes vertical walls, the apse, the triumphal arches, the bell tower and the chapel, and it has been used a mesh size of about 70 cm per side, refined where deemed necessary, in particular in correspondence with the portion of the nave affected by the collapse mechanism identified by Malena et al. (2019) [164] and Funari et al. (2021) [174].

A simplified mesoscale modelling strategy is employed to take into account the effect of the blocks' interlocking: the vertical interfaces are modelled as not aligned in the macro-element scale. The mesh is automatically generated, maintaining the average shape ratio of units reported in [164]. In the models, the average in-plane dimensions of macro-elements are 1600mm x 800mm, while the actual dimensions of units can be assumed to be 800mm x 400mm. Therefore, each macro-element represents a masonry volume corresponding to about 2x2 units. Thus, the discrete model comprises of 1433 quad elements, 37 vertex and 3719 interfaces and , and 10235 degrees of freedom overall. Figure

73 shows 3D view of the DMEM-G model implemented in the software HiStrA.

On the other hand, the simplified model of the façade (DMEM-F), including only the façade and the discrete distribution of non-linear links accounting for the interaction with the lateral walls, comprises 141 macro-elements, 5 rigid elements, 34 non-linear links, and 318 interfaces with 1017 degrees of freedom, corresponding to approximately 10% of the DMEM-G's model. Figure 74 shows 3D view (Figure 74a) and the mechanical scheme (Figure 74b) of the simplified model (DMEM-F) of the façade.

For the distribution of nonlinear links an elasto-plastic constitutive law with a fixed ultimate displacement is considered. The elastic stiffness (K), both in tension and compression, is calculated assuming the yielding displacement equal to 1.5 mm and the ultimate force (F_u) equal to:

$$F_u = N \cdot \mu + c \cdot A \qquad 7.1$$

being *N* the axial force and *A* the transversal section of a single horizontal block-to-block interlocking surface. Finally, the ultimate displacement d_u is assumed to equal 50% of the average length of the stone blocks. The results of the nonlinear links calibration are summarised in Table 10. For the sake of simplicity, the value of *N* is evaluated considering the vertical loads and is kept constant during the pushover analysis.

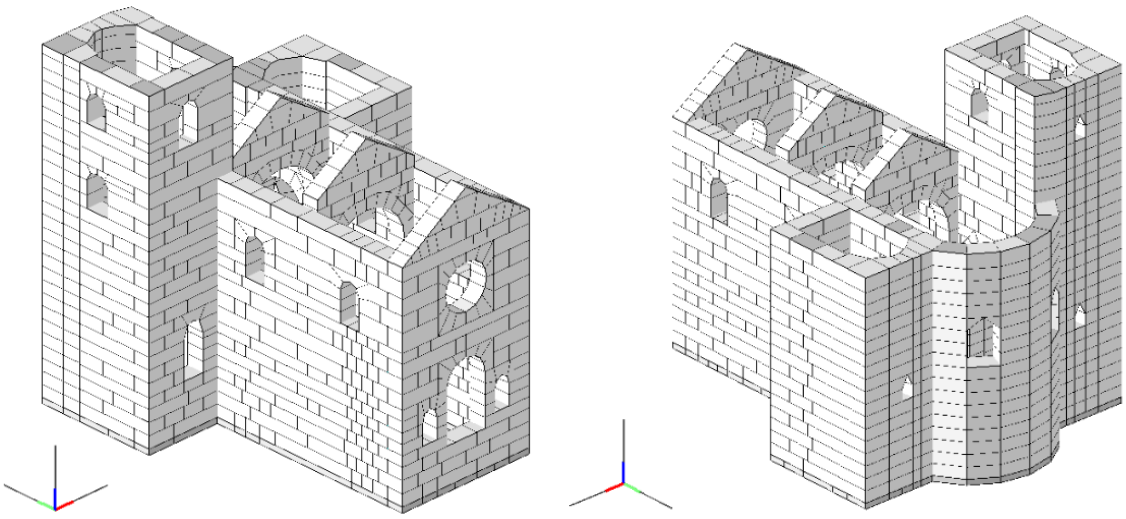

Figure 73 - 3D view of the DMEM-G model of the Church

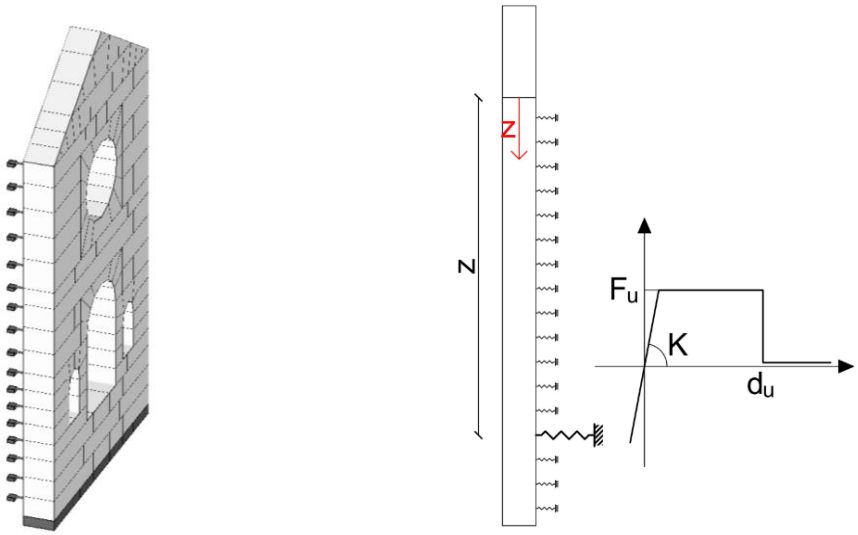

(a) (b)

Figure 74 - (a) Simplified model (DMEM-F) of the facade; (b) mechanical scheme

Quote of the link z [mm]	Tributary area Δz [mm]	Axial force N [kN]	Elastic stiffness K [kN/mm]	Ultimate force F_u [kN]	Ultimate displacement d_u [mm]
692	692	3.19	2.987	4.48	285
1505	813	6.94	4.489	6.73	285
2329	824	10.75	6.011	9.01	285
3148	819	14.53	7.523	11.28	285
4110	962	18.97	9.300	13.95	285
5365	522	21.38	10.264	15.39	285
4632	733	24.77	11.618	17.42	285
6108	743	28.20	12.990	19.48	285
6850	742	31.62	14.360	21.54	285
7398	548	34.15	15.372	23.05	285
7946	548	36.68	16.384	24.57	285
8494	548	39.21	17.3967	26.09	285
9042	548	41.74	18.408	27.61	285
9590	548	44.27	19.420	29.13	285
10228	638	47.22	20.599	30.89	285
10868	640	50.17	21.781	32.67	285
11508	640	53.13	22.962	34.44	285

Table 10 - Calibration of the lateral non-linear links according to Eq. 7.1

7.2.2 Nonlinear static analysis

In this section, the results of the nonlinear static analysis are reported both in terms of capacity curves and collapse mechanisms at the last step of the analysis, considering and neglecting the P-Delta effects.

Figure 75 shows the load multiplier vs. displacement curves for the global model and the facade models considering and neglecting the P-Delta effects. The difference between the two models is due to the different collapse mechanisms shown in Figure 76. In particular, the DMEM-F model, cannot describe the collapse mechanism involving portions of the orthogonal walls.

In order to investigate the differences between the global and simplified models, and the role of lateral walls on the response of the façade, a parameter α "bond coefficient", ranging from 0 to 1, and multiplying the strength and ductility capacity of the non-linear links that simulate the presence of lateral walls, is considered (the results reported in Figure 75 and Figure 76 can be seen associated with the value α=1). In the latter figure, the colour map shows the ratio between the maximum plastic deformation over the ultimate plastic deformation at the last step of the analyses for the two developed models.

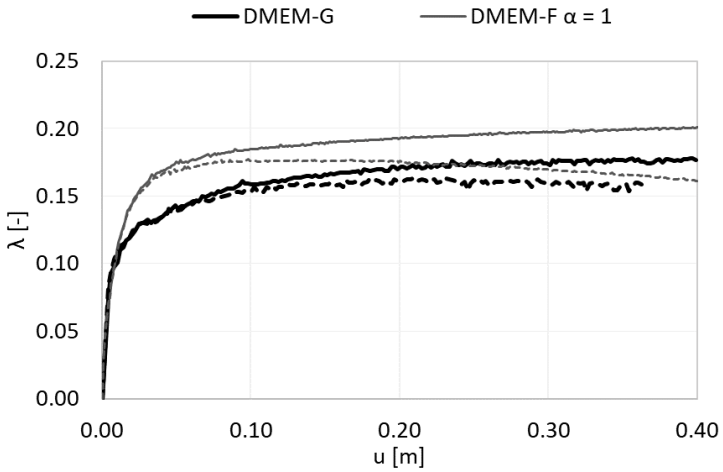

Figure 75 - Pushover curves considering (continue lines) and neglecting (dashed lines) P-Delta effects

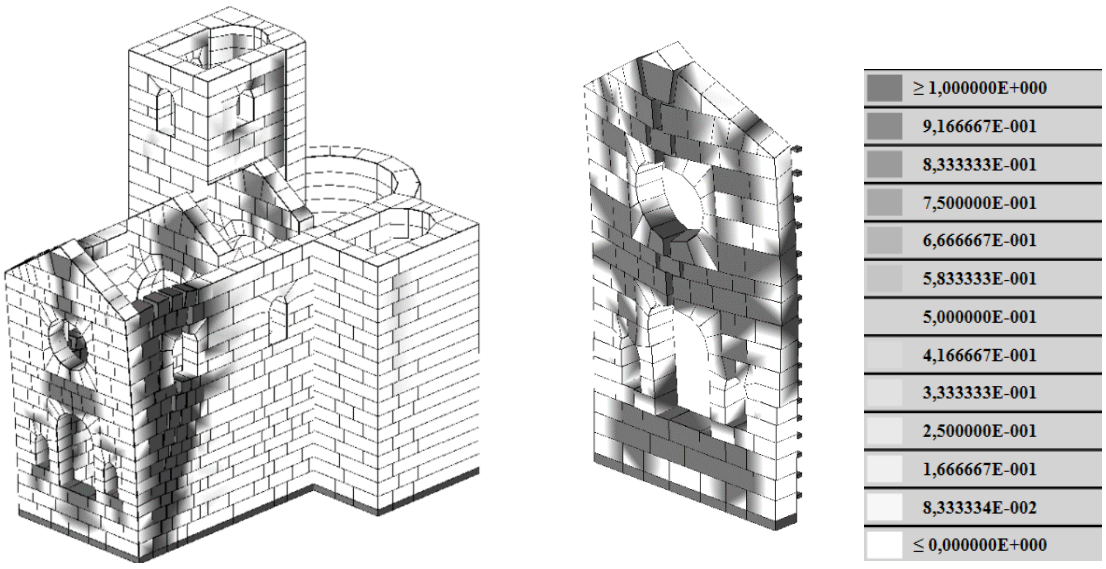

Figure 76 - Distributions of plastic deformations at the last step of the analysis for the a) DMEM-G model and b) DMEM-F model.

Figure 77 shows the pushover curves obtained varying the value of α. It is worth noting that for $\alpha \geq 0.5$ (Figure 78a and Figure 78b) the collapse mechanism does not involve the failure of the links, and the façade fails by activating a vertical central crack. Conversely, values of $\alpha < 0.5$ (Figure 78c) lead to the yield of a significant number of links, consistent with the damage observed in the lateral walls of the global model (Figure 76a) and a façade damage pattern similar to that observed in the façade of the DMEM-G model. These results may be justified by the fact that the global model allows for combined shear-flexural mechanisms involving the lateral walls due to the low axial load level. In contrast, the facade model considers a pure cohesive-friction mechanism.

Comparing the curves obtained by including and neglecting P-Delta effects, it can be noted that they start diverging at about 0.1m of displacement (9% of the wall thickness). After that level of displacement, the capacity curves of the analyses with P-Delta effects show a softening behaviour, while the analyses without P-Delta effects show a hardening response, leading to a significant overestimation of the load capacity of the system, with higher errors observed in the case of weak connections (low values of α).

Finally, Figure 79 shows the axial stresses of the normal nonlinear links. It can be observed that the highest links (with the smallest abscissa z) are those subject to the greatest deformations, reaching their limit of ductility capacity in the case of $\alpha < 0.5$, where the axial stress goes to zero (indicated with the white colour in Figure 79).

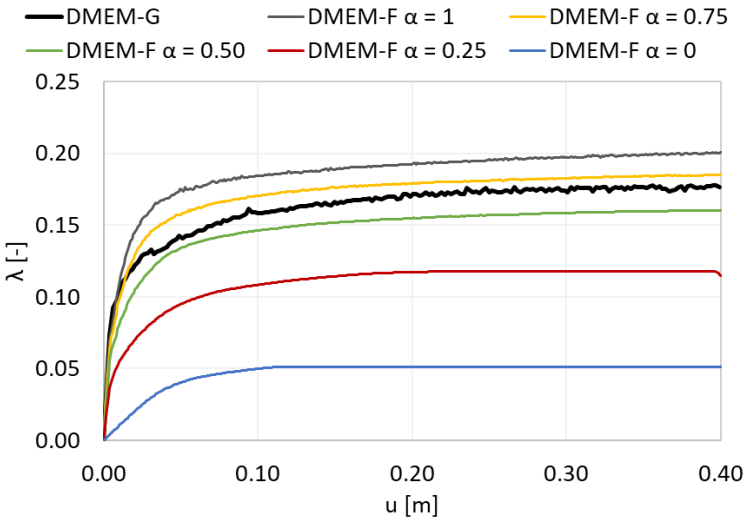

(a)

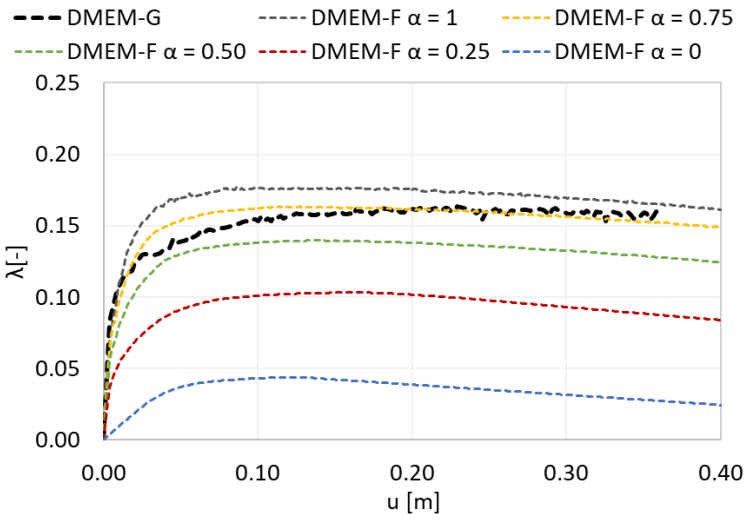

(b)

Figure 77 - Pushover curves for the DMEM-G model and the DMEM-F model varying the quality factor α: a) neglecting and b) considering P-Delta effects.

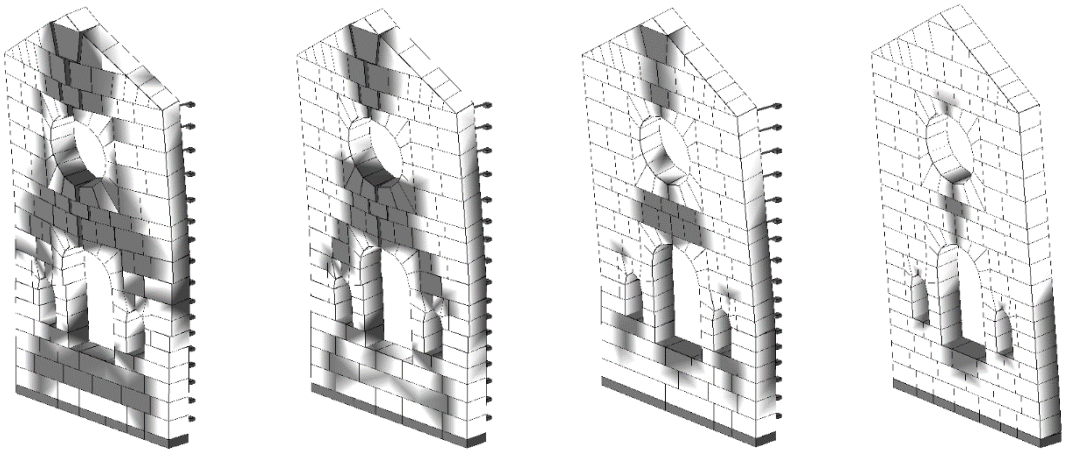

(a) (b) (c) (d)

Figure 78 - Collapse mechanisms of simplified models for a) α = 0.75; b) α = 0.50; c) α = 0.25; d) α = 0

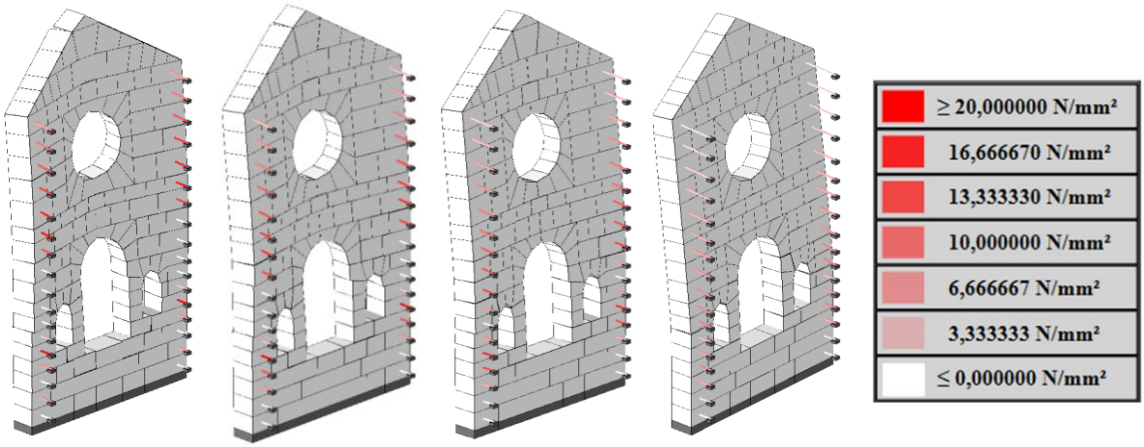

(a) (b) (c) (d)

Figure 79 - Stresses in the links of the simplified model for a) α = 1; b) α = 0.75; c) α = 0.50; d) α = 0.25.

Moreover, non-linear static analyses are carried out on DMEM-G model, considering a distribution of lateral loads proportional to the mass along two different loading directions: the transverse direction (x-axis) parallel to the transept and the longitudinal direction (y-axis) parallel to the nave.

The results are once again reported in terms of pushover curves and collapse mechanisms considering and neglecting P-Delta effects. In addition, the horizontal displacements of three control points are monitored, namely the point at the top of the façade and two at the top of the two lateral walls.

In order to investigate the overall nonlinear response of the structural, nonlinear dynamic analysis are carried out also in the transversal direction and in the slanting direction (Figure 80). Moreover, the horizontal displacement of three different control points is monitored during the analysis for all the five load directions. The control points are located at the top of the main façade (PT1 - Figure 80) and at the top of the two transversal walls (PT2 and PT3 - Figure 80) in order to fully describe the response of the church when an OOP collapse mechanism which involves the main façade is activated.

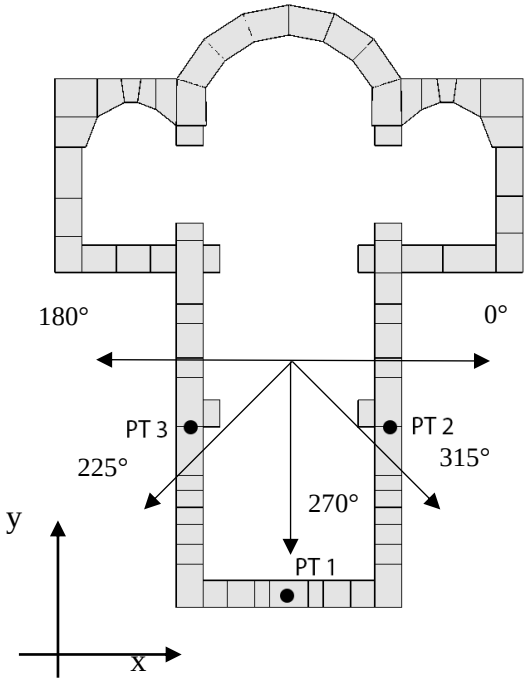

Figure 80 - Load directions and control points of static nonlinear analysis

Again, the results are reported in terms of both capacity curves and collapse mechanisms obtained considering and neglecting P-Delta effects respectively for each of the considered directions. In the capacity curves are reported both the results obtained

considering (continue line) and neglecting (dashed line) P-Delta effects. The reported collapse mechanisms are related to the last step of each analysis.

From the capacity curves it is evident that not considering P-Delta leads to an overestimation of the bearing capacity of the structure in all the considered directions. In particular, at the last step of the analysis the capacity of the structure in terms of strength decreased by about 35% and 13% for the +x (0°) (Figure 81) and -x (180°) (Figure 82) direction respectively. At the last step of the analysis, the bearing capacity is reduced by 13% also with reference to the longitudinal directions (270°) (Figure 84). While for the two oblique directions (225° and 315°) the reduction of the bearing capacity is lower (Figure 83 and Figure 85). It is worth noting that the difference between the curves obtained considering and neglecting P-Delta effects begin to be evident starting from 10 cm of displacement of the control points. As regard the collapse mechanisms there are no obvious differences when delta effects are considered. In particular, DMEM strategy predicts a collapse mechanism that essentially involves in-plane failures in the main façade and in the triumphal arches, parallel to the main façade when a transversal load direction is considered (Figure 81 and Figure 82). Diagonal cracks are observed in the façade between the openings and in the lower part of the chapel, while the longitudinal walls parallel to y-z plane remain almost undamaged. On the other hand, when a longitudinal load direction is considered, the models predict the overturning of the main façade and a portion of the sidewalls where a diagonal crack open starting from the openings (Figure 84). As imaginable, an intermediate mechanism between those activated for the transversal and longitudinal directions is activated for the oblique directions (Figure 83 and Figure 85).

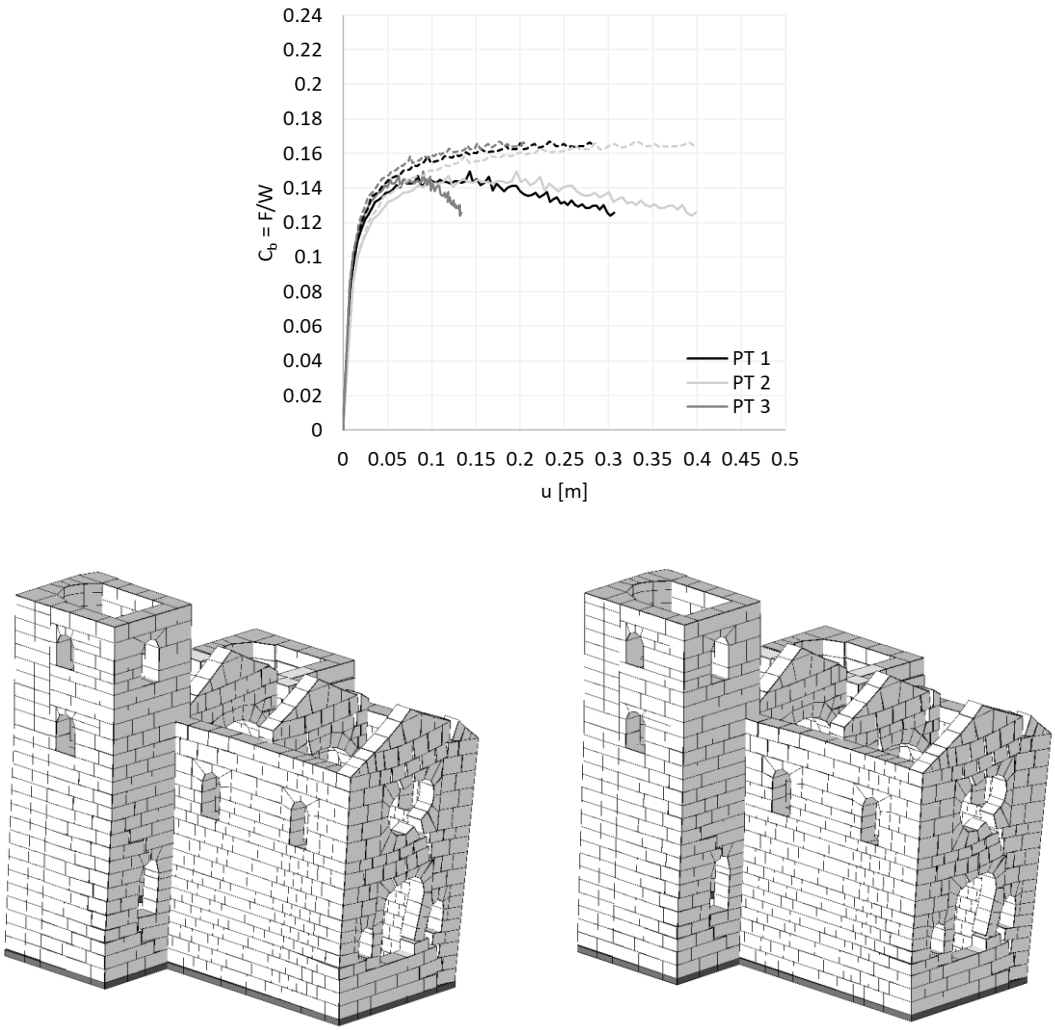

Figure 81 - Pushover curves and collapse mechanisms - 0° direction

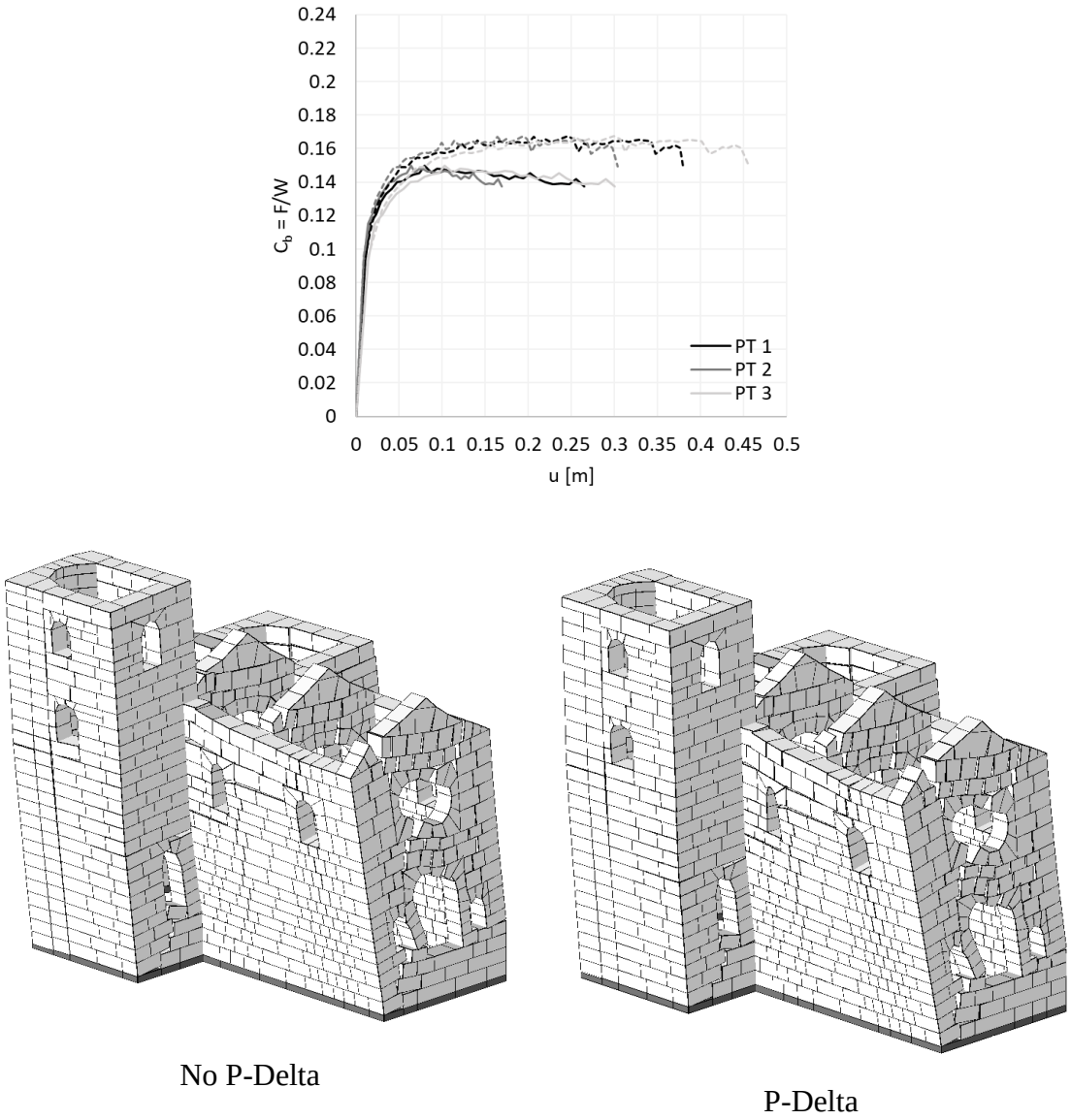

Figure 82 - Pushover curves and collapse mechanisms – 180° direction

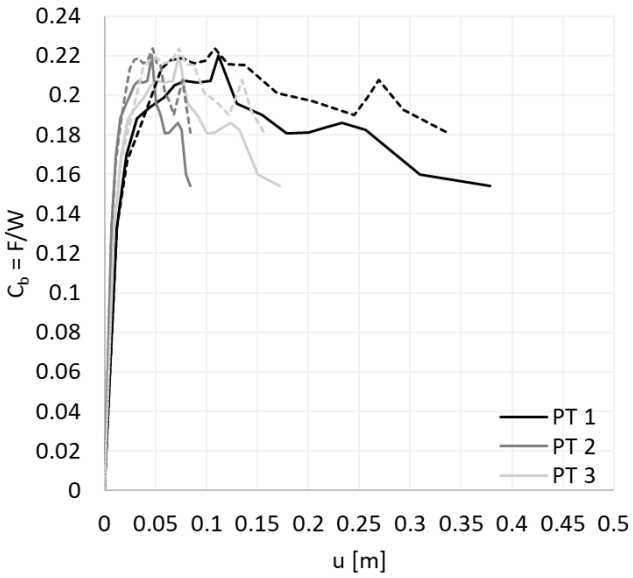

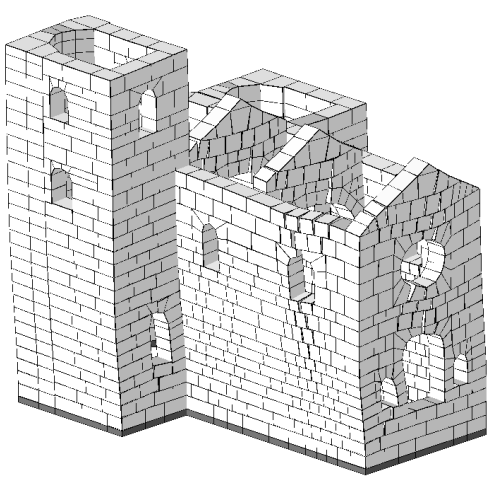

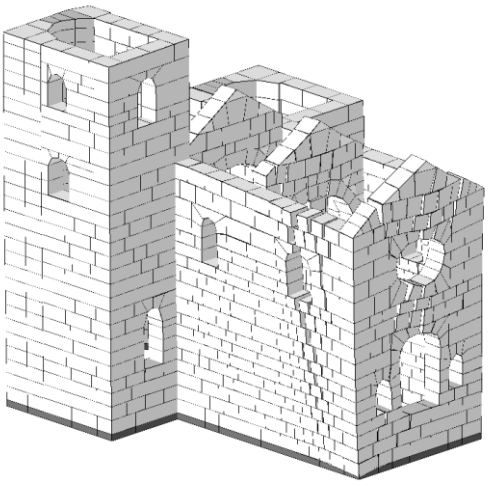

No P-Delta P-Delta

Figure 83 - Pushover curves and collapse mechanisms - 225° direction

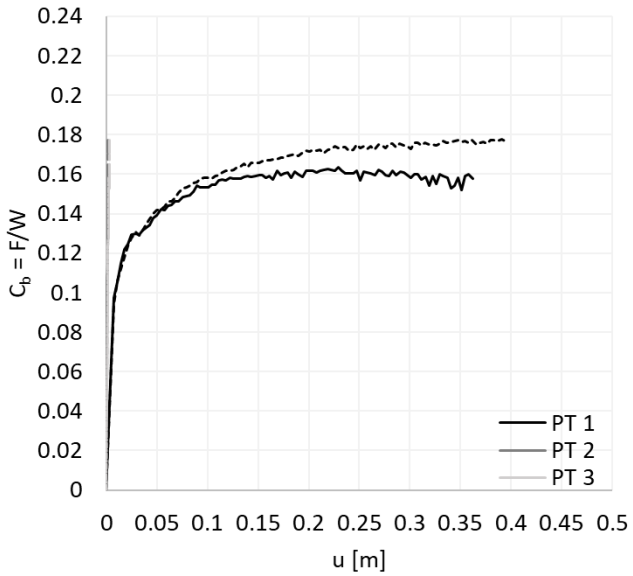

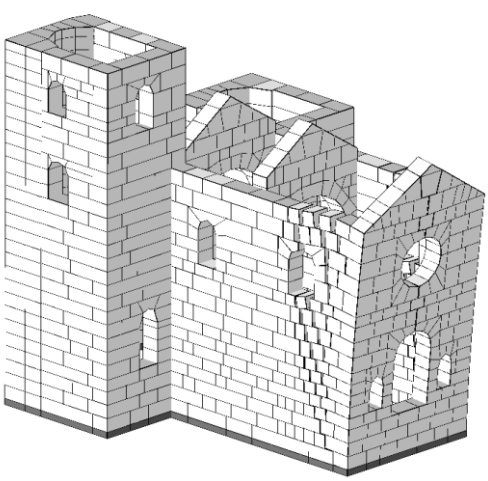

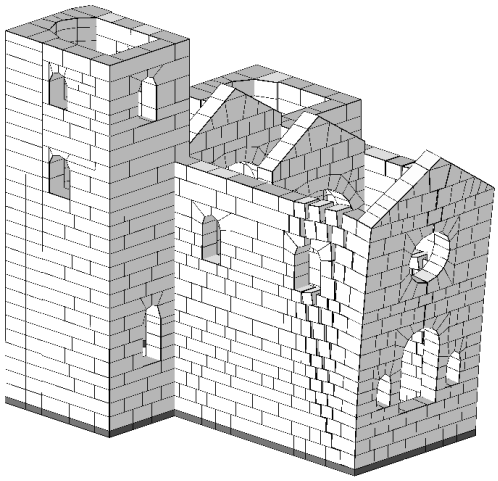

No P-Delta P-Delta

Figure 84 - Pushover curves and collapse mechanisms - 270° direction

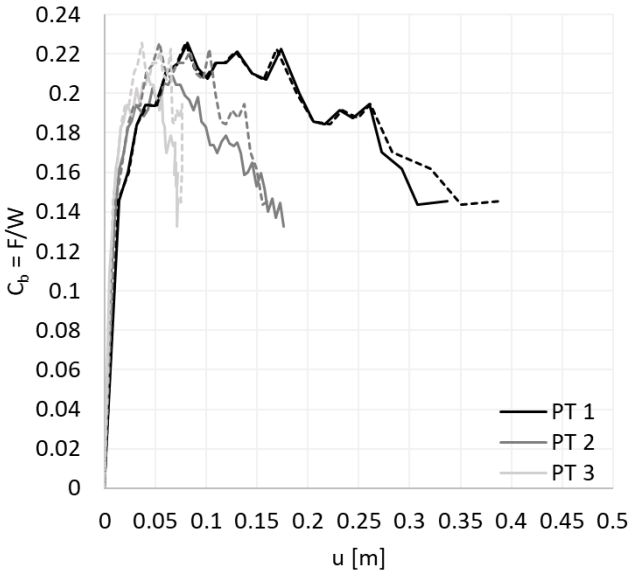

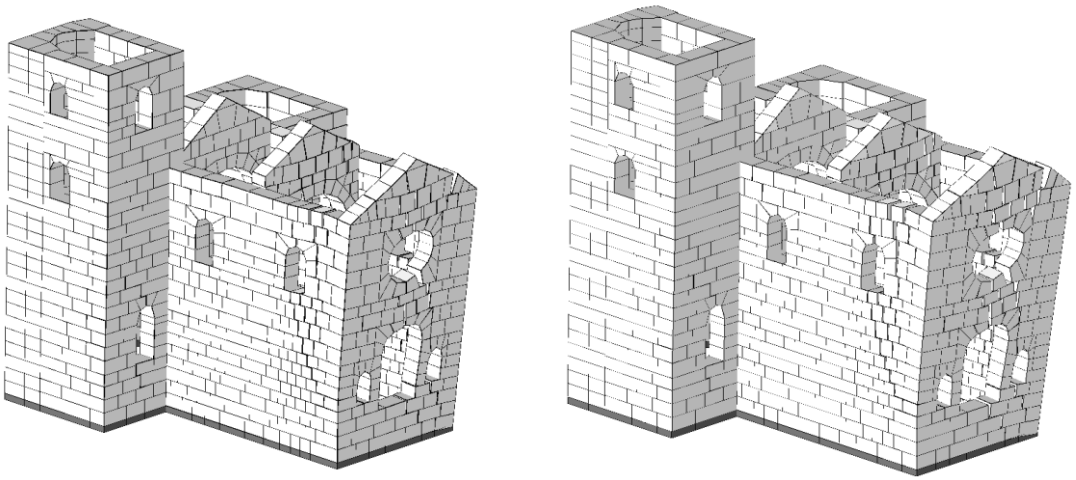

No P-Delta P-Delta

Figure 85 - Pushover curves and collapse mechanisms - 315° direction

8. CONCLUSIONS

This work aims to assess the out-of-plane (OOP) seismic behavior of URM structures when they are subjected to seismi loading. Response of unreinforced masonry walls to out-of-plane actions is one of the most complex, yet inadequately addressed, themes in seismic analysis.

Contemporary seismic codes for design of new masonry buildings provide dimensioning and detailing rules that make out-of-plane failure almost improbable even under severe seismic load. In contrast, out-of-plane collapse is a recurring mechanism in existing URM buildings: when the connections between walls or, more in general, between vertical and horizontal structural elements do not guarantee a box-type behavior (as most of the historic structures), the out-of-plane mechanism represents the main source of severe structural damage and collapse.

Observations after strong earthquakes shows that OOPfailures of unreinforced masonry (URM) buildings constitutes the most serious life-safety hazard for this type of construction. Additionally, even if connections to floors and transverse walls are effective, OOP failures can occur in slender walls, parapets, long unrestrained top spandrels. As consequence several types of OOP mechanism can be activate.

The seismic response of walls undergoing OOP rocking motions is rather complex due to the discontinuous and non-homogeneous nature of masonry, the high nonlinear constitutive behavior and the interaction with the remainder of the building. Moreover, the wall response is mainly related to geometric stability rather than to the strength of materials. For this reason, in the assessment of the out-of-plane behavior of URM structure geometric nonlinearities play a fundamental role, making the seismic behavior even more complex.

This work presents a further development of the Discrete Macro-Element Method (DMEM) model by including an effective way for accounting the geometric nonlinearities of the vertical applied loads, P-delta effects. These effects are particularly significant when

failure mechanisms associated to the out-of-plane behavior and, in particular, to the rocking of masonry walls occur, typical of unreinforced masonry (URM) buildings and structures. A simplified, but robust, P-Delta formulation is presented and implemented within a standard iterative Newton-Raphson method in the HiStrA software which implements the DMEM numerical approach. DMEM has the great advantage of being very simple, thanks to its mechanical scheme and the straightforward fiber calibration of its interfaces, but, at the same time, very accurate and computational inexpensive if compared to the classical FEM and DEM strategies usually used for the assessment of the OOP behavior.

The proposed P-Delta formulation does not require assembling and updating the geometrical matrix of the system, conversely, the geometrical nonlinearities are addressed during the analyses by updating the global load vector according to the macro-elements' current configurations. Specifically, according to the proposed strategy, the equilibrium is imposed considering the system's undeformed configuration, while the global load vector is computed at each step of the analysis according to the current position of loads. As a result, the proposed model does not require a significant increase of the computational cost compared to DMEM models not accounting for the P-Delta effects.

The proposed model is validated, in the static field, against analytical, numerical and experimental results demonstrating its capacity to describe the mechanical and geometrical nonlinearities characterizing the response of masonry walls subjected to different boundary conditions. The results show the accuracy of the proposed model, which was able to describe the pre-peak and post-peak response as well as the ultimate lateral strength and the displacement capacity of masonry walls exhibiting common OOP rocking mechanisms. Namely, cantilever and vertical spanning mechanisms for different geometrical layouts, loading and boundary conditions confirmed the model's potential to be employed for real structural assessments of masonry structures whose nonlinear response is characterized by the activation of rocking failure mechanisms. Parametric analyses have been conducted to investigate the role of i) modelling parameters, like the mesh discretization and the interface link discretization; (ii) masonry deformability; iii) axial compression loads, iv) mechanical parameters like tensile strength and fracture energy.

The P-Delta formulation is extended in the dynamic field and validated against analytical prevision on the period of vibration of the rigid block proposed by Housner (1963). The results of numerical simulations confirm the importance of considering geometric nonlinearities when masonry walls experience OOP mechanisms.

Additionally, to compare results with numerical and experimental simulations, a local damping model is introduced in order to simulate the loss of energy related to the impacts typically of the rigid blocks' dynamic. A viscous damping model proportional to the local stiffness matrix of the rocking interface is adopted able to reproduce the rigid block dynamic. The viscous damping ratio is calibrated according to an empirical ξ-e relationship recently proposed in literature by Vlachakis et al. (2021). The model predictions are compared to those obtained by analytical solutions and FEM models obtained by Vlachakis. The comparisons show the capability of the model to effectively dissipates the energy when impacts occur.

Finally, different case studies are considered. Firstly, church façade has been subjected to dynamic loads in order to study the influence of considering the P-Delta effects in a structural model of masonry buildings. In particular, harmonic and earthquake dynamic nonlinear analyses have been conducted. More specifically, a set of nonlinear analyses considering a sinusoidal signal with seven values of the amplitude and varying the load frequency, for each amplitude, between 0.025 Hz and 3.0 Hz, have been considered. The analyses were conducted considering and neglecting the P-Delta effects, respectively and they confirmed that the collapse region is larger, both in terms of displacement and amplitude, when the P-Delta effects are taken into account. Incremental dynamic analyses were conducted considering three different seismic inputs characterized by different magnitude levels. This latter analysis pointed out the lower sensitivity to signal and mechanical parameters of the model when P-Delta effects are considered.

A second case study was investigated in order to investigate the stabilising contribution of retaining walls when P-Delta effects are considered. With reference to the case study of the San Nicolò di Capodimonte Church (Italy), two different models are developed, namely a 3D model of the entire church accounting for the unit interlocking between the façade and retaining walls, and a simplified model of the façade in which a

discrete distribution of non-linear links with an ad-hoc calibration accounts for the contribution of the retaining walls. Both models are analysed through pushover analyses performed along with the direction orthogonal to the façade to i) assess the role of lateral walls; ii) validate the simplified model of the façade; iii) assess the role of P-Delta effects on the façade response. With these aims, the analyses are performed considering and neglecting the P-Delta effects and considering different strength and ductility values for the facade-to-lateral-wall connections. For the investigated case study, the P-Delta effects become significant at a level of displacement magnitude of the control point of the façade approximately of 10% of the masonry thickness, with larger discrepancies between the two models observed in the presence of weaker connections.

These results confirm that neglecting the P-Delta effects may lead to significant errors in the ultimate limit checks, for which the displacement threshold mentioned above is easily reached or passed by the seismic demand. The comparisons between the global model and the simplified one show a reasonable accuracy of the simplified model, with the introduction of a bond coefficient, requiring a significantly lower computational effort, so confirming its applicability for assessing large facades.

Overall, the presented results demonstrate the importance of including geometric nonlinearities in assessing masonry walls subjected to seismic rocking motion and confirm the accuracy of the proposed model, which can provide good predictions of the ultimate behavior of rocking walls to large lateral displacements, maintain the advantage of the DMEM strategy consisting in limiting the computational effort.

8.1 Future developments

Despite the results presented in this work are particularly interesting in the study of the out-of-plane behavior of masonry structures providing additional insight regarding the assessment of the seismic behavior of masonry structures characterised by predominant out-of-plane failure mechanisms. Nevertheless, several aspects still need to be investigated due to the complexity of this behavior; therefore, further investigations should be

conducted, performing nonlinear static and dynamic simulations on more complex 3D rocking scenarios relative to free-standing objects. Moreover, the effects of other mechanical parameters characterising the behavior of masonry constructions will be investigated, such as the deformability and the compressive strength of the blocks, also investigating the influence of the wall slenderness and “scale-effects”.

Future developments and further calibrations are needed to extend the damping model localised at the interface to describe the energy dissipation in multi-block rocking systems. Such a development will allow DMEM to properly simulate energy dissipation concentrated at mortar joints or newly retrofitting strategies for enhancing the performance of masonry structures by using dissipative joints [178].

Finally, future developments will investigate more real case studies in static and dynamic fields. Moreover, probabilistic assessments on complex monumental structures will be carried out by constructing fragility curves, both considering and neglecting P-Delta effects.

REFERENCES

[1] Dizhur D., Ismail N., Knox C., L. R., and Ingham J. M., "Performance of unreinforced and retrofitted masonry buildings during the 2010 darfield earthquake," *Bull. New Zeal. Soc. Earthq. Eng.*, vol. 43, no. 4, pp. 321–339, 2010.

[2] Dizhur D. *et al.*, "Performance of masonry buildings and churches in the 22 February 2011 Christchurch earthquake," *Bull. New Zeal. Soc. Earthq. Eng.*, vol. 44, no. 4, pp. 279–296, 2011.

[3] Ingham J. M. and Griffith M. C., "Performance of unreinforced masonry buildings during the 2010 darfi eld (Christchurch, NZ) earthquake," *Aust. J. Struct. Eng.*, vol. 11, no. 3, pp. 207–224, 2011.

[4] D'Ayala D. and Paganoni S., "Assessment and analysis of damage in L'Aquila historic city centre after 6th April 2009," *Bull. Earthq. Eng.*, vol. 9, no. 1, pp. 81–104, 2011.

[5] Kaplan H., Bilgin H., Yilmaz S., Binici H., and Öztas A., "Structural damages of L'Aquila (Italy) earthquake," *Nat. Hazards Earth Syst. Sci.*, vol. 10, no. 3, pp. 499–507, 2010.

[6] Romão X. *et al.*, "Field observations and interpretation of the structural performance of constructions after the 11 May 2011 Lorca earthquake," *Eng. Fail. Anal.*, vol. 34, pp. 670–692, 2013.

[7] Hilsdorf H. K., "Investigation into the Failure Mechanism of Brick Masonry Loaded in Axial Compression," *Des. Eng. Constr. with Mason. Prod.*, pp. 34–41, 1969.

[8] Lourenço P. B., Rots J. G., and Blaauwendraad J., "Continuum Model for Masonry: Parameter Estimation and Validation," *J. Struct. Eng.*, vol. 124, no. 6, pp. 642–652, 1998.

[9] Asteris P. G. *et al.*, "Seismic vulnerability assessment of historical masonry structural systems," *Eng. Struct.*, vol. 62–63, pp. 118–134, 2014.

[10] Angelillo M., Lourenço P. B., and Milani G., “Masonry behavior and modelling,” in *Mechanics of Masonry Structures*, 2014. doi: 10.1007/978-3-7091-1774-3.

[11] B. Ghiassi and G. Milani, *Numerical modeling of masonry and historical structures. From Theory to application*, 1st ed. Woodhead Publishing, 2019.

[12] Vlachakis G., Vlachaki E., and Lourenço P. B., “Learning from failure: Damage and failure of masonry structures, after the 2017 Lesvos earthquake (Greece),” *Eng. Fail. Anal.*, vol. 117, p. 104803, Nov. 2020.

[13] Lagomarsino S., “Seismic assessment of rocking masonry structures,” *Bull. Earthq. Eng.*, vol. 13, no. 1, pp. 97–128, 2015.

[14] N. A. Pino, D. Giardini, and E. Boschi, “Italy , earthquake ’ Waveform modeling of regional seismograms,” *J. Geophys. Res.*, vol. 105, no. B11, pp. 25,473-25,492, 2000.

[15] G. Valensise and D. Pantosti, “A 125 Kyr-long geological record of seismic source repeatability: the Messina Straits (southern Italy) and the 1908 earthquake (Ms 7/2),” *Terra Nov.*, 1992.

[16] Pantò B. and Caliò I., “Numerical modeling for the seismic assessment of masonry structures,” in *Seismic Vulnerability Assessment of Civil Engineering Structures at Multiple Scales: From Single Buildings to Large-Scale Assessment*, no. January, 2021, pp. 85–126.

[17] Pantò B. and Caliò I., “Numerical modeling for the seismic assessment of masonry structures,” *Civ. Struct. Eng.*, pp. 85–126, 2022.

[18] Milani G. and Tralli A., “Out-of-plane large displacement analysis of unreinforced masonry façades,” in *XX Congresso AIMETA Associazione Italiana di MEccanica Teorica e Applicata.*, 2011.

[19] Vanin F., Penna A., and Beyer K., “A three-dimensional macroelement for modelling the in-plane and out-of-plane response of masonry walls,” *Earthq. Eng. Struct. Dyn.*, vol. 49, no. 14, pp. 1365–1387, 2020.

[20] Bracchi S., Galasco A., and Penna A., "A novel macroelement model for the nonlinear analysis of masonry buildings. Part 1: Axial and flexural behavior," *Earthq. Eng. Struct. Dyn.*, vol. 50, no. 8, pp. 2233–2252, 2021.

[21] Giuffré A., "A mechanical model for statics and dynamics of historical masonry buildings," *Engineering*, pp. 71–152, 1996.

[22] Casapulla C., Cascini L., Portioli F., and Landolfo R., "3D macro and micro-block models for limit analysis of out-of-plane loaded masonry walls with non-associative Coulomb friction," *Meccanica*, vol. 49, pp. 1653–1678, 2014.

[23] Casapulla C., Giresini L., and Lourenço P. B., "Rocking and kinematic approaches for rigid block analysis of masonry walls: State of the art and recent developments," *Buildings*, vol. 7, no. 3, 2017.

[24] Casapulla C., Argiento L. U., Maione A., and Speranza E., "Upgraded formulations for the onset of local mechanisms in multi-storey masonry buildings using limit analysis," *Structures*, vol. 31, no. June, pp. 380–394, 2021, doi: 10.1016/j.istruc.2020.11.083.

[25] "Eurocode 8: Design of structures for earthquake resistance," 2004, doi: 10.1680/cien.144.6.55.40618.

[26] "Norme tecniche per le costruzioni. DM 17/1/2018," *Gazz. Uff. della Repubb. Ital.*, pp. 1–198, 2018.

[27] Casapulla C. and D'Ayala D. F., "In-plane collapse behaviour of masonry walls with frictional resistances and openings," in *Proc. V International Conference on "Structural Analysis of Historical Constructions" (SAHC06)*, 2006, pp. 1159–1166.

[28] Casapulla C. and Argiento L. U., "The comparative role of friction in local out-of-plane mechanisms of masonry buildings. Pushover analysis and experimental investigation," *Eng. Struct.*, vol. 126, pp. 158–173, 2016.

[29] Funari M. F., Pulatsu B., S. S., and Lourenço P. B., "A solution for the frictional resistance in macro-block limit analysis of non-periodic masonry," *Structures*, vol. 43, no. June, pp. 847–859, 2022, doi: 10.1016/j.istruc.2022.06.072.

[30] J. Vaculik, M. C. Griffith, and G. Magenes, “Dry stone masonry walls in bending-Part II: Analysis,” *Int. J. Archit. Herit.*, vol. 8, no. 1, pp. 29–48, 2014, doi: 10.1080/15583058.2012.663060.

[31] Casapulla C. and Maione A., “Out-of-plane local mechanisms in masonry buildings. The role of the orientation of horizontal floor diaphragms,” *Proc. 9th Australas. Mason. Conf. Queenstown, New Zeal.*, no. January 2015, pp. 225–235, 2011.

[32] Portioli F., Casapulla C., Cascini L., D’Aniello M., and Landolfo R., “Limit analysis by linear programming of 3D masonry structures with associative friction laws and torsion interaction effects,” *Arch. Appl. Mech.*, vol. 83, no. 10, pp. 1415–1438, 2013.

[33] A. Orduña and P. B. Lourenço, “Three-dimensional limit analysis of rigid blocks assemblages. Part I: Torsion failure on frictional interfaces and limit analysis formulation,” *Int. J. Solids Struct.*, vol. 42, no. 18–19, pp. 5140–5160, 2005, doi: 10.1016/j.ijsolstr.2005.02.010.

[34] S. Szabó, M. F. Funari, B. Pulatsu, and P. B. Lourenço, “Lateral Capacity of URM Walls: A Parametric Study Using Macro and Micro Limit Analysis Predictions,” *Appl. Sci.*, vol. 12, no. 21, p. 10834, 2022, doi: 10.3390/app122110834.

[35] Doherty K. T., Griffith M. C., Lam N., and Wilson J. L., “Displacement-based seismic analysis for out-of-plane bending of unreinforced masonry walls,” *Earthq. Eng. Struct. Dyn.*, vol. 31, no. 4, pp. 833–850, 2002.

[36] J. Vaculik and M. C. Griffith, “Out-of-plane shaketable testing of unreinforced masonry walls in two-way bending,” *Bull. Earthq. Eng.*, vol. 16, no. 7, pp. 2839–2876, 2018, doi: 10.1007/s10518-017-0282-8.

[37] M. J. N. Priestley, “Displacement-based seismic assessment of reinforced concrete buildings,” *J. Earthq. Eng.*, vol. 1, no. 1, pp. 157–192, 1997, doi: 10.1080/13632469708962365.

[38] Housner G. W., “The behavior of Inverted Pendulum Structures during Earthquakes,” *Bull. Seismol. Soc. Am.*, vol. 53, no. 2, pp. 403–417, 1963.

[39] D’Altri A. M., de Miranda S., Castellazzi G., and Sarhosis V., “A 3D detailed micro-

model for the in-plane and out-of-plane numerical analysis of masonry panels," *Comput. Struct.*, vol. 206, pp. 18–30, 2018.

[40] Petracca M., Pelà L., Rossi R., Zaghi S., Camata G., and Spacone E., "Micro-scale continuous and discrete numerical models for nonlinear analysis of masonry shear walls," *Constr. Build. Mater.*, vol. 149, pp. 296–314, 2017.

[41] Macorini L. and Izzuddin B. A., "A non-linear interface element for 3D mesoscale analysis of brick-masonry structures," *Int. J. Numer. Methods Eng.*, vol. 85, pp. 1584–1608, 2011.

[42] Minga E., Macorini L., and Izzuddin B. A., "Enhanced mesoscale partitioned modelling of heterogeneous masonry structures," *Int. J. Numer. Methods Eng.*, vol. 113, no. 13, pp. 1950–1971, 2018, doi: 10.1002/nme.5728.

[43] Roca P., Cervera M., Pelà L., Clemente R., and Chiumenti M., "Continuum FE models for the analysis of Mallorca Cathedral," *Eng. Struct.*, vol. 46, pp. 653–670, Jan. 2013.

[44] Pantò B., Chisari C., Macorini L., and Izzuddin B. A., "Hybrid continuum-discrete macro-modelling of multi-ring masonry arch bridges," *Comput. Sci.*, pp. 1–44, 2022.

[45] Lemos J. V., "Discrete element modeling of masonry structures," *Int. J. Archit. Herit.*, vol. 1, no. 2, pp. 190–213, 2007.

[46] Bui T. T., Limam A., Sarhosis V., and Hjiaj M., "Discrete element modelling of the in-plane and out-of-plane behaviour of dry-joint masonry wall constructions," *Eng. Struct.*, vol. 136, pp. 277–294, 2017.

[47] Lemos J. V., "Discrete element modeling of the seismic behavior of masonry construction," *Buildings*, vol. 9, no. 2, 2019.

[48] Meriggi P., De Felice G., De Santis S., Gobbin F., Mordanova A., and Pantò B., "Distinct Element Modelling of Masonry Walls under Out-Of-Plane Seismic Loading," *Int. J. Archit. Herit.*, vol. 13, no. 7, pp. 1110–1123, 2019.

[49] Brencich A., Gambarotta L., and Lagomarsino S., "A macroelement approach to the

three-dimensional seismic analysis of masonry buildings," in *11th Europe an Conferen ce on Ear thqua ke Engineering*, 1998, vol. 90, no. JANUARY, pp. 1–10.

[50] Caliò I., Cannizzaro F., and Pantò B., "A macro-element approach for modeling the nonlinear behaviour of monumental buildings under static and seismic loadings," *World Conf. Earthq. Eng.*, 2012.

[51] Quagliarini E., Maracchini G., and Clementi F., "Uses and limits of the Equivalent Frame Model on existing unreinforced masonry buildings for assessing their seismic risk: A review," *J. Build. Eng.*, vol. 10, no. December 2016, pp. 166–182, 2017.

[52] Lagomarsino S., Penna A., Galasco A., and Cattari S., "TREMURI program: An equivalent frame model for the nonlinear seismic analysis of masonry buildings," *Eng. Struct.*, vol. 56, pp. 1787–1799, 2013, doi: https://doi.org/10.1016/j.engstruct.2013.08.002.

[53] Magenes G., "a Method for Pushover Analysis in Seismic Assessment of Masonry Buildings," in *12th World Conference on Earthquake Engineering*, 2000, no. May, pp. 1–8.

[54] Magenes G. and Calvi G. C., "In-plane seismic response of brick masonry walls," *Earthq. Eng. Struct. Dyn.*, vol. 26, no. 11, pp. 1091–1112, 1997, doi: 10.1002/(SICI)1096-9845(199711)26:11<1091::AID-EQE693>3.0.CO;2-6.

[55] Penna A. and Galasco A., "A macro-element model for the nonlinear analysis of masonry members including second order effects," in *ECCOMAS Thematic Conference - COMPDYN 2013: 4th International Conference on Computational Methods in Structural Dynamics and Earthquake Engineering, Proceedings - An IACM Special Interest Conference*, 2013, no. January, pp. 3496–3509.

[56] Pantò B., Caliò I., and Lourenço P. B., "Evaluation of the Seismic Vulnerability of Infill Frame Structures," in *XVII Convengno ANIDIS. L'ingegneria sismica in Italia*, 2017, no. September.

[57] Chácara C., Cannizzaro F., Pantò B., Caliò I., and Lourenço P. B., "Seismic vulnerability of URM structures based on a Discrete Macro-Element Modeling

(DMEM) approach," *Eng. Struct.*, vol. 201, p. 109715, Dec. 2019.

[58] Vadalà F., Cusmano V., Funari M. F., Caliò I., and Lourenço P. B., "On the use of a mesoscale masonry pattern representation in discrete macro-element approach," *J. Build. Eng.*, vol. 50, no. December 2021, 2022.

[59] Ferreira T. M., Costa A. A., and Costa A., "Analysis of the Out-of-Plane Seismic Behavior of Unreinforce Masonry: A Literature Review," *Int. J. Archit. Herit.*, vol. 9, pp. 949–972, 2015.

[60] Doherty K. T., "An investigation of the weak links in the seismic load path of unreinforced masonary buildings," University of Adelaide, 2000.

[61] Gruppo Sismica s.r.l, "HiStrA - Computer program for modelling historical and monumental masonry buildings." Catania, Italy, 2022. [Online]. Available: http://www.lms-grupposismica.it

[62] Priestley M. J. N., "Seismic Behaviour of Unreinforced," *Bull. New Zeal. Soc. Earthq. Eng.*, vol. 18, no. 2, pp. 191–205, 1985.

[63] Al Shawa O., Liberatore D., and Sorrentino L., "Dynamic One-Sided Out-Of-Plane Behavior of Unreinforced-Masonry Wall Restrained by Elasto-Plastic Tie-Rods," *Int. J. Archit. Herit.*, vol. 13, no. 3, pp. 340–357, 2019.

[64] De Felice G. and Giannini R., "Out-of-plane seismic resistance of masonry walls," *J. Earthq. Eng.*, vol. 5, no. 2, pp. 253–271, 2001.

[65] Lam N. T. K., Wilson J. L., and Hutchinson G. L., "The seismic resistance of unreinforce masonry cantilever walls in low seismicity areas," *Bull. New Zeal. Natl. Soc. Earthq. Eng.*, vol. 28, no. 3, pp. 179–195, 1995.

[66] De Felice G., "Out-of-plane seismic capacity of masonry depending on wall section morphology," *Int. J. Archit. Herit.*, vol. 5, no. 4–5, pp. 466–482, 2011.

[67] D'Altri A. M. *et al.*, "Modeling Strategies for the Computational Analysis of Unreinforced Masonry Structures: Review and Classification," *Arch. Comput. Methods Eng.*, vol. 27, pp. 1153–1185, 2020.

[68] da Porto F., Mosele F., and Modena C., "Cyclic out-of-plane behaviour of tall reinforced masonry walls under P-Δ effects," *Eng. Struct.*, vol. 33, no. 2, pp. 287–297, 2011.

[69] Casolo S., "Modelling in-plane micro-structure of masonry walls by rigid elements," *Int. J. Solids Struct.*, vol. 41, no. 13, pp. 3625–3641, 2004.

[70] Casolo S., "A Specific Rigid Element Model for Macro-Scale Dynamics of Monumental Masonry considering Damage and Micro-Structure Effects," *Earthquake*, 2006.

[71] Malomo D., DeJong M. J., and Penna A., "Distinct element modelling of the in-plane failure mechanisms of URM walls," *Proc. Int. Mason. Soc. Conf.*, vol. 0, no. 222279, pp. 581–594, 2018.

[72] Y. Zhang, L. Macorini, and B. A. Izzuddin, "Mesoscale partitioned analysis of brick-masonry arches," *Eng. Struct.*, vol. 124, no. December 2017, pp. 142–166, 2016, doi: 10.1016/j.engstruct.2016.05.046.

[73] Lourenço P. B., "Computations on historic masonry structures," *Prog. Struct. Eng. Mater.*, vol. 4, no. 3, pp. 301–319, 2002.

[74] C. Papantonopoulos, I. N. Psycharis, D. Y. Papastamatiou, J. V. Lemos, and H. P. Mouzakis, "Numerical prediction of the earthquake response of classical columns using the distinct element method," *Earthq. Eng. Struct. Dyn.*, vol. 31, no. 9, pp. 1699–1717, 2002, doi: 10.1002/eqe.185.

[75] Kawai T., "New discrete models and their application to seismic response analysis of structures," *Nucl. Eng. Des.*, vol. 48, no. 1, pp. 207–229, 1978.

[76] Casolo S. and Peña F., "Rigid element model for in-plane dynamics of masonry walls considering hysteretic behavior and damage," *Earthq. Eng. Struct. Dyn.*, no. 36, pp. 1029–1048, 2007, doi: 10.1002/eqe.

[77] P. A. Cundall, "A computer model for simulating progressive, large-scale movements in blocky rock systems," 1971.

[78] Cundall A. P., “Formulation of a three-dimensional distinct element model-Part I. A scheme to detect and represent contacts in a system composed of many polyhedral blocks,” *Int. J. Rock Mech. Min. Sci.*, vol. 25, no. 3, pp. 107–116, 1988.

[79] V. Šmilauer, E. Catalano, and B. Chareyre, “Yade Documentation.” The Yade Project, 2015.

[80] 3DEC, “(3-Dimensional distinct element code).” 2013.

[81] Meguro K. and Tagel-Din H., “Applied Element Method Used for Large Displacement Structural Analysis,” *J. Nat. disaster Sci.*, vol. 24, no. 1, pp. 25–34, 2002.

[82] Meguro K. and Tagel-Din H., “Applied Element Method for Structural Analysis,” *Doboku Gakkai Ronbunshu*, vol. 2000, no. 647, pp. 31–45, 2000.

[83] Malomo D., Pinho R., and Penna A., “Applied Element Modelling of the Dynamic Response of a Full-Scale Clay Brick Masonry Building Specimen with Flexible Diaphragms,” *Int. J. Archit. Herit.*, vol. 14, no. 10, pp. 1484–1501, 2020.

[84] Tomaževic M., “The computer program POR,” *Report ZRMK*. 1978.

[85] Braga G. and Liberatore D., “A finite element for the analysis of the response of masonry buildings,” in *5th North America masonry conference*, 1990, pp. 201–212.

[86] Braga F., Liberatore D., and Spera G., “A computer program for the seismic analysis of complex masonry buildings,” in *Computer Methods in Structural Masonry - 4th International Symposium*, 1997, pp. 309–316.

[87] D’Asdia P. and Viskovic A., “Analyses of a masonry wall subjected to horizontal actions on its plane, employing a non-linear procedure using changing shape finite element,” *Trans. Model. Simul.*, vol. 10, pp. 519–26, 1995.

[88] D’Asdia P. and Viskovic A., “Analisi tridimensionale della resistenza di edifici in muratura, storici e recenti, soggetti ad azioni orizzontali di tipo sismico,” in *Convegno Nazionale La meccanica delle murature tra teoria e progetto*, 1996.

[89] Siano R. *et al.*, “Numerical investigation of non-linear equivalent-frame models for

regular masonry walls," *Eng. Struct.*, vol. 173, no. June, pp. 512–529, 2018.

[90] Gambarotta L. and Lagomarsino S., "On the dynamic response ofmasonry panels," in *Proceedings ofthe National Conference "Masonry Mechanics between Theory and Practice"*, 2014.

[91] Penna A., Lagomarsino S., and Galasco A., "A nonlinear macroelement model for the seismic analysis of masonry buildings," *Earthq. Eng. Struct. Dyn.*, vol. 43, pp. 159–179, 2014.

[92] Caliò I., Marletta M., and Pantò B., "A new discrete element model for the evaluation of the seismic behaviour of unreinforced masonry buildings," *Eng. Struct.*, vol. 40, pp. 327–338, 2012, doi: 10.1016/j.engstruct.2012.02.039.

[93] L. Sorrentino, D. D'Ayala, G. de Felice, M. C. Griffith, S. Lagomarsino, and G. Magenes, "Review of Out-of-Plane Seismic Assessment Techniques Applied To Existing Masonry Buildings," *Int. J. Archit. Herit.*, vol. 11, no. 1, pp. 2–21, 2017, doi: 10.1080/15583058.2016.1237586.

[94] ABK, "Methodology for Mitigation of Seismic Hazards in Existing Unreinforced Masonry Buildings: The Methodology," El Segundo, 1984.

[95] Bruneau M., "State-of-Art report on seismic performance on Unreinforced masonry Buildings," *Can. J. Civ. Eng.*, vol. 21, pp. 512–539, 1994.

[96] Griffith M. C., Magenes G., Melis G., and Picchi L., "Evaluation of out-of-plane stability of unreinforced masonry walls subjected to seismic excitation," *J. Earthq. Eng.*, vol. 7, no. January, pp. 141–169, 2003.

[97] Derakhshan H., Griffith M. C., and Ingham J. M., "Out-of-Plane Behavior of One-Way Spanning Unreinforced Masonry Walls," 2013.

[98] Heyman J., "The stone skeleton," *Int. J. Solids Struct.*, vol. 2, no. 2, pp. 249–279, 1966.

[99] Giuffré A., *Letture sulla meccanica delle murature storiche*, Kappa. Roma, 1989.

[100] Giuffré A., "Mechanics of Historical Masonry and Strengthening Criteria," in *XV*

Regional Seminar of Earthquake Engineering, 1991, pp. 60–122.

[101] D'Ayala D. and Speranza E., "Definition of Collapse Mechanisms and Seismic Vulnerability of Historic Masonry Buildings," *Earthq. Spectra*, vol. 19, no. 3, pp. 479–509, 2003.

[102] Makris N. and Konstantinidis D., "The rocking spectrum and the limitations of practical design methodologies," *Earthq. Eng. Struct. Dyn.*, vol. 32, no. 2, pp. 265–289, 2003.

[103] Priestley M. J. N., Evison R. J., and Carr A. J., "Seismic Response of Structures Free To Rock on Their Foundations.," *Bull. New Zeal. Natl. Soc. Earthq. Eng.*, vol. 11, no. 3, pp. 141–150, 1978.

[104] Aslam M., Godden W. G., and Scalise D. T., "Earthquake rocking response of rigid bodies.," *J. Struct. Div. ASCE*, vol. 106, no. ST2, Proc. Paper, 15182, pp. 377–392, 1980.

[105] Yim C., Chopra A. K., and Penzien J., "Rocking Response of Rigid Blocks to Earthquake," Berkeley, California, 1980.

[106] Ishiyama Y., "Motions of Rigid Bodies and Criteria for Overturning By Earthquake Excitations.," *Bull. New Zeal. Natl. Soc. Earthq. Eng.*, vol. 17, no. 1, pp. 24–37, 1983.

[107] Sorrentino L., Kunnath S., Monti G., and Scalora G., "Seismically induced one-sided rocking response of unreinforced masonry façades," *Eng. Struct.*, vol. 30, no. 8, pp. 2140–2153, 2008.

[108] Sorrentino L., Al Shawa O., and Decanini L. D., "The relevance of energy damping in unreinforced masonry rocking mechanisms. Experimental and analytic investigations," *Bull. Earthq. Eng.*, vol. 9, no. 5, pp. 1617–1642, 2011.

[109] Al Shawa O., De Felice G., Mauro A., and Sorrentino L., "Out-of-plane seismic behaviour of rocking masonry walls," *Earthq. Eng. Struct. Dyn.*, vol. 41, no. 5, pp. 949–968, 2012.

[110] Giouvanidis A. I. and Dimitrakopoulos E. G., “Rocking amplification and strong-motion duration,” *Earthq. Eng. Struct. Dyn.*, vol. 47, no. 10, pp. 2094–2116, 2018.

[111] Giresini L., Fragiacomo M., and Lourenço P. B., “Comparison between rocking analysis and kinematic analysis for the out-of-plane behavior of masonry walls,” in *Pacific Conference on Earthquake Engineering*, 2015, vol. 44, pp. 2359–2376.

[112] Mauro A., De Felice G., and DeJong M. J., “The relative dynamic resilience of masonry collapse mechanisms,” *Eng. Struct.*, vol. 85, pp. 182–194, 2015.

[113] Giresini L. and Sassu M., “Horizontally restrained rocking blocks: evaluation of the role of boundary conditions with static and dynamic approaches,” *Bull. Earthq. Eng.*, vol. 15, no. 1, pp. 385–410, 2017.

[114] Spanos P. D., Roussis P. C., and Politis N. P. A., “Dynamic analysis of stacked rigid blocks,” *Soil Dyn. Earthq. Eng.*, vol. 21, no. 7, pp. 559–578, 2001.

[115] D’Ayala D. and Shi Y., “Modeling masonry historic buildings by multi-body dynamics,” *Int. J. Archit. Herit.*, vol. 5, no. 4–5, pp. 483–512, 2011.

[116] Psycharis I. N., “Dynamic behaviour of rocking two-block assemblies,” *Earthq. Eng. Struct. Dyn.*, vol. 19, no. 4, pp. 555–575, May 1990.

[117] Gabellieri R., Landi L., and Diotallevi P. P., “A 2-DOF model for the dynamic analysis of unreinforced masonry walls in out-of-plane bending,” *ECCOMAS Themat. Conf. - COMPDYN 2013 4th Int. Conf. Comput. Methods Struct. Dyn. Earthq. Eng. Proc. - An IACM Spec. Interes. Conf.*, no. June, pp. 3510–3522, 2013.

[118] Tomassetti U., Graziotti F., Sorrentino L., and Penna A., “Modelling rocking response via equivalent viscous damping,” *Earthq. Eng. Struct. Dyn.*, vol. 48, no. 11, pp. 1277–1296, 2019.

[119] Giouvanidis A. I. and Dimitrakopoulos E. G., *Nonsmooth dynamic analysis of sticking impacts in rocking structures*, vol. 15, no. 5. Springer Netherlands, 2017.

[120] Mehrotra A. and DeJong M. J., “A methodology to account for interface flexibility and crushing effects in multi-block masonry collapse mechanisms,” vol. 55, no. 6,

pp. 1237–1261, 2020.

[121] De Felice G., De Santis S., Lourenço P. B., and Mendes N., "Methods and Challenges for the Seismic Assessment of Historic Masonry Structures," *Int. J. Archit. Herit.*, vol. 11, no. 1, pp. 143–160, 2017.

[122] Vlachakis G., Giouvanidis A. I., Mehrotra A., and Lourenço P. B., "Numerical Block-Based Simulation of Rocking Structures Using a Novel Universal Viscous Damping Model," *J. Eng. Mech.*, vol. 147, no. 11, p. 04021089, 2021.

[123] Galvez F., Sorrentino L., Dizhur D., and Ingham J. M., "Damping considerations for rocking block dynamics using the discrete element method," *Earthq. Eng. Struct. Dyn.*, vol. 51, no. 4, pp. 935–957, 2022.

[124] Anagnostopoulos A. S., "Equivalent viscous damping for modeling inelastic impacts in earthquake pounding problems," *Earthq. Eng. Struct. Dyn.*, vol. 33, no. 8, pp. 897–902, 2004.

[125] Imanishi N., Inque Y., Shibata K., Sato K., and Yamasaki Y., "Effect of Base Shape on Damping of Rocking of Rigid Body," *J. Syst. Des. Dyn.*, vol. 6, no. 1, pp. 109–119, 2012.

[126] DeJong M. J., "Seismic Assessment Strategies for Masonry Structures," 2009.

[127] R. Giannini and R. Masiani, "Risposta in frequenza del blocco rigido: Stabilita delle soluzioni," in *Proc., 10th Italian National Conf. of Theoretical and Applied Mechanics*, 1990.

[128] C.-T. Cheng, "Energy dissipation in rocking bridge piers under free vibration tests," *Earthq. Eng. Struct. Dyn.*, vol. 36, pp. 503–518, 2007, doi: 10.1002/eqe.640.

[129] Costa A. A., "Seismic assessment of the out-of-plane performance of traditional stone masonry walls," 2012.

[130] M. Tomaževic, P. Weiss, and T. Velechovsky, "The influence of rigidity of floors on the seismic behaviour of old stone-masonry buildings," *Eur. Earthq. Eng.*, vol. 5, pp. 28–41, 1991.

[131] D. Benedetti, P. Carydis, and P. Pezzoli, “Shaking table tests on 24 simple masonry buildings,” *Earthq. Eng. Struct. Dyn.*, vol. 27, no. 1, pp. 67–90, 1998, doi: 10.1002/(SICI)1096-9845(199801)27:1<67::AID-EQE719>3.0.CO;2-K.

[132] Lam N. T. K., Griffith M. C., Wilson J. L., and Doherty K. T., “Time-history analysis of URM walls in out-of-plane flexure,” *Eng. Struct.*, vol. 25, no. 6, pp. 743–754, 2003.

[133] Griffith M. C., Vaculik J., Lam N. T. K., Wilson J. L., and Lumantarna E., “Cyclic testing of unreinforced masonry walls in two-way bending,” *Earthq. Eng. Struct. Dyn.*, vol. 36, no. 6, pp. 801–821, May 2007.

[134] Candeias P. X., Campos Costa A., Mendes N., Costa A. A., and Lourenço P. B., “Experimental assessment of the out-of-plane performance of masonry buildings through shaking table tests,” *Int. J. Archit. Herit.*, vol. 11, no. 1, pp. 31–58, 2017.

[135] Costa A., “Determination of mechanical properties of traditional masonry walls in dwellings of Faial Island, Azores,” *Earthq. Eng. Struct. Dyn.*, vol. 31, no. 7, pp. 1361–1382, 2002.

[136] J. G. Tumialan, N. Galati, and A. Nanni, “Field Assessment of Unreinforced Masonry Walls Strengthened with Fiber Reinforced Polymer Laminates,” *J. Struct. Eng.*, vol. 129, no. 8, pp. 1047–1056, 2003, doi: 10.1061/(asce)0733-9445(2003)129:8(1047).

[137] Arêde A., Costa A., Costa A. A., Oliveira C., and Neves F., “Experimental In-Situ Testing of Typical Masonry Constructions of Faial Island-Azores,” *14th world Conf. Earthq. Eng. Beijing, China*, no. June 2017, pp. 12–14, 2008.

[138] Dizhur D., Derakhshan H., Lumantarna R., Ingham J. M., and Griffith M. C., “In-situ out-of-plane testing of unreinforced masonry wall segment in Wintec Block F building,” in *Proceedings of the 11th Canadian Masonry Symposium*, 2009, pp. 1–8.

[139] N. Ismail and J. M. Ingham, “In-situ and laboratory based out-of-plane testing of unreinforced clay brick masonry walls strengthened using near surface mounted

twisted steel bars," *Constr. Build. Mater.*, vol. 36, pp. 119–128, 2012, doi: 10.1016/j.conbuildmat.2012.04.087.

[140] Sorrentino L., D'Ayala D., de Felice G., Griffith M. C., Lagomarsino S., and Magenes G., "Review of Out-of-Plane Seismic Assessment Techniques Applied To Existing Masonry Buildings," *Int. J. Archit. Herit.*, vol. 11, no. 1, pp. 2–21, 2017.

[141] *Eurocode 6: Design of masonry structures*. 2005.

[142] Ministero Delle Infrastrutture E Dei Trasporti, "Istruzioni per l'applicazione dell'<<Aggiornamento delle 'Norme Tecniche per le Costruzioni'>> di cui al Decreto Ministeriale 17 gennaio 2018." 2019.

[143] Giuffré A., "A Mechanical Model for Statics and Dynamics of Historical Masonry Buildings," in *Protection of the Architectural Heritage Against Earthquakes*, Springer Vienna, 1996, pp. 71–152. doi: 10.1007/978-3-7091-2656-1_4.

[144] Lagomarsino S. and Resemini S., "The Assessment of Damage Limitation State in the Seismic Analysis of Monumental Buildings," *Earthq. Spectra*, vol. 25, May 2009.

[145] Magenes G., Penna A., Senaldi I. E., Rota M., and Galasco A., "Shaking Table Test of a Strengthened Full-Scale Stone Masonry Building with Flexible Diaphragms," *Int. J. Archit. Herit.*, vol. 8, no. 3, pp. 349–375, May 2014.

[146] P. Fajfar, "Capacity spectrum method based on inelastic demand spectra," *Earthq. Eng. Struct. Dyn.*, vol. 28, no. 9, pp. 979–993, 1999, doi: 10.1002/(SICI)1096-9845(199909)28:9<979::AID-EQE850>3.0.CO;2-1.

[147] G. Guerrini, F. Graziotti, A. Penna, and G. Magenes, "Improved evaluation of inelastic displacement demands for short-period masonry structures," *Earthq. Eng. Struct. Dyn.*, vol. 46, no. 9, pp. 1411–1430, 2017, doi: 10.1002/eqe.2862.

[148] Pantò B., "Un Nuovo Macromodello Per La Valutazione Della Resistenza Sismica Di Edifici in Muratura," University of Catania, 2004.

[149] Pantò B., Cannizzaro F., Caddemi S., and Caliò I., "3D macro-element modelling

approach for seismic assessment of historical masonry churches," *Adv. Eng. Softw.*, vol. 97, pp. 40–59, 2016.

[150] Cannizzaro F., Pantò B., Caddemi S., and Caliò I., "A Discrete Macro-Element Method (DMEM) for the nonlinear structural assessment of masonry arches," *Eng. Struct.*, vol. 168, no. October 2020, pp. 243–256, 2018.

[151] Pantò B., Cannizzaro F., Caliò I., and Lourenço P. B., "Numerical and Experimental Validation of a 3D Macro-Model for the In-Plane and Out-Of-Plane Behavior of Unreinforced Masonry Walls," *Int. J. Archit. Herit.*, vol. 11, no. 7, pp. 946–964, 2017.

[152] Chácara C., L. P. B., and C. F., "Macro-element mass matrix for the dynamic assessment of unreinforced masonry structures," *Congr. Métodos Numéricos en Ing.*, no. July, 2017.

[153] Macorini L. and Izzuddin B. A., "A non-linear interface element for 3D mesoscale analysis of brick masonry structures," *Int. J. Numer. Methods Eng.*, no. February, pp. 1102–1119, 2010.

[154] Caliò I. and Pantò B., "A macro-element modelling approach of Infilled Frame Structures," *Comput. Struct.*, vol. 143, pp. 91–107, 2014, doi: 10.1016/j.compstruc.2014.07.008.

[155] Cannizzaro F., "The seismic behavior of historical buildings: a macro-element approach," University of Catania, 2010.

[156] C. J. Chácara E., "Macro-Element Nonlinear Dynamic Analysis for the Assessment of the Seismic Vulnerability of Masonry Structures. (PhD thesis)," *PhD Thesis*, no. February, pp. 1–173, 2018.

[157] T. Takeda, "Reinforced Concrete response to simulated earthquakes," *J. Struct. Div.*, vol. 96, pp. 2557–2573, 1970.

[158] S. Mazzoni, F. Mckenna, M. H. Scott, and G. L. Fenves, "OpenSees User Manual." University of California, Berkley, U.S.A., 2000.

[159] Turnšek V. and Čačovič F., "Some experimental results on the strength of brick masonry walls," in *Proceedings of the 2nd International Brick Masonry Conference*, 1971, pp. 149–156.

[160] Turnšek V. and S. P., "The shear and flexural resistance of masonry walls," in *Proceedings of international research conference on earthquake engineering*, 1981, pp. 517–73.

[161] Cusmano V., Pantò B., Rapicavoli D., and Caliò I., "A Discrete Macro-Element Approach accounti for P-Delta Effects," *Earthq. Eng. Struct. Dyn.*, 2023, doi: 10.1002/eqe.3867.

[162] L. Corradi dell'Acqua, *Meccanica delle strutture - Le toerie strutturale e il metodo degli elementi finiti*. 1992.

[163] de B. Renè, M. A. Crisfield, J. J. C. Remmers, and C. V. Verhoosel, *Non-linear Finite Element Analysis of Solids and Structures*, Second. 2012.

[164] Malena M., Portioli F., Gagliardo R., Tomaselli G., Cascini L., and De Felice G., "Collapse mechanism analysis of historic masonry structures subjected to lateral loads: A comparison between continuous and discrete models," *Comput. Struct.*, vol. 220, pp. 14–31, 2019.

[165] Pantò B., Casapulla C., and Caliò I., "Discrete rotating links model for the non-linear torsion−shear behaviour of masonry joints," in *Proceedings of the Institution of Civil Engineers - Engineering and Computational Mechanics*, 2021, vol. 174, no. 4, pp. 215–235.

[166] Griffith M. C., Lam N. T. K., Wilson J. L., and Doherty K. T., "Experimental Investigations of Unreinforced Brick Masonry Walls in Flexure," *J. Struct. Eng.*, vol. 130, no. 3, pp. 423–432, 2004.

[167] Minga E., "3D Meso- and Macro-Scale Models for Nonlinear Analysis of Masonry Systems," Imperial College, London, 2017.

[168] Pantò B., Macorini L., and Izzuddin B. A., "A two-level macroscale continuum description with embedded discontinuities for nonlinear analysis of brick/block

masonry," *Comput. Mech.*, vol. 69, no. 3, pp. 865–890, 2022.

[169] Milani G., "3D upper bound limit analysis of multi-leaf masonry walls," *Int. J. Mech. Sci.*, vol. 50, no. 4, pp. 817–836, 2008.

[170] Peña F., Prieto F., Lourenço P. B., Campos Costa A., and Lemos J. V., "On the dynamics of rocking motion of single rigid-block structures," *Earthq. Eng. Struct. Dyn.*, vol. 36, pp. 2383–2399, 2007, doi: 10.1002/eqe.739.

[171] C. J. E. Chácara, P. B. Lourenco, B. Pantò, F. Cannizzaro, and I. Caliò, "Macro-element Mass Matrix for the Dynamic Assessment of Unreinforced Masonry Structures," *Congr. Métodos Numéricos en Ing.*, no. July, 2017.

[172] L. Giresini, C. Casapulla, R. Denysiuk, J. Matos, and M. Sassu, "Fragility curves for free and restrained rocking masonry façades in one-sided motion," *Eng. Struct.*, vol. 164, no. March, pp. 195–213, 2018, doi: 10.1016/j.engstruct.2018.03.003.

[173] Giresini L., Pantò B., Caddemi S., and Caliò I., "Out-of-plane seismic response of masonry façades using discrete macro-element and rigid block models," in *COMPDYN Proceedings*, 2019, vol. 1, no. June, pp. 702–717.

[174] M. F. Funari, A. Mehrotra, and P. B. Lourenço, "A tool for the rapid seismic assessment of historic masonry structures based on limit analysis optimisation and rocking dynamics," *Appl. Sci.*, vol. 11, no. 3, pp. 1–22, 2021, doi: 10.3390/app11030942.

[175] V. Cusmano, B. Pantò, C. Casapulla, and I. Caliò, "OUT-OF-PLANE RESPONSE OF MASONRY CHURCH FACADES INCLUDING P-DELTA EFFECTS," in *Proceedings of the 9th ECCOMAS Thematic Conference on Computational Methods in Structural Dynamics and Earthquake Engineering (COMPDYN2023)*, 2023.

[176] Giresini L., Casapulla C., Denysiuk R., Matos J., and Sassu M., "Fragility curves for free and restrained rocking masonry façades in one-sided motion," *Eng. Struct.*, vol. 164, no. March, pp. 195–213, 2018.

[177] Casapulla C., Giresini L., Argiento L. U., and Lagomarsino S., "Incremental Static and Dynamic Analyses of the Out-of-Plane Response of a Incremental Static and

Dynamic Analyses of the Out-of-Plane Response of a Masonry Church damaged by 2016-2017 Central Italy Earthquakes," *Proc. XVII ANIDIS Conf. "L'ingegneria sismica Ital.*, no. September, 2017.

[178] P. K. Dhir, E. Tubaldi, A. Orfeo, and H. Ahmadi, "Cyclic shear behaviour of masonry triplets with rubber joints," *Constr. Build. Mater.*, vol. 351, no. September, 2022, doi: 10.1016/j.conbuildmat.2022.128356.